

ABSTRACT

Nondestructive Inspection and Characterization of Complex Engineering Materials via Ultrasound Techniques

Sarah L. Stair, Ph.D.

Mentor: David A. Jack, Ph.D.

Nondestructive evaluation methods have grown increasingly popular and necessary in a variety of industries. For example, the aerospace industry uses such techniques to inspect aircraft components for damage prior to making a repair. The focus of the present dissertation is the development of ultrasonic techniques for inspecting highly attenuative materials.

The first study presented in this work involved a pulse-echo ultrasound technique for inspecting damage at the bondline between a carbon fiber reinforced laminated composite and aluminum. The sample was inspected from both the aluminum side as well as from the composite side, and the areas of delamination were successfully identified. The novelty of this inspection technique was the bondline inspection between dissimilar materials since previous studies focused on the bondline inspection between similar materials.

The second study presented in this dissertation involved using a normal incidence through transmission ultrasound technique for monitoring the phase and temperature of a

material. Using the proposed technique, two different waxes, EcoSoya wax and Rigidax machinist wax, were inspected as they were melted and allowed to re-solidify. From the results of the study, the phase of the material can be identified from the ultrasound data, and a correlation between the ultrasound data and temperature data was identified.

The final study of this dissertation involved the design and implementation of an oblique-incidence through transmission c-scan ultrasound technique. As laminated composites are incorporated into new aircraft, there is an increased desire for nondestructive methods for not just damage inspections but also for characterizing the material properties of the part post-manufacturing or after extended use in the field. Aluminum and carbon fiber reinforced laminated composites were inspected with this technique, and the wave scatter was observed using a c-scan technique. The wave scatter varied considerably from the isotropic aluminum plate to the laminated composite plate, and the wave scatter is shown to be a function of the number of lamina within the part. Future work involves comparing the measured results from this dissertation with results generated via a mathematical model, based on the model developed by Newberry [1], to determine the elastic constants of the laminated composite.

Nondestructive Inspection and Characterization of Complex Engineering Materials via
Ultrasound Techniques

by

Sarah L. Stair, B.S.M.E., M.S.M.E.

A Dissertation

Approved by the Department of Mechanical Engineering

Kenneth Van Treuren, Ph.D., Chairperson

Submitted to the Graduate Faculty of
Baylor University in Partial Fulfillment of the
Requirements for the Degree
of
Doctor of Philosophy

Approved by the Dissertation Committee

David A. Jack, Ph.D., Chairperson

David G. Moore, M.S.M.E.

Byron Newberry, Ph.D.

William Jordan, Ph.D.

Jill Klentzman, Ph.D.

Yang Li, Ph.D.

Accepted by the Graduate School
August 2017

J. Larry Lyon, Ph.D., Dean

Copyright © 2017 by Sarah L. Stair

All rights reserved

TABLE OF CONTENTS

ABSTRACT.....	i
TABLE OF CONTENTS.....	v
LIST OF FIGURES	vii
ACKNOWLEDGMENTS	xxii
DEDICATION.....	xxiv
CHAPTER ONE.....	1
Introduction.....	1
CHAPTER TWO	10
Review of Literature	10
2.1 Introduction.....	10
2.2 Manufacturing Laminated Composites.....	13
2.3 The Need for Nondestructive Inspection Methods for Composite Materials	19
2.4 Basic NDE Terminology with an Emphasis on Ultrasound Terminology	22
2.5 Ultrasound Techniques for Monitoring Temperature.....	31
2.6 Nondestructively Evaluating Porosity	35
2.7 NDE of Transversely Isotropic Laminated Composites	38
2.8 Applications Involving Two or More Components Bonded Together	41
2.9 NDE Methods for Evaluating Bondlines	43
2.10 Conclusion	50
CHAPTER THREE	52
Ultrasound Methods for Inspecting the Bondline between a Carbon Fiber Reinforced Laminated Composite and Aluminum.....	52
3.1 Introduction.....	52
3.2 Sample Preparation	53
3.3 Contact Ultrasound Transducer Technique	62
3.4 Immersion Ultrasound Pulse Echo Technique.....	71
3.5 Conclusions from the Bondline Study	86

CHAPTER FOUR.....	89
Identification of Phase Change and Temperature of Highly Attenuative Materials via a Through Transmission Ultrasound Technique	89
4.1 Introduction.....	89
4.2 EcoSoya Wax Experiment	90
4.3 Machinist Wax – Small Acrylic Box	136
4.4 Machinist Wax Experimental Results – Small Steel Box.....	169
4.5 Conclusions and Future Work	191
CHAPTER FIVE	199
Oblique Incidence, Through Transmission Ultrasound Method for Inspecting Carbon Fiber Reinforced Laminated Composites	199
5.1 Introduction.....	199
5.2 Experimental Setup and Snell’s Law Calculations for Aluminum Plate	201
5.3 C-scan Measurement Results for the Aluminum Plate	211
5.4 C-scan Inspection of Carbon Fiber Reinforced Laminated Composites	214
5.5 Summary and Future Work.....	225
CHAPTER SIX.....	228
Conclusions and Future Work	228
6.1 Conclusions.....	228
6.2 Future Work	232
APPENDICES	242
APPENDIX A.....	243
Additional Results from Bondline Inspection	243
A.1 Contact Transducer Results	243
A.2 Immersion Inspection Results	247
APPENDIX B	249
Results from Additional Wax Experiments	249
B.1 Results from EcoSoya Experiment Two	249
B.2 Results from EcoSoya Experiment Three	269
B.3 Results from EcoSoya Experiment Four	289
B.4 Results from Machinist Wax in Small Acrylic Box Experiment Two.....	308
BIBLIOGRAPHY.....	322

LIST OF FIGURES

Figure 2.1. The (a) BMW i8 automobile incorporates carbon fiber reinforced laminated composites into the (b) frame as indicated by the blue arrow.....	11
Figure 2.2. Ultrasound methods for identifying a defect within a part using (a) an unfocused probe and (b) a spherically focused probe.....	23
Figure 2.3. Ultrasound techniques commonly used for inspecting samples include (a) through transmission method and (b) pulse echo method. In the diagram above, the black arrows refer to the direction of travel for the ultrasound wave	25
Figure 2.4. B-scan image of aluminum bonded to a 12 ply carbon fiber reinforced laminated composite. The unbonded area between the two materials is highlighted by the red arrow	26
Figure 2.5. C-scan representation of the ultrasound signal as it propagates through the aluminum-to-composite bond. The laminate in this case is 12 plies thick. The red area of the C-scan indicates an unbonded area where the reflected wave has a high signal amplitude and the blue area indicates a bonded area with a low signal amplitude.....	27
Figure 3.1. (a) The top surface of the co-cured carbon fiber reinforced laminated composite bonded to an aluminum step wedge. (b) A side view of the co-cured sample	55
Figure 3.2. The thickness associated with the 12 ply, 8 ply and 4 ply laminates are shown from left to right, respectively	56
Figure 3.3. Ultragel II Ultrasonic Couplant (a) being applied to the sample surface and (b) being smeared across the surface to form a more even layer prior to the laminate being placed on the surface	59
Figure 3.4. The area coated in ultrasound gel is encompassed by the red dashed line and the area denoted by the blue arrows is starved of the ultrasound gel.....	61
Figure 3.5. The area encompassed by the red dashed lines correspond to areas that are wetted with ultrasound couplant. Outside of the areas indicated by the red dashed lines there is no ultrasound couplant.....	61
Figure 3.6. Experimental setup with the contact transducer placed at the center of the 4 ply laminate region of the bonded sample.	62

Figure 3.7. (a) The contact probe is placed on the aluminum surface. The A-scan (upper image) and FFT (lower image) results are presented for the (b) unbonded and (c) bonded cases. The vertical dashed line represents the operating frequency of the probe 65

Figure 3.8. (a) The contact probe is placed in on the surface of the carbon fiber reinforced laminate. The A-scan (upper image) and FFT (lower image) results are presented for the (b) unbonded and (c) bonded cases. The vertical dashed line corresponds to the operating frequency of the probe 72

Figure 3.9. (a) This C-scan image for the aluminum-to-composite bondline for the 12 ply laminate. (b) The A-scan signal associated with the unbonded location marked ‘x’ in (a). (c) The A-scan signal associated with the bonded location marked ‘+’ in (a) 75

Figure 3.10. (a) The C-scan obtained while inspecting the composite-to-aluminum bondline. The light blue region indicates an unbonded location whereas the dark blue region indicates a bonded region. (b) The A-scan associated with the unbonded location marked by ‘x’. (c) The A-scan for the bonded location marked by ‘+’ 78

Figure 3.11. The C-scan image results for the immersion ultrasound testing with the aluminum surface facing the transducer. Unbonded locations are highlighted by arrows 79

Figure 3.12. The C-scan results obtained for the immersion ultrasound testing with the aluminum surface facing the transducer. Unbonded regions are labeled with arrows 81

Figure 3.13. The C-scan image results for the immersion ultrasound testing with the carbon fiber reinforced laminated composite surface facing the transducer. The C-scan for the 12 ply laminate is farthest left, the C-scan for the 8 ply laminate is located in the middle, and the C-scan for the 4 ply laminate is located farthest right 81

Figure 3.14. The C-scan results associated with scanning the sample with the composite laminate facing the transducer. The 12 ply laminate region is on the far left and the 4 ply laminate region is on the far right 82

Figure 3.15. (a) The C-scan associated with the aluminum-to-composite bondline for the 12 ply laminate region and (b) the FFT of the ultrasound signal located within the A-scan gate for the unbonded (red) and bonded (blue) locations corresponding to the ‘x’ and the ‘+’, respectively, in the C-scan image in (a) 84

Figure 3.16. (a) The C-scan associated with the composite-to-aluminum bondline for the 12 ply laminate region and (b) the FFT of the ultrasound signal within the A-scan gate for the unbonded (red) and bonded (blue) locations corresponding to the 'x' and the '+' in the C-scan image in (a).....	85
Figure 4.1. Top view diagram of the experimental setup and dimensions associated with the box as well as the placement of the ultrasound probes.....	91
Figure 4.2. Top view diagram of the experimental setup and dimensions for the placement of the thermocouples	92
Figure 4.3. Side view of the experimental setup and dimensions for the placement of the components used in the experiment. The * in the figure refers to the average thermocouple depth. The square is the heater block and the circles indicate transducers	93
Figure 4.4. The Watlow EZ-Zone temperature controller	94
Figure 4.5. Experimental setup in the laboratory with each of the components labeled ..	95
Figure 4.6. Channel listing for the experimental setup used with the EcoSoya wax.....	96
Figure 4.7. A-scan signal associated with the solid EcoSoya wax. The black dot indicates the first point that meets or exceeds the amplitude threshold.....	98
Figure 4.8. A-scan signal associated with the liquid EcoSoya wax. The black dot indicates the first point that meets or exceeds the amplitude threshold.....	100
Figure 4.9. B-scan for channel 4, which is located farthest away from the heater. Although the experiment time and gate time correspond to the horizontal and vertical axes, respectively, the greyscale colors observed in Figure 4.9 directly correspond to the A-scan signal amplitude, and the interpretation of this image will be discussed in the following section	102
Figure 4.10. Highlighting the sections of interest in the B-scan.....	104
Figure 4.11. The EcoSoya wax does not melt much below the heater block depth	105
Figure 4.12. (a) The B-scan associated with Channel 4 where the solid black line corresponds to the high amplitude region shown in the (b) A-scan for the solid EcoSoya wax and dashed black line corresponds to (c) the A-scan for the liquid EcoSoya wax.....	106
Figure 4.13. The speed of sound for channel 1 (top), which is located closest to the heater, and the temperature measured via thermocouples throughout the experiment (bottom).....	109

Figure 4.14. The speed of sound for channel 2 (top) and the temperature measured via thermocouples throughout the experiment (bottom).....	110
Figure 4.15. The speed of sound for channel 3 (top) and the temperature measured via thermocouples throughout the experiment (bottom).....	111
Figure 4.16. The speed of sound for channel 4 (top) and the temperature measured via thermocouples throughout the experiment (bottom).....	112
Figure 4.17. Comparing the calculated speed of sound for channels 4 and 14.....	114
Figure 4.18. Comparing the calculated speed of sound for channels 1 through 4.....	115
Figure 4.19. The temperatures throughout the experimental setup as monitored by the thermocouples. The average temperature for each bar of thermocouples has been included in this image along with the temperature at the heater block	116
Figure 4.20. Experimental diagram with the ultrasound probe locations and the thermocouple locations relative to the box. The thermocouple estimations (purple) are also indicated relative to the actual thermocouples (orange).	118
Figure 4.21. The temperatures calculated along the ultrasound probe path for channels 1 through 4	119
Figure 4.22. The speed of sound versus temperature for channel 1, which is located closest to the heater block	120
Figure 4.23. The speed of sound versus temperature at channel 2	122
Figure 4.24. The speed of sound versus temperature for channel 3	123
Figure 4.25. Speed of sound versus temperature for channel 4	124
Figure 4.26. A diagram of the one dimensional heat transfer problem	125
Figure 4.27. A diagram defining the lengths, temperatures, h_L and h_S , used in the finite element model calculations	125
Figure 4.28. Temperature distribution between thermocouple bars 1 and 2 as determined from the finite element analysis of the one-dimensional heat transfer problem	126
Figure 4.29. Comparison of the results obtained via the finite element analysis of the one-dimensional heat transfer problem and a linear distribution of temperatures between thermocouple bars 1 and 2.....	127

Figure 4.30. Comparison of the speed of sound versus temperature plots for channels 1 through 4. The heating portion of the curves is provided in the red and purple colors whereas the cooling portion of the curves (when the heater is off) is provided in the blue and green colors	128
Figure 4.31. Speed of sound versus temperature where the axes have been reduced such that the material's transition from solid to liquid during the melting stage is highlighted by the near step change in speed of sound.....	129
Figure 4.32. Comparison of the A-scans obtained for channels 1 through 4 at 24 minutes into the experiment.....	130
Figure 4.33. Speed of sound versus temperature as the material is cooling	132
Figure 4.34. A-scans for channels 1 through 4 when the wax is liquid (at 169 minutes into the experiment)	133
Figure 4.35. Comparison of the speed of sound versus temperature plots at channel 4 for all four of the EcoSoya experiments performed	134
Figure 4.36. Comparison of the speed of sound versus temperature results for channel 4 in all of the EcoSoya tests as the material is re-solidifying	134
Figure 4.37. A-scan (left) and Fast Fourier Transform (right) results for solid machine wax at 24 minutes into the test	135
Figure 4.38. A-scan (left) and Fast Fourier Transform (right) results for liquid machine wax at 169 minutes into the test	136
Figure 4.39. (a) The solid EcoSoya wax and (b) the solid machinist wax in their respective experimental setup configurations. The EcoSoya wax has a smoother texture than the pellet-like appearance of the machinist wax	137
Figure 4.40. Drawing of the experimental setup of ultrasound probe placement for the machinist wax experiment with the small acrylic box. All dimensions are inner dimensions and do not include wall thickness	138
Figure 4.41. Top view diagram for the placement of thermocouples in the machinist wax experimental setup.....	139
Figure 4.42. Side view of the experimental setup for the machinist wax experiment in the small acrylic box. All dimensions provided are inner dimensions and do not include the wall thickness. The rectangle represents the heater block and the circles represent transducers	140

Figure 4.43. Channel listing for the experimental setup used with the machinist wax experiment in the acrylic box.....	142
Figure 4.44. DSC experimental setup and chamber. The sample is located in one of the small pans in the zoomed in callout image	143
Figure 4.45. The DSC test results for the machinist wax for a heat/cool/heat/cool cycle where the blue line represents the temperature being varied by 1 °C/min and the red line corresponds to the temperature being changed by 2 °C/min.....	144
Figure 4.46. The DSC results for the heat/cool/heat/cool experiment performed in both the 1°C/min test (blue) and the 2 °C/min test (red).	146
Figure 4.47. A-scan associated with the solid machinist wax 59 minutes into the test ..	147
Figure 4.48. A-scan associated with the liquid machinist wax at 249 minutes into the machinist wax melt test.....	148
Figure 4.49. B-scan for channel 1 data	149
Figure 4.50. B-scan for channel 1 data with specific the solid and liquid portions of the experiment highlighted by ovals, the transition from solid to liquid highlighted by (i) and the dashed line indicating the heater was turned off.....	150
Figure 4.51. Speed of sound (top) and temperature as measured by thermocouples for data collected at channel 1, which is closest to the heater block	152
Figure 4.52. Speed of sound (top) and temperature as measured by thermocouples for data collected at channel 2, which is farthest from the heater block	153
Figure 4.53. A-scans for the machinist wax along channel 1 at minutes (a) 27, (b) 29, (c) 37 and (d) 38.	155
Figure 4.54. Speed of sound results for channel 1 (top) and channel 2 (bottom) when a 30% signal threshold was used to determine the TOF.....	156
Figure 4.55. Comparison of the speed of sound results for channels 1 and 1b	157
Figure 4.56. Comparison of the speed of sound results for channels 1 (closest to the heater block) and 2 (farthest from the heater block).....	158
Figure 4.57. Temperature values as obtained from thermocouple measurements throughout the experiment	159
Figure 4.58. Diagram of the temperature estimation locations relative to the probe channels as well as the remaining components in the experimental setup	160

Figure 4.59. The average temperature estimates obtained for the ultrasound probe path at channels 1 and 2 in the experimental setup.....	161
Figure 4.60. Speed of sound versus temperature plot for channel 1	162
Figure 4.61. Speed of sound versus temperature plot for channel 2.....	164
Figure 4.62. Comparison of the speed of sound versus temperature plot for channel 1 and channel 2. The red and purple lines represent the heater being on during each test whereas the blue and green lines correspond to the cooling portion of each experiment.....	165
Figure 4.63. Comparison of the speed of sound versus temperature results for channels 1 and 2 as the machinist wax cools.....	166
Figure 4.64. A-scan (left) and Fast Fourier Transform (right) results for solid machinist wax at 59 minutes into the test.....	167
Figure 4.65. A-scan (left) and Fast Fourier Transform (right) results for liquid machinist wax at 249 minutes into the test.....	168
Figure 4.66. Top view of the experimental setup for the machinist wax experiment in the steel box. The digital drawing was provided by Sandia National Laboratories .	170
Figure 4.67. Three-dimensional representation of the steel box experimental setup used for this experiment. The digital drawing was provided by Sandia National Laboratories	171
Figure 4.68. Side view diagram of the experiment, which highlights the location of the heater relative to the ultrasound probes. The digital drawing was provided by Sandia National Laboratories.....	172
Figure 4.69. Channel listing for the ultrasound probes used in the machinist wax experiment with the steel box. The digital drawing was provided by Sandia National Laboratories.....	173
Figure 4.70. Photograph taken of the experimental setup. The melted wax is propagating upward along the all-thread and across the top surface of the wax. This photograph was provided by Sandia National Laboratories.....	174
Figure 4.71. A-scan for the solid machinist wax at 24 minutes into the experiment.....	175
Figure 4.72. A-scan for the liquid machinist wax at 129 minutes into the experiment..	176
Figure 4.73. B-scan for channel 1	177

Figure 4.74. Explaining the B-scan for channel 1 by highlighting important features...	178
Figure 4.75. B-scan for channel 2	179
Figure 4.76. Speed of sound calculations for channel 1	180
Figure 4.77. Speed of sound calculations for channel 2	181
Figure 4.78. Explaining the discontinuities in the speed of sound graph (bottom) by comparing it with the B-scan (top).	182
Figure 4.79. The speed of sound versus time plot (top) and temperature versus time plot (bottom) for channel 1 using a higher signal intensity threshold	183
Figure 4.80. Speed of sound versus time plot (top) and temperature versus time plot (bottom) for channel 2 with the modified vertical axis.....	183
Figure 4.81. Comparison between the speed of sound for channels 1 and 2.....	184
Figure 4.82. The speed of sound versus temperature plot for channel 1. The red curve corresponds to the heater being on whereas the blue curve represents the heater being turned off and the machinist wax cooling.....	185
Figure 4.83. The speed of sound versus temperature plot for channel 2. The red curve corresponds to the heater being on whereas the blue curve represents the heater being turned off and the machinist wax cooling.....	186
Figure 4.84. Comparison of the speed of sound versus temperature plots for channels 1 and 2.....	187
Figure 4.85. Comparison of the speed of sound versus temperature plots for channels 1 and 2 where the box width across channel 2 was decreased by 1 millimeter.....	188
Figure 4.86. Comparison of the speed of sound versus temperature results for channel 1 in the experiments performed at Baylor University and channel 2 in the experiment performed at Sandia National Laboratories	189
Figure 4.87. A-scan (left) and Fast Fourier Transform (right) results for solid machine wax at 24 minutes into the test	190
Figure 4.88. A-scan (left) and Fast Fourier Transform (right) results for solid machine wax at 129 minutes into the test	191
Figure 4.89. The ultrasound wave along channel 1 in an EcoSoya wax experiment encounters a solid wax region followed by a liquid wax region followed by another solid wax region.....	198

Figure 5.1. BMW i8 present at the 2015 Society of Plastics Engineers Automotive Composites Conference and Exhibition in Novi, Michigan. Photo by author.....	200
Figure 5.2. Side view diagram of experimental setup	201
Figure 5.3. The receiver was rotated to a new angle relative to the horizontal axis.....	202
Figure 5.4. The receiver orientation was changed from 5 degrees to 14 degrees relative to the horizontal axis.....	203
Figure 5.5. The geometry of the pulser relative to the different receiver probe angles..	204
Figure 5.6. A visual representation of the geometry defining the distance in water between the pulser at 5° orientation and the receiver at 14° orientation	204
Figure 5.7. Experimental setup with the aluminum sample placed between the pulser and receiver ultrasound probes	205
Figure 5.8. Top view photograph of the experimental setup configuration.....	206
Figure 5.9. Side photograph of the experimental setup configuration.....	206
Figure 5.10. Graphical depiction of the components used in Snell’s Law calculations for the shear wave propagating through the aluminum	208
Figure 5.11. Diagram of the components used in the Snell’s Law calculations for the longitudinal wave propagating through the thickness of the aluminum sample.....	209
Figure 5.12. Diagram of the components used in the Snell’s law calculations for both the longitudinal and shear waves. The diagram shows the shear and longitudinal wave relative to one another within the sample.....	209
Figure 5.13. C-scan results for the aluminum plate	212
Figure 5.14. C-scan and A-scan signal comparison.....	213
Figure 5.15. Diagram of 8 harness satin woven fabric	215
Figure 5.16. C-scan for oblique incidence through transmission ultrasound wave propagating through an 8 ply carbon fiber reinforced laminated composite	216
Figure 5.17. Comparing the A-scans to locations on the C-scan for the inspection of an 8 ply carbon fiber reinforced laminated composite.....	217

Figure 5.18. Frequency intensity plot corresponding to the 5 MHz component of the FFT analysis performed on each A-scan from the C-scan provided in Figure 5.17	219
Figure 5.19. C-scan results for varying the incident angle for the ultrasound wave (by varying the orientation of the pulser relative to the sample surface normal).....	220
Figure 5.20. C-scan results for varying the angle of the receiving probe relative to the sample surface normal	222
Figure 5.21. C-scan results for rotating 8 ply laminate sample with respect to the z axis	223
Figure 5.22. C-scan results obtained for 2, 4, 8, and 16 ply laminated composites with the pulse oriented at 10° and the receiver oriented at 18°	224
Figure A.1. (a) Contact transducer inspection of aluminum-to-composite bondline for 4 ply laminate region. Results for (b) no couplant and (c) couplant between the two adherends	243
Figure A.2. (a) Contact transducer inspection of aluminum-to-composite bondline for 8 ply laminate region. Results for (b) no couplant and (c) couplant between the two adherends.	244
Figure A.3. (a) Contact transducer inspection of composite-to-aluminum bondline for 4 ply laminate region. A-scan (top) and FFT (bottom) results for (b) no couplant and (c) couplant between the two adherends	245
Figure A.4. (a) Contact transducer inspection of composite-to-aluminum bondline for 8 ply laminate region. Results for (b) no couplant and (c) couplant between the two adherends	246
Figure A.5. (a) C-scan image of the bondline at the aluminum-to-composite interface for the 4 ply laminate region of the co-cured sample inspected with the immersion ultrasound method. (b) FFT results for the gated region of the A-scan corresponding to the bondline.....	247
Figure A.6. (a) C-scan image of the bondline at the aluminum-to-composite interface for the 8 ply laminate region of the co-cured sample inspected with the immersion ultrasound method. (b) FFT results for the gated region of the A-scan corresponding to the bondline.....	247
Figure A.7. (a) C-scan image of the bondline at the composite-to-aluminum interface for the 4 ply laminate region of the co-cured sample inspected with the immersion ultrasound method. (b) FFT results for the gated region of the A-scan corresponding to the bondline.....	248

Figure A.8. (a) C-scan image of the bondline at the aluminum-to-composite interface for the 8 ply laminate region of the co-cured sample inspected with the immersion ultrasound method. (b) FFT results for the gated region of the A-scan corresponding to the bondline.....	248
Figure B.1. A-scan signal associated with the solid EcoSoya wax. The black dot indicates the first point that meets or exceeds the amplitude threshold.....	249
Figure B.2. A-scan signal associated with the liquid EcoSoya wax. The black dot indicates the first point that meets or exceeds the amplitude threshold.....	250
Figure B.3. B-scan for channel 4, which is located farthest away from the heater	251
Figure B.4. The speed of sound for channel 1 (top), which is located closest to the heater, and the temperature measured via thermocouples throughout the experiment (bottom).....	252
Figure B.5. The speed of sound for channel 2 (top), and the temperature measured via thermocouples throughout the experiment (bottom).....	253
Figure B.6. The speed of sound for channel 3 (top), and the temperature measured via thermocouples throughout the experiment (bottom).....	254
Figure B.7. The speed of sound for channel 4 (top), and the temperature measured via thermocouples throughout the experiment (bottom).....	255
Figure B.8. Comparing the calculated speed of sound for channels 4 and 14.....	256
Figure B.9. Comparing the calculated speed of sound for channels 1 through 4	257
Figure B.10. The temperature throughout the experimental setup as monitored by the thermocouples. The average temperature for each bar of thermocouples has been included in this image along with the temperature at the heater block.....	258
Figure B.11. The temperatures calculated along the ultrasound probe path for channels 1 thorough 4	259
Figure B.12. The speed of sound versus temperature for channel 1, which is located closest to the heater block	260
Figure B.13. The speed of sound versus temperature at channel 2.....	261
Figure B.14. The speed of sound versus temperature at channel 3.....	262
Figure B.15. The speed of sound versus temperature at channel 4.....	263

Figure B.16. Comparison of the speed of sound versus temperature plots for channels 1 through 4. The heating portion of the curves is provided in the red and purple colors whereas the cooling portion of the curves (when the heater is off) is provided in the blue and green colors.....	264
Figure B.17. Speed of sound versus temperature where the axes have been reduced such that the material’s transition from solid to liquid during the melting stage is highlighted by the near step change in speed of sound.....	265
Figure B.18. Speed of sound versus temperature as the material is cooling.	266
Figure B.19. A-scan (left) and Fast Fourier Transform (right) results for solid EcoSoya wax at 24 minutes into the test.	267
Figure B.20. A-scan (left) and Fast Fourier Transform (right) results for liquid EcoSoya wax at 199 minutes into the test.	268
Figure B.21. A-scan signal associated with the solid EcoSoya wax. The black dot indicates the first point that meets or exceeds the amplitude threshold.....	269
Figure B.22. A-scan associated with the liquid EcoSoya wax. The black dot indicates the first point that meets or exceeds the amplitude threshold.	270
Figure B.23. B-scan for channel 4, which is located farthest away from the heater..	271
Figure B.24. The speed of sound for channel 1 (top), which is located closest to the heater, and the temperature measured via thermocouples throughout the experiment (bottom).....	272
Figure B.25. The speed of sound for channel 2 (top), and the temperature measured via thermocouples throughout the experiment (bottom).....	273
Figure B.26. The speed of sound for channel 3 (top), and the temperature measured via thermocouples throughout the experiment (bottom).....	274
Figure B.27. The speed of sound for channel 4 (top), and the temperature measured via thermocouples throughout the experiment (bottom).....	275
Figure B.28. Comparing the calculated speed of sound for channels 4 and 14.....	276
Figure B.29. Comparing the calculated speed of sound for channels 1 through 4	277
Figure B.30. The temperatures throughout the experimental setup as monitored by the thermocouples. The average temperature for each bar of thermocouples has been included in this image along with the temperature at the heater block.	278

Figure B.31. The temperatures calculated along the ultrasound probe path for channels 1 through 4.	279
Figure B.32. The speed of sound versus temperature for channel 1, which is located closest to the heater block.	280
Figure B.33. The speed of sound versus temperature for channel 2.	281
Figure B.34. The speed of sound versus temperature for channel 3.	282
Figure B.35. The speed of sound versus temperature for channel 4.	283
Figure B.36. Comparison of the speed of sound versus temperature plots for channels 1 through 4. The heating portion of the curves is provided in the red and purple colors whereas the cooling portion of the curves (when the heater is off) is provided in the blue and green colors	284
Figure B.37. Speed of sound versus temperature where the axes have been reduced such that the material's transition from solid to liquid during the melting stage is highlighted by the near step change in speed of sound.	285
Figure B.38. Speed of sound versus temperature as the material is cooling	286
Figure B.39. A-scan (left) and Fast Fourier Transform (right) results for solid EcoSoya wax at 24 minutes into the test.	287
Figure B.40. A-scan (left) and Fast Fourier Transform (right) results for liquid EcoSoya wax at 149 minutes into the test.	288
Figure B.41. A-scan signal associated with the solid EcoSoya wax. The black dot indicates the first point that meet or exceeds the amplitude threshold.	289
Figure B.42. A-scan signal associated with the liquid EcoSoya wax. The black dot indicates the first point that meets or exceeds the amplitude threshold.	290
Figure B.43. B-scan for channel 4, which is farthest way from the heater.	291
Figure B.44. The speed of sound for channel 1 (top), which is located closest to the heater, and the temperature measured via thermocouples throughout the experiment (bottom).	292
Figure B.45. The speed of sound for channel 2 (top), and the temperature measured via thermocouples throughout the experiment (bottom).	293
Figure B.46. The speed of sound for channel 3 (top), and the temperature measured via thermocouples throughout the experiment (bottom).	294

Figure B.47. The speed of sound for channel 4 (top), and the temperature measured via thermocouples throughout the experiment (bottom).....	295
Figure B.48. Comparing the calculated speed of sound for channels 1 through 4.	296
Figure B.49. The temperatures throughout the experimental setup as monitored by the thermocouples. The average temperature for each bar of thermocouples has been included in this image along with the temperature at the heater block.	297
Figure B.50. The temperatures calculated along the ultrasound probe path for channels 1 through 4.	298
Figure B.51. The speed of sound versus temperature for channel 1, which is located closest to the heater block.	299
Figure B.52. The speed of sound versus temperature for channel 2.....	300
Figure B.53. The speed of sound versus temperature for channel 3.....	301
Figure B.54. The speed of sound versus temperature for channel 4.....	302
Figure B.55. Comparison of the speed of sound versus temperature plots for channels 1 through 4. The heating portion of the curves is provided in the red and purple colors whereas the cooling portion of the curves (when the heater is off) is provided in the blue and green colors.	303
Figure B.56. Speed of sound versus temperature where the axes have been reduced such that the material's transition from solid to liquid during the melting stage is highlighted by the near step change in speed of sound.....	304
Figure B.57. Speed of sound versus temperature as the material is cooling.	305
Figure B.58. A-scan (left) and Fast Fourier Transform (right) results for solid EcoSoya wax at 24 minutes into the test.	306
Figure B.59. A-scan (left) and Fast Fourier Transform (right) results for liquid EcoSoya wax at 299 minutes into the test.	307
Figure B.60. A-scan associated with the solid machinist wax at 9 minutes into the test.	308
Figure B.61. A-scan associated with the liquid machinist wax at 174 minutes into the test.	309
Figure B.62. B-scan for channel 1 data.....	310

Figure B.63. Speed of sound (top) and temperature as measured by thermocouples (bottom) for data collected at channel 1, which is closest to the heater block.	311
Figure B.64. Speed of sound (top) and temperature as measured by thermocouples (bottom) for data collected at channel 2, which is farthest from the heater block....	312
Figure B.65. Comparison of the speed of sound results for channels 1 and 1b.....	313
Figure B.66. Comparison of the speed of sound results for channels 1 (closest to the heater block) and 2 (farthest from the heater block).....	314
Figure B.67. Temperature values as obtained from thermocouple measurements throughout the experiment.	315
Figure B.68. The average temperature estimates obtained for the ultrasound probe path at channels 1 and 2 in the experimental setup.....	316
Figure B.69. Speed of sound versus temperature plot for channel 1.	317
Figure B.70. Speed of sound versus temperature plot for channel 2.	318
Figure B.71. Comparison of the speed of sound versus temperature plot for channel 1 and channel 2. The red and purple lines represent the heater being on during each test whereas the blue and green lines correspond to the cooling portion of each experiment.	319
Figure B.72. A-scan (left) and Fast Fourier Transform (right) results for solid machinist wax at 109 minutes into the test.	320
Figure B.73. A-scan (left) and Fast Fourier Transform (right) results for liquid machinist wax at 224 minutes into the test.	321

ACKNOWLEDGMENTS

The past three years have taught me many lessons, both in research and in life. I would like to gratefully acknowledge the support and guidance of my dissertation committee members: Dr. Byron Newberry, Dr. William Jordan, Dr. Jill Klentzman, Dr. Yang Li, Dr. Charles Baylis, and Dr. David Jack from Baylor University and Mr. David Moore from Sandia National Laboratories. I would like to acknowledge and thank Mr. David Moore for his guidance and mentorship. While working with Mr. Moore, my knowledge of ultrasound techniques and data analysis has grown exponentially, and I am grateful for his continued support throughout my doctoral studies. The meetings and discussions that Dr. Byron Newberry and I had immeasurably assisted me in gaining a better understanding of the mathematical description for ultrasound wave propagation through laminated composites. I am thankful for these conversations and for his guidance. From Dr. David Jack, my dissertation committee chairman, I have learned many lessons with respect to research, resource management, and communication that I will carry with me for the rest of my life.

I would like to take a moment to acknowledge and thank those who supported me as I completed my dissertation research. First and foremost, I would like to thank the Lord for helping me to successfully complete this doctoral program. When I thought I could not persevere any longer, He was alongside me and strengthened me to continue along the path He had planned for me. I would like to acknowledge Ms. Ciji Nelson for her assistance in collecting some of the data that was used in this dissertation, as well as

for being a great friend and colleague these past few years. I would like to express my gratitude to my other coworkers at Sandia National Laboratories for their support of my dissertation studies. I would also like to thank Ms. Jill Combs and Mr. Bobby Cryns for making the Baylor Research and Innovation Collaborative a great place to work. Jill and Bobby always made me smile and talking with them was often one of the highlights of my day. I feel truly blessed to have had the opportunity to get to know you both. The National Science Foundation Graduate Research Fellowship supported me in my goal of obtaining a doctoral degree, and I am grateful for their financial support as well.

Last but certainly not least, I would also like to acknowledge the love and support of my family. Completion of this program would have been much more difficult without their listening ears and supportive words. The love, encouragement and prayers I received from my parents have been a blessing. I love you both very much. Thank you.

Sandia National Laboratories is a multi-mission laboratory managed and operated by National Technology and Engineering Solutions of Sandia, LLC., a wholly owned subsidiary of Honeywell International, Inc., for the U.S. Department of Energy's National Nuclear Security Administration under contract DE-NA0003525.

This material is based upon work supported by the National Science Foundation Graduate Research Fellowship under Grant No. DGE-1356113. Any opinion, findings, and conclusions or recommendations expressed in this material are those of the author(s) and do not necessarily reflect the views of the National Science Foundation.

DEDICATION

To my loving parents who have supported me in all my endeavors.

CHAPTER ONE

Introduction

The need for nondestructive evaluation methods for inspecting complex materials, such as composites and materials with porosity and/or aggregate, is increasing as industries move away from primarily metal components and incorporate these lighter and often polymer-based alternatives. The focus of this dissertation is on the development and implementation of nondestructive evaluation techniques, specifically ultrasound techniques, for inspecting such materials. The two material applications presented in this dissertation are inspection of composites and the monitoring of the phase and temperature of attenuative materials.

The composites of interest in this dissertation are carbon fiber fabric reinforced laminated composites. This dissertation presents ultrasound techniques for inspecting carbon fiber fabric reinforced laminated composites as well as the bondline between a carbon fiber fabric reinforced laminated composite and an aluminum plate. The second application discussed in this dissertation presents an ultrasonic technique for monitoring the phase and temperature of two highly attenuative wax materials as they are exposed to heat and then allowed to re-solidify.

There are three main research goals in this dissertation; nondestructive inspection of the bondline in a composite, a through transmission technique for temperature monitoring, and an oblique scanning method for inspecting composite laminates. These

three goals are each discussed and presented in, respectively, Chapters Three, Four, and Five of this dissertation.

The first goal was the design and implementation of an ultrasound technique for nondestructively evaluating the quality of the bondline between a carbon fiber reinforced laminated composite and a metal structure, in this case aluminum. The novelties of the proposed method include the ability to clearly identify, via the A-scan and C-scan ultrasound data, the shape of the unbonded region between the laminate and aluminum regardless of which side of the sample, laminate or aluminum, is facing the ultrasound probe and the ability to correlate features observed in the intensity versus frequency plots to a bonded or unbonded area at the composite-to-aluminum bondline. Different laminate thicknesses were analyzed in this study to show that the presented ultrasound technique is capable of identifying the unbonded regions for a variety of laminate thicknesses. The results obtained using a traditional contact probe method are compared with those obtained using an immersion ultrasound technique. The unbonded areas are correctly identified using each method with the immersion method using a spherically focused transducer providing a better spatial resolution of the unbonded area. The resolution using the contact method is limited to the diameter of the contact probe (approximately 0.5 inches) whereas the immersion approach yielded a resolution of 0.04 inches in the configuration used within this dissertation.

The second scientific contribution in this dissertation is the use of a through transmission ultrasound method with contact transducers to monitor the phase and temperature of an attenuative wax material as the material is exposed to heat and then allowed to cool. The uniqueness of the present approach is the monitoring of both the

heating and the cooling of a material as well as some of the analysis methods for displaying the measured results, such as the B-scan image that presents the wave amplitude as a function of A-scan time and experiment time. Additionally, the ultrasound results are compared with results from digital scanning calorimetry measurements where the melt and re-solidification temperatures were determined and observations about the material's heat capacity were noted. Two different waxes are analyzed in the study, a soy-based wax called EcoSoya and a machinist wax called Rigidax. The two waxes are quite different from one another with the machinist wax having a higher heat capacity and increased porosity as compared to that for the soy-based wax. Throughout the experiment, the temperature of the wax is monitored by thermocouples, and the ultrasound data is collected for locations spaced throughout the length of the rectangular container. From the measured ultrasound data the following metrics were analyzed and plotted: A-scan for each minute of the experiment time, B-scan displaying the signal amplitude as a function of A-scan time and experiment time, speed of sound versus time plots, speed of sound versus temperature plots, and comparison plots of speed of sound versus time and speed of sound versus temperature. Due to the increased porosity and high heat capacity of the machinist wax as compared to the soy-based wax, the analysis process needed to be updated when analyzing the machinist wax because the ultrasound signal through the solid portion of the machinist wax was near the same amplitude as the signal noise with the signal gain at 80dB. Thus, when using the same (unmodified) analysis program as for the EcoSoya wax, the speed of sound plots for the machinist wax displayed erroneous results because some data points used the noise for the speed of sound calculations instead of the actual signal. The author describes these results and the

efforts to plot the appropriate speed of sound values for the machinist wax in Chapter Four.

In general, the two wax materials showed similar trends with the material's speed of sound decreasing as its temperature increased and increasing as the material re-solidified. The two materials had a different speed of sound and melting temperature, but once the material melted, the speed of sound for both the EcoSoya wax and the machinist wax decreased until the heater was turned off. Then, the speed of sound for each material started to increase. The plot of the speed of sound versus temperature shows the relationship between these two metrics, with the cooling portion of the experiment providing the clearest relationship between the speed of sound and temperature. The cooling portion of the experiment provides the clearest relationship between the temperature and speed of sound because the wax throughout the box was at the same temperature and underwent uniform cooling as compared to the non-uniform heating process where the heater was at one end of the box and generated a thermal gradient across the box.

The third scientific contribution in this dissertation is the creation of an oblique, through transmission ultrasound technique for inspecting a carbon fiber reinforced laminated composite. This work is anticipated to be one part in a larger research effort involving the creation of a mathematical model. The mathematical model will compare the experimental results from this dissertation with results obtained using a paraxial approximation of wave displacement through the laminated composite sample [1]. The desired outcome of the broader effort is to nondestructively determine the orthotropic elastic constants for the bulk laminated composite. This study involved the design and

implementation of an oblique incidence through transmission immersion ultrasound setup to observe and record how the ultrasound wave propagates through the thickness of the laminate. From the C-scan results, the user gains a better understanding of how the wave spreads and scatters as it propagates through the sample thickness. The presence of side lobes associated with the longitudinal wave can also be identified from the scan. In the future work section of Chapter Six, aspects of the proposed mathematical model, whose foundation is the model developed by Newberry in his doctoral dissertation [1], are discussed including a proposed iterative approach for obtaining the elastic constants from the ultrasound scan data presented in Chapter Five.

Chapter Two of this dissertation includes a description of non-destructive testing (NDT) methods, which covers an array of technology options available in that field. These different NDT methods are summarized based on their application to the inspection of carbon fiber reinforced laminated composites. Benefits and limitations of these nondestructive inspection technologies are discussed with the focus of the discussion being on the application of various ultrasound inspection techniques.

Chapter Three discusses the sample manufacturing process and experimental setup associated with the bondline analysis experiment. Two different samples were evaluated in this experiment, and both were manufactured using an 8 harness satin prepreg carbon fiber fabric. One was a co-cured part while the other was a pre-cured part. The co-cured technique involved curing the laminate directly onto the aluminum. The pre-cure technique involved curing the laminate with a release agent applied to the aluminum. Then, a coupling medium, to represent an adhesive, was applied between the laminate and the aluminum for the pre-cured part. Three laminate thicknesses (4 plies, 8

plies and 12 plies) were made with each of these two manufacturing methods. Each of these laminate thicknesses were then inspected using a contact transducer similar to techniques used in industry and then again using an immersion system. Both methods were able to correctly identify the unbonded regions, but the results obtained with the immersion technique provided a clearer description of the geometry of the unbonded area at the interface between the two materials with a spatial resolution of 0.04 inches. A frequency analysis was performed on the ultrasound data obtained in this study. The comparison of the frequency intensity indicates that the bonded and unbonded regions can be correctly identified with the amplitude of the frequency intensity of the unbonded location being larger than that of the bonded location. The samples were inspected from both the aluminum side as well as from the composite side, and although the signal attenuated more quickly when inspecting the bondline from the composite side of the sample, the bondline could be identified regardless of which side was facing the transducer. This ability to monitor from either side is important when considering that a field inspector may only have access to one side of the part.

Chapter Four is focused on the temperature monitoring study where the investigated waxes were exposed to heat to melt the material and then allowed to cool and re-solidify. Throughout the experiment, the temperature of the wax is monitored via thermocouples spaced throughout the rectangular container holding the sample wax. Ultrasound transducers are placed on each of the two long sides of the rectangular box. Three different experimental setups are presented to observe which aspects of the experiment might change when the experimental geometry and box material are varied. A heating element was placed within the box and the heater is turned on and slowly melts

the wax. Once the wax across all acoustic paths being monitored has melted, the heater is turned off and the wax is allowed to re-solidify. From the ultrasound data, the phase of the material may be identified a few different ways. The first method demonstrated uses the onset of the signal within an individual A-scan where the onset of the ultrasound signal occurs at a different location in time for the solid versus the liquid material. The second method, and one of the unique contributions of this dissertation, is through a temporal B-scan. From the B-scan the change in the phase of the material may be clearly and unambiguously observed from the onset of the signal as it varies throughout the experiment. The axes used on the B-scan are A-scan time (microseconds) and experiment time (minutes) with the plot intensity corresponding to the A-scan signal amplitude. Third, the phase of the material may be observed from the speed of sound plots when the material is in the molten state. As the material melts, the speed of sound decreases, but as the material re-solidifies, the speed of sound increases. An analysis of the speed of sound versus temperature indicates that the subtle changes in the speed of sound as the wax cools may be able to assist in determining the temperature of the material without using thermocouples in future experiments. The melt and re-solidification temperatures for each wax, as determined from the analysis figures, were validated via differential scanning calorimetry (DSC) measurements. The DSC data for the EcoSoya wax was presented in Gregg's masters thesis, and the DSC data for the machinist wax is presented in this dissertation.

Chapter Five introduces the experimental setup for the oblique incidence, through transmission immersion ultrasound technique for the inspection of a carbon fiber laminate. The composite laminate samples were manufactured using the same carbon

fiber 8 harness satin material and cure cycle as those samples used in the bondline inspection study. The pulser and receiver were placed at a variety of orientations with the pulser being placed at an orientation of 5 degrees and 10 degrees and the receiver's orientation being varied from 2 to 20 degrees relative to the sample surface normal. For each scan the pulser remained fixed as the receiver, placed on the opposite side of the laminate, performed the C-scan measurements of the ultrasound data. The results from the C-scan image provide the user with information regarding the scattering experienced by the ultrasound wave as it propagates through the sample thickness as well as the location of the side lobes associated with the longitudinal wave. The data analysis procedure and the measured results are presented in this chapter along with the variations of the experimental setup parameters that were studied.

Chapter Six provides a conclusive summary of the results obtained in the bondline inspection study, material phase and temperature monitoring study, and the results obtained in the oblique incidence through transmission immersion ultrasound study for the laminated composite. From the bondline study, both the contact and the immersion ultrasound techniques were capable of identifying the location of unbonded regions between the laminate and the aluminum, regardless of which side, laminate or aluminum, was facing the ultrasound probe in the pulse-echo study. The material phase and temperature monitoring study performed with the contact ultrasound probes operating in through transmission mode provided information allowing the user to correctly identify whether the material was solid, liquid or undergoing a transition between phases. Additionally, plots of the relationship between the speed of sound and temperature provided preliminary results as to how the relationship between these two metrics could

be used in future experiments to eliminate the need for thermocouples to monitor the temperature of the material and thus noninvasively monitor the internal temperature. Finally, the results from the oblique incidence through transmission study provide useful information about how the wave scatters as it propagates through the thickness of the laminated composite as well as the location of the side lobes relative to the longitudinal wave, which the author hypothesizes may be more sensitive to changes in the material properties than is the longitudinal wave. The potential increased sensitivity of the side lobes to the material's properties may allow for more accurate results in the determination of the elastic constants once the mathematical model portion of this larger project is incorporated. Areas where future work may be performed with respect to these studies is also included in Chapter Six along with a discussion of how these challenges may be resolved. A discussion of how the oblique transmission results from Chapter Five will be compared to the results from the mathematical model of Newberry [1] and how those will be used to infer the orthotropic material constants of a laminate is also provided in the future work section of Chapter Six.

CHAPTER TWO

Review of Literature

2.1 Introduction

Composite materials are often praised for their high strength to weight ratios and ability to improve fuel efficiency of airplanes and automobiles. While these materials bring several benefits to the design table, they also carry with them a set of engineering difficulties that make life prediction, quality and inspection more difficult than that for metal components. These engineering difficulties will be defined in this chapter, and methods for mitigating such factors will be presented in this dissertation.

The term composite material refers to a material consisting of two or more base materials. For example, a fiber-reinforced composite consists of fibers surrounded by a polymer matrix. United Launch Alliance, a business venture between Boeing and Lockheed Martin Corporation, used a fiber reinforced polymer along with fused deposition modeling (also referred to as 3D printing) to manufacture components for their Atlas V rocket [2], and Airbus has filed for a patent for 3D printing an entire airplane [3].

The material of interest in the present study is carbon fiber reinforced laminated composites. This material has been included in some of BMW's most recent designs including the BMW i8 (see e.g. Figure 2.1) as well as in the new Boeing 787 airplane [4, 5]. In the new Boeing 787 nearly the entire fuselage is manufactured using composite materials [4]. The most common type of fibers used in fiber reinforced laminated composites are: fiberglass (or E-glass), carbon fiber, boron [4] and Kevlar [6, 7]. Several

manufacturing methods exist for making fiber reinforced laminated composites, and a selection of these will be described in a later section.

One benefit of fiber reinforced laminated composites is the tailorability of the material properties [8]. The laminate stacking sequence directly affects the final stiffness properties of the bulk laminate [9]. Thus, during the design process, the engineer has significant control over the properties of the final, as-manufactured part. Although tailorability of the stiffness is a wonderful capability to have, one must be cautious and acknowledge that the final product is only as good as the quality that can be verified. For example, during the manufacturing process a ply may be placed upside down or at a different angle than what the design specification stated. There is a limited amount of technology available for evaluating the orientation, ply type and thickness of each layer within a laminated composite, and those interested in such technology are encouraged to read the author's masters thesis [10].

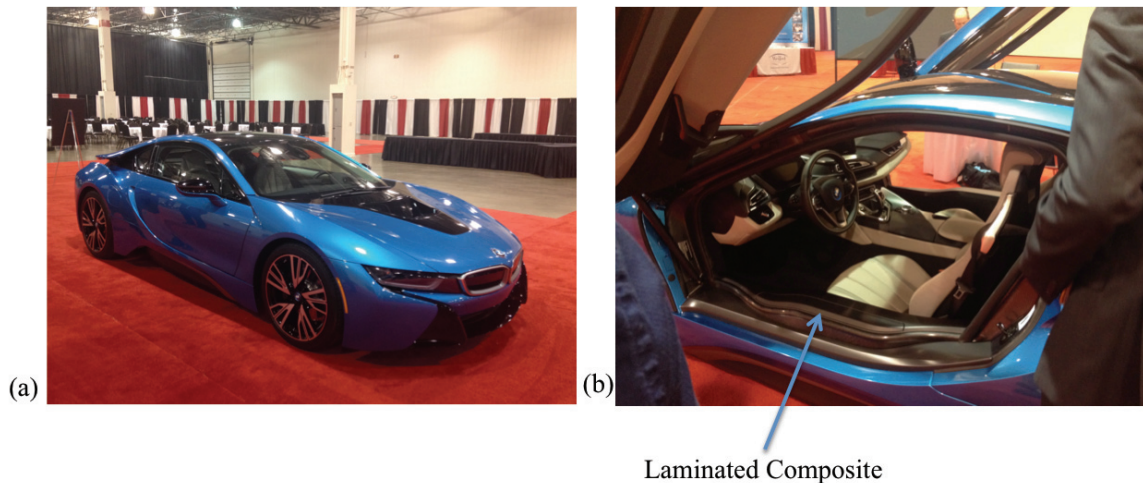


Figure 2.1 The (a) BMW i8 automobile incorporates carbon fiber reinforced laminated composites into the (b) frame as indicated by the blue arrow

A variety of the engineering difficulties associated with composite laminated materials arise during the manufacturing process. While manufacturing a laminate, one must be careful to lay down the as-designed ply stacking sequence. Simply flipping the ply from a 45° to a -45° rotation could affect the dimensional stability and the overall properties of the as-manufactured laminate [9, 11]. Though the aforementioned manufacturing error seems like an improbable occurrence, this error is possible when the fabric is either unidirectional or a biased weave, and the ply is laid upside down on the ply stack. In an effort to reduce orientation variability and ply stacking errors, techniques are implemented to automate the laying down of the stacking sequence [12] while others have introduced quality control forms [13]. The automated stacking sequence is thought to produce fewer errors than a human while the quality control forms seek to make the person who is stacking the laminate more cognizant of the stacking sequence that should be used for a particular part. While manufacturing laminates, the author has found that the latter option has prevented her from stacking a 45° unidirectional ply rather than a -45° unidirectional ply.

Once a laminated composite has been manufactured, visual detection of a misaligned interior ply is impossible. One could destructively determine the ply orientation by performing a burn-off test, where the laminate is exposed to high temperatures to burn off the resin matrix leaving the reinforcing fiber behind [14]. When the matrix has been burned away from the fibers, each ply may be removed individually and the orientation measured. Thus, for situations where the laminate must continue to be used in service, a nondestructive method for evaluating the quality of such parts is not only desired but also necessary. There are five main areas of nondestructive testing:

ultrasound, dye penetrant, electromagnetic particle, x-ray, and eddy current [15].

Although the focus of this study is on ultrasonic methods of inspecting composite parts, a brief description of a variety of nondestructive testing methods will be included in Section 2.4 to provide the reader with a background on other nondestructive evaluation methods (NDE) that are available.

The literature review introduces several popular methods for producing fiber reinforced laminated composites, along with the prepreg process used in the present study. An overview is presented of common NDE terms and techniques used for evaluating composites. A review of previous studies regarding ultrasound methods for determining a laminate's porosity and a transversely isotropic laminate's elastic constants are presented. The literature review will conclude with a discussion of applications requiring two or more materials to be bonded to one another and how to nondestructively inspect the bondline between the materials.

2.2 Manufacturing Laminated Composites

There are a variety of methods available for manufacturing fiber reinforced laminated composites. Three techniques commonly found in literature [10, 14] are: wet lay-up, vacuum assisted resin transfer molding (VARTM) and fiber fabrics preimpregnated with resin (also referred to as "prepreg", for short). Each of these methods will be described in further detail in the following subsections. The choice of manufacturing technique is often determined by a few criteria. For example, how large is the part? If the part is considerably large in size, like a boat, a wet lay-up technique may be used. If the part is an autobody component, it may be manufacturing using the

VARTM technique or prepreg method which could provide quicker manufacturing times and improve the ease of molding a component that contains curved surfaces.

Another criterion that can assist in determining which manufacturing method to use is the allowable fiber volume content. Wet lay-up processes tend to produce resin-rich parts with a low fiber volume content [16]. For applications requiring high fiber volume content, VARTM and prepreg manufacturing processes would be the technique of choice. Furthermore, if time constraints on manufacturing were a concern, the prepreg technique removes the need to mix the resin/hardener mixture as the manufacturer has already preimpregnated the fibers with the desired resin mixture. The downside of prepreg material is that the user has less control over which resin system is applied to the fibers, unless they work directly with the manufacturer to produce a specific prepreg material for their needs. In general, the ease of use of prepreg material has made this manufacturing technique popular with university researchers and industries alike.

2.2.1 Wet Lay-up Method

The wet lay-up method is one of the messiest methods for manufacturing carbon fiber reinforced laminated composites. The process starts with cutting out the desired ply orientations from a roll of dry carbon fiber fabric. Next, each of the plies are laid according to the desired stacking sequence and are ready for the wetting process [10].

The resin and hardener chosen for the manufacturing application are measured into lab beakers according to the manufacturer recommended weight ratios. With the beaker sitting atop a laboratory scale, the desired amount of resin is poured into the container. Next, the proper amount of hardener, as determined from the manufacturer recommended resin to hardener weight ratio, is added to the same beaker. Then, the resin

and hardener are thoroughly mixed together. To eliminate the formation of bubbles and reduce the amount of porosity in the as-manufactured laminated composite, the jar containing the resin/hardener mixture is placed in an ultrasonic bath for approximately 3-5 minutes. While sitting in the ultrasonic bath, ultrasonic pulses essentially shake out the air bubbles within the resin hardener mixture. Next, each of the laminate plies is dipped in the resin mixture and laid on top of a piece of tooling in the desired laminate stacking sequence. Once all of the plies have been wetted and laid on top of the tooling, the system is vacuum bagged and placed in a furnace to undergo the manufacturer recommended cure cycle. Usually, the resin/hardener mixture that is used when manufacturing laminates is a thermoset epoxy [10]. During the cure cycle, the resin/hardener mixture forms chemical crosslinks as the mixture undergoes a phase change from liquid to solid [17]. Thus, when the as-manufactured laminate is exposed to high temperatures, the solidified resin matrix will char rather than melt, as is the case with a thermoplastic.

Depending on the resin/hardener system used, the cure cycle may last anywhere from minutes to days [18, 19]. Throughout the cure cycle, many manufacturers [12, 20-23] require that the laminate be held under vacuum pressure to reduce the number of voids and to assist in compacting the laminate thus increasing the fiber volume fraction in the as-manufactured part [24, 25, 26].

2.2.2 Vacuum Assisted Resin Transfer Molding (VARTM) Method

The first couple of steps related to the vacuum assisted resin transfer molding method are identical to those used for the wet lay-up method previously described. The desired ply orientations are cut from a roll of carbon fiber fabric and laid down according

to the designed stacking sequence. Next, the components of the resin/hardener mixture are measured and mixed together. The mixture is then exposed to an ultrasonic bath that removes the excess air bubbles thus preventing additional porosity within the final part [10, 14].

Rather than applying the resin/hardener mixture by hand to each of the plies in the stacking sequence, the dry fabric plies, ordered in the desired stacking sequence, are laid on top of the desired tooling, and inlet and outlet tubes are placed along the edges of the tooling plate [14]. The inlet tube feeds into a spiral wrap that allows the resin to flow through and propagate across the width of the plate in order to cover the span of the laminate [14]. An outlet tube is placed on the opposite side of the tooling and carries the excess resin away from the laminate and into a resin trap which prevents it from entering the vacuum pump. A peel ply fabric is laid on top of the composite part and serves two purposes. First, the peel ply assists in separating the laminate from the bagging material upon completion of the cure cycle, and second, the peel ply assists in preventing the texture of the infusion mesh from being imprinted on the surface of the laminate. The purpose of the infusion mesh is to aid the propagation of the resin across the surface of the laminate [14].

Next, a vacuum bag is placed around the tooling with the inlet and outlet tube extending outward from the bagging material. The inlet tube is placed in the container holding the resin/hardener mixture while the outlet tube is placed in the resin trap. Also attached to the resin trap is the vacuum pump. When the vacuum pump is turned on, the excess air is removed from the bagging material, and the resin is pulled through the inlet

tube, across the laminate stack where it is absorbed through the stack thickness and the excess resin is pulled into the resin trap [10, 14].

Special care must be given to ensure that the inlet tube does not get exposed to air but stays immersed in the resin mixture. If the inlet tube is exposed to air, the air will enter into the vacuum bagged laminate, and the probability of the laminate containing an unacceptable amount of porosity is significantly increased. To prevent air from entering the bagged laminate, the author and her peers who have worked with this manufacturing method usually place a hose clip on the inlet tube so that the inlet channel may be closed off once the resin has propagated across the part or when the resin container is near empty [10].

The use of vacuum pressure to wet the carbon fiber laminate stacking sequence reduces, although does not completely eliminate, the presence of air bubbles or voids within the final part. In 2005, Afendi *et al.* [27] studied methods of further reducing the amount of voids within the final part by exposing the resin/hardener mixture to a degassing step.

The inlet and outlet tubes are frequently placed on either side of the laminate, but in general, the placement and number of inlet and outlet tubes could be reconfigured to a variety of different setups. Although a variety of setups could be used, the placement of the inlet and outlet tubes does affect the laminate's wetting process. Correia *et al.* [28] performed a study where they determined a set of equations to describe this process. Some of the authors then continued this research by investigating how the resin flow could be controlled using flow controls in-line with the inlet and outlet tubes that could

monitor and control the VARTM process based on real-time video feedback of the wetting process [29].

Although this method may appear simple and less messy as compared to the wet lay-up process, several iterations are required before one can honestly state they have mastered this manufacturing process [30]. Once a person has experience with this method, manufacturing high quality parts is a highly repeatable process and often produces parts with higher fiber volume content than parts manufactured with the wet lay-up process.

2.2.3 Prepreg Method

Unlike the previous two methods for manufacturing carbon fiber reinforced laminated composites, the prepreg method does not require the user to manually combine the resin/hardener mixture. For this reason, the prepreg process is considered a cleaner, and often easier, technique than those previously described. The term “prepreg” refers to a type of fabric that has been preimpregnated with a resin/hardener system. Often the prepreg material is stored in a freezer to both lengthen its shelf life as well as slow down the chemical reaction between the resin and hardener. Journals, such as *REINFORCEDplastics* (see e.g., [31, 32]), have promoted the benefits of using prepreg material versus dry fabric. For example, prepreg material can actually reduce the time required to manufacture a part since the resin and hardener system no longer need to be measured, mixed and applied to the ply stack.

The time required to cure the laminate using this method depends on the resin system that is applied to the fabric. Each prepreg material comes with a manufacturer recommended cure cycle. As with the previous two methods, the laminate remains under

vacuum pressure throughout the entire cure cycle, and the pressure combined with the increased temperature are what assist in coating all of the fibers within the laminate with the resin/hardener mixture [33, 34]. When the resin/hardener mixture is exposed to the increased temperature, it becomes less viscous and spreads across each ply in the laminate via the vacuum pressure being applied to the system. Once the cure cycle is complete, the laminate is removed from the bagging material and is ready to be inspected for quality.

Three of the manufacturing methods used to fabricate fiber reinforced laminated composites have been reviewed in the preceding subsections. Although these methods have been referenced throughout the literature as a means of creating such components, the quality of these parts should be assessed to ensure they are suitable for their intended application [35]. The following section will discuss the reasons why quality assurance of such components is important.

2.3 The Need for Nondestructive Inspection Methods for Composite Materials

There are a variety of common manufacturing defects that can affect the final part quality and performance. For example, the formation of voids within a laminate during the manufacturing process is common, and the allowable void content is often a limiting factor regarding part quality [36]. As manufacturers repeatedly produce the same components, their part quality also becomes highly repeatable. Some amount of void content is expected, but if the manufacturing process experiences an abnormality, such as a significant change in the surrounding humidity or a new employee manufacturing the components, the void content for that particular batch may be different. If the void content is above the allowable threshold, the batch should be discarded. Since voids act

as stress concentrators within the part [37], there exists a void content above which the part can no longer be guaranteed to withstand the designed load conditions.

Void content is simply one example of the defects that can be commonly found within fiber reinforced laminated composites. Other examples include but are not limited to: delaminations, microcracks, misaligned fibers, and resin rich regions [38]. As the amount of laminated composites used in industry continues to grow, there is a greater need to inspect such materials using non-destructive testing methods [39]. Areas of application for such nondestructive testing methods include the inspection of laminated composite automotive components, wind turbine blades that are commonly manufactured using fiberglass, and airplane components like those seen on the Boeing 787 [40].

Composites are non-homogeneous, viscoelastic, anisotropic materials that are inherently different from the homogeneous, elastic, isotropic metals that have long been considered the norm in manufacturing. Nondestructive evaluation inspectors should receive copious amounts of training to assist them in making well-informed decisions about the quality of such complex composite materials. Goglia [41], an expert in the field of nondestructive testing, expresses his concerns about the quality of the inspection of composite materials due to the lack of training received by inspectors. To assist with satisfying such industry needs, GE has developed a training facility in Lewistown, Pennsylvania for the inspectors [42].

A variety of nondestructive methods have been designed and implemented to detect defects within a part. These methods include but are not limited to: thermal (see e.g., [43, 44, 45]), optical (see e.g., [43, 44, 46]), and ultrasonic (see e.g., [40, 47-49]). The following paragraphs will expand on these referenced studies.

Amaro *et al.* [47] evaluated the accuracy of a variety of nondestructive testing methods for inspecting the location and size of damage in carbon fiber reinforced laminated composites. The methods evaluated in this study included: electronic speckle pattern interferometry (ESPI), shearography, ultrasound, and X-radiography. Amaro *et al.* [47] found that ultrasound was the only nondestructive testing technique investigated that was able to characterize the damage not only in the planar dimension of the laminate but also along the thickness of the laminate. Asmatulu and Movva [50] also looked at a variety of nondestructive testing techniques for inspecting composite materials, and they too found that ultrasound gave the most pertinent and useful information when locating and characterizing defects within the sample. Amaro *et al.* [48] developed a mathematical technique for predicting the damage incurred by a carbon fiber reinforced laminated composite that is exposed to an impact load. They compared their mathematical predictions with measured results, and they were in good agreement with one another.

Bendada *et al.* [44] and Cuadra *et al.* [46] also evaluated the damage incurred by fiber reinforced laminated composites exposed to impacting loading conditions, but their inspection methods of choice were thermal techniques. By exposing the fiber reinforced laminated composites to increased temperature for a short period of time the researchers observed how the heat dissipates through the material. Damaged regions leave a different heat signature than healthy regions of a sample, and these results were observed in the two studies. Ben *et al.* [49] investigated damage to composite samples using ultrasonic Lamb-based waves. The damage inflicted on the composites included drilled holes, slots and impact damage. Each sample was inspected both pre- and post-damage. Using this

technique, Ben *et al.* [49] were able to identify and characterize the damage to the composite sample.

Although a variety of nondestructive testing methods are available for characterizing the damage experienced by the composite laminates, the nondestructive testing method of choice used in the present study is ultrasound. As will be discussed in future sections of this literature review, ultrasound has many different applications and capabilities when it comes to inspecting and characterizing a part. The following section will introduce the reader to common ultrasound terminology, which will be useful background knowledge for understanding the content in the remaining chapters of this dissertation.

2.4 Basic NDE Terminology with an Emphasis on Ultrasound Terminology

Nondestructive inspection technology is a continuously growing field. As industries begin incorporating more fiber reinforced composites into their product lines, they need a reliable method of inspecting the quality of their final product. Recall, nondestructive testing has five main areas: magnetic particle testing, radiographic testing, liquid penetrant testing, electromagnetic testing, and ultrasound testing [35]. The studies described in this dissertation focus on the application of ultrasound technology to inspect and characterize composites and the bondline at a composite-to-metal interface. The following discussion introduces the reader to frequently used ultrasound terms, which may be helpful while discussing the present study.

2.4.1 What Is Ultrasound Testing?

Ultrasound testing is a nondestructive method that has a variety of applications. As described in the previous section, a large portion of the research papers related to ultrasound research focus on defect identification and characterization. The term “characterization” is used in this context to indicate the geometry and any additional characteristics of the defect that may be of interest to the inspector. When the ultrasound wave approaches a material boundary (i.e. a void or a resin rich region), a portion of the ultrasound wave reflects back toward the transducer and the remaining portion of the wave refracts deeper into the part, as seen in Figure 2.2(a) [51]. Additional applications for ultrasound inspection include determining the elastic constants of the material (see e.g. [52, 53, 54]) and determining the ply type, orientation and thickness of each lamina in the bulk laminate [10, 55]. The author’s master’s work was focused on the later application, and two patents were produced from the research [56, 57].

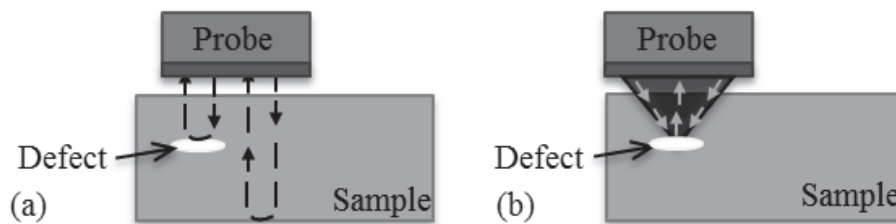


Figure 2.2 Ultrasound methods for identifying a defect within a part using (a) an unfocused probe and (b) a spherically focused probe

In ultrasound testing, there are a variety of transducers that could be used for a given application, but two of the most common transducers are a flat front transducer as seen in Figure 2.2(a) and a spherically focused transducer as seen in Figure 2.2(b). The flat front transducer emits a pressure wave from the transducer and the diameter of the

transducer directly affects the areal resolution of the results [58]. The spherically focused transducer uses a lens to focus the ultrasound wave as seen in Figure 2.2(b) [59]. The benefit of using a spherically focused transducer is the increased resolution when inspecting parts. For example, when inspecting a carbon fiber reinforced laminate to determine the ply type and orientation of each lamina within the bulk laminate, a spherically focused ultrasound probe should be used as it will enable the inspector to detect the tows of the carbon fiber fabric (see e.g. the author's work in [55, 60, 61]).

Although there are a variety of transducers that are available for inspecting samples, there are also different experimental setups that could be used. Figure 2.3 depicts both the through transmission method (Figure 2.3(a)) and the pulse echo method (Figure 2.3(b)) for performing ultrasound inspections. Most notably, the through transmission method involves two transducers, where one transducer emits the initial ultrasound wave and the second transducer listens and receives the wave after it has traveled through the part [58]. When operating in through transmission mode, the probes could be placed on either side of the part (as shown in Figure 2.3(a)), or they could be placed on the same side of the part as seen in the oblique incidence bondline analysis study performed by Pilarski and Rose [62].

When evaluating the ultrasound data, there are three types of graphical representations which may be used. These graphical representations of the data are most commonly referred to as: A-scans, B-scans and C-scans. An A-scan is equivalent to looking at the ultrasound signal at one specific point location. With the A-scan, the

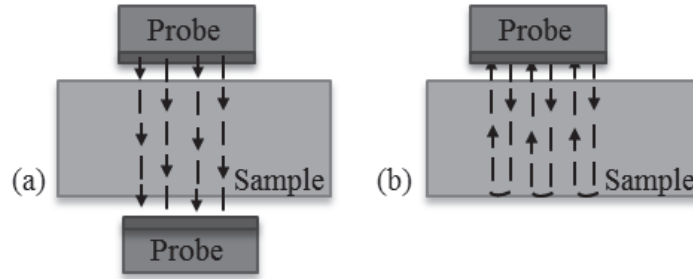


Figure 2.3 Ultrasound techniques commonly used for inspecting samples include (a) through transmission method and (b) pulse echo method. In the diagram above, the black arrows refer to the direction of travel for the ultrasound wave

inspector can identify the front surface of the sample, the back surface of the sample, and any anomalies, such as defects, along the thickness of the sample. Furthermore, the inspector can identify the location of the anomaly with respect to the thickness of the sample [63].

The B-scan represents the ultrasound data collected along a line, thus providing a planar view of the sample. The B-scan is the view of choice when needing to look at a cross-sectional view of the sample [63]. Figure 2.4 shows a B-scan obtained from an ultrasonic inspection of a 12 ply carbon fiber composite laminate bonded to a metal plate. The red line observed horizontally across the image represents the front surface of the laminate, and the vertical axis corresponds to the time it takes in microseconds for the wave to propagate through the thickness of the sample. Thus, the vertical axis could be interpreted as relating to the sample thickness. As observed in Figure 2.4, a high amplitude signal exists within the part. The right-most arrow indicates an unbonded location between the composite laminate and a piece of aluminum [63].

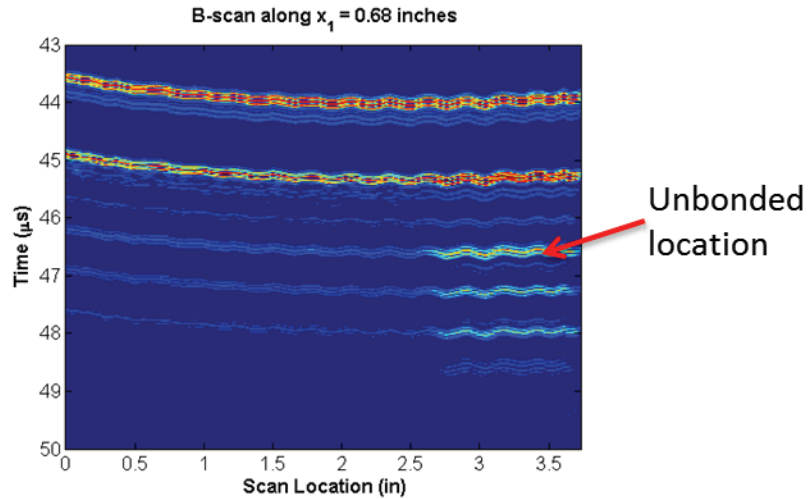


Figure 2.4 B-scan image of aluminum bonded to a 12 ply carbon fiber reinforced laminated composite. The unbonded area between the two materials is highlighted by the red arrow

An areal perspective of the ultrasound data is provided in a C-scan, and this form of displaying the data is commonly used when inspecting large areas and/or large parts. An example of a C-scan is provided in Figure 2.5. This figure is a C-scan representation of the ultrasound inspection of the composite-to-metal bondline between a 12 ply carbon fiber reinforced laminated composite and an aluminum plate. Notice the red area in the C-scan corresponds to a disbond between the carbon fiber and the aluminum whereas the rest of the area corresponds to a bonded region. The difference between the bonded and disbonded regions are verified by inspection of the A-scans, and this process will be described in more detail in Chapter Three where the bondline analysis study is provided.

2.4.2 How the Ultrasound Wave Interacts with Materials

There are a variety of ways in which an ultrasound wave can propagate through material. The four main methods of propagation are: longitudinal wave, shear wave, surface (Rayleigh) wave, and plate (Lamb) wave. Each of these wave propagation

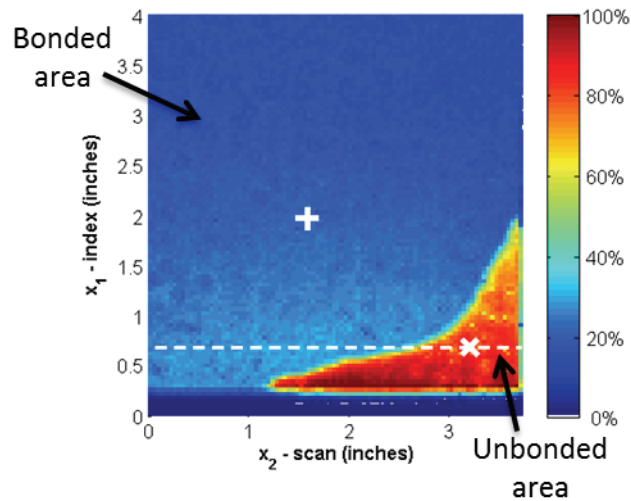


Figure 2.5 C-scan representation of the ultrasound signal as it propagates through the aluminum-to-composite bond. The laminate in this case is 12 plies thick. The red area of the C-scan indicates an unbonded area where the reflected wave has a high signal amplitude and the blue area indicates a bonded area with a low signal amplitude.

methods involves different types of particle motion. For example, the longitudinal wave is a compressive wave where the particles are displaced parallel to the direction of wave propagation. For a shear wave, the particle displacement is normal to the direction of wave propagation [64].

Each material has a sound wave velocity. This value represents the velocity at which sound will propagate through the material and is dependent on the material's internal structure [65]. Just as there are a variety of methods for the wave to propagate through the material, there are also multiple sound wave velocities that can be measured. The most frequently referenced sound wave velocity is the longitudinal velocity. The longitudinal velocity is associated with the time required for the longitudinal ultrasound wave to travel through a known thickness of the material [64]. As a rule of thumb, the shear wave velocity is approximately one-half the value of the longitudinal velocity [66].

When an ultrasound wave approaches a material boundary, a portion of the wave reflects back toward the transducer while the remainder of the wave transmits into the next material [64]. Carbon fiber reinforced laminated composites inherently have a multitude of material boundaries as each time the ultrasound wave approaches a transition from a fiber tow to a resin region, the wave will form a reflection/refraction pair. Furthermore, the carbon fiber reinforced laminated composite has a natural tendency to attenuate and scatter the ultrasound wave (see e.g., [67-69]), and as the wave scatters and attenuates, the intensity of the ultrasound signal decreases. Thus, for increasing composite thickness, the signal attenuation of the ultrasound wave will also increase. Based on this relationship, lower frequency ultrasound probes are typically used to inspect thick composite samples [55].

A material's acoustic impedance is a measure of the opposition to the sound wave propagation through the material and is defined mathematically as

$$Z = \rho c \quad (2.1)$$

where Z is the acoustic impedance of the material, ρ is the material density and c is the sound velocity through the material. The acoustic impedance can then be used to determine the loss of the energy (dB loss) in the wave that is reflected toward the transducer using the following equation

$$\text{dB loss} = 10 \log_{10} \left(\frac{(Z_2 - Z_1)^2}{(Z_2 + Z_1)^2} \right) \quad (2.2)$$

where Z_2 is the acoustic impedance of the second material at the boundary (i.e. the material into which the wave transmits) and Z_1 is the acoustic impedance of the material through which the wave has traveled [64].

Another metric for explaining the loss of energy at the material boundary is the reflection coefficient. The reflection coefficient is a ratio between 0 and 1 that describes the amount of energy reflected back toward the transducer from a material interface. The reflection coefficient, R , is defined as

$$R = \frac{(Z_2 - Z_1)^2}{(Z_2 + Z_1)^2} \quad (2.3)$$

where Z_1 and Z_2 are the same as defined in the previous equation [70]. The reflection coefficient is a parameter that has been used when inspecting the bondline between two materials, and this application will be discussed in further detail in a later section.

2.4.3 Velocity Dispersion

Dispersive materials are defined as materials whose phase velocity is different than their group velocity, and the measured velocity is dependent on the frequency of the transducer used for inspection [35]. The group velocity represents the velocity at which the peak amplitude in the ultrasound signal, which consists of many frequencies, travels through the sample thickness. The phase velocity identifies the time required for a continuous sinusoidal wave, which corresponds to a single frequency, to propagate through the sample thickness [35].

Using the phase spectrum of a broadband pulse, Sachse and Pao [71] determined the dispersion relation and the phase and group velocities of a fiber reinforced laminated composite. This dispersion of the ultrasound wave may be explained by a number of factors including but not limited to: sample geometry, frequency dependence of material properties, scattering, dissipation of signal energy and nonlinear effects [71]. The technique proposed by Sachse and Pao [71] reduced the time required to perform such

analysis when compared to continuous wave techniques, which accomplish the same task but take considerably longer to perform.

Strohm and Kolios [72] investigated the effects of dispersion on the measured phase velocity for perfluorocarbon liquids. They applied a photoacoustic method to measure the sound velocity and attenuation for three perfluorocarbon liquids. In the photoacoustic method, a pulsed laser is fired at a thin film of either gold or ink, and upon the laser beam's impact with the thin layer, an ultrasound wave is generated. An ultrasound transducer was placed near, though not in line, with the laser and served as the receiver. This setup is similar to a through transmission setup where both transducers are on the same side of the sample. The experiment was performed twice for each of three perfluorocarbon fluids, with the difference between the two experiments being the center frequency of the receiving transducer (375 MHz and 700 MHz). The results indicate that the measured phase velocity increased by 1.5% with the increase in the receiving transducer frequency. The measured attenuation for all three perfluorocarbons was approximately the same [72].

Research has demonstrated that the different types of signal pulses may be affected differently by dispersion. For example, Edwards [73] performed a study that included analysis of three different types of pulses: a rectangular pulse and two types of pulsed sine waves (one with constant amplitude and one with an amplitude varying with sine-squared). The sample of interest was dispersive and had a constant group velocity, but the identity of the material was not given in the paper. The goal of Edwards's study [73] was to evaluate the distortion experienced by the different ultrasound signal pulses as the wave propagates through the sample. Although there was little distortion of the

sine wave signals, the rectangular pulse did experience distortion. Thus, Edwards's study [73] demonstrated that some signal pulses, in this case a rectangular pulse, can be affected by dispersion differently than other pulses.

2.5 Ultrasound Techniques for Monitoring Temperature

As previously discussed, there are many uses for ultrasound technology. One of the applications of interest in this dissertation, particularly in Chapter Four, is the use of ultrasound to monitor the temperature and phase of a material. In recent years, studies have developed and presented ultrasound methods for monitoring temperature in a variety of scenarios, and several of these techniques are presented in this section.

Tsai *et al.* [74] developed an ultrasonic thermometer capable of identifying the temperature of the surrounding air by monitoring changes in the A-scan signal's time of flight and phase shifts. Their technique also accounted for the environment's humidity and was able to self correct the calculated temperature by using the relationship between humidity and speed of sound. Experiments were performed to validate their approach, and the calculated temperature was accurate to within 0.3°C on a temperature scale from 0°C to 80°C [74].

Huang *et al.* [75] also monitored the temperature of air, but instead of using time of flight measurements, their method focused on the identification of phase shift variations in the ultrasound signal. Their experimental setup includes two 40 kHz transducers operating in a through transmission configuration. The distance between the two transducers is kept constant, and changes in the phase angle of the ultrasound wave are measured using a FPGA digital phase detector. Using a microchip computer, Huang *et al.* [75] have the system programmed to calculate the temperature of the air up to every

10 milliseconds and display the results on an LCD screen. The accuracy of their method is within 0.05°C.

The studies performed by Tsai *et al.* [74] and Huang *et al.* [75] are similar to the study presented in Chapter Four of this dissertation in that they apply an ultrasound technique to identify the temperature of a particular medium. However, the study presented in this dissertation also monitors the phase of the material (e.g. solid or liquid), and from the analysis results, a multi-dimensional representation of the temperatures throughout the experimental setup may be obtained.

Chen *et al.* [76] measured the temperature of polymer extrusion using an ultrasound technique that included a piezoelectric transducer and a waveguide. The waveguide had two discontinuities at the end of the steel rod, and the difference in the time of flight measured between these two points was used to calculate the temperature of the polymer extrusion. Chen *et al.* [76] compared their results with thermocouple measurements, and the results were in good agreement with one another. Their study shows applicability of ultrasound techniques to polymer materials; however, their study considered melted polymer as it was extruded and did not consider different phases of the material (e.g. solid and melted).

Balasubramaniam *et al.* [77] developed an ultrasound technique to measure the temperature and viscosity of glass as it was melted. Their method included the use of an ultrasound sensor and a delay line probe. During the experiment, the shear reflectance from the solid-to-molten glass boundary was measured, and the time of flight was analyzed. Their technique improved upon the state of the art by being accurate on a wider range of both temperatures and viscosities. Balasubramaniam *et al.* [77] compared the

results of their ultrasound experiment with those obtained from independent measurements of both temperature and viscosity, and the results compared well with one another. The material analyzed in their study was molten glass, but they proposed the applicability of their method to polymer melt and manufacturing involving molten metals [77].

Ihara and Tomomatsu [78] applied a pulse echo ultrasound technique and finite difference calculations for identifying the one-dimensional temperature distribution of an alumina rod that is exposed to heating conditions on one end. The ultrasound transducer used in their study generated a shear wave rather than a longitudinal wave, and this probe was chosen in an effort to improve the accuracy of the temperature measurement. The experimental technique was applied to two alumina rods, and the temperature calculated from the ultrasound results was compared with temperatures obtained via infrared measurements. The results from the two methods compared well with one another, but there was a slight discrepancy. However, Ihara and Tomomatsu [78] were able to present the feasibility of their technique to being able to monitor the temperature of ceramic materials throughout the manufacturing process.

Ihara and Takahashi [79] applied a pulse echo ultrasound technique to monitoring the temperature and the temperature gradient in a steel plate that was heated on one side. The time of flight was measured and was correlated to the temperature and temperature gradient in the steel sample. The temperature measurements obtained via the ultrasound method were compared with those obtained using thermocouples placed inside of the steel, and the results were close to one another. Thus, the proposed method presented by Ihara and Takahashi [79] was demonstrated as having potential to match the results

obtained using thermocouples and would provide a non-invasive and non-destructive means of measuring the metal's temperature.

The material of interest in a study performed by Simon *et al.* [80] was body tissue that was exposed to thermal therapy. Using high intensity, focused ultrasound, the temperature of damaged body tissue was increased as part of a thermal therapy rehabilitation technique. Using a pulse echo ultrasound approach, the echoes off of the tissue were monitored, and the temperature of the tissue as estimated from this ultrasound approach was accurate to within 0.5°C [80]. Although this study has interesting applications in the medical industry, it did not consider different phases of material, which is considered in Chapter Four of this dissertation.

The studies mentioned thus far have successfully correlated the ultrasound signal to temperature values. Related to the study presented in Chapter Four of this dissertation, previous papers have been written that describe aspects of the project completed thus far. Moore *et al.* [81] presented initial work on a Discontinuous Galerkin Model (DGM) for analyzing the wax experiment described in the present dissertation, and the work was expanded upon by Moore *et al.* [82] in 2016. Although the DGM model did share some similarities with the measured results, there are a few aspects that require future work. For example, there was a high frequency component present in the analytical results that was not observed in the experiment. More recently, in his masters thesis, Gregg [83] performed further data collection and analysis using the same experimental setup as will be presented in chapter 4 of this dissertation. Gregg's work was a continuation of the work that was published by Lau *et al.* [84], and the present author worked on that study and was a co-author on that paper. This dissertation provides details of the early work on

this project including a discussion of the analysis methods developed for monitoring the temperature and phase of attenuative wax materials [85].

2.6 Nondestructively Evaluating Porosity

Ultrasound waves do not propagate well in air due to the acoustic impedance of air. Thus, the amount of porosity (small air pockets) within a carbon fiber reinforced laminated composite affects how the ultrasound wave propagates through the thickness of the sample. As mentioned in an earlier section, since fiber reinforced laminated composite manufacturing requires one material, the fiber plies, to be coated with another material, the resin/hardener matrix, the formation of voids at areas where the two materials do not bond well with one another is a common occurrence. Acknowledging that the presence of voids can alter the ultrasound wave's travel path through the thickness of a composite, a literature review was performed to gain a better understanding of this phenomenon.

Hsu and Nair [86] applied through transmission and pulse echo ultrasound techniques for evaluating the amount of porosity within carbon fiber reinforced laminated composites and how the porosity of the sample affects the measured attenuation slope. From their experiments, Hsu and Nair [86] found there are three factors, namely, volume content of pores, frequency of the transducer, and location of the pores relative to the ultrasound wave's travel path, that significantly affect the propagation of the ultrasound wave and the measured attenuation slope. They concluded that the attenuation slope associated with a sample linearly increases for increasing amounts of porosity within the sample.

Daniel *et al.* [87] measured the attenuation constant of a unidirectional carbon fiber reinforced laminated composite using an ultrasound technique that combines the pulse echo and through transmission methods. The ultrasound method used in this study involved placing an ultrasound transducer on either side of the sample, aligning them with one another, and operating the transducers in pulse echo mode. As the ultrasound transducers were operating simultaneously in pulse echo mode, they would receive a portion of the ultrasound signal sent from the opposing transducer. From this experimental data, Daniel *et al.* [87] were able to determine the attenuation constants for a set of points across the sample surface. After the ultrasound measurements were completed, the locations that were measured were viewed under a microscope to determine the volume fraction of porosity associated with each location. Like Hsu and Nair [86], Daniel *et al.* [87] also found that the measured attenuation constant increases as the volume fraction of porosity increases.

Instead of evaluating the attenuation constants, Reynolds and Wilkinson [88] studied the effects of porosity on the strength of the fiber reinforced laminated composite. In their study, Reynolds and Wilkinson [88] evaluated glass fiber reinforced laminated composites with fiber volume fractions ranging between 40% and 70% and carbon fiber reinforced laminated composites. They evaluated the change in the material's stiffness by measuring the sound velocity, which is related to the sample's elastic constants. If there is no significant change in the measured sound velocity, then there is no significant change in the sample's elastic constants. The results obtained for the glass fiber reinforced laminated composites indicated there was no significant change in the material properties for the fiber volume contents studied. The results were not the same for the carbon fiber

reinforced laminated composites. Reynolds and Wilkinson [88] found that the elastic constants for the carbon fiber reinforced laminated composites do vary depending on the fiber volume content, and furthermore, the measured sound velocity varies depending on the porosity content within the samples as well.

Throughout this discussion, the volume content of pores has been less than 30%. What happens if the volume content of pores is larger than 30%? Waterman and Truell [89] and Ying and Truell [90] developed mathematical models, which predicted that as porosity within the sample increased so would the sound velocity. Sayers and Smith [91] did not agree with these proposed models, and subsequently, they developed a theory that accounts for and considers parts containing volume fraction of porosities greater than 30%. Based on their results, Sayers and Smith [91] observed a decrease in the sample's sound velocity for increasing amounts of porosity. One of their theory's limitations is that it does not take into account pores that coalesce within the part. Thus, each pore is considered to be spherical, not ellipsoidal in shape. A spherical pore does not adequately represent all of the pores within a laminated composite. As observed from imaging and microscopic analysis of fiber reinforced laminates, the pores and voids often found in such parts are typically elongated and more ellipsoidal in shape. Therefore, when needing to consider different pore geometries, the approach of Sayers and Smith [91] would need to be revised to account for such geometry changes. In general, the qualitative aspect of their results would be expected to remain the same, where there is a decrease in measured sound velocity for increasing amounts of porosity.

2.7 NDE of Transversely Isotropic Laminated Composites

Unidirectional laminated composites are transversely isotropic meaning that the material properties parallel to the fiber are different than those in the plane transverse to the fiber direction. In addition to being able to identify and characterize defects within and the porosity of laminated composites, previous studies have also applied ultrasound techniques to determining the elastic constants associated with these materials.

One of the first ultrasound techniques for evaluating the elastic constants associated with a unidirectional laminated composite was developed by Markham [52] in 1970. To determine the elastic constants of a unidirectional carbon fiber reinforced laminated composite, Markham [52] applied a through transmission ultrasound technique to the inspection of a composite sample. Using the collected A-scan signals, Markham determined the longitudinal and shear wave velocities measured through the part for a variety of incident angles. Since the elastic constants and the measured sound velocities are directly related to one another, the measured values of the sound velocities can be used to calculate the elastic constants.

In Markham's [52] experimental setup, the part was placed on a rotation table in the center of a stage, and the transmitting and receiving transducers were placed on either side of the laminate. To generate the oblique incident angles, the laminate was rotated relative to the transducers using the rotation table. When the transducers were located normal to the sample surface, only a longitudinal wave was observed propagating through the sample thickness. When the transducers were located at an oblique incidence angle relative to the sample surface, both a longitudinal and a shear wave were observed propagating through the thickness of the sample. Using these measured longitudinal and

shear velocities, Markham [52] was able calculate the five elastic constants associated with the unidirectional carbon fiber reinforced laminated composite.

Nearly twenty years later, Rokhlin and Wang [53, 54] applied a double through transmission ultrasound technique for identifying the elastic constants of a unidirectional carbon fiber reinforced laminated composite. In their study, Rokhin and Wang [53, 54] identified an error in the method proposed by Markham [52] where Markham used the group velocities rather than the phase velocities for calculating the elastic constants associated with the laminate. The group velocity represents the velocity at which the peak amplitude in the ultrasound signal, which consists of many frequencies, travels through the sample thickness. The phase velocity identifies the velocity at which a continuous sinusoidal wave, which corresponds to a single frequency, propagates through the sample thickness [37].

The experimental setup used by Rokhlin and Wang [53, 54] consisted of a single transducer and a reflective cylinder, which is a key component in the successful implementation of a double through transmission technique. The sample was placed in the center of the reflective cylinder, the ultrasound probe was placed on one side of the sample, and a reflective plate was placed directly behind the sample. The double through transmission aspect refers to the wave propagating through the thickness of the sample twice. In this technique, the incident ultrasound wave was emitted from the transducer, propagated through the sample thickness, reflected off of the reflective plate located behind the sample, propagated back through the sample thickness using its original travel path and was received by the transducer [53, 54]. Much like the approach developed by

Markham [47], Rokhlin and Wang [53, 54] measured the signal velocities corresponding to a variety of incident angles by simply rotating the sample relative to the transducer.

After collecting the measured velocities, Rokhlin and Wang [53, 54] applied a least squares regression to the optimization of the Christoffel equation combined with Cardan's solution [92] for determining the elastic constants associated with the unidirectional carbon fiber reinforced laminated composite. They also considered the effect of signal noise in their results by artificially adding up to 5% signal noise in their data. Based on their calculations, no significant changes in the calculated elastic constants were observed when the signal noise was considered [53, 54].

Newberry [1] considered this research topic from a mathematical approach and developed a paraxial approximation for the ultrasound wave propagating through liquid and solid materials, and a carbon fiber reinforced laminated composite was one of the materials considered in his dissertation. One aspect of Newberry's model [1] to keep in mind is that to estimate the wave amplitude as it propagates through the sample thickness, the elastic constants of the sample material must be known. To validate his model's accuracy, Newberry compared the predicted results with measured values, and they were in good agreement with one another. For his experimental measurements, Newberry used a through transmission technique with a spherically focused pulser and a microprobe receiver. Based on the small size (0.5 mm) of the piezoelectric element in the microprobe transducer, it is considered a point receiver. A more in-depth description of Newberry's mathematical approach will be included in Chapter Five of this dissertation where the development of the mathematical analysis proposed as future work is presented.

Another mathematical approach was created by Sinha *et al.* [93]. They considered transversely isotropic formations near wellbores and created a finite difference time-domain approach using perfectly matched layers for estimating the phase slowness (where slowness is the inverse of velocity) in a given ultrasound wave propagation direction. They compared their model's results with measured phase slowness values, and the results compared well with one another.

Minachi *et al.* [94] considered thick, unidirectional, transversely isotropic carbon fiber reinforced laminated composites and developed an acoustoultrasonic method for determining the elastic constants associated with the sample material. Their approach is unique in that it requires access to only one side of the material whereas the experimental methods described thus far require access to both sides of the sample.

To obtain three out of the five elastic constants for the transversely isotropic material, Minachi *et al.* [94] measured longitudinal and shear wave velocities with probes at normal incidence to the sample surface. The acoustoultrasonic technique identified the remaining two elastic constants and used two contact longitudinal wave transducers with the pulser located at an oblique angle relative to the sample surface.

2.8 Applications Involving Two or More Components Bonded Together

As the aerospace and automotive industries increasingly incorporate composite laminates into their product lines, applications where the composite laminate is bonded to a metal structure are occurring more often. The interface between these two materials is of great interest as the quality and safety of such a component must be verified via inspection of the bonded surface. As many destructive tests, such as peel tests or tensile

tests [95], would permanently damage the component, the development of nondestructive methods for inspecting such parts is of great interest to these industries.

Baker [8, 96] provides an excellent review of bonded composite patch repairs in the aerospace industry and some of the issues that are posed by such repair techniques. Baker [8] describes in detail the common composite repair procedures used for metal aircraft and follows it with a description of a model he developed for predicting the crack growth in a patched specimen. The results of his model compare well with the measured results. Throughout his paper, Baker [8] outlined examples of composite bond repairs from a variety of aircraft components including: F111 wing pivot and wing-skin, Boeing 767 Keel beam, Lockheed C141 Starlifter wing-skin, and MD-82 slats. Baker describes both cocured and precured composite repair techniques and the difficulty in certifying that the repair meets or exceeds the required loading criteria. A cocured technique cures the fiber reinforced composite laminate at the same time as the repair adhesive. A precured technique first cures the fiber reinforced composite repair piece. Then, the cured composite is adhered to the original structure [8].

Baker [8] also made a brief statement about corrosion at the interface between the metal and composite repair patch. He stated that the presence of corrosion between the metal and composite repair is usually caused by moisture ingress from an improperly sealed repair area and is rather uncommon if proper procedures are followed. However, the mismatch of the coefficient of thermal expansion for the two materials causes residual stresses to form between the aluminum and composite materials in the repair [97], and this could contribute to the formation of disbonds between the two materials.

In one of his more recent papers [96], Baker describes the design and implementation of a “smart patch” that is capable of monitoring the composite patch repair in real-time. The smart patch operates by calculating the ratio of the strain at the composite patch repair and the strain at a location a given distance away from the composite repair. Once the ratio of strains begins to change, this indicates to the inspector that the bondline is weakened or is in the process of debonding and that additional repair is needed on the component. A benefit of the smart patch is that the certification process for these patches is not as difficult because it monitors the bond real-time. A disadvantage to this method is the price of the smart patch, and Baker suggests that this method be reserved for monitoring patches on primary structures where the importance or need for the live feedback can counteract the associated cost [96].

2.9 NDE Methods for Evaluating Bondlines

There exist a variety of defects that can occur at the bondline between two adherends. Some of these defects include: moisture ingress that causes plasticization of the epoxy adhesive, voids, cracks (caused by thermal shrinkage) and improperly cured resin [38]. Adams and Cawley [38] discuss some of the NDE methods that are available for inspecting such parts and identifying these defects. A few of the NDE techniques described by Adams and Cawley [38] include: ultrasound, eddy current testing, passive and active thermographic approaches and optical holography. Nieminen and Koenig [95] provide an excellent overview of macroscopic and microscopic NDE methods for identifying bonds and debonds between two aluminum structures, honeycomb materials, and composite structures. While some of the NDE techniques they propose overlap with those described by Adams and Cawley [38], Nieminen and Koenig [95] also describe

methods such as coin tapping, radiography, mechanical impedance method and electronic speckle pattern interferometry. However, the majority of Nieminen and Koenig's paper and the NDE method that receives the most attention is ultrasound.

Nieminen and Koenig [95] describe the many benefits of using ultrasound for inspecting the bondline between two materials. The phrase "inspecting the bondline" refers to identification of whether or not a bond exists between the two adherends, and in this context, is not meant to imply information relating to the strength of the bond. They provide an excellent discussion on the wave's reflection coefficient, which is a number between zero and one that refers to the amount of the wave that is reflected back toward the transducer when the wave encounters a material interface. The higher the reflection coefficient, the larger the portion of the wave reflected toward the transducer. Due to the low acoustic impedance of air, which is usually present in defects, the reflection coefficient for a poorly bonded or unbonded location will be near unity as the majority of the wave reflects back toward the transducer. When the two adherends are well bonded to one another with a thin layer of adhesive and both components are the same material (e.g. aluminum bonded to aluminum), the reflection coefficient will be near zero as the wave considers this type of bonded sample to be one continuous piece of the material [95, 98].

Using an ultrasound technique, Wang *et al.* [99] captured the change in the reflection coefficient at the bondline interface as an epoxy adhesive was allowed to cure from a liquid to a solid. The experimental setup that consisted of placing the bonded sample in the center of a reflective cylinder with the single transducer placed along the arc of the cylinder is nearly identical to the experimental setup, referred to as a goniometer, used by Rokhlin and Wang [53]. To vary the adhesive strength of the epoxy,

Wang, *et al.* [99] examined a variety of samples whose epoxy adhesive contained different amounts of hardener ranging from the amount recommended by the manufacturer (20%, indicating it will fully solidify) to no hardener (0%, indicating it cannot fully solidify).

2.9.1 Aluminum-Aluminum Bondline Evaluation Methods

The groundwork for ultrasonic inspection of bondlines between two adherends was performed primarily on aluminum-aluminum interfaces. These types of bonds were, and still are, frequently found in aerospace applications as described by Baker [8, 96]. Cawley and Hodson [100] used an ultrasonic spectroscopy technique for determining not only the thickness of the adhesive bond between two aluminum plates but also the apparent modulus of the adhesive using the first mode of the longitudinal wave in combination with a second measured longitudinal wave mode. These two longitudinal wave modes allowed Cawley and Hodson [100] to differentiate between a change in the adhesive's thickness and modulus since the first mode is independent of the adhesive modulus. This approach was an improvement upon an earlier method developed by Guyott and Cawley [101] as it decreased the error in the adhesive's modulus from 20% to approximately 6.5%. The accuracy with which Cawley and Hodson [100] measured the adhesive thickness matched that of measuring the thickness with a micrometer.

Drinkwater and Cawley [98] ultrasonically inspected the contact between two aluminum plates in contact with one another without being adhesively bonded. As they increased applied compressive pressure to the plates, the reflection coefficient decreased. Intuitively, this makes sense since the contact between the two plates increases as the surface roughness, or asperities, are flattened out with increasing applied pressure.

Ultimately, the reflection coefficient reaches an asymptotic value, such that the two surfaces are in as intimate contact as possible regardless of whether the pressure is continually increased. Drinkwater and Cawley [98] also observed that the reflection coefficient was frequency dependent. Drinkwater *et al.* [102] considered the relationship between the reflection coefficient and repeated loading cycles. In that study, Drinkwater *et al.* [102, 103] considered the contact between two aluminum plates. Similar to the study performed by Drinkwater and Cawley [98], Drinkwater *et al.* [102, 103] varied the applied pressure on the two aluminum plates and observed the corresponding changes in the measured reflection coefficient. Using the cyclic loading profile, Drinkwater *et al.* [102, 103] noticed that the measured reflection coefficients for the first cycle were different than the measured coefficients for the subsequent cycles. They observed that a small amount of plastic deformation occurred during the first loading cycle, which flattened out the asperities on the aluminum surface. After the plastic deformation occurred during the first loading cycle, the remaining loading cycles exhibited a repeatable pattern of elastic deformation where the measured reflection coefficients were near unity for low values of applied pressure and were near zero for higher values of applied pressure.

Vine *et al.* [104, 105] studied the degradation of the bondline between two aluminum plates that had been exposed to an elevated temperature (50 °C) water bath. The water bath plasticized the epoxy adhesive between the two aluminum plates, and thus the bondline quality deteriorated. Using a combination of normal and oblique incident waves, Vine *et al.* [104, 105] inspected the quality of the bondline between the two aluminum plates and identified weak regions of the bond. Pilarski and Rose [62]

performed a similar experiment, but they looked exclusively at the interface between aluminum and epoxy.

2.9.2 Composite-Composite Bondline Evaluation Methods

Drinkwater *et al.* [103] inspected a bondline between graphite composite materials in a manner similar to that of Drinkwater and Cawley [98] and Drinkwater *et al.* [102] in that they measured the reflection coefficient as a function of applied pressure. No adhesive was used between the two graphite composite bricks, and the measured reflection coefficient was near unity when applied pressure was low and near zero when pressure was high. Using the measured reflection coefficients, Drinkwater *et al.* [103] estimated the stiffness at the interface between the two bricks. Their measured results were compared with that predicted using the model developed by Webster and Sayles [106], and there was a discrepancy between the two results. Drinkwater *et al.* [103] attributed this discrepancy to the modulus value used for representing the graphite composite in the model. The graphite bricks are comprised of two forms of graphite: granular and amorphous. The granular component of the graphite is the stronger of the two components with its modulus ranging from 1 GPa to 100 GPa depending on the orientation of the grains. Drinkwater *et al.* [103] proposed that if a modulus value more indicative of the granular portion of the graphite had been used in the model, there would have been less discrepancy between the results.

In a related article by Robinson *et al.* [107], the same authors as in [103] performed a study of the relationship between cyclic loading and the reflection coefficient at the interface of the two graphite bricks. Similar to the results observed by Drinkwater *et al.* [103], Robinson *et al.* [107] observed some plastic deformation of the

surface asperities, also referred to as the surface roughness elements, and after the first load cycle, the subsequent loading cycles exhibited repeatable elastic deformation under loading. The elastic nature of the material deformation is observed in the similarity between the measured reflection coefficients. With the exception of the first loading cycle, the measured reflection coefficients were nearly identical between loading cycles which indicates that same type of deformation occurred and relaxed during those subsequent loading cycles [107].

Using a combination of normal and oblique incident angles, Vijaya Kumar *et al.* [108] used ultrasound technology to evaluate the quality of the bondline between two unidirectional laminated composites. In an effort to produce known degradation at the sample bondline, Vijaya Kumar *et al.* [108] created a sample set where some of the samples had the manufacturer recommended amount of resin and hardener in the epoxy adhesive while other samples included varying amounts of polyvinyl alcohol, a mold release agent. The polyvinyl alcohol made the resin mixture porous and was used to simulate a degraded bondline. The increased porosity indicated an increased amount of degradation at the interface between the two laminates. As was mentioned previously, the acoustic impedance for air is low compared to that of the surrounding material. Thus, the reflection coefficient measured for samples with increased amounts of porosity were higher than those with less or no amounts of porosity [108].

Adler *et al.* [109] developed an approach called Angle Beam Ultrasonic Spectroscopy (ABUS) for inspecting the bondline between two composites. ABUS used a combination of normal and oblique incident ultrasound waves and evaluates the frequency response of the wave as it propagates through the material. The contribution of

the oblique incident wave is the ability to tell the difference between kissing bonds, or weakened bonds, from a good, strong bond. To form the weakened bonds between the composites, Adler *et al.* [109] exposed the samples to a propriety environmental aging process designed by the Ohio State University. This environmental exposure generated interfacial adhesion bonding defects rather than the cohesive bonding failure that occurs when there is a defect with the epoxy adhesive. Adler *et al.* [109] were able to linearly correlate the effective modulus values calculated with their ABUS approach to measured values and were thus able to correlate their results to the strength of the bond between the two composites.

2.9.3 Composite-Aluminum Bondline Evaluation Methods

Several applications exist in the aerospace and automotive industries where composite materials are being bonded to metals (see e.g., [8, 96, and 110]). For example, the aerospace industry has been using repair processes involving patching a metal aircraft component with a composite patch since the late 1980's. One of the concerns that the automotive industry has expressed regarding the use of laminated composites alongside aluminum components is the occurrence of galvanic corrosion in the aluminum, which then weakens the bond between the two materials [111].

The study performed by Mantong *et al.* [112] evaluated the corrosion energy associated with various types of high-strength metals that were bonded to carbon fiber reinforced composite laminates. The three types of metals considered were titanium, aluminum, and stainless steel. Of the three metals, the aluminum had the highest tendency to experience galvanic corrosion when bonded to the carbon fiber reinforced composite and exposed to a variety of sodium chloride solutions. The corrosion energy

associated with the sample remained relatively constant throughout the time period studied, which was 72 hours. Mantong *et al.* [112] found that the types of treatments and sealants used on the aluminum surface could assist in decreasing the corrosion energy associated with the bonded sample, especially when considering crevice corrosion.

Baker [8, 96] also described the importance of treating and sealing the aluminum when he described composite patch repair methods being used in the aerospace industry in Australia. Baker claims that if the aluminum is properly treated and sealed, galvanic corrosion is not an issue.

The nondestructive inspection of composites bonded to aluminum surfaces was studied by Stair, Moore, and Nelson [113] and by Stair *et al.* [114]. In these studies, a variety of ultrasound methods and data analysis techniques were considered for inspecting the bondline between a composite and aluminum structure. The details of this study are provided in Chapter Three of this dissertation. One feature that inspectors and quality control officials will appreciate is that the bondline can be evaluated regardless of whether the inspector has access to the aluminum surface, the composite surface or both surfaces. In their studies, Stair, Moore and Nelson [113] and Stair *et al.* [114] applied a contact transducer technique, an immersion ultrasound technique, and a phased array technique. The Fast Fourier Transform of the data obtained using the immersion technique was also examined and provided insight regarding whether a bond or a disbond was present at a given location.

2.10 Conclusion

The following chapters present the author's work in three areas highlighted throughout this chapter: application of ultrasound techniques for inspecting the bondline

between a carbon fiber reinforced laminated composite and aluminum, temperature and phase monitoring of attenuative materials using an ultrasound through transmission technique, and inspection of carbon fiber reinforced laminated composites using an oblique incidence through transmission ultrasound method. Throughout the literature review, similarities and differences have been drawn between the state of the art with respect to each of these three topic areas and the work presented in this dissertation. Chapters Three, Four and Five present in detail the work that was performed as part of this dissertation and how each accomplishment has added a scientific contribution to this field of study.

CHAPTER THREE

Ultrasound Methods for Inspecting the Bondline between a Carbon Fiber Reinforced Laminated Composite and Aluminum

3.1 Introduction

The purpose of this study is to design and implement an ultrasound technique for identifying the unbonded regions between a carbon fiber reinforced laminated composite and aluminum. As mentioned in the previous chapter, a variety of methods exist for inspecting these parts including: thermography, electron speckle pattern interferometry, x-ray and coin tapping [95]. Yet, as researchers have found in previous studies, ultrasound technology remains one of the most common and cost effective nondestructive evaluation methods for this task [8, 96].

The focus of this study is not to identify the weakest location at the bondline interface between the two materials. Rather, the purpose of this study is to compare the inspection results obtained with conventional contact ultrasound techniques with results obtained using an immersion ultrasound technique. Both of these techniques use ultrasound transducers operating in pulse echo mode, but the spherically focused transducer used in the immersion testing provides an improved spatial resolution of the inspection. Part of the uniqueness of the present approach is the inspection of the bondline between dissimilar materials. Previous studies (see e.g. [98, 102, 103]) have focused on the bondline inspection between similar materials, such as two composites or two aluminum plates. The present study involves the bondline inspection between a homogeneous, isotropic aluminum plate and a nonhomogeneous, orthotropic carbon fiber

reinforced laminated composite. The sample is inspected from both sides to demonstrate that the bondline between these two dissimilar materials can be evaluated regardless of which of the two materials is facing the transducer. This analysis is also different from previous studies because the inspector should be aware of how the ultrasound wave will propagate in each material and how the signal in each material may constructively or destructively interfere with one another. Furthermore, a frequency analysis of both the contact transducer data and the immersion ultrasound data is performed in an effort to correlate changes in the frequency content at the bondline to regions where the two materials are not bonded to one another. From the frequency analysis, changes in the frequency intensity can be used to identify whether a location at the interface is bonded or unbonded.

3.2 Sample Preparation

Two samples were used in this study. The first sample was manufactured using a co-cure technique, in which case the laminate was bonded directly onto the aluminum during the curing process, whereas the second sample was manufactured using a pre-cure technique, where the laminate was cured separately and then bonded to the aluminum. The reason for studying both of these cases deals with the types of systems that may be inspected in the field. For example, some manufacturing methods may use the co-cure technique while making a component, but when the part is in service, it may be repaired using a pre-cure technique where a pre-manufactured laminate is bonded to the aluminum plate as a replacement for the original laminate. Both samples include an aluminum step wedge and three laminate thicknesses (4 plies, 8 plies and 12 plies). The aluminum step wedge was machined such that when the laminates were placed on the top surface of the

aluminum, the entire sample would have approximately the same thickness. For example, the 4 ply laminate was placed at the thickest step in the aluminum wedge, and the 12 ply laminate was placed at the thinnest step in the aluminum wedge as depicted in Figure 3.1. The as-manufactured laminate is shown in Figure 3.1, and the different laminate thicknesses are highlighted in both Figures 3.1(a) and 3.1(b). The two manufacturing techniques used in this study are described in detail in sections 3.2.1 and 3.2.2.

3.2.1 Co-cure Manufacturing Technique

In a co-curing technique, the uncured carbon fiber reinforced laminated composite is laid on the aluminum step wedge without release agent and the full structure is cured at once. In this study we use an 8 harness satin prepreg fabric with a UF3352 TCRTM resin that has already been wetted into the carbon fiber fabric. The laminate stacking sequence is kept simple at $[0/90]_{n,s}$ and is laid directly onto the aluminum step wedge without a release agent. The 8 HS fabric has a warp and weft direction, and the weft direction aligned along the horizontal direction is referred to as the 0 degree orientation. The fabric weave is what prevents the 0 degree orientation from being the same as the 90 degree orientation. The subscript 'n' in the laminate stacking sequence definition represents the half-number of the laminate plies for that particular stacking sequence whereas the subscript 's' indicates that the stack is symmetric about the center. For example, the expanded method of writing the stacking sequence for the 4 ply laminate is $[0/90/90/0]$. The value of 'n' is equal to 2, 4, and 6 when referring to the 4, 8 and 12 ply laminates, respectively. As the laminate undergoes its manufacturer-recommended cure cycle, it will form cohesive bonds with the aluminum surface as the epoxy resin matrix crosslinks and solidifies throughout the cure cycle.

Based on experimental observation, this part experienced high stress along the edges where the composite laminate began to peel away from the surface of the aluminum step wedge. These stresses along the edges are caused in part by the mismatch



Figure 3.1 (a) The top surface of the co-cured carbon fiber reinforced laminated composite bonded to an aluminum step wedge. (b) A side view of the co-cured sample

of the coefficient of thermal expansion between the resin matrix and the carbon fiber fabric [115]. The research performed by Pipes *et al.* [115] and Stair *et al.* [97] confirm the presence of stress along the edges of a carbon fiber reinforced laminated composite caused by the mismatch of the coefficient of thermal expansion between the resin matrix and the carbon fiber. Furthermore, residual stresses form during the cure cycle between the aluminum and the carbon fiber laminate due to the mismatch in the coefficient of thermal expansion for these two materials [8], and this mismatch in the coefficient of thermal expansion likely produces the majority of the stresses at the bondline interface between the two materials. Since the purpose of the present study is the nondestructive

evaluation of the bondline, the study of the applicability of the Pipes *et al.* [115] model to the effects of the mismatch of the coefficient of thermal expansion between the laminate and the aluminum is not pursued here, but it could prove to be an interesting study in the future.

The thickness of each aluminum step and the thickness of each laminate section is depicted in Figure 3.2, and the image is not to scale. Figure 3.2 provides the sample dimensions used for both the co-cured technique and the pre-cured technique. The difference is that the pre-cure technique also has a thin layer of acoustic couplant (on the order of a few mils) between the aluminum and the carbon fiber whose purpose is to acoustically couple the two materials during the inspection process. Further details about the pre-cure technique are provided in section 3.2.2.

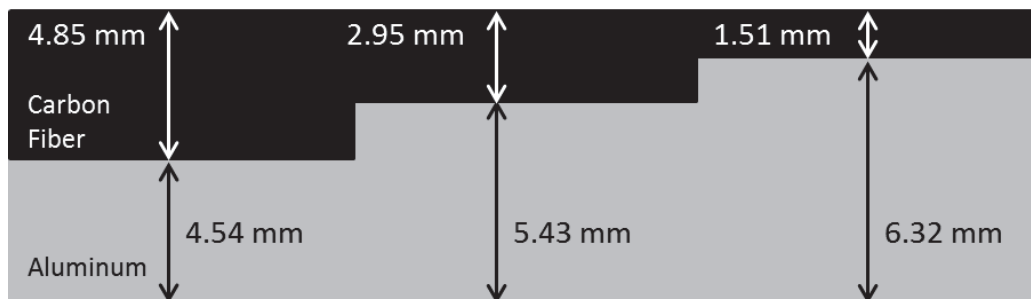


Figure 3.2 The thickness associated with the 12 ply, 8 ply and 4 ply laminates are shown from left to right, respectively

3.2.2 Pre-Cure Manufacturing Technique

The second sample was manufactured using a pre-cure technique. The laminate stacking sequences are the same as those mentioned for the co-cure technique. The difference with this manufacturing method is that a release agent is applied to the aluminum prior to the laminate being stacked on top of the metal during the

manufacturing process. Thus, as the epoxy resin matrix undergoes its cure cycle and forms crosslinks, the epoxy will not form a bond with the aluminum surface. Once the laminate cure cycle is complete, the laminate is removed from the surface of the aluminum, and an adhesive (or another similar acoustic coupling medium) is placed between the two surfaces to bond them to one another.

For this study, an adhesive was not chosen to bond the aluminum to the carbon fiber reinforced laminated composite. This decision was made such that the same aluminum step wedge and carbon fiber reinforced laminated composite could be used in a variety of tests with different coupling mediums. For example, if an epoxy resin, which solidifies through an irreversible process involving the cross-linking of its polymer chains, had been used to bond the two materials to one another, then, the separation of the adherends from one another after the inspection was completed would likely have caused damage to one if not both of the adherends. In this study, a glycerin-based ultrasound couplant (Ultrigel II Ultrasonic Couplant) was placed at the bondline between the two materials. After the inspection was completed, the two adherends were separated without imposing damage, and the couplant was wiped off the surfaces. Theoretically, a variety of other materials, such as a high viscosity shear couplant or petroleum jelly, could also have been used in this study as a coupling medium between the two adherends. Using the couplant to represent an adhesive in this study is a reasonable alternative to the more permanent epoxy resin adhesive because throughout the study the focus is on the inspection of the bondline using longitudinal waves. Thus, the inability of the glycerin couplant to hold a shear wave is not an issue. Furthermore, the couplant and the adhesive are both isotropic mediums that are present between the two adherends. Although the

material properties of the couplant and the adhesive may be different from one another, the material properties between different adhesives could potentially be different from one another. The main takeaway is whether or not a medium is present between the two adherends to allow the ultrasound wave to propagate from one adherend into the other. If no such medium exists, the majority of the ultrasound wave reflects back toward the transducer as described in section 2.9 of the previous chapter. The presence of couplant between the materials will be termed a “bond” in the present context because there is an acoustic path between the adherends, and the absence of couplant will be terms an “unbonded” region due to the absence of an acoustic path between the adherends.

For the pre-cured sample the outcome is not to measure the surface area of the bond, but to have a binary test for comparing the signals where there was a “bonded” region (with couplant) and a region without any couplant. Thus, the quality and uniformity of the acoustic couplant is not as vital of an issue. Figure 3.3 shows the Ultrigel II Ultrasonic Couplant from Echo Laboratories being applied to the aluminum surface that is in contact with the 8 ply laminate. After applying a dime size amount of the ultrasound couplant to the aluminum surface, the gel is smoothed out by hand as seen in Figure 3.3(b) prior to placing the laminate on top of the aluminum. This manual spreading of the gel is not absolutely necessary since the manual pressing of the laminate to the aluminum will naturally disperse the gel; however, the author chose to manually spread out the ultrasound gel to assist in providing a more even distribution of the couplant across the surface and for preventing the formation of voids at the bondline when placing the laminate on the surface of the aluminum. Notice that ultrasound gel has

also been placed on the 12 ply (left) and 4 ply (right) laminate surfaces to ultrasonically couple the contact probe to the material.

Since the ultrasound gel was applied at the center of where the laminate would be in contact with the aluminum, the edges of the laminate remained naturally unbonded to the aluminum surface as the gel did not spread to fully cover the interfacial area between the laminate and the aluminum. This is acceptable because while collecting data, the ultrasound probe was placed at the center of the surface of each laminate. Since the gel



Figure 3.3 Ultrigel II Ultrasonic Couplant (a) being applied to the sample surface and (b) being smeared across the surface to form a more even layer prior to the laminate being placed on the surface.

was applied to the center of the interface, the inspector knew the two materials would be acoustically bonded to one another at this location. When the sample was turned over such that the transducer was in contact with the aluminum, the probe was again placed at the center of the surface for each of the three regions of interest. While examining this

pre-cured sample, the goal was to identify differences in the ultrasound signal when inspecting bonded (coupled) and unbonded (uncoupled) regions. Thus, knowing the location of the acoustic couplant at the bondline is acceptable. The inspection of the co-cured sample, whose immersion ultrasound inspection results are discussed in detail in section 3.4, was performed not knowing a-priori where the unbonded locations were located, and the inspector was required to identify them based solely on the ultrasound data. After performing the study with the pre-cure sample, the inspector knew what features, such as how the signal decays at a bonded location, to look for in the A-scan signal to identify whether a particular scan location was associated with a bonded or unbonded location.

Figure 3.4 highlights the area of the 4 ply laminate that had couplant on it and identifies the area of the laminate that did not have couplant on it. In Figure 3.4, the edges of the 4 ply laminate appear grey in color due to the camera flash. The area coated in ultrasound gel is encompassed by the red dashed line and has a higher reflection with striations of gel running vertically along the surface. These striations were formed when the laminate was removed from the surface of the aluminum. The matte, grey area of the laminate surface denoted by blue arrows corresponds to the dry area of the laminate that is starved of the ultrasound gel couplant.

Similarly, Figure 3.5 shows the area of the laminate surface and the area of the aluminum surface that were coated in ultrasound gel and were acoustically coupled (or bonded) to one another. The area encompassed by the red dashed lines indicates the area coated with ultrasound gel, whereas the area outside of the red dashed lines corresponds to the unbonded region between the aluminum and laminated composite. Again, to ensure

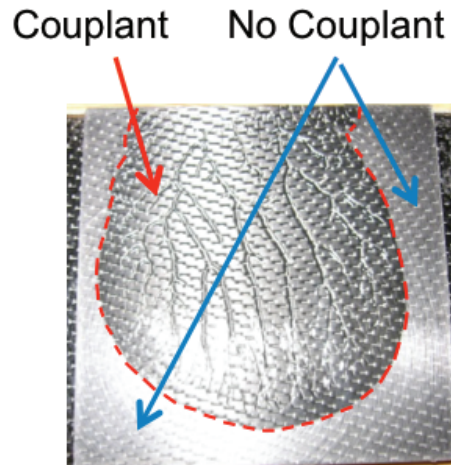


Figure 3.4 The area coated in ultrasound gel is encompassed by the red dashed line and the area denoted by the blue arrows is starved of the ultrasound gel.

the contact probe was evaluating a bonded region between the aluminum and composite, the probe was placed at the center of the laminate surface where it remained far away from the unbonded edge region. An example of where the probe was located relative to the sample surface is provided in Figure 3.6 where the experimental setup for the contact transducer measurements is presented.

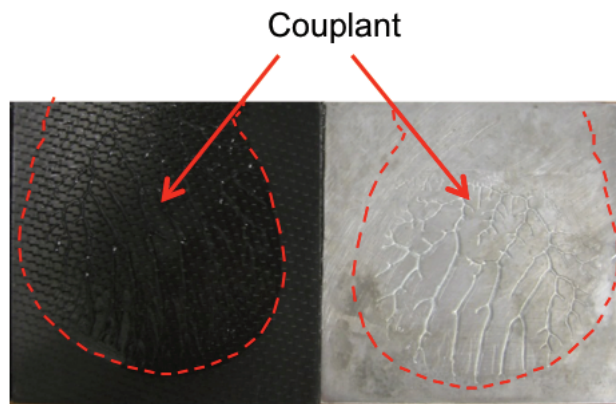


Figure 3.5 The area encompassed by the red dashed lines corresponds to areas that are wetted with ultrasound couplant. Outside of these areas there is no ultrasound couplant.

3.3 Contact Ultrasound Transducer Technique

A contact transducer technique was the first ultrasound method used in this study while inspecting the bondline between the carbon fiber reinforced laminated composite and the aluminum step wedge. The probe is placed on the sample surface with some of the Ultragel II couplant acoustically coupling the probe to the sample surface. The couplant on the part's outer surface provides an acoustic path for the ultrasound wave generated by the transducer to penetrate through sample surface. When the ultrasound wave interacts with an unbonded region within the sample, the majority of the ultrasound wave reflects back toward the transducer from which it originated.

In Figure 3.6, the ultrasound contact probe is placed at the center of the 4 ply laminate surface, and the aluminum step wedge is located beneath the laminated composite. This figure also presents the experimental setup used while collecting the data for the contact ultrasound probe technique. The experimental setup and data collection process is described in detail in the following section.

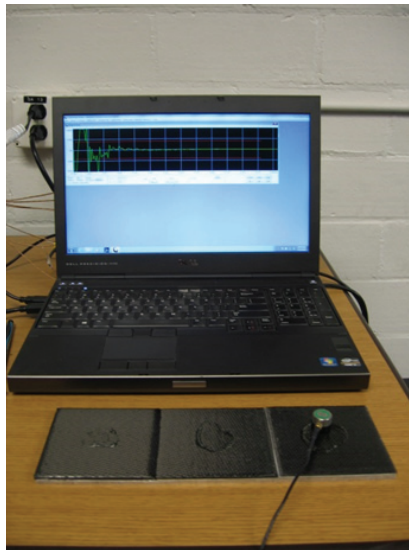


Figure 3.6 Experimental setup with the contact transducer placed at the center of the 4 ply laminate region of the bonded sample.

3.3.1 Data Collection

Data was collected using TD PocketScan software that controlled the pulser, the receiver, and the data storage. The sampling rate was 100 MHz, and the A-scan data from 0.52 μs to 19.92 μs was stored for further analysis. This range of data was chosen to ensure the entire signal of interest was saved during the experiment. A 5 MHz contact ultrasound probe was used for this experiment. The high pass filter used while collecting data was 2.5 MHz while the low pass filter was 7.5 MHz to allow frequencies through that surround the 5 MHz operating frequency of the probe. The A-scan data was saved in the TD PocketScan software in a .scn file format. Once the data collection was completed, the .scn file was exported to a .txt file format so it could be evaluated in Matlab. The files were then read into Matlab and analyzed using a program written by the author. Within the Matlab program, the bondline region of the A-scan is gated, and a FFT of the gated region is performed. The term ‘gated’ refers to only looking at the portion of interest in the A-scan signal. For example, in Figure 3.7, the blue horizontal line indicates the gated region of interest in A-scan signal, and the criteria used for identifying the region of interest in the A-scan is explained in the following section with respect to the aluminum-to-composite bondline inspection data.

A data file containing the signal intensity of the receiver as a function of time was created and stored for each of the cases considered. These cases included inspecting the composite-to-aluminum bondline interface for the 4 ply, 8 ply and 12 ply laminates as well as inspecting the aluminum-to-composite bondline interface for each of the three laminate thicknesses. Each of the measurements was performed when there was no couplant between the two materials and when there was couplant between the two

materials. Thus, a total of 12 cases were considered, and the results are discussed in the following sections.

3.3.2 Results for Aluminum-to-Composite Interface

The aluminum-to-composite interface for the pre-cured sample was inspected using a 5 MHz contact transducer probe whose planar resolution is similar to that of the probe diameter. There were two goals for this inspection. The first goal was to identify how the ultrasound signal and the FFT of the gated region of the A-scan vary depending on whether a bonded or unbonded location was being inspected. The second goal was to form a baseline for analysis of the immersion ultrasound scan results, which will require the A-scan analysis to be performed many times in an automated fashion.

During this inspection, the contact probe was placed on the aluminum surface of the sample as seen in Figure 3.7(a). A thin layer of glycerin-based ultrasound gel couples the ultrasound probe to the sample surface and enables the ultrasound wave to propagate from the probe into the sample. The wave propagates through the aluminum to the aluminum-to-composite bondline, and if the two materials are bonded to one another, the wave continues to propagate through to the composite laminate. Figures 3.7(b) and 3.7(c) each present an A-scan amplitude plot (upper image) and an FFT plot associated with the gated region of the A-scan (lower image). Figure 3.7(b) corresponds to the unbonded case where no acoustic couplant was placed between the aluminum and the 12 ply carbon fiber reinforced laminated composite. The results obtained for the 12 ply laminate region lead to the same conclusions as those obtained for the 8 and 4 ply laminate regions as well, and these figures are given in Appendix A. Figure 3.7(c) corresponds to a bonded

region where ultrasound couplant was placed at the interface between the aluminum and the 12 ply carbon fiber reinforced laminated composite.

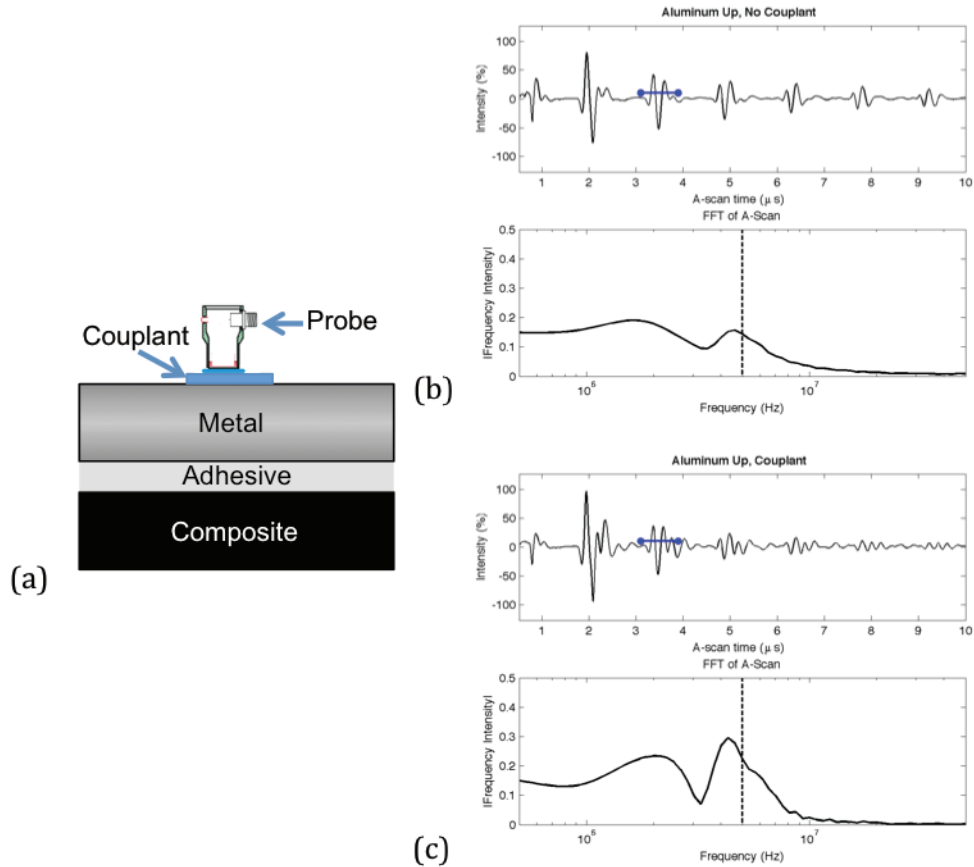


Figure 3.7 (a) The contact probe is placed on the aluminum surface. The A-scan (upper image) and FFT (lower image) results are presented for the (b) unbonded and (c) bonded cases. The vertical dashed line represents the operating frequency of the probe.

A comparison of the shape and amplitude of the A-scans presented in Figures 3.7(b) and 3.7(c) shows the difference in the A-scan obtained for the unbonded and bonded cases, respectively. Looking at the peak located near $2 \mu\text{s}$ in each A-scan, the shapes of each of these peaks are nearly identical to one another. However, the tail end of this peak for the bonded case in Figure 3.7(c) has an increase in the signal amplitude as compared to the tail end of this peak for the unbonded case in Figure 3.7(b). This

corresponds to the wave entering the composite laminate in the bonded case. The second peak (located near $3.5 \mu\text{s}$ in each of the A-scans in Figure 3.7(b) and 3.7(c)) was chosen as the comparison peak between the bonded and unbonded cases because for the bonded case, the shape of the signal has changed due to effects of the reflection/refraction wave pairs that are generated as the wave propagates through the laminate thickness.

Figure 3.7(b) shows a consistently spaced signal repeating throughout the A-scan. Although the amplitude of the signal decays with time due to energy losses, the evenly spaced nature of the signal and the gradual decay in signal amplitude indicates the ultrasound wave is ringing within the aluminum. The time required for the ultrasound wave to propagate through the thickness of the aluminum with the probe operating in pulse echo mode is equal to the quotient of twice the aluminum thickness (4.54 mm) divided by the speed of sound of the aluminum ($6.32 \text{ mm}/\mu\text{s}$ [116]) [63]. The result is $1.44 \mu\text{s}$, which is equal to the time between the evenly spaced peaks observed in the A-scan in Figure 3.7(b). The ringing within the aluminum can also be observed in Figure 3.7(c) for the bonded sample, but the intensity of the ringing and the signal shape decay more rapidly in the bonded sample. The difference in signal amplitude between the unbonded and bonded samples is highlighted by the region gated with the blue horizontal line in the A-scan in Figures 3.7(b) and 3.7(c). As the ringing continues, the signal amplitude drops precipitously for the bonded sample. Part of the observed difference in signal amplitude is explained by the difference in the reflection coefficient for the different material interfaces as well as the signal attenuation that occurs within the composite.

For the unbonded case, the ultrasound wave approaches an aluminum-to-air boundary. The acoustic impedance for air, the medium at the disbond, is approximately zero when compared to that for the aluminum and for the composite meaning that, without accounting for attenuation, the majority of the wave (99.9%) is reflected back through the aluminum and returned to the contact transducer. When the bonded sample is inspected, the ultrasound wave approaches a metal-to-composite interface, and a fraction of the wave propagates into the composite while the remaining portion of the wave reflects back toward the contact transducer. When a portion of the wave enters the composite laminate, the amount of wave energy reflected from the bondline and back toward the transducer is less than the wave energy reflected at an unbonded location. This loss of signal energy into the composite accounts for the decrease in the signal amplitude as well as the increase in the peak signal duration observed in the A-scan in Figure 3.7(c). The reflections generated as the wave propagates through the thickness of the laminated composite have constructive and destructive interference with the other portions of the signal that are being reflected toward the transducer. Thus, the peak observed in the A-scan appears more complicated in shape and appears to occur over a longer period of time than that for the unbonded case. It is worth noting that regardless of the material bonded to the aluminum, the signal amplitude will always decrease as a portion of the signal energy is transferred into the second adherend as long as there is a bond present between the adherends. Since the aluminum is bonded to the laminated composite in Figure 3.7(c), some of the energy is passed through the bondline (couplant) and into the composite, and therefore, the intensity of the reflected ultrasound signal that remains in the aluminum is decreased.

The fraction of the wave that reflects back to the transducer from the aluminum-to-composite bondline can be determined as long as the acoustic impedances of the aluminum and the carbon fiber reinforced laminated composite are known. The reflection coefficient is a term that denotes the percentage of the wave that is reflected as the ultrasound wave exits material one and enters material two (see e.g. [117]). For example, in this situation, material one would refer to the aluminum adherend and material two would refer to the composite laminate adherend. The equation for the reflection coefficient for the unbonded and bonded locations can be written, respectively, as

$$R_{unbonded} = \frac{Z_{al} - Z_{air}}{Z_{air} + Z_{al}} \times 100\% \quad (3.1)$$

$$R_{bonded} = \frac{Z_{al} - Z_{cf}}{Z_{cf} + Z_{al}} \times 100\% \quad (3.2)$$

where $R_{unbonded}$ is the reflection coefficient for the unbonded sample, R_{bonded} is the reflection coefficient for the bonded sample, Z_{al} is the acoustic impedance for the aluminum, Z_{air} is the acoustic impedance for air, and Z_{cf} is the acoustic impedance for the carbon fiber reinforced composite laminate. The difference in the reflection coefficients calculated using Equations (3.1) and (3.2) quantitatively explains the reason for the precipitous decay in the signal decay for the bonded case as compared to that for the unbonded case. Since the acoustic impedance of air is near zero, nearly all of the wave energy reflects back toward the contact transducer for the unbonded case. For the bonded case, about 54% of the wave energy is expected to reflect back toward the transducer.

The FFT plots shown in Figures 3.7(b) and 3.7(c) were created using Matlab's built-in FFT function for the data obtained with the gated region of the A-scans as

indicated by the blue horizontal lines. The gated region captures the second reflection from the aluminum-to-composite interface for both the unbonded and bonded cases. From the FFT figures shown in Figures 3.7(b) and 3.7(c), both the bonded and unbonded cases have local maximums near 4.5 MHz, which is just slightly less than the probe's operating frequency of 5 MHz. The bonded case also has a local maximum near 2.2 MHz while the unbonded case has a local maximum near 1.8 MHz. The high frequency content of the ultrasound signal attenuated less quickly in the bonded sample than it did in the unbonded sample. Through comparison of the frequency content of the ultrasound signal in the FFT plot for the bonded and unbonded cases, an inspector would be able to distinguish the difference between the two cases. When the high frequency content attenuates slower, the inspector has identified a bonded region. If the high frequency content attenuates quickly, the inspector has identified an unbonded region. Additionally, the FFT plot for the bonded location has a more pronounced difference between its maximum and minimum value than does the unbonded location. Recall, results for the 8 and 4 ply laminate regions are provided in Appendix A.

3.3.3 Results for Composite-to-Aluminum Interface

The same contact transducer inspection was performed with the transducer placed in contact with the 12 ply composite laminate surface as depicted in Figure 3.8(a). The signal intensity and FFT results obtained from this inspection are provided in Figures 3.8(b) and 3.8(c) for the unbonded and bonded samples, respectively. Similar to the analysis from the aluminum side, the ringing observed within the bonded sample decays more rapidly than it decays within the unbonded sample as seen within the blue gated region of the A-scans in Figures 3.8(b) and 3.8(c), respectively. The difference between

the bonded and unbonded samples can still be determined via comparison of the A-scan signals in Figures 3.8(b) and 3.8(c). Similar conclusions are made for the 4 ply and 8 ply laminate regions of the sample, and these figures are included in Appendix A.

As discussed in section 3.3.2, the blue horizontal lines in the A-scans seen in Figures 3.8(b) and 3.8(c) are gates that highlight signal content showing the signal amplitude difference between the unbonded and bonded samples, respectively. Between Figures 3.8(b) and 3.8(c) the decay in signal amplitude is readily apparent, and the shape of the signal is noticeably different between the two A-scans. For example, look at $5.5 \mu\text{s}$ on each of the A-scans in Figure 3.8. Figure 3.8(c) has a peak located near $5.5 \mu\text{s}$ that is not observed in the A-scan in Figure 3.8(b) associated with the unbonded location. This peak in Figure 3.8(c) represents the backwall of the aluminum adherend. Once the ultrasound wave has reached the backwall of the aluminum, the wave continues to ring between the top and bottom surfaces of the aluminum, and this ringing caused the A-scan signal to appear more chaotic.

As noted from the inspection on the aluminum side of the part, the FFT plot in Figure 3.8(b) corresponding to the unbonded sample depicts a more rapid decay of the high frequency content than does the FFT plot for the bonded sample shown in Figure 3.8(c). The unbonded sample has a peak energy frequency near 1.8 MHz whereas the bonded sample has a peak energy frequency near 2.5 MHz. The peak energy frequency for the bonded sample in Figure 3.8(c) was also observed as a local maximum in Figure 3.7(c). The peak energy frequency observed in Figures 3.8(b) and 3.8(c) occurs at these lower frequencies because the high frequency content attenuated more quickly in the viscoelastic composite than it did through

the elastic aluminum. In Figure 3.7, the ultrasound wave traveled through the aluminum and into the composite, and in Figure 3.8, the ultrasound wave traveled through the composite first where the frequency components above 2.5 MHz attenuated quickly. The FFT for the unbonded sample shown in Figure 3.8(b) has a single peak frequency of 1.8 MHz, and the FFT for the bonded sample shown in Figure 3.8(c) has two peaks. The first peak is located near 2.5 MHz, as previously mentioned, and the second peak occurs near 5 MHz. The amplitude of the 5 MHz frequency intensity appears to correspond to the absence or presence of a bond between the two adherends with the presence of a bond being associated with a larger frequency intensity for 5 MHz in the FFT plot.

3.4 Immersion Ultrasound Pulse Echo Technique

Although the contact transducer method was able to identify the difference between acoustically coupled (bonded) and acoustically uncoupled (unbonded) locations between the aluminum and composite laminate in the pre-cure sample, an immersion technique using a spherically focused ultrasound probe is capable of presenting high resolution results that show an areal view of the dislocation in the form of a C-scan image. As will be shown in this section, a properly gated C-scan image allows an inspector to quickly identify regions at the interface that are unbonded. An FFT analysis of the A-scan signal is also discussed in this section.

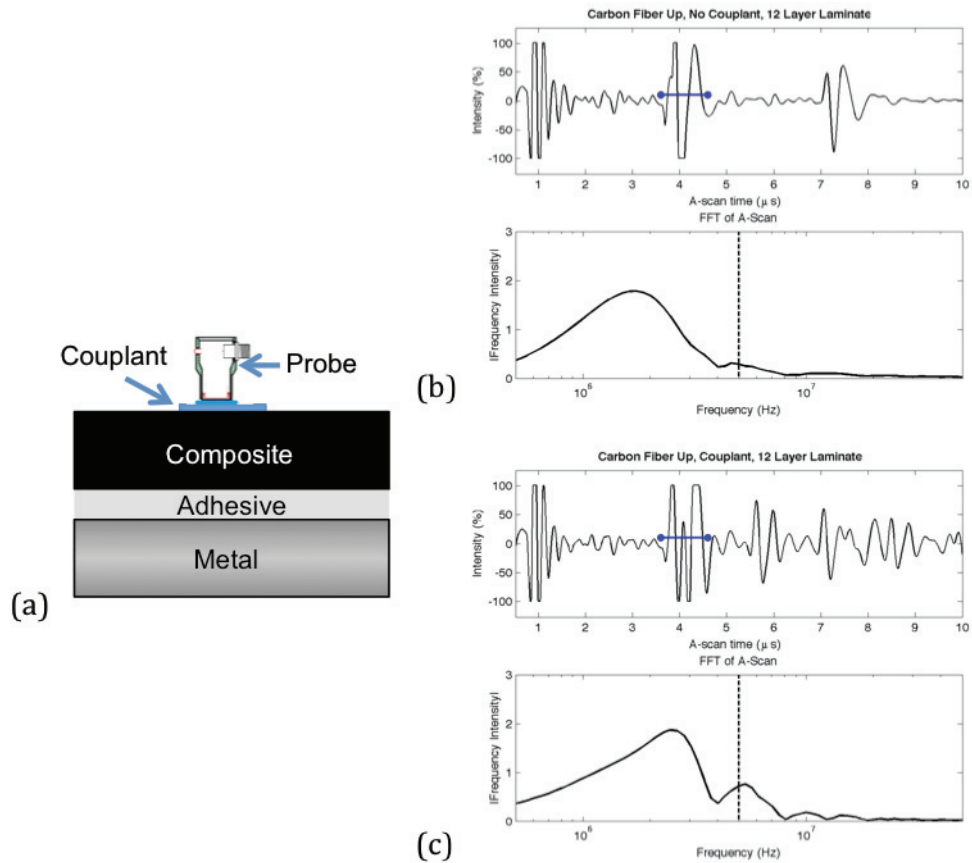


Figure 3.8 (a) The contact probe is placed in on the surface of the carbon fiber reinforced laminate. The A-scan (upper image) and FFT (lower image) results are presented for the (b) unbonded and (c) bonded cases. The vertical dashed line corresponds to the operating frequency of the probe.

3.4.1 Data Collection

The immersion ultrasound inspection used a 10 MHz spherically focused transducer operating in pulse echo mode. The focal length of the probe was 5.4 centimeters and the water path was 4.6 centimeters. The edges of the sample were sealed with superglue to provide a water barrier when the sample was immersed and C-scan data was being collected. The superglue barrier prevented water ingress during the ultrasound scan and maintained the air gap at locations where the aluminum and composite laminate were unbonded from one another. A Mistras UPK-T36 ultrasound system was used in

this study. The system consisted of a traverse system with x, y, and z axes, a pulser, and UTwin software to control the system and collect and store data. The data was stored in the UTwin *.csc file format, and after the data was collected, the file was exported in a *.csv file format. The *.csv format was then read and analyzed in a custom Matlab program written as part of this research. Using the Matlab program, the individual A-scans for each measurement were stitched together to form a C-scan image.

The sample of interest in this discussion is the co-cured sample. The co-cured sample provides the real-world test aspect that was desired in this portion of the study. The unbonded locations were unknown to the inspector prior to the scan being performed. The laminate was cured directly onto the aluminum step wedge as the laminate underwent its cure cycle. As the resin matrix began to cross-link, bonds were formed between the laminate and the aluminum surface. Throughout the cure cycle, stresses were formed along the edges of the part due to the mismatch in the coefficient of thermal expansion between the laminate and the aluminum. The largest stresses are predicted to occur along corners and then the edges of the sample (see e.g. [97, 115]). These high stresses along the edges are hypothesized to cause delaminations between the laminate and the aluminum. The following sections will present images confirming this hypothesis.

After the sample was manufactured, it was scanned using the Mistras UPK-T36 ultrasound system, and the data was analyzed in Matlab to identify areas where the composite laminate was unbonded from the aluminum. The sample was scanned from both sides and for all three laminate thicknesses. The step size chosen for the C-scan was 0.04 inches (1.02 mm) as it provided a relatively fine spatial resolution compared to the

sample dimensions and it prevented the file size from becoming too large that it became difficult to post-process due to computational limitations. The size of the files collected in this experiment was approximately 0.5 gigabytes, but when the file is exported as a *.csv file, the size increases by a factor of 10.

3.4.2 Results for Aluminum-to-Composite Interface

The sample was first scanned with the aluminum side facing the transducer, and the aluminum-to-composite bondline was inspected. Figure 3.9(a) shows the C-scan image for the ultrasound scan of the 12 ply laminate region of the sample. The red and orange area in the lower right hand corner corresponds to the unbonded region while the blue area corresponds to the bonded region. Figure 3.9(b) is the A-scan associated with the unbonded location denoted by the 'x' in the lower right hand corner of the C-scan, and Figure 3.9(c) is the A-scan corresponding to the bonded location denoted by the '+' in the C-scan. The C-scan was generated using the gated region of the A-scan, where the gate is denoted by the blue horizontal line in Figures 3.9(b) and 3.9(c), and the color scale on the C-scan image corresponds to the peak signal amplitude within the gated region. The blue color in the C-scan corresponds to a low signal amplitude within the gate whereas the red color associated with the unbonded region corresponds to a high signal amplitude within the gate. This difference in color provides the inspector with a quick identification that there is a physical abnormality (i.e. delaminations) between these two materials. From the pre-cure analysis that was performed in section 3.3, the same analysis of the A-scan may be applied to the A-scans obtained using the immersion ultrasound pulse echo approach. Thus, the controlled experiment (where the bonded and unbonded locations were known for the pre-cure laminate) assisted the inspector in being able to

correctly identify the location of the bonded and unbonded regions of the co-cured laminate. The unbonded region occurs at the lower right corner of the 12 ply laminate region where the corner is exposed to a free boundary condition and where the largest stresses formed during the manufacturing process are located (see e.g., [97, 115]). The separation between the aluminum and the laminate can be visually observed at the corner of the sample; however, the ultrasound C-scan results are able to show how far, with respect to the planar view of the sample, the unbonded location extends. Destructive testing methods for identifying the bonded and unbonded regions at the interface were not performed as part of this study.

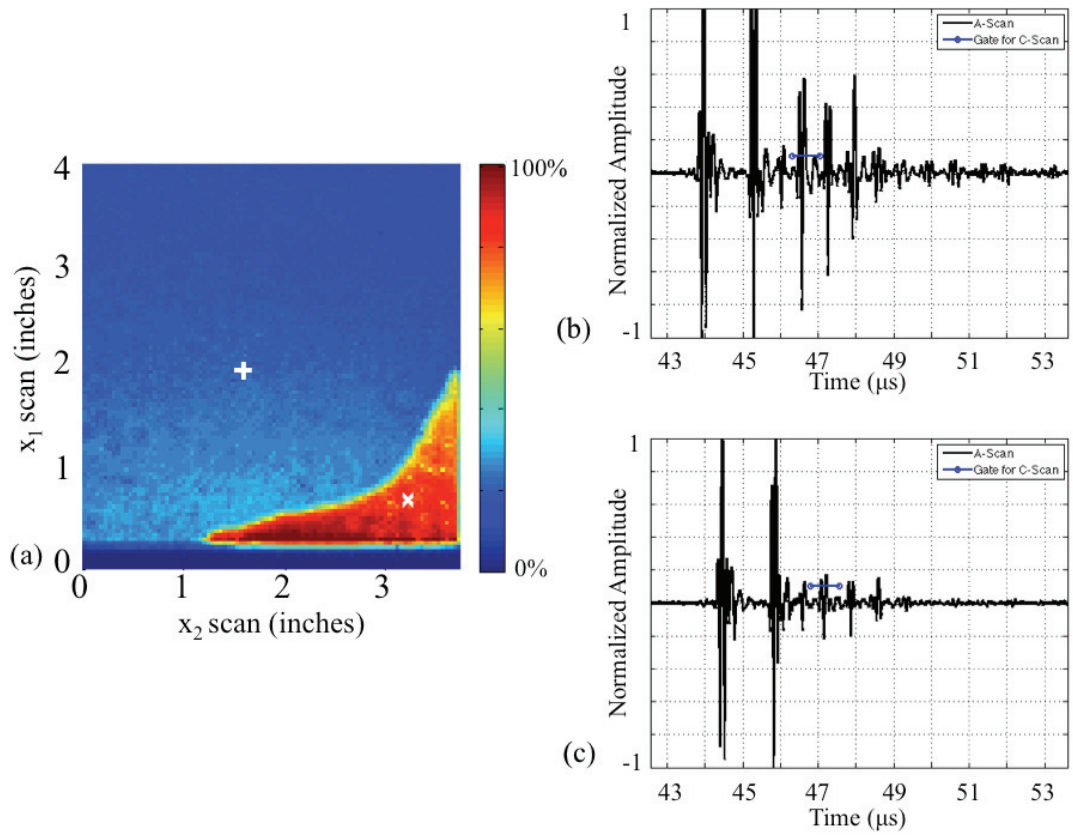


Figure 3.9 (a) This C-scan image for the aluminum-to-composite bondline for the 12 ply laminate. (b) The A-scan signal associated with the unbonded location marked 'x' in (a). (c) The A-scan signal associated with the bonded location marked '+' in (a).

As observed in Figures 3.7 and 3.8 in the previous section, the gated region within the A-scans shown in Figures 3.9(b) and 3.9(c) indicate a higher signal amplitude for the unbonded location as compared to the signal amplitude for the bonded location, respectively. The gate width is the same in Figures 3.9(b) and 3.9(c). This difference in signal amplitude is highlighted by the signal within the gates, which corresponds to the second reflection of the ultrasound signal at the bondline between the two materials. The second signal reflection was chosen for the comparison because the first signal reflection saturated the receiver, which is a common method of inspecting samples as it enables the inspector to watch the ring-down, or signal decay, amongst the multiple reflections. The acoustic impedance mismatch between the composite laminate, aluminum and air causes the A-scans for the bonded and unbonded sections to be distinguishable from one another, as previously discussed.

3.4.3 Results for Composite-to-Aluminum Interface

The same C-scan measurement was performed on the co-cured part with the carbon fiber reinforced laminated composite surface facing the transducer. Figure 3.10(a) shows the C-scan obtained from the data collection for the 12 ply laminate region. The C-scan was generated using the gated region, which corresponds to the bondline between the composite laminate and aluminum, in the collected A-scans. The timing of the signal within the gated region of the A-scans in Figure 3.9(b) and 3.9(c) corresponds to that calculated by dividing the travel distance by the speed of sound as discussed in section 3.3. The gated region is depicted in the A-scans in Figures 3.10(b) and 3.10(c) by the blue horizontal line. Figure 3.10(b) corresponds to the unbonded location denoted by the 'x' in

the C-scan and Figure 3.10(c) corresponds to the bonded location indicated by the '+' in the C-scan.

The teal blue and the royal blue colors shown in the C-scan in Figure 3.10(a) indicate there is an acoustic difference between these two areas of the part, namely an unbonded and bonded location on the part, respectively. This observation coincides with the observation made in the previous section with regard to the C-scan in Figure 3.9(a). This significant difference in color on the C-scan image provides the inspector with enough information to know that something is different between these two locations and that the A-scans should be inspected further to determine if an unbonded location (i.e. a delamination) exists. The unbonded location is now located on the lower left side of the C-scan image in Figure 3.10(a), which is expected since the part was been flipped over such that the composite laminate now faces the ultrasound probe. Knowing the speed of sound ($c = 2.8 \text{ mm}/\mu\text{s}$) and the thickness of the composite, the time required for the ultrasound wave to propagate to the bondline and reflect back toward the ultrasound probe can be calculated by dividing the total distance traveled by the speed of sound. The result is approximately $1.9 \mu\text{s}$, which corresponds to the difference between the front surface of the laminate in the A-scan and the signal within the gate in Figure 3.10(b). Notice there is a small signal reflection present in the gate in the A-scan associated with the bonded location in Figure 3.10(c), but the backwall echo occurs at approximately $48.5 \mu\text{s}$. The time between the bondline and the backwall echo is approximately $1.4 \mu\text{s}$ which is equal to the calculated time it would take the wave to propagate through the aluminum thickness. Comparison of the A-scans in Figures 3.10(b) and 3.10(c) provides the inspector with the indicators of the reflection at the interface, and in the case of Figure

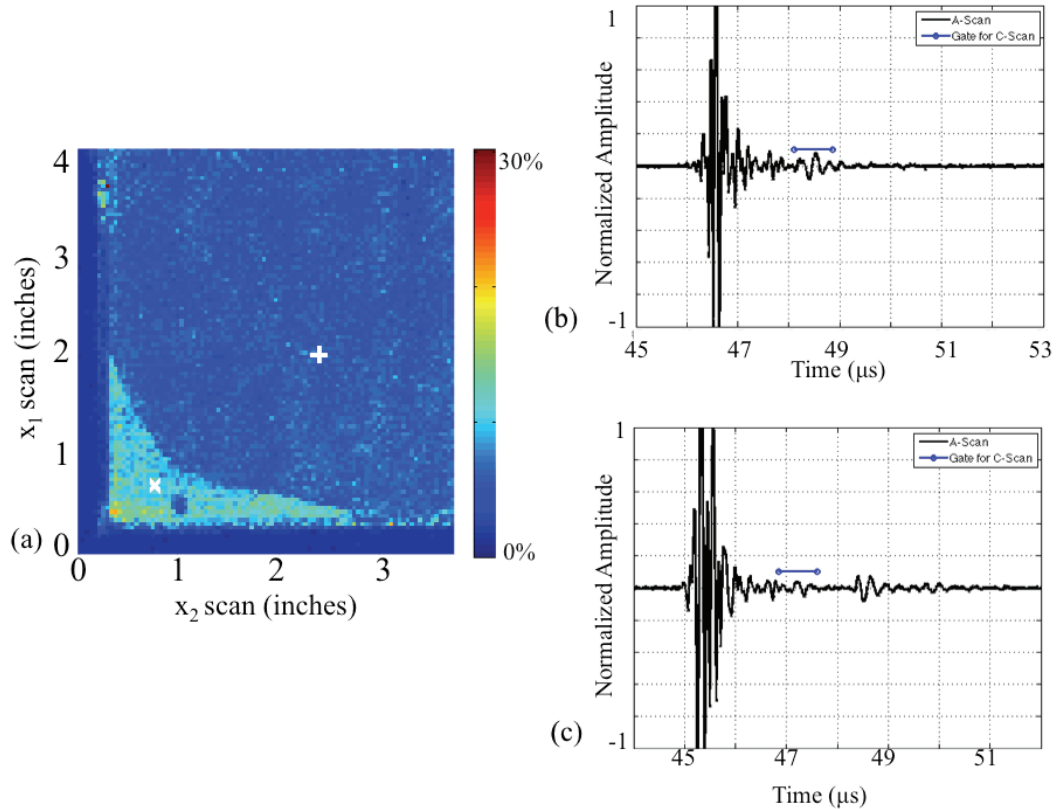


Figure 3.10 (a) The C-scan obtained while inspecting the composite-to-aluminum bondline. The light blue region indicates an unbonded location whereas the dark blue region indicates a bonded region. (b) The A-scan associated with the unbonded location marked by 'x'. (c) The A-scan for the bonded location marked by '+'.
 3.10(c), the presence of the back wall echo off of the back surface of the aluminum. The observation that the A-scan in Figure 3.10(b) does not have a back wall echo associated with the back surface of the aluminum, and that the amplitude of the reflection at the interface is higher than that observed in Figure 3.10(c) indicates that the A-scan in Figure 3.10(b) is an unbonded location.

3.10(c), the presence of the back wall echo off of the back surface of the aluminum. The observation that the A-scan in Figure 3.10(b) does not have a back wall echo associated with the back surface of the aluminum, and that the amplitude of the reflection at the interface is higher than that observed in Figure 3.10(c) indicates that the A-scan in Figure 3.10(b) is an unbonded location.

3.4.4 Inspecting All Three Laminate Thicknesses

During each of the C-scan measurements, the entire sample surface, including all three laminate thicknesses was scanned with a user-defined spatial resolution of 0.04 inches (1.02 millimeters). The previous two sections discussed the 12 ply laminate region

of the sample, and this section will present the C-scan results obtained for all three laminate thicknesses. The same conclusions regarding the A-scan analysis were found when analyzing the inspection results for the 8 and 4 ply laminate regions. Figure 3.11 shows the C-scan images obtained when the aluminum surface of the sample is facing the ultrasound transducer. The C-scans were generated using the gating associated with the aluminum-to-composite bondline, which was selected using the same method as that described in sections 3.3 and 3.4.2, for each of the three laminate thicknesses. Thus, each of the three C-scans provided in Figure 3.11 corresponds to a different A-scan gate and, subsequently, a different planar depth within the sample. The far left C-scan image represents the 12 ply laminate region, the middle image represents the 8 ply laminate region, and the rightmost image represents the 4 ply laminate region.

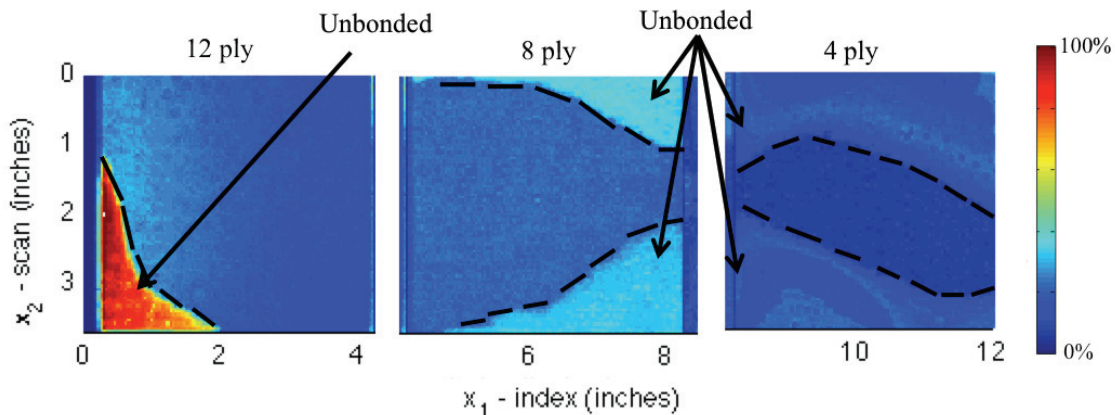


Figure 3.11 The C-scan image results for the immersion ultrasound testing with the aluminum surface facing the transducer. Unbonded locations are highlighted by arrows.

In each of the three C-scan images shown in Figure 3.11, the bonded and unbonded regions can be identified, and for convenience, the author has highlighted and labeled these unbonded regions using black dashed lines. It is worth noting that the majority of the unbonded locations occur along the edge of the sample where the stresses

from the manufacturing process were the highest. These unbonded regions exhibit increased signal intensity compared to the bonded regions, which are represented by dark blue.

The results provided in Figure 3.12 correspond to a single C-scan measurement, and the results across the entire sample are plotted with respect to the gate for the location of the aluminum-to-composite bondline for the 12 ply laminated composite. Thus, the A-scan gate used for identifying the bondline between the 12 ply laminated composite and the aluminum was the same gate that was used while plotting the bondline inspection results for the 8 ply laminated composite region and the 4 ply laminated composite region. Viewing the bonded and unbonded locations using the same gate for all three laminate regions (as seen in Figure 3.12) was possible due to the high speed of sound of the aluminum and the fact that the gates used in Figure 3.11 overlapped with each other. As seen in the sample dimensions provided in Figure 3.2, the composite-to-aluminum bond occurs at a different depth for each laminated composite since the overall thickness of the sample was maintained at a constant value. Thus, placing the gate of interest at a single location, such as the portion of the A-scan signal corresponding to the aluminum-to-12 ply composite laminate interface, rather than looking at the bondline depth for each step may provide the inspector with a more time efficient method for inspecting a sample with internal step discontinuities.

The analysis described in the previous two paragraphs was also performed on the C-scan inspection data obtained with the carbon fiber reinforced laminated composite was facing the ultrasound transducer. Figure 3.13 shows the C-scans obtained for the 12 (left), 8 (middle) and 4 (right) ply laminate regions, and each C-scan is plotted using the

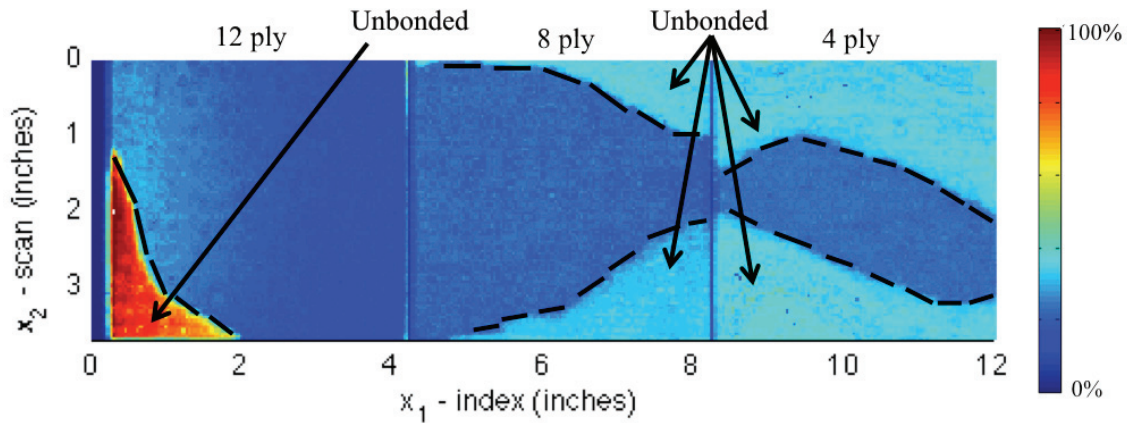


Figure 3.12 The C-scan results obtained for the immersion ultrasound testing with the aluminum surface facing the transducer. Unbonded regions are labeled with arrows.

gate associated with the bondline location along the depth of the sample for each of the three laminate thicknesses. The gate locations are not the same for each of the three laminate thicknesses. As in Figure 3.11, the difference in the color highlights where the unbonded regions are located within the sample.

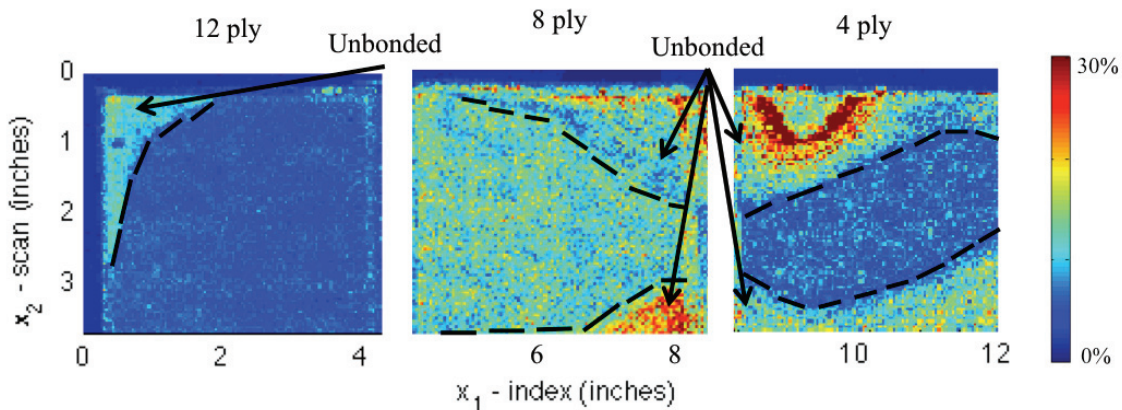


Figure 3.13 The C-scan image results for the immersion ultrasound testing with the carbon fiber reinforced laminated composite surface facing the transducer. The C-scan for the 12 ply laminate is farthest left, the C-scan for the 8 ply laminate is located in the middle, and the C-scan for the 4 ply laminate is located farthest right.

Figure 3.14 presents the C-scan results obtained from the ultrasound scan when the carbon fiber reinforced laminated composite was facing the ultrasound probe, and the

results across all three sections of the sample are plotted with respect to the gate associated with the composite-to-aluminum bondline location for the 12 ply laminate. The unbonded region in Figure 3.14 is clearly distinguishable for the 12 ply laminate region, which is to be expected, but the unbonded regions are more difficult to identify for the 8 and 4 ply laminate regions. The reason this approach (using one gate while plotting the C-scan for all three sections) does not work as well as when inspecting the sample from the aluminum side is because of the energy losses experienced by the ultrasound wave as it propagates through the thickness of the composite as compared to the aluminum. The ultrasound wave experiences more energy losses as it propagates through the composite, due to reflection/refraction pairs and attenuation, than the wave experience propagating in the aluminum. Thus, when inspecting a sample with internal step discontinuities and the composite laminate side is facing the transducer, the most accurate identification of the unbonded regions is achieved when the gates for each of the

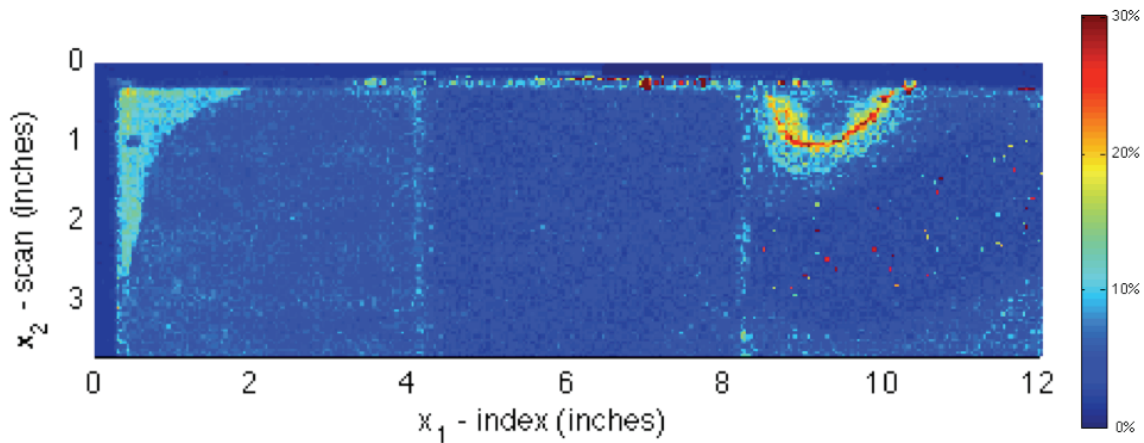


Figure 3.14 The C-scan results associated with scanning the sample with the composite laminate facing the transducer. The 12 ply laminate region is on the far left and the 4 ply laminate region is on the far right.

laminates sections corresponds to its bondline location along the thickness of the sample. Therefore, the analysis provided in Figure 3.13 would be the best tool for identifying unbonded regions when scanning the sample from the composite side.

3.4.5 FFT Results for Immersion Ultrasound Data

The results of the A-scan and C-scan analysis provided in this chapter were further investigated by calculating the Fast Fourier Transform of the signal within the gated region of each of the A-scans provided in Figures 3.9 and 3.10. This FFT analysis was performed using a custom Matlab program written as part of this research. The frequency intensity was calculated for both the bonded and unbonded locations, and the results are provided in Figures 3.15 and 3.16 for the aluminum-to-composite bondline and the composite-to-aluminum bondline, respectively.

The C-scan for the aluminum-to-composite bondline is provided in Figure 3.15(a), and this is the same image that was shown in Figure 3.9(a). The image is provided again here for convenience while comparing the FFT results for the bonded and unbonded locations. Figure 3.15(b) displays the frequency intensity for the bonded (blue) and unbonded (red) locations as indicated by the '+' and 'x', respectively, in the C-scan. The black vertical line in Figure 3.15(b) corresponds to the operating frequency of the ultrasound probe.

As observed in Figure 3.15(b), there is little difference in the shape of the frequency intensity plot for the bonded and unbonded locations; however, the peak intensity associated with the unbonded location is considerably larger than the peak intensity for the bonded location. For both the bonded and unbonded locations, the peak frequency intensity occurs at approximately 7.5 MHz, which is less than the 10 MHz

operating frequency of the probe indicated by the vertical black line. For the C-scan measurements obtained when the aluminum side of the sample is facing the ultrasound probe, the frequencies appear to attenuate independently of the presence of an unbonded region since the general shape of the two curves is nearly identical. Thus, the difference

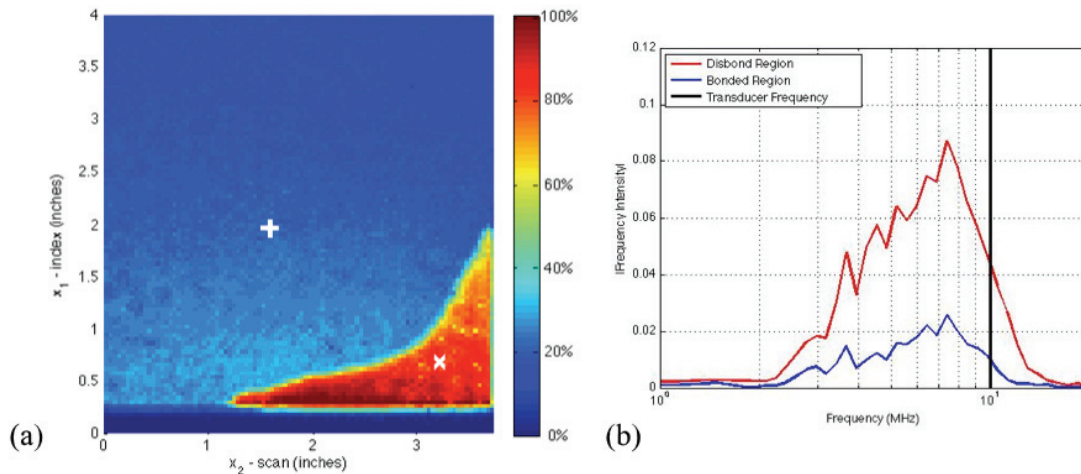


Figure 3.15 (a) The C-scan associated with the aluminum-to-composite bondline for the 12 ply laminate region and (b) the FFT of the ultrasound signal located within the A-scan gate for the unbonded (red) and bonded (blue) locations corresponding to the ‘x’ and the ‘+’, respectively, in the C-scan image in (a).

between the bonded and unbonded locations is determined by looking at the intensity. Although there is no new information gleaned about the bondline from this portion of the study, the benefit of this analysis is that it provides the inspector with information regarding the frequency at which the wave propagates through the material.

The FFT analysis was also performed on the data obtained when scanning the sample with the carbon fiber reinforced laminated composite facing the transducer, and the results are presented in Figure 3.16. The vertical axis provided for the frequency intensity plot in Figure 3.16(b) is the same as the vertical axis in Figure 3.15(b), so that they may be directly compared with one another. As in Figure 3.15, the frequency

intensity plots for the bonded and unbonded locations in Figure 3.16 are nearly identical to one another in shape, but their difference lies in the frequency intensity. Again, the frequency intensity of the unbonded location is higher than the frequency intensity of the bonded location. When comparing Figure 3.15(b) to Figure 3.16(b), one of the main observed differences is the frequency intensity. The frequency intensities plotted in Figure 3.15(b), which correspond to the inspection from the aluminum side of the sample, are much higher than the frequency intensities observed from the data collected when the ultrasound probe was facing the composite laminate surface of the sample seen in Figure 3.16(b). The second key difference between the frequency intensity plots provided in Figures 3.15 and 3.16 is the location of the peak frequency intensity. In Figure 3.15, the peak frequency intensity occurred near 7.5 MHz whereas in Figure 3.16, the peak frequency intensity occurs near 3.5 MHz. The peak frequency intensity is greatly reduced

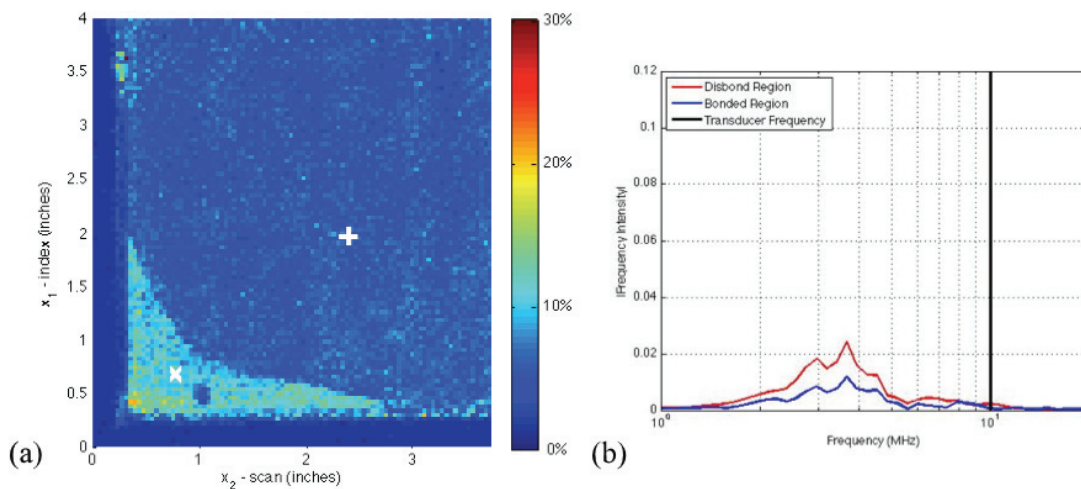


Figure 3.16 (a) The C-scan associated with the composite-to-aluminum bondline for the 12 ply laminate region and (b) the FFT of the ultrasound signal within the A-scan gate for the unbonded (red) and bonded (blue) locations corresponding to the 'x' and the '+' in the C-scan image in (a).

when the sample is inspected from the composite laminate side because the high frequency content attenuates more quickly in the resin matrix of the composite than it does in the aluminum. This observation is a function of the material being inspected, not necessarily a function of the probe.

3.5 Conclusions from the Bondline Study

The purpose of this study was to identify bonded and unbonded regions at the interface between a carbon fiber reinforced laminated composite and aluminum. Two ultrasound methods were investigated for inspecting the bondline between these materials. These two methods were a contact transducer method and an immersion ultrasound method, both of which had the ultrasound probe operating in pulse-echo mode. From analysis of the inspection data, both methods were able to accurately identify bonded versus unbonded locations at the interface between the aluminum and composite laminate, regardless of the side of the sample on which the inspection was performed and the thickness of the laminate region inspected in this study. Recall, the uniqueness of this analysis is the consideration of a sample comprised of dissimilar materials, with one material being isotropic and the other being orthotropic. Many of the previous studies (see e.g., [102, 103, 105]) in this research area focused on analysis of similar materials, such as aluminum bonded to aluminum, but as the use of laminated composite materials continues to increase in industry, the nondestructive inspection capabilities, such as that discussed in this chapter, grow increasingly important in the quality assurance and repair processes.

A frequency analysis was performed on the inspection data obtained from scanning both sides of the sample. Although the frequency analysis did not provide new

information regarding the presence of a bonded or unbonded location at the interface between the two materials, the presence of a bonded or unbonded location could be identified from the frequency analysis, and furthermore, the frequency at which the ultrasound wave propagated through the materials was obtained from this analysis. The frequency at which the wave propagates through the sample is greater when the sample is inspected from the aluminum side than when the sample is inspected from the carbon fiber reinforced laminate side. As the wave propagates through the carbon fiber reinforced laminated composite the higher frequencies in the signal attenuate more quickly than when the wave propagates through the aluminum.

Both the contact and the immersion ultrasound methods were able to correctly identify bonded and unbonded regions at the interface between the composite laminate and the aluminum, but the immersion method, which used a spherically focused ultrasound probe, provided results with a higher spatial resolution allowing the inspector to actually outline the shape of the unbonded region at the bondline between the two materials. Future work in this area may include the development and implementation of a mathematical model to demonstrate how the measured results compare with the physics of the problem. Throughout this chapter the use of time of flight and speed of sound calculations served as mathematical confirmations of the reasonableness of the analysis results. A mathematical model generated in a program, such as COMSOL Multiphysics, could provide further support of the measured results by mathematically modeling the wave propagation through the water, the aluminum, the bondline and the composite, and then, the results could be compared with the results from the measured data. The conclusions gained from the present study have assisted in improving the understanding

of the ultrasound inspection at the bondline between a carbon fiber reinforced laminated composite and metal. Similar techniques to the ones presented in this study could be used to inspect composite-metal components that are in-service and whose structural integrity needs to be inspected on a periodic basis.

CHAPTER FOUR

Identification of Phase Change and Temperature of Highly Attenuative Materials via a Through Transmission Ultrasound Technique

4.1 Introduction

The identification of phase change and temperature often relies on visual inspection and physically invasive measurement techniques, such as thermocouples. Though previous studies have focused on the investigation of either heating or cooling of a material (see e.g., [118, 119]), applications exist in the oil, food and plastics industries that could benefit from the inspection of both the heating and cooling cycle of a material, and this is one of the contributions made in the present study.

The work presented in this chapter includes analysis of two different waxes (pillar blend, soy based EcoSoya wax and a machinist wax called Rigidax) and seeks to identify which results are dependent and which results are independent of material choice. For example, can the same analysis technique be applied to both materials, or does the analysis technique need to be modified from one material to the next? Additionally, the present work considers different experimental setup geometries, which will be described for each of the tests performed. From inspecting the results obtained with different experimental geometries, the algorithms used for analyzing the ultrasound data indicate which aspects of the experiment are geometry dependent and which aspects of the experiment are independent of geometry.

A discussion of the relationship between the speed of sound calculated from the ultrasound data and the temperatures obtained from the thermocouples will be provided

and indicates that the measured speed of sound is dependent on whether or not the heater is on. Although several metrics are presented by which to interpret the test data, including the A-scan, B-scan, speed of sound, temperature, and Fast Fourier Transform, the metric that provides the most useful information about the test data in a single image is the B-scan. The B-scan provides a summary of the multi-hour test in one figure. From the B-scan, the user can identify the following: time of flight (which is used when calculating the speed of sound), the time at which the heater is turned off, and the gradual shift in the time of flight as the material heats and cools.

The future use of this technology could be applied to the oil industry as they seek to identify the temperature of the materials being pumped through the pipes, the food industry as companies monitor the temperature of ingredients throughout the cooking process, and the polymer and composites industry as plastics must be heated to certain temperatures during the manufacturing of various components to ensure optimal strength properties. For example, in the composites industry a future application of this work could be the monitoring of the curing of a thermoset resin. The proposed technique would monitor the temperature of the liquid resin matrix as well as the solidification and cooling of the resin as the polymer chains form chemical crosslink bonds during the cure cycle. Throughout this chapter, the aforementioned scientific contributions will be discussed with respect to the waxes and experimental geometries considered in this experiment.

4.2 EcoSoya Wax Experiment

The first material analyzed in this study was a pillar blend, soy-based wax called EcoSoya. As observed in the digital scanning calorimetry measurements performed in Gregg's masters thesis [83], the melting temperature of this wax is approximately 53 °C.

Four experiments were performed with this material, and the heater block was set to 149 °C (300 °F) in each experiment. The next section presents the experimental setup used for these experiments and following sections present the data analysis, which includes the presentation of metrics such as the A-scan, B-scan and the speed of sound.

4.2.1 EcoSoya Wax Experimental Setup – Large Acrylic Box

The experimental setup used for these experiments is presented in Figures 4.1 through 4.3. Figure 4.1 shows a top view diagram of the placement of the ultrasound probes relative to one another and the walls of the box. Notice, probe 4 and probe 8 are located directly across the box from one another, and the same may be said for the other three ultrasound probe pairs. All of the thermocouples used in this experiment are K-type thermocouples. There are two thermocouples located on the heater block; one thermocouple is located inside of the heater block while the other is located atop the

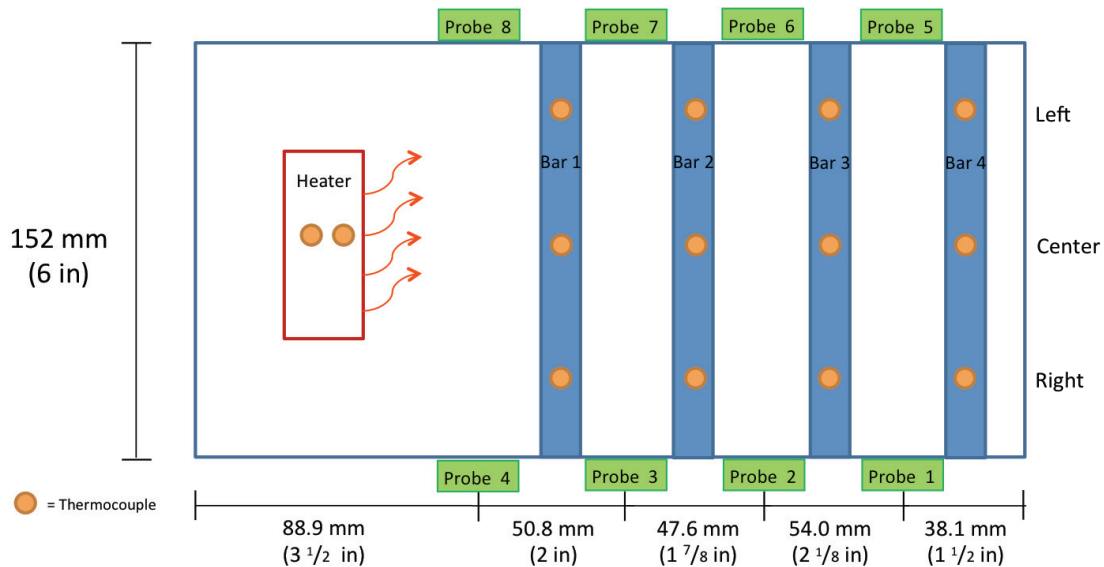


Figure 4.1 Top view diagram of the experimental setup and dimensions associated with the box as well as the placement of the ultrasound probes.

heater block. The thermocouple located inside of the heater block is connected to the heater control feedback loop and ensures that the temperature of the heater block remains at the programmed temperature throughout the experiment. The second thermocouple on the heater block is connected to the thermocouple data logger and records the temperature on the heater block throughout the experiment. Bars 1 through 4 each contain three thermocouples that monitor the temperature of the wax throughout the length and width of the box. The dimensions for the placement of the thermocouples relative to one another and to the box walls are provided in Figure 4.2.

The box itself is manufactured using quarter inch thick acrylic, which assists in insulating the ultrasound probes from the heat of the wax. The box was manufactured using this material because the acrylic's transparency allowed the visual monitoring of the experiment including the melting and re-solidification of the wax. The visual

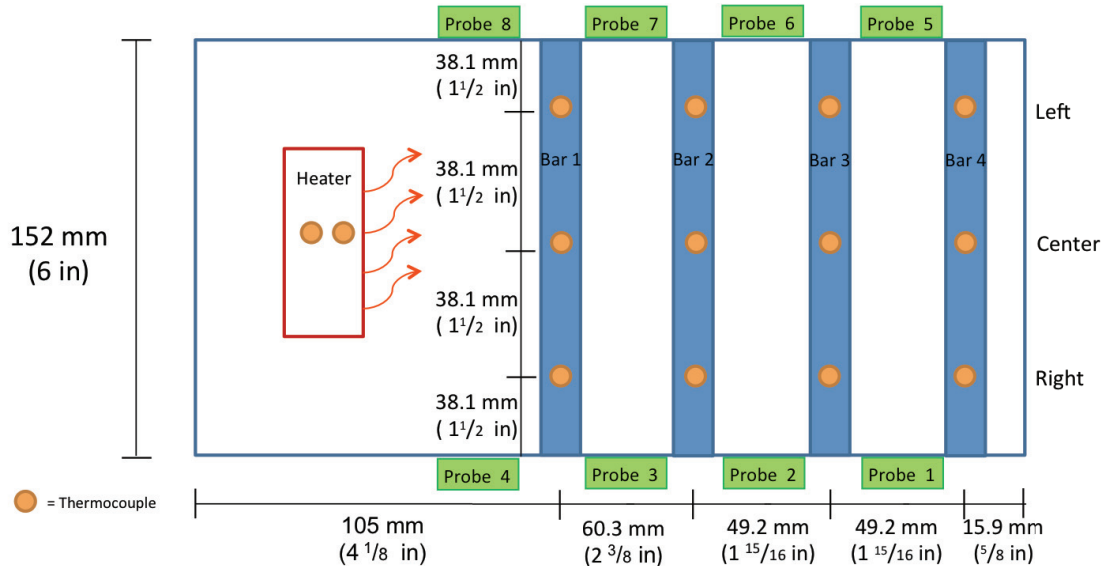


Figure 4.2 Top view diagram of the experimental setup and dimensions for the placement of the thermocouples.

monitoring served as another confirmation of the author’s interpretation of the ultrasound data and subsequent analysis.

The placement of the ultrasound probes, thermocouples and heater block relative to one another and to the box walls is provided in Figure 4.3. The average depth of the thermocouples as indicated by the ‘*’ in Figure 4.3 is 79.8 millimeters. The standard deviation between the measured thermocouple depths was 2.8 millimeters. The heater block is 1” x 1” x 4” and is located approximately halfway down the height of the box as seen in Figure 4.3.

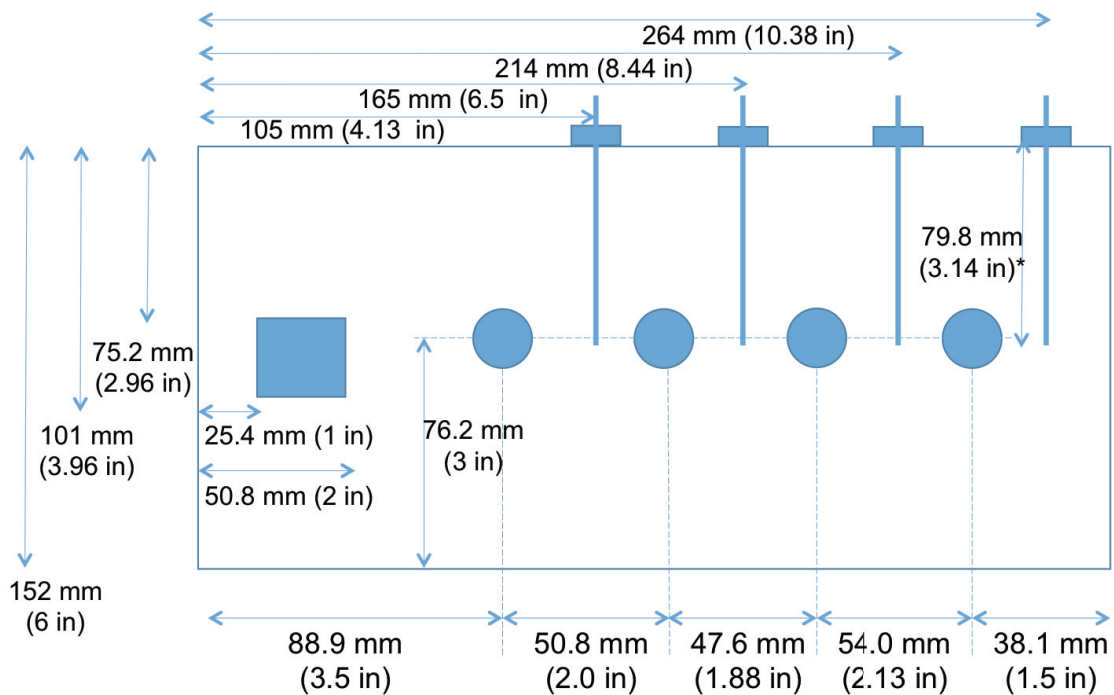


Figure 4.3 Side view of the experimental setup and dimensions for the placement of the components used in the experiment. The * in the figure refers to the average thermocouple depth. The square is the heater block and the circles indicate transducers.

The ultrasound probes used in this experiment were purchased from Panametrics and were 0.5 MHz with a one-inch diameter. The ultrasound probes were adhered to the side of the acrylic box using Loctite Super Gel adhesive. To remove the probes from the box, a shear force must be applied to the transducer because the adhesive is weaker in shear than it is in tension or compression. Then, these same ultrasound probes may be used in multiple experimental configurations.

The heating element used throughout the experiment was a Watlow 250 Watt, 3/8" outer diameter, 2 7/8" long heater that was housed inside of an aluminum block that was 1"x1"x4" in dimension. A Watlow EZ-Zone temperature controller controlled the temperature of the heating element, and the thermocouple placed inside of the heater block alongside the heating element provided feedback to the temperature controller. The Watlow EZ-Zone temperature controller is shown in Figure 4.4 and is shown in relation

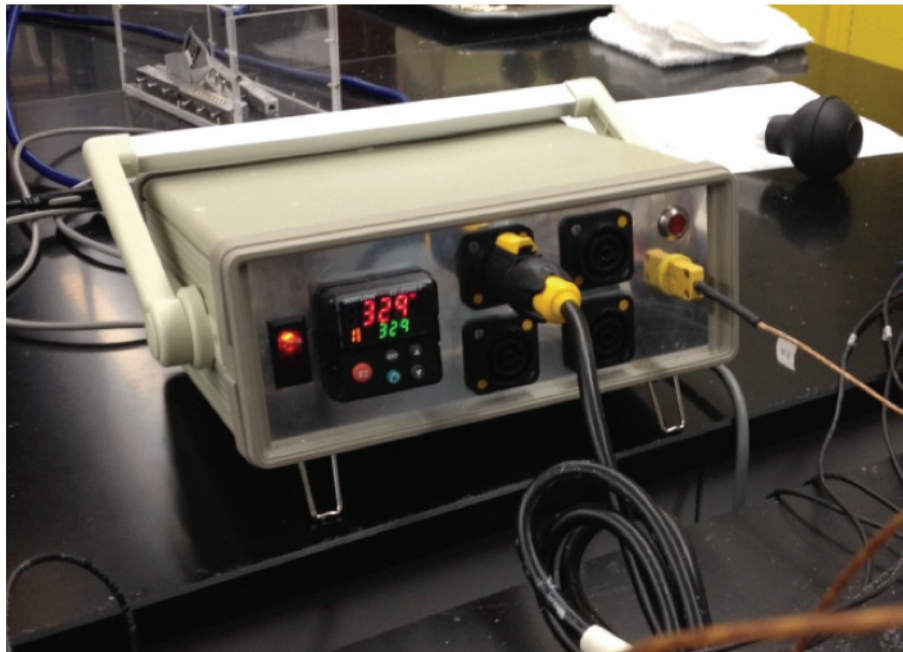


Figure 4.4 The Watlow EZ-Zone temperature controller

to the rest of the experimental setup in Figure 4.5. The thermocouple data was collected and stored to a laptop for further analysis using a Graphtec GL820 midi logger. The thermocouple data can be stored to the midi logger console as well as to the laptop.

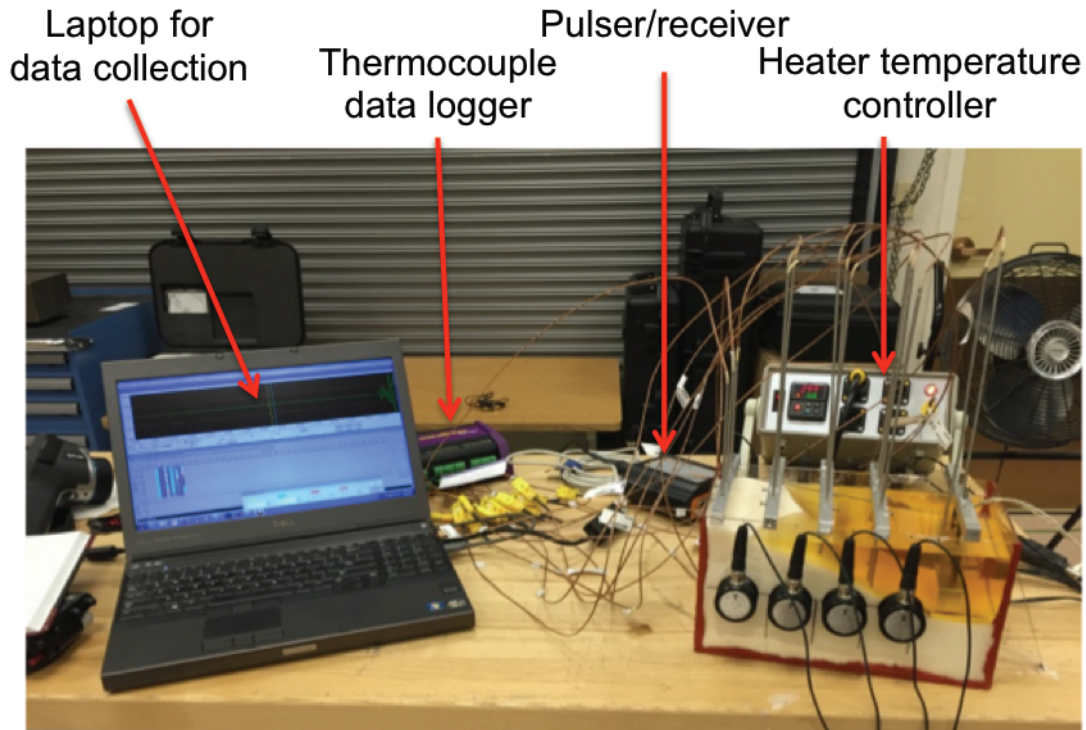


Figure 4.5 Experimental setup in the laboratory with each of the components labeled.

The ultrasound data was collected using a Pocket Scan PS45 pulser/receiver manufactured by Technology Design. The Pocket Scan PS45 is controlled via the TD Pocket Scan program where the user may input the test parameters. For example, the gate start and end locations, gain, voltage, and low and high pass filters are some of the many test parameters that may be selected by the user. The data is saved as a .scn file and can be exported as a .txt file after the test is complete. For this experiment, the data was exported to a .txt file format for further analysis using a custom program written in

Matlab. The Matlab program generates figures for the A-scans, B-scans, speed of sound, and temperature plots associated with the ultrasound data.

During the experiment, eight ultrasound signals (referred to as channels throughout the remainder of this chapter) were monitored as defined in Figure 4.6. For each channel, the tail of the arrow is nearest the probe that emits the ultrasound wave and the tip of the arrow is nearest the probe that receives the transmitted wave signal. For example, channel 1 consists of probe 4 emitting the ultrasound pressure wave and probe 8 receives the wave signal once it has propagated across the width of the box. Similarly, channel 11 has probe 8 emitting the ultrasound pressure wave while probe 4 receives the signal after it has propagated across the width of the box. A comparison of the results obtained from these two channels will be provided in a later section. The gain for each

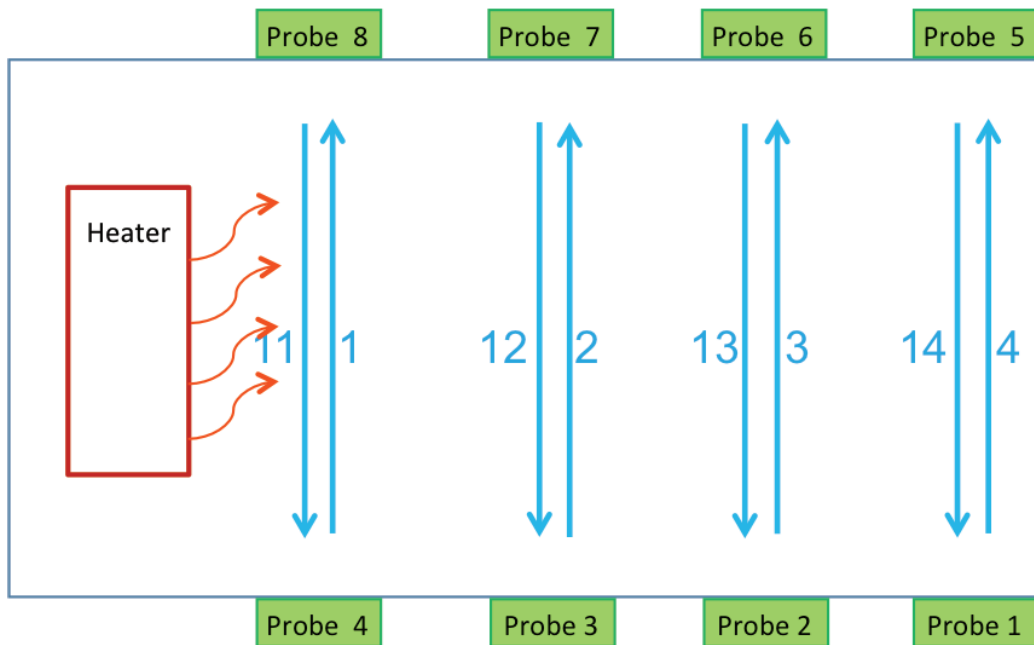


Figure 4.6 Channel listing for the experimental setup used with the EcoSoya wax.

ultrasound channel may be controlled independently from one another using the TD Pocket Scan software.

Throughout the experiment, the ultrasound data was collected once per minute, and the thermocouple data was recorded twice per minute. The temperature data was recorded more frequently than the ultrasound data because the temperature was changing more rapidly than the ultrasound signal. Any changes to the ultrasound signal gain were made in between ultrasound data point collections, and the gain changes were recorded in a notebook to keep a record of changes and for further analysis of identifying data trends. Once the test was complete and the wax had begun to pull away from the sides of the container, as it was prone to do as it underwent thermal contractions during the cooling stage of the test, the data was analyzed using the previously described custom Matlab program to generate the images that will be discussed in the following sections.

4.2.2 A-scan Measurements

One of the most common methods for viewing ultrasound data is the A-scan. The A-scan represents the ultrasound wave signal as it would appear on an oscilloscope and can be used for identifying the time of flight (TOF). The TOF refers to the time it takes the wave to propagate from the ultrasound probe emitting the incident pressure wave, propagate through the thickness of the material and be received by the second transducer in a through transmission setup as was used in this experiment.

The A-scan shown in Figure 4.7 represents the ultrasound signal propagating across the width of the wax box while the wax is still a solid material, and the black dot represents the first point in the A-scan signal, which meets or exceeds the user-defined threshold. The threshold used in this analysis was 10% because this value was larger than

the signal noise meaning that it would capture the onset of the signal corresponding to the wave propagation across the box rather than the signal noise. The black dot in Figure 4.7 indicates that the TOF is approximately 89 μs . Since the walls of the box are in the line of sight of the ultrasound probes, the 89 μs TOF corresponds to the time required for the wave to propagate through the box wall, through the wax, and through the next wall. To obtain a TOF corresponding to the wax alone, the time required for the wave to propagate through the walls must first be calculated.

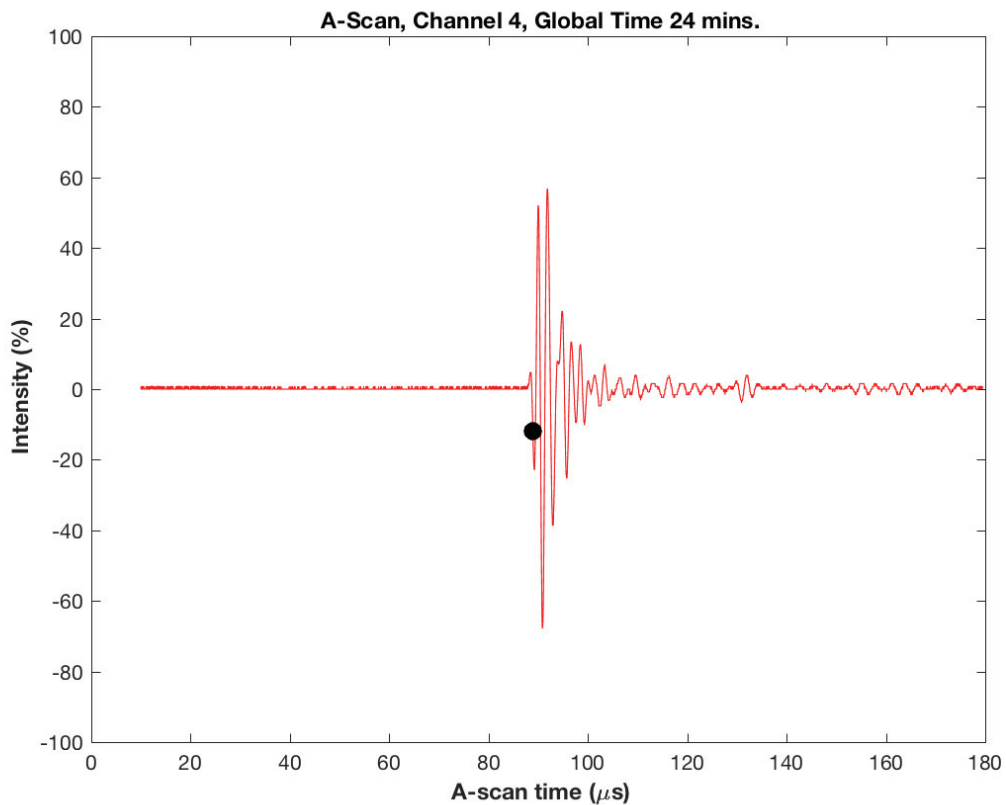


Figure 4.7 A-scan signal associated with the solid EcoSoya wax. The black dot indicates the first point that meets or exceeds the amplitude threshold.

The speed of sound of acrylic is 0.1070 in/ μs (or 2730 m/s) [116], and the wall thickness is 1/4" per wall. The ultrasound wave propagates through two acrylic walls

(one on each side of the box), and thus propagates through 1/2" of acrylic. The time required for the wave to propagate through the acrylic box wall can be calculated as seen in Equation 4.1 as

$$t_{wall} = \frac{2h_{wall}}{c_{acrylic}} \quad (4.1)$$

where t_{wall} is the time the ultrasound wave spends propagating through the wall thickness, h_{wall} is the wall thickness, and $c_{acrylic}$ is the speed of sound for the acrylic. Based on this calculation, the ultrasound wave spends 9.35 μ s propagating through the wall thickness.

The time spent by the wave propagating through the wax, t_{wax} is then given by

$$t_{wax} = TOF - t_{wall} \quad (4.2)$$

This same analysis may also be performed when the wax has fully melted. An A-scan corresponding to the melted wax is presented in Figure 4.8. Notice the onset of the signal appears later in time than it did for the solid wax. The TOF associated with the liquid wax is approximately 120 μ s as indicated by the location of the black dot relative to the A-scan signal in Figure 4.8. In his masters thesis, Gregg [83] found that the speed of sound of the acrylic walls was independent of temperature for the temperature range of interest in this study. Thus, the results from Equation 4.1 do not change since the speed of sound of the acrylic and the wall thickness do not change even though the wax has melted. The results from Equation 4.2 will change as the time required for the wave to propagate through the liquid wax is different than the time required for the wave to propagate through the solid wax.

This difference in the time required for the wave to propagate through the different phases of wax is one of the metrics sought in this experiment because it can be used to calculate the speed of sound in each of the materials and provides insight as to

how the signal changes as the material undergoes a phase change. As observed in the experiment, as the wax would melt, the signal corresponding to the liquid wax would increase in amplitude while the signal corresponding to the solid wax would decrease in amplitude. As the signal dominated by the liquid wax continued to increase in strength on the A-scan, the gain was decreased to keep the signal within +/- 100% intensity. Typical gain setting for the solid wax was near 70 decibels (or dB) whereas the typical gain setting for the liquid wax was near 30 dB.

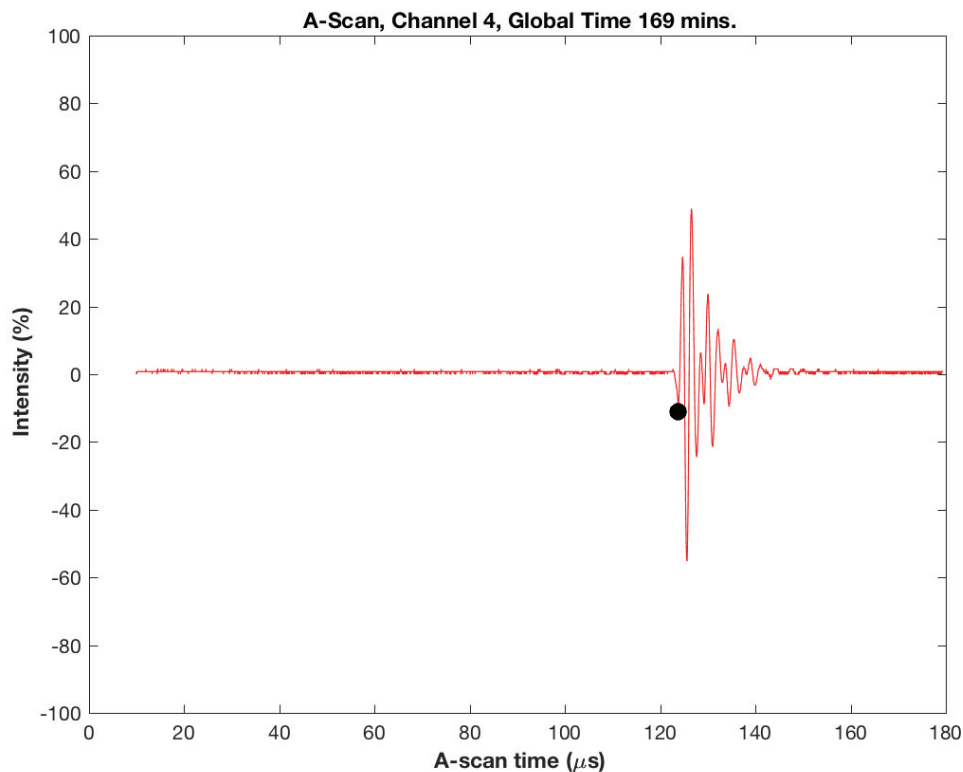


Figure 4.8 A-scan signal associated with the liquid EcoSoya wax. The black dot indicates the first point that meets or exceeds the amplitude threshold.

4.2.3 Creating and Interpreting the B-scan Image

Although the A-scan is a useful method for monitoring the changes in the ultrasound signal throughout the test, the B-scan provides a method for viewing all of the

data collected throughout the multi-hour test in a single image. The next subsection will describe how to generate the B-scan image, and the following subsection will describe how to interpret a B-scan plot.

4.2.3.1 Creating the B-scan image. The B-scan image is generated using the A-scan signals collected throughout the experiment. While recreating the A-scans in Matlab, the test parameters, which are saved in the .txt file exported from the TD Pocket Scan software, are written into a .dat file, and the A-scan data is written to a Matlab .mat file for future use. The first step in creating the B-scan image in Matlab is to input the test parameters and read-in the A-scan data. Since the data is collected once per minute, the number of A-scans collected directly corresponds to the number of minutes in the test. Then, a time variable is created by defining an array that is the same length as the number of A-scans where the time step between each point is equal to the frequency of A-scan data collection (1 minute). Thus, if the experiment collected 515 A-scans at a rate of one A-scan per minute, then, the experiment was 515 minutes long. This time array will serve as the horizontal axis when plotting the B-scan.

Unlike when defining the TOF or plotting the A-scan, no thresholding is used while plotting the B-scan. Rather, the B-scan is a representation of the full A-scan so that any phenomena, such as the ultrasound wave propagating along the box as will be discussed in one of the machinist wax experiments, may be observed throughout the experiment. For the EcoSoya wax experiment, there were no phenomena indicative of a strong ultrasound signal propagating along the box wall.

After defining the time array, the A-scan data and time array are used for plotting the B-scan image. The Matlab built-in function used for plotting the B-scan is 'imagesc'.

This function accepts as inputs the following: the time array, the A-scan time and the A-scans. As previously mentioned, the time array defines the horizontal axis. The A-scan time corresponds to the gate used while collecting the ultrasound data. For example, in Figure 4.9, the vertical axis corresponds to an A-scan gate time that ranges from 70 μs to 159.9 μs .

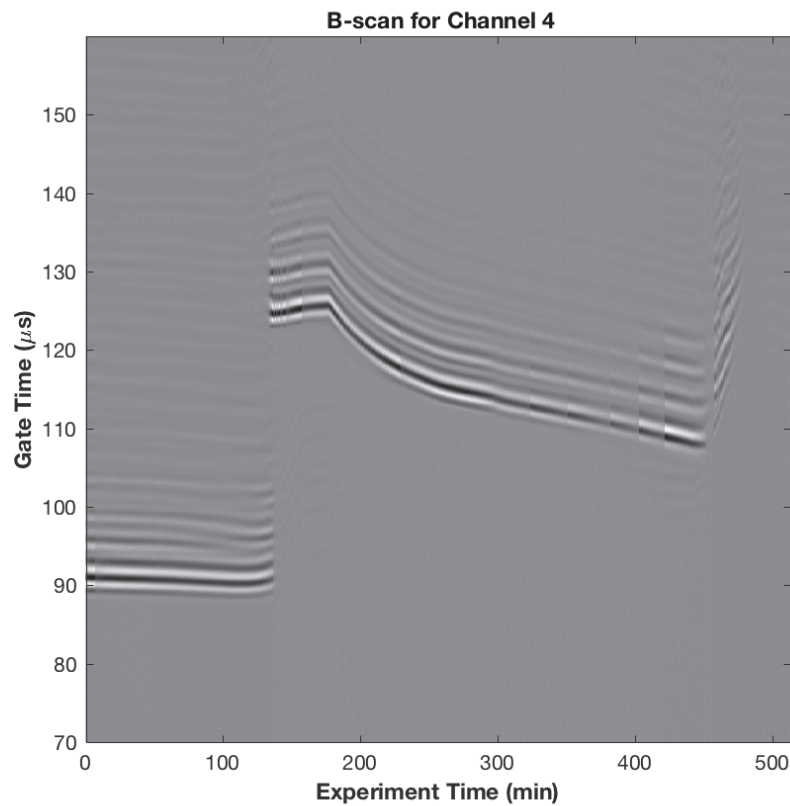


Figure 4.9 B-scan for channel 4, which is located farthest away from the heater. μs . Although the experiment time and gate time correspond to the horizontal and vertical axes, respectively, the greyscale colors observed in Figure 4.9 directly correspond to the A-scan signal amplitude, and the interpretation of this image will be discussed in the following section.

4.2.3.2 Interpreting the B-scan image. As observed in Figure 4.9, the A-scan signal changes as the wax material is heated and allowed to cool during the experiment. The B-scan provided in Figure 4.9 corresponds to channel 4, which is located furthest

away from the heater block. Knowing the placement of this channel relative to the rest of the experimental setup, consider the physics of what is occurring in the box. The heater is at the opposite end as channel 4 indicating that the phase change from solid wax to liquid wax will occur at channel 4 after a period of time. Then, once the wax melts at channel 4, the heater will be turned off, and the entire box of wax will be allowed to cool. To assist with explaining how these physical events occur with respect to the B-scan, Figure 4.10 has highlighted multiple artifacts that can be used for explaining the relationship between the image and what is physically being observed during the experiment.

First, the region highlighted by the leftmost oval corresponds to the solid EcoSoya wax. As the material along channel 4 begins to melt, the onset of the A-scan signal shifts to later in time (TOF increases), and this shift is denoted by the small region marked as (i) in Figure 4.10. The melted wax and the first part of the re-solidification process is highlighted by the rightmost oval in Figure 4.10. The heater is turned off at 177 minutes into the experiment, and this time step can be identified in the B-scan as the point at which there is a sharp change in slope. Prior to the heater being turned off, the curve observed in the rightmost oval had a positive slope, and after the heater was turned off, the slope became negative indicating that the TOF began to decrease. As the EcoSoya wax cools, it thermally contracts and pulls away from the wall at which point the ultrasound signal is lost. The portion of the experiment where the wax has pulled away from the wall is denoted by (ii) in Figure 4.10. The reason a signal is present at the beginning of the experiment is because water was poured between the solid wax and the side of the wall. As the wax melts, the water flows to the bottom of the container and beneath the heater block. As shown in Figure 4.11, the EcoSoya wax does not melt much

below the depth of the heater block. Since the water is denser than the wax, the water does not impact the results with the exception of providing a signal at the beginning of the test. If the water were not present, there would be no relevant ultrasound signal until the wax had melted.

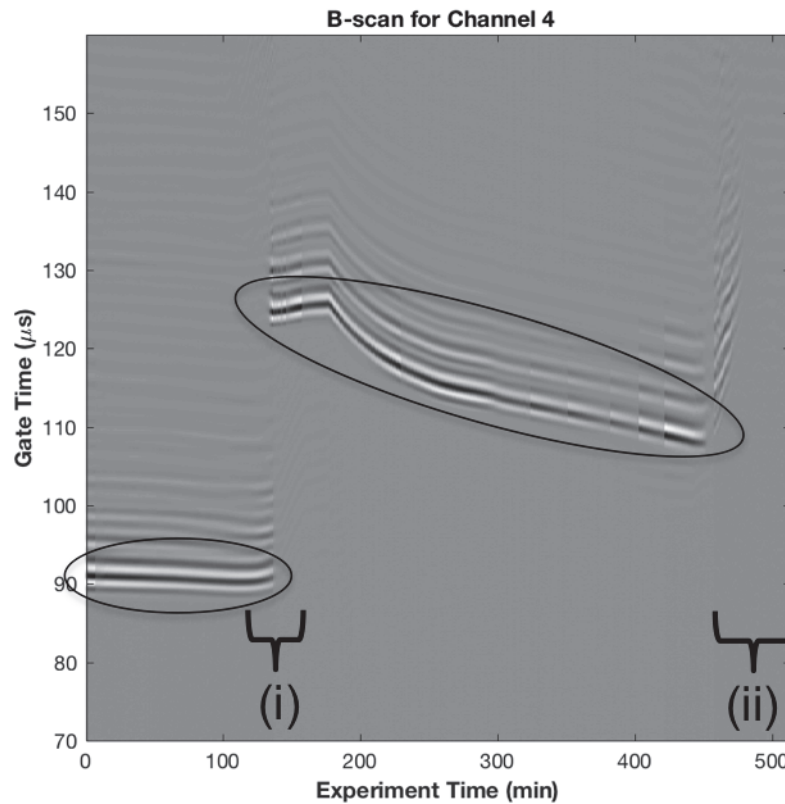


Figure 4.10 Highlighting the sections of interest in the B-scan.

One of the first features to catch the reader's eye when looking at the B-scan is likely the dark grey and bright grey curves as encompassed by the ovals in Figure 4.10. As previously mentioned, the region encompassed by the leftmost oval corresponds to the A-scan signal representing the solid EcoSoya wax whereas the region encompassed by



Figure 4.11 The EcoSoya wax does not melt much below the heater block depth.

the rightmost oval corresponds to the A-scan signal representing the liquid wax. These features encompassed by the ovals correspond to the high amplitude portion of the A-scan signal, where a high positive value on the A-scan amplitude corresponds to the light grey color and a large negative amplitude on the A-scan corresponds to the dark grey color.

Figure 4.12 provides a comparison between the B-scan and A-scan signals for the solid and liquid wax. The solid wax is represented by the solid vertical black line at an experiment time of 24 minutes in Figure 4.12(a), and the corresponding A-scan for that experiment time step is provided in Figure 4.12(b). Notice the high amplitude regions denoted by the height of the solid black line in Figure 4.12(a) correspond to the high amplitude regions highlighted by the solid black oval in the A-scan in Figure 4.12(b). The dashed vertical line in Figure 4.12(a) corresponds to the time step of 169 minutes where the EcoSoya is liquid. The corresponding A-scan is provided in Figure 4.12(c). Again,

notice that the high amplitude region indicated by the dashed line in the B-scan corresponds to the high amplitude portions of the A-scan signal provided in Figure 4.12(c).

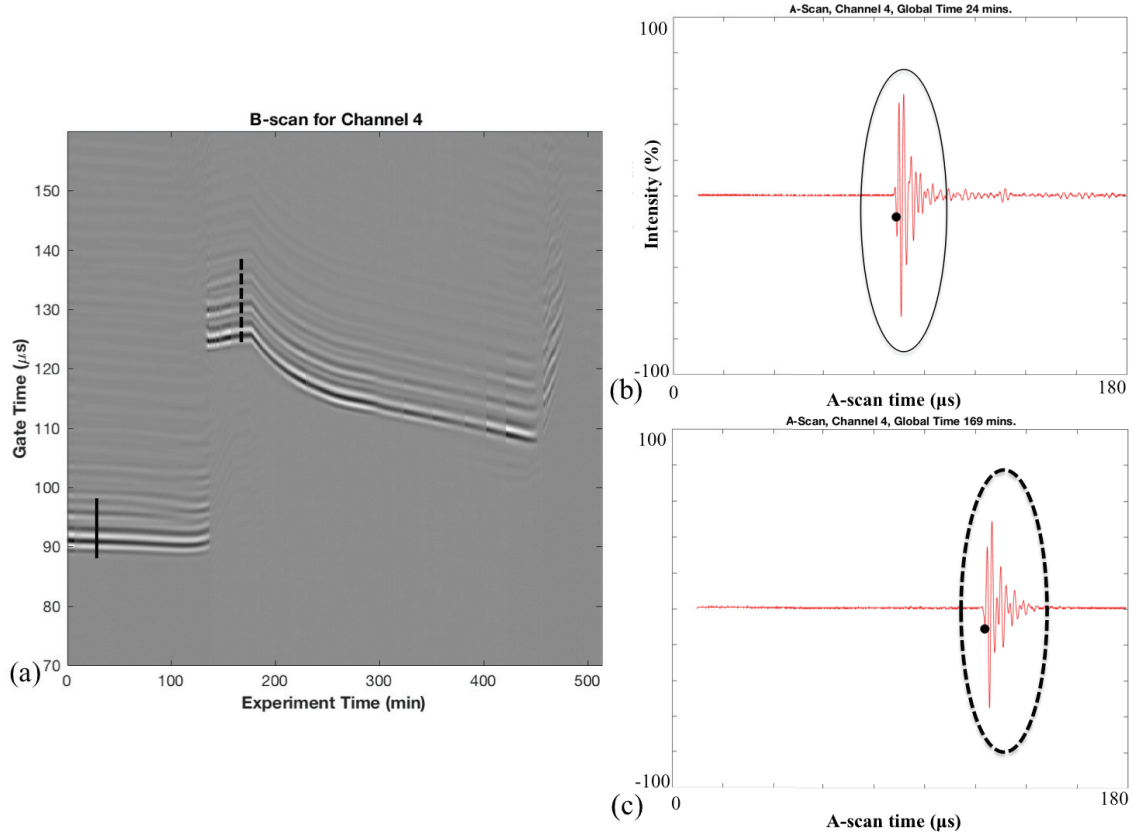


Figure 4.12 (a) The B-scan associated with Channel 4 where the solid black line corresponds to the high amplitude region shown in the (b) A-scan for the solid EcoSoya wax and dashed black line corresponds to (c) the A-scan for the liquid EcoSoya wax.

The features in the B-scan that appear as ripples and are located just above the previously mentioned regions corresponding to the high amplitude portion of the A-scan signals correspond to the lower amplitude portions of the A-scan signal. Notice in Figures 4.12(b) and 4.12(c) that the A-scan signals have low amplitude signals located past the high amplitude portion of the A-scan encompassed in the ovals. These lower amplitude regions are what appear in the B-scan as ripples. Although these phenomena are

interesting to note, they do not contribute significantly to the analysis of the B-scan with respect to the TOF measurement and identification of phase changes.

Although the identification of the phase change has been identified via the B-scan signal, one of the goals of this study was to identify a correlation between the ultrasound signal and the temperature. During the heating portion of the experiment, the phase change from solid to liquid wax occurs relatively quickly, and the relationship between the changes in the A-scan and the temperature is not very clear. However, once the wax has melted, the B-scan indicates a positive slope indicating that as the temperature of the wax continued to increase, the TOF also continued to increase. Once the heater block was turned off 177 minutes into the experiment, the slope in the B-scan became negative indicating that as the temperature decreased so did the TOF. The relationship between the TOF and temperature will be explored in further detail in section 4.2.6 where the TOF will be represented in the speed of sound calculation.

4.2.4 Speed of Sound Calculations and Results

Another metric that can be used for analyzing ultrasound data is the speed of sound. The speed of sound is calculated using the measured TOF and the thickness of the material. Section 4.2.4.1 will describe how to calculate the speed of sound for the EcoSoya wax used in this experiment, and the results obtained for channels 1 through 4 will be provided. Section 4.2.4.2 will provide a comparison of the results obtained from channels 1 and 11 as well as a comparison of the speed of sound results obtained for channels 1 through 4.

4.2.4.1 *Calculating the speed of sound.* As previously mentioned, the speed of sound is calculated using the measured TOF and the thickness of the material. Generally, this equation can be expressed as

$$c = \frac{h}{t} \quad (4.3)$$

where c is the speed of sound, h is the thickness of the material, and t is the time required for the ultrasound wave to propagate through the material. However, equation 4.3 must be modified for this experiment since the ultrasound wave also propagates through two of the box walls (one wall prior to propagating through the wax and one wall after). Recall, the time required for the ultrasound wave to propagate through the wall (t_{wall}) was calculated using Equation 4.1 in section 4.2.2, and the time required for the ultrasound wave to propagate through the wax after having accounted for the propagation through the walls (t_{wax}) was calculated using Equation 4.2 in section 4.2.2. Please note that since the water gap between the wall and the wax was quite small, the time the wave spent propagating through the water was not accounted for in the speed of sound calculations. Thus, accounting for the wave's propagation through the box walls, the speed of sound for the wax (c_{wax}) can be calculated using Equation 4.4,

$$c_{wax} = \frac{h_{wax}}{t_{wax}} \quad (4.4)$$

where h_{wax} is the width of the wax (also referred to as the inner box dimension) and t_{wax} is as defined in Equation 4.2.

The speed of sound is calculated for each A-scan collected throughout the experiment, and since the ultrasound data is recorded once per minute, the number of A-scans equals the length of time, in minutes, of the experiment. Additionally, the speed of

sound is calculated for each channel in the experiment as defined in Figure 4.6. The results for the speed of sound for channels 1 through 4 are provided in Figures 4.13 through 4.16. Each of these figures also includes a plot of the temperature data collected via the thermocouples throughout the experiment. The legend for the temperature plot shows that the thermocouple on the heater block is represented along with five additional curves. The first four of these curves (black, red, blue and cyan) correspond to the

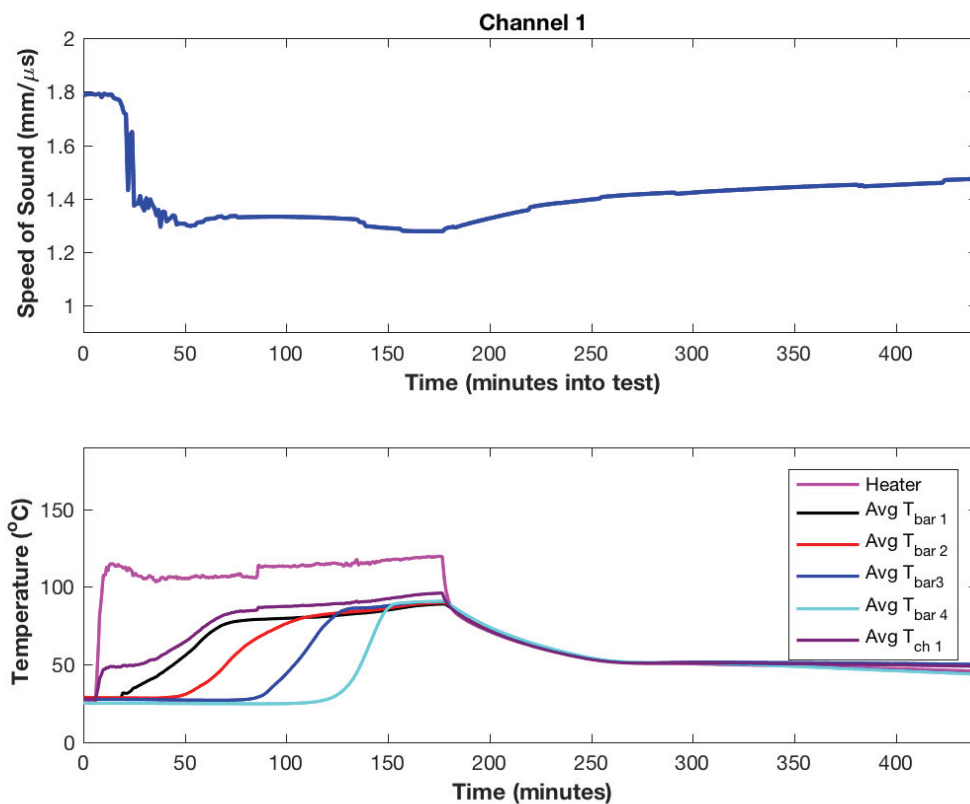


Figure 4.13 The speed of sound for channel 1 (top), which is located closest to the heater, and the temperature measured via thermocouples throughout the experiment (bottom).

average temperature along heater bars one through four, respectively. The last temperature defined in the legend corresponds to the average temperature along the channel of interest. For example, in Figure 4.13, the final temperature in the legend

corresponds to the average temperature along channel 1. Recall, there are no thermocouples in the line of sight of the ultrasound probes. Thus, the temperatures corresponding to channel 1 were estimates obtained from the surrounding thermocouples. The process for estimating the temperature along each of the channels will be described in further detail in the following section.

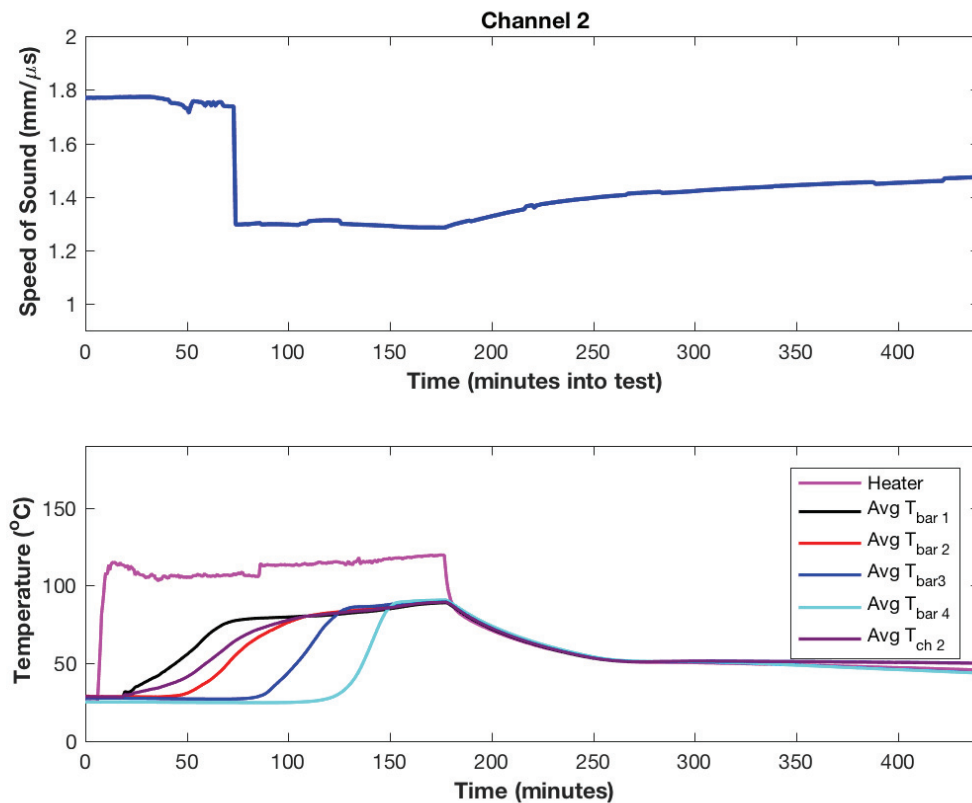


Figure 4.14 The speed of sound for channel 2 (top) and the temperature measured via thermocouples throughout the experiment (bottom).

The speed of sound figures for channels 1 through 4 each indicate a change in the slope of the speed of sound curve at the moment the heater is turned off at 177 minutes into the experiment. Another common feature amongst these plots is the sudden drop in the speed of sound from approximately 1.8 μs to 1.25 μs. This transition from solid to

liquid appears as though it is a step change; however this is not the case. The transition from solid wax to liquid wax does occur quickly, but it takes on the order of 10-15 minutes for the ultrasound wave to go from being fully dominated by the solid wax signal to being dominated by the liquid wax signal. During the intermediate period between being fully dominated by the solid or liquid signal, both signals appear in the A-scan. This means that a signal appears near $89 \mu\text{s}$ as well as near $125 \mu\text{s}$. As long as the solid signal has a signal amplitude larger than or equal to the signal threshold, the onset of that

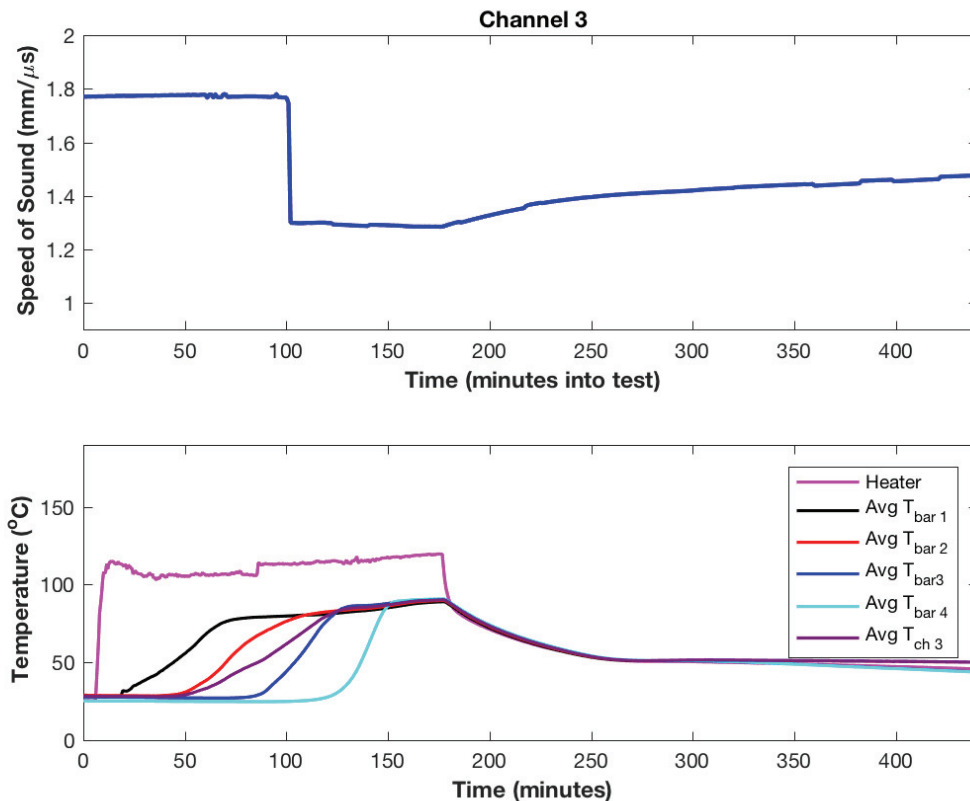


Figure 4.15 The speed of sound for channel 3 (top) and the temperature measured via thermocouples throughout the experiment (bottom).

portion of the signal will be used for calculating the time of flight. Once the solid wax signal drops below the signal threshold, the onset of the liquid wax signal will be used for

identifying the time of flight for the signal. Thus, the change from solid to liquid appears as a step change in Figures 4.13 through 4.16.

Once the heater is turned off, the speed of sound begins to increase. This increase in the speed of sound corresponds to a decrease in the TOF meaning the ultrasound signal observed on the A-scan is starting to move earlier in time (or toward the left). Notice that once the heater is turned off, the speed of sound curve and the temperature curve appear to be mirror images of one another. This observation lends itself to the possibility that the speed of sound may be used to estimate the temperature of the material, which is a topic that will be explored in further detail in a later section.

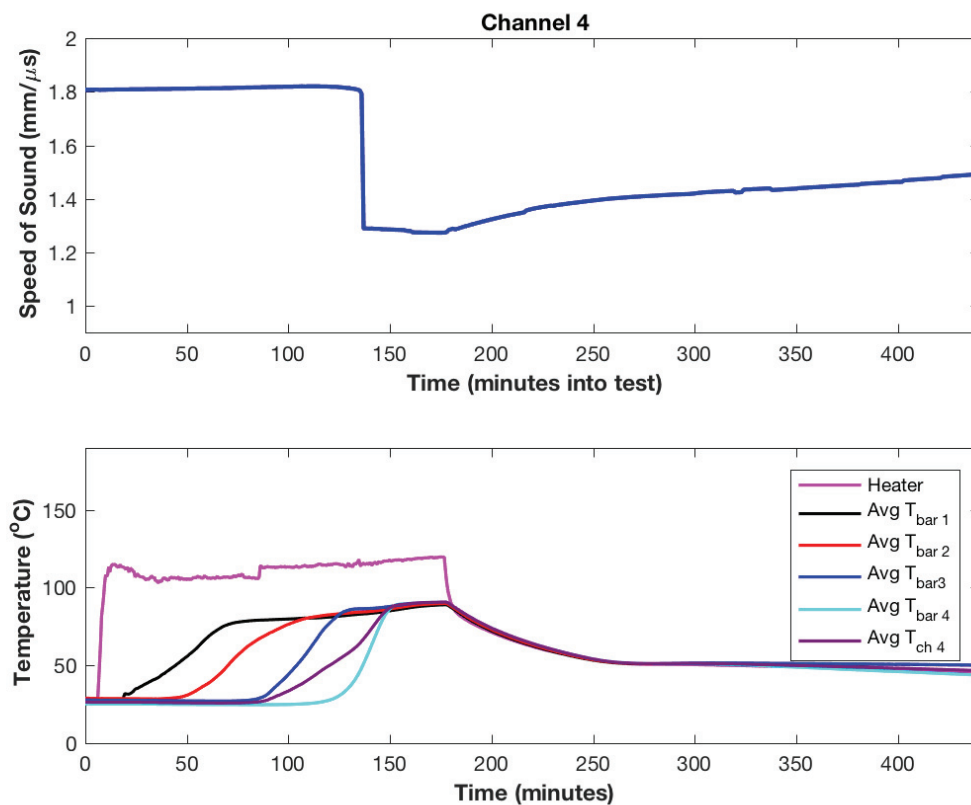


Figure 4.16 The speed of sound for channel 4 (top) and the temperature measured via thermocouples throughout the experiment (bottom).

As previously noted, the EcoSoya wax contracts during the cooling portion of this experiment and pulls away from the wall. At 455 minutes, the wax along channel 4 was at the early stages of losing contact with the box wall, and by 475 minutes, the wax along channel 4 has completely lost contact with the walls of the box. For this reason, the speed of sound plots in Figures 4.13 through 4.16 display only those results associated with the wax being in contact with the box wall, which includes data up to 440 minutes.

4.2.4.2 Comparing the speed of sound. The channel guide presented in Figure 4.6 showed eight channels defined throughout the experimental setup with channels 1 through 4 having reciprocal channels labeled 11 through 14 where the same ultrasound probes were used for sending and receiving the ultrasound wave, but in the reverse order as that defined for channels 1 through 4. Since the same ultrasound probes were used for the reciprocal channels, channels 11 through 14 would be expected to provide the same results as those obtained by channels 1 through 4, respectively. Figure 4.17 provides a comparison of the results for channels 4 and 14 where the speed of sound for channel 4 is in blue and the speed of sound for channel 14 is in red. The line thickness for channel 4 was increased so that the reader may see it; otherwise, the speed of sound plot for channel 4 would be completely covered by the speed of sound plot for channel 14 since the results lie on top of one another. Figure 4.17 confirms that the results obtained using the reciprocal channels matches the results obtained from channels 1 through 4.

A comparison of the speed of sound results for channels 1 through 4 are presented in Figure 4.18. The legend provided in the graph identifies which line corresponds to each channel. From Figure 4.18, the propagation of the melt front can be observed as the results indicate that the solid wax melted first at channel 1 followed by melt at channel 2

followed by melt at channel 3 and finally melt at channel 4. Once all of the channels have melted wax sitting between the two thermocouples, the channels register the same speed of sound as indicated from the lines sitting nearly on top of one another from approximately 140 minutes in the test until the heater was turned off at 177 minutes into

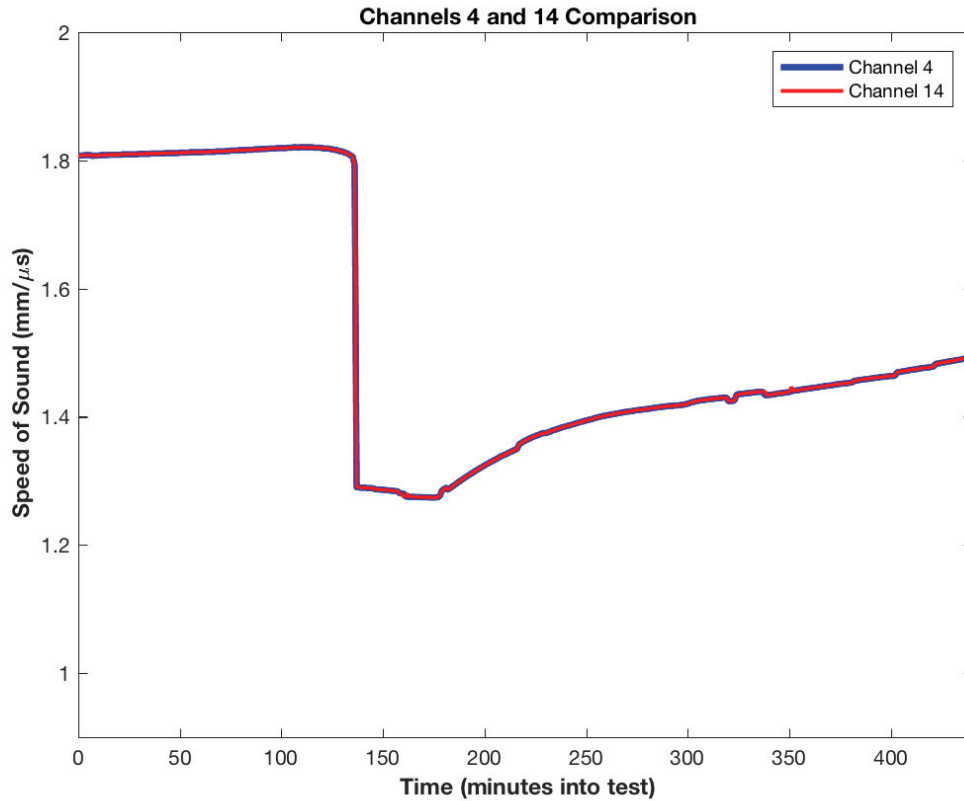


Figure 4.17 Comparing the calculated speed of sound for channels 4 and 14.

the test. Once the heater was turned off, the speed of sound measured for channels 1 through 4 continue to be nearly identical to one another, which is expected since the wax is at a uniform temperature. The similarities in the speed of sound results for channels 1 through 4 continue to compare well with one another.

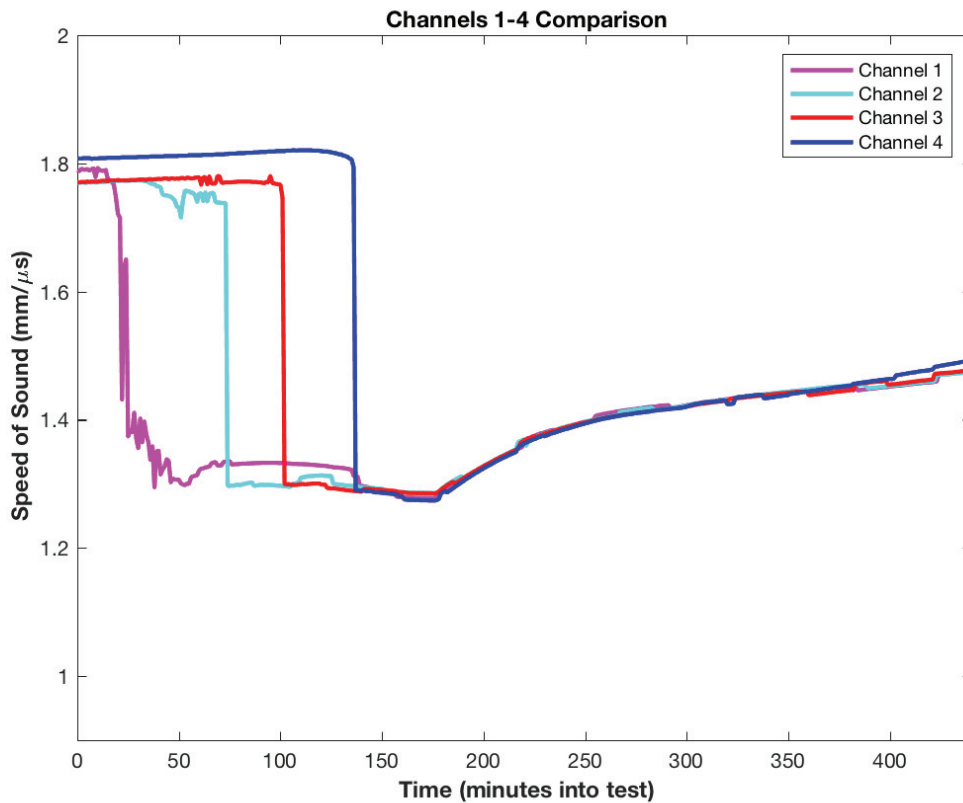


Figure 4.18 Comparing the calculated speed of sound for channels 1 through 4.

4.2.5 Temperature Measurements and Corrections

During the experiment, no thermocouples were placed in the line of sight of the ultrasound probes; however, for an accurate comparison of the speed of sound to the temperature of the wax, the temperature along the probe path should be known, or at least estimated. As observed from Figure 4.19, the temperature at bar 1 increases about thirty minutes before the temperature at bar 2 increases. Thus, the temperature along probe channel 2 in the ultrasound setup should be something in between the temperature of these two thermocouple bars.

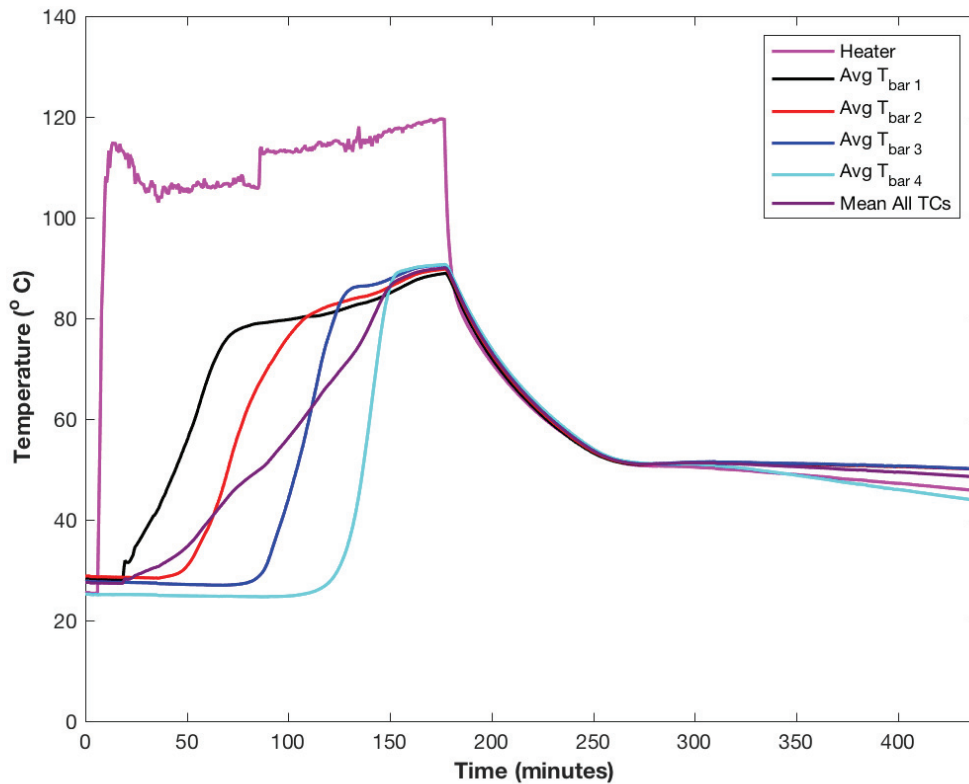


Figure 4.19 The temperatures throughout the experimental setup as monitored by the thermocouples. The average temperature for each bar of thermocouples has been included in this image along with the temperature at the heater block.

The Matlab built-in function ‘scatteredInterpolant’ was used in combination with the thermocouple data and the thermocouple (x,y) locations relative to the top view planar box geometry (where z refers to depth of the thermocouple) to estimate the temperature along each of the probe channels. For each channel, the thermocouples on the bars directly to the left and right of the ultrasound probes were used in the temperature estimation. Notice, channel 1 does not have a bar of thermocouples to the left and instead has the heater block. When estimating the temperature along channel 1, only four thermocouples were used: the heater block thermocouple and the three thermocouples on bar 1. Since the heater block was considerably warmer than the other

thermocouples placed throughout the box, the temperature along channel 1 was overestimated as compared to the temperatures for channels 2 through 4. Channels 2 through 4 each had six thermocouples that were used in the temperature estimation with three thermocouples representing the thermocouple bar to the left and three thermocouples representing the thermocouple bar to the right of the probe channel. For example, thermocouples from bars 1 and 2 were used to estimate the temperature along probe channel 2.

The `scatteredInterpolant` function uses the (x, y) locations and temperature values at each thermocouple of interest to create an interpolant of the form $F(x, y)$ that corresponds to the surface defining the relationship amongst the data points provided. The `scatteredInterpolant` function performs a linear interpolation of the data provided, and outputs the interpolant $F(x, y)$. This interpolant is used for calculating the temperature value at any point on the surface between the two thermocouple bars used while creating the interpolant. Thus, the interpolant created from the linear regression between thermocouple bars 1 and 2 could be used to estimate the temperature along probe channel 2, which is how the temperatures were estimated along each of the probe channels.

Since each of the thermocouple bars contained three thermocouples, the temperature estimation was performed at three locations along the probe channel and as indicated by the purple circles in Figure 4.20. These estimated thermocouples along the probe channels are at the same spatial location with respect to the y-axis as the thermocouples located in the thermocouple bars. The temperature at each of the thermocouple estimates is calculated using the interpolant that was created for each of the probe channels. Once the three thermocouple estimates have been calculated for each

probe channel, the average temperature along the three thermocouple estimates is calculated. Then, the thermocouple estimates are plotted in a similar manner (see e.g. Figure 4.21) as the results that were obtained from the thermocouples themselves in Figure 4.19.

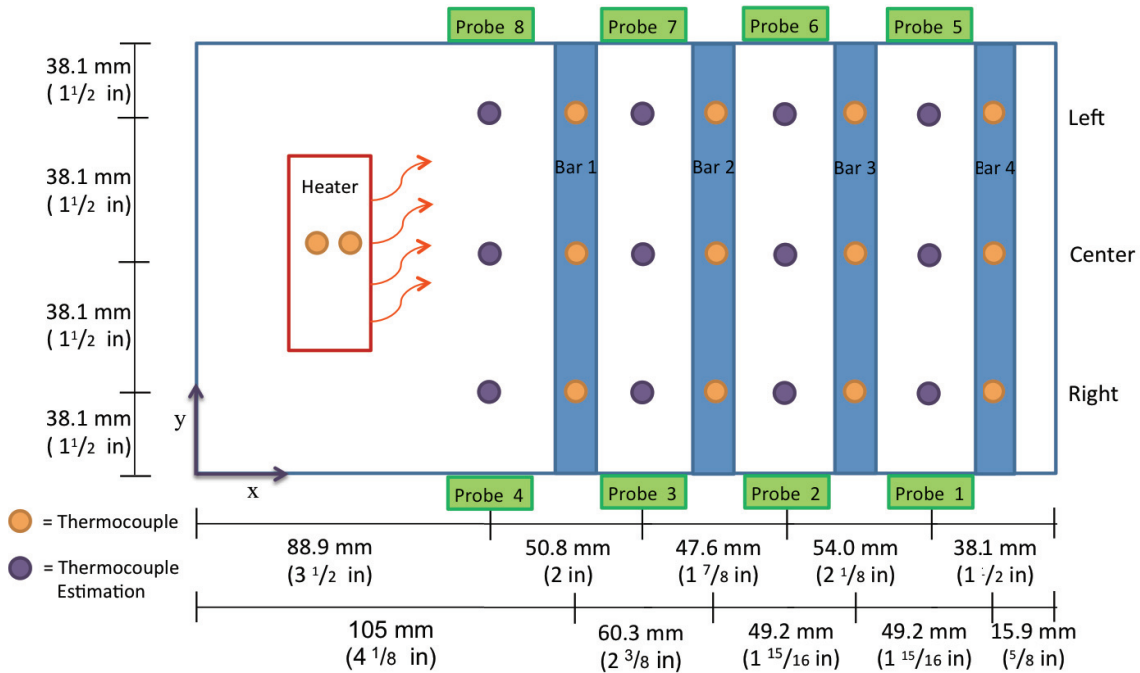


Figure 4.20 Experimental diagram with the ultrasound probe locations and the thermocouple locations relative to the box. The thermocouple estimations (purple) are also indicated relative to the actual thermocouples (orange).

In Figure 4.21, the average temperatures plotted for each probe channel are labeled in the legend according to which probe channel they represent. Thus, ‘Avg $T_{ch 1}$ ’ corresponds to the calculated average temperature along channel 1. Notice that the results for channel 1 follow a slightly different trend than the results for the other three channels. This difference is explained by which thermocouples were used for estimating the temperature along channel 1. Recall, there is no thermocouple bar to the left of channel 1, so the thermocouple at the heater block was used for the estimation of the temperature

along channel 1. Thus, the trend observed for the estimated average temperature along channel 1 is a combination of the trend observed at the heater block and the trend observed along the other probe channels. The following section will compare the speed of sound calculations with the average temperature estimates along channels 1 through 4.

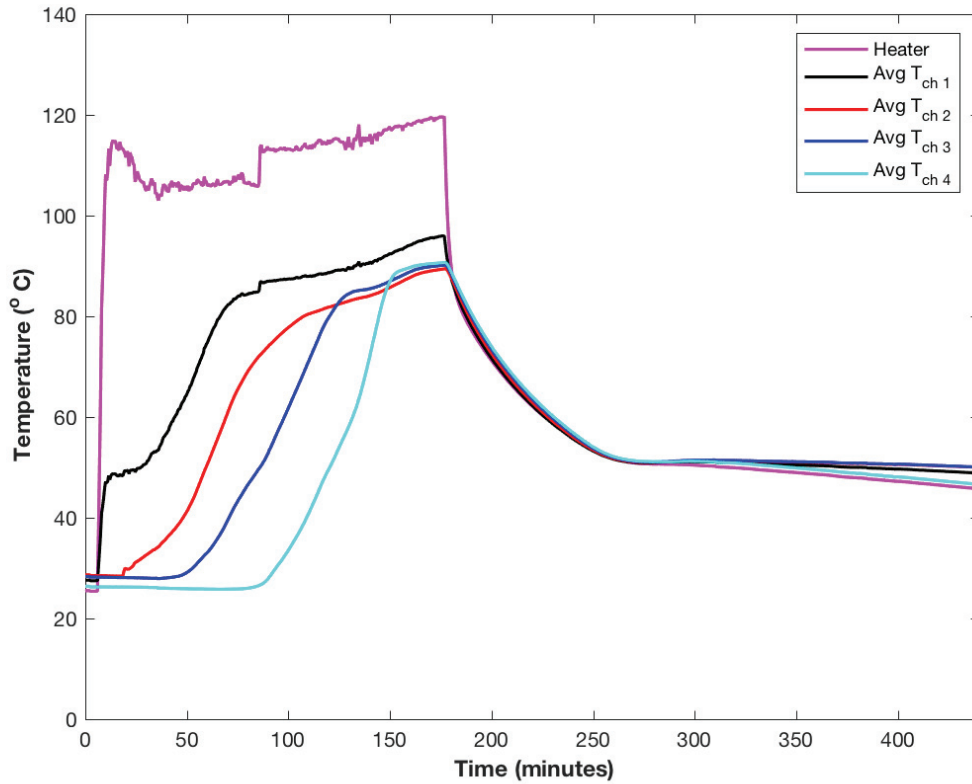


Figure 4.21 The temperatures calculated along the ultrasound probe path for channels 1 through 4.

4.2.6 Correlation between Speed of Sound and Temperature

One of the goals of this project is to identify a relationship between the ultrasound data and the temperature of the material. As previously demonstrated, the phase of the material can be determined by the large change in the speed of sound as the material is heated. The present section will directly compare the calculated speed of sound and the estimated temperature along the probe channel to identify trends that may provide insight

as to how the ultrasound signal may be used to identify the temperature of the material at a given moment during the experiment.

The speed of sound versus estimated temperature along channel 1 is presented in Figure 4.22. The portion of the test corresponding to the heater being on is plotted in red whereas the portion of the experiment during which the heater is turned off is plotted in blue. During the initial heating of the EcoSoya wax, the speed of sound remains approximately constant at about 1.8 mm/ μ s as the temperature increases from room temperature to about 46 °C. Then, the speed of sound begins to drop precipitously with

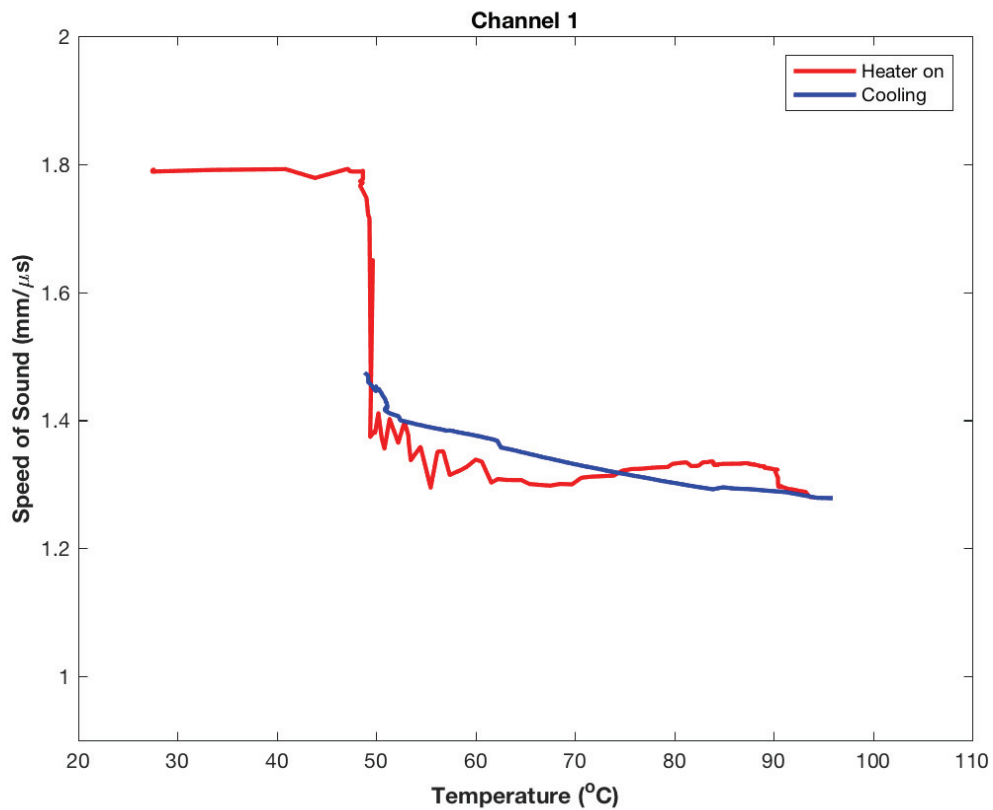


Figure 4.22 The speed of sound versus temperature for channel 1, which is located closest to the heater block.

small changes in temperature until about 50 °C. From 50 °C until roughly 60 °C the speed of sound continues to decrease about another 0.1 mm/μs. Then, there is little change in the speed of sound until the heater is turned off. Throughout the cooling portion of the experiment, the speed of sound steadily increases as the temperature decreases until the wax begins to pull away from the box wall near 47 °C.

The cooling portion of the graph shown in Figure 4.22 indicates that the speed of sound could be used for estimating the temperature of the wax since a clear trend exists. Although this observation is helpful in many respects, the heating portion of the experiment does not lend itself as easily to such usage. Prior to the wax melting, the speed of sound remains nearly constant while the temperature of the material is increasing. This observation may stem back to the discussion of the transition between the solid and liquid wax where both signals are present in the A-scan, but the amplitude of the solid wax signal is equal to or greater than the threshold being used to identify the TOF. Future work in this area may keep track of both the solid wax signal and the liquid wax signal and create a speed of sound versus temperature plot for both signals. A comparison of those results may provide additional information about the relationship between the speed of sound and temperature for the heating portion of the experiment.

The portion of Figure 4.22 corresponding to the heating portion of the experiment does indicate the temperature at which the wax melts because the speed of sound precipitously decreases over a small temperature range. The same can be observed for channels 2 through 4 as seen in Figures 4.23 through 4.25; however, the temperature at which the EcoSoya wax melts is different for channels 2 through 4 than what is observed for channel 1. The results for channel 1 as observed in Figure 4.22 indicates the melt

temperature is near 48 °C whereas Figures 4.23 through 4.25 indicate the melt temperature is in the temperature range of 63-66 °C.

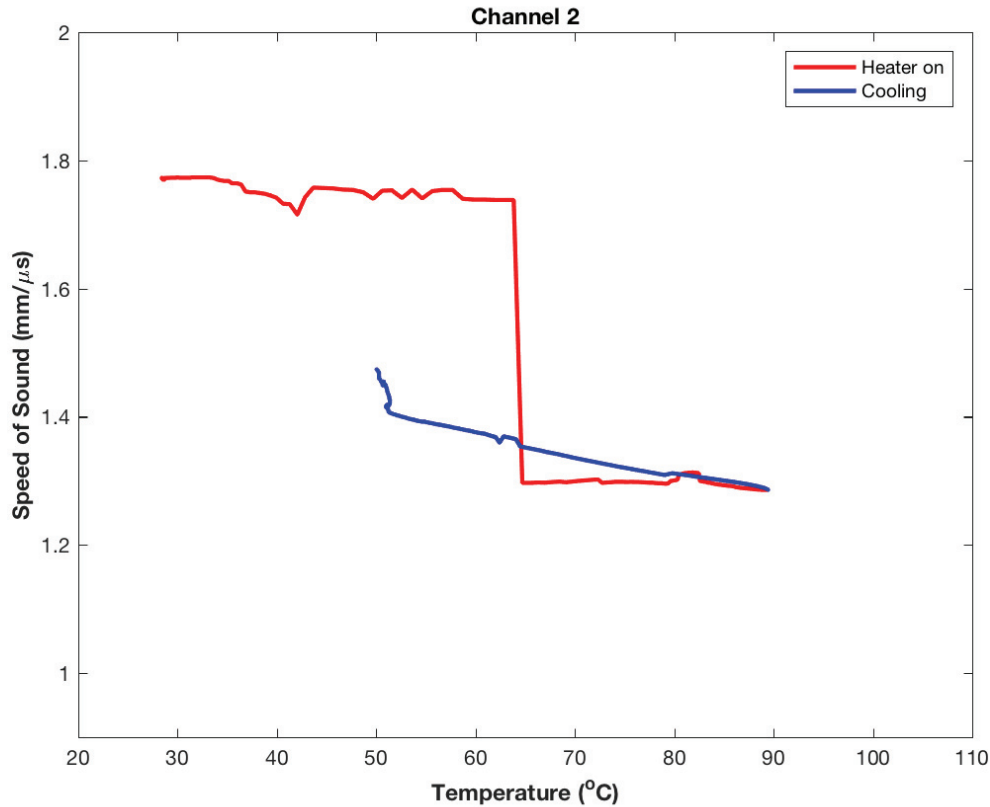


Figure 4.23 The speed of sound versus temperature at channel 2.

In his masters thesis, Gregg [83] performed multiple differential scanning calorimetry (DSC) tests to identify the melting temperature and re-solidification temperature of the EcoSoya wax. From his DSC experiments, Gregg [83] found that the melting temperature of the EcoSoya wax was 53 °C. This is approximately 10 °C less than the temperature that Figures 4.23 through 4.25 estimate the wax is melted. However, recall that the scatteredInterpolation method used in Matlab for estimating the temperature along the channels applied a linear interpolation between the thermocouple bars. The author hypothesizes that there is a nonlinear relationship between the

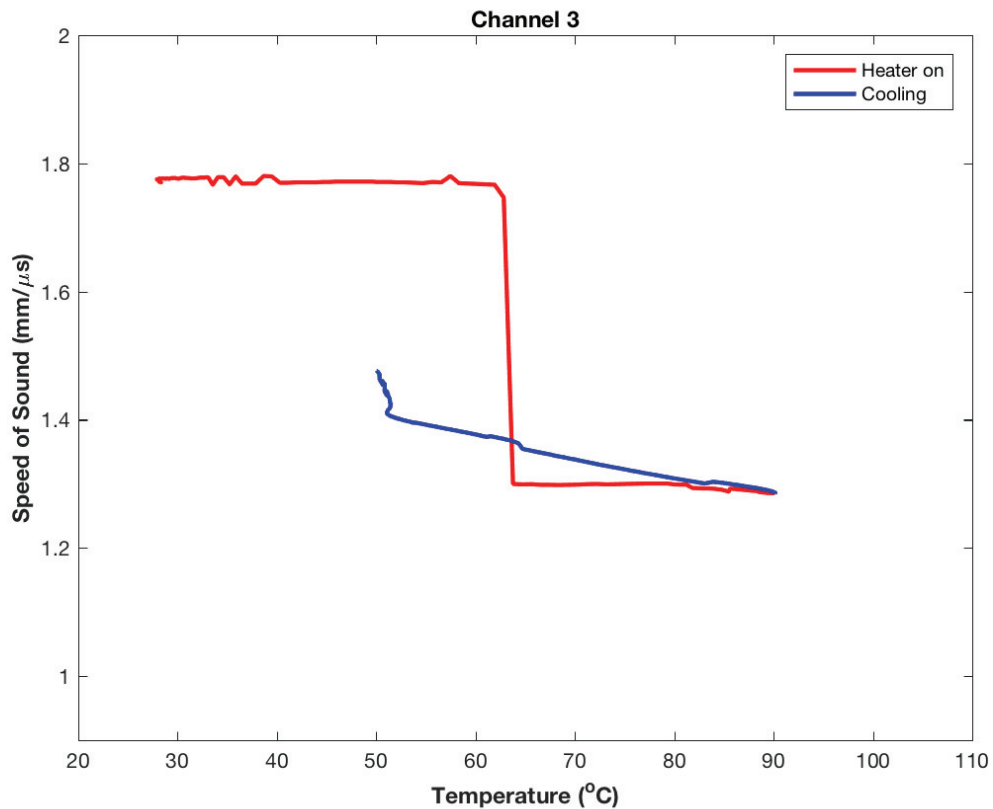


Figure 4.24 The speed of sound versus temperature for channel 3.

temperatures measured at different thermocouple bars while the wax is being heated because she hypothesizes that the solid and liquid EcoSoya wax have different thermal conductivities. To confirm this hypothesis, a one-dimensional heat transfer problem was studied using the solid and liquid thermal conductivities for a paraffin wax as obtained from a 2009 paper by Ukrainczyk *et. al* [120]. A diagram explaining the heat transfer problem being studied is provided in Figure 4.26 and is presented in relation to channel 2 used in the present experiment, where channel 2 is located in between thermocouple bars 1 and 2. The scenario being studied in this heat transfer problem consists of the bar 1 thermocouples being exposed to liquid paraffin wax whereas the thermocouples on bar 2

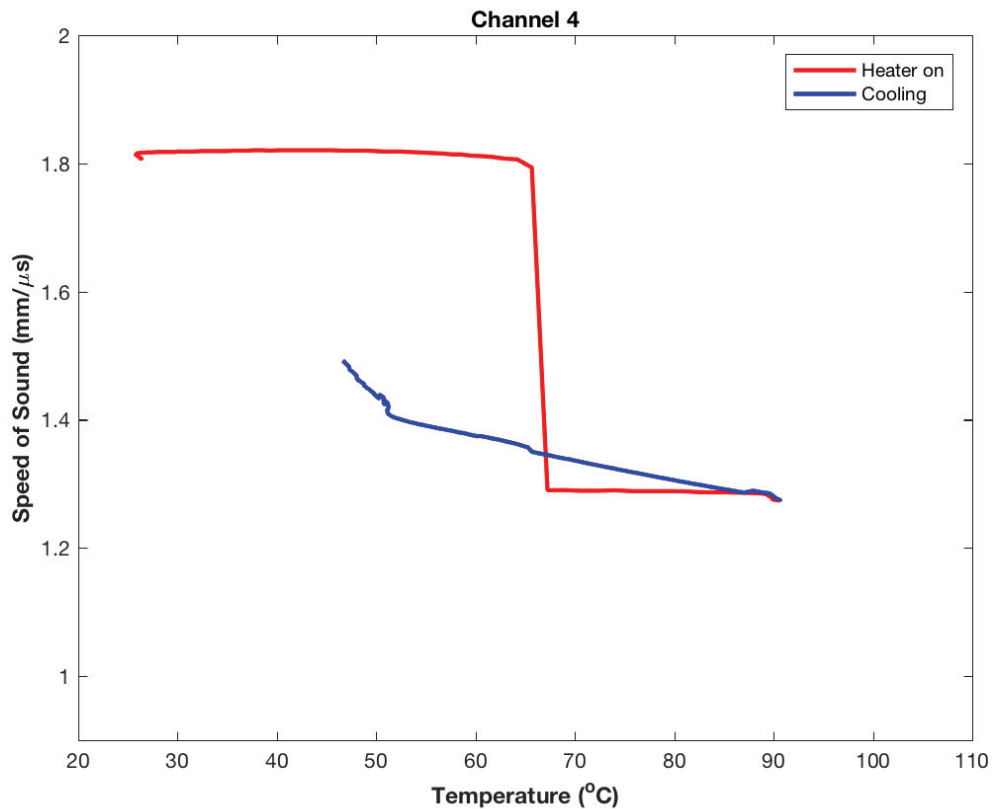


Figure 4.25 Speed of sound versus temperature for channel 4.

are exposed to solid paraffin wax. The average temperatures of the bar 1 and bar 2 thermocouples as used in this heat transfer study were obtained from a visual inspection of Figure 4.19 where the average thermocouple measurements for bars 1 through 4 were presented. Terms corresponding to the liquid paraffin wax in Figure 4.26 are denoted by the subscript 'L' whereas the terms corresponding to the solid wax are denoted by the subscript 'S'. The temperature along channel 2 is denoted by the blue dot in the middle of Figure 4.26. In this one-dimensional heat transfer example, the distance between bar 1 and bar 2 is 0.05 m and channel 2 is located at the midpoint between bars 1 and 2.

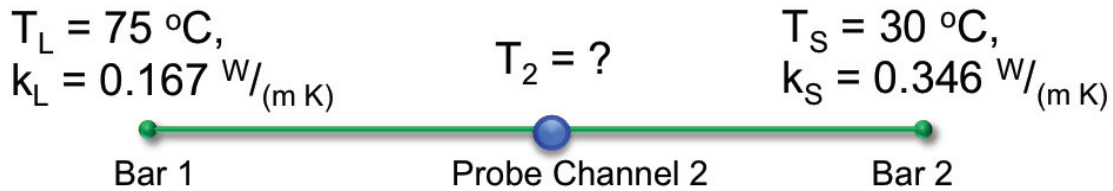


Figure 4.26 A diagram of the one dimensional heat transfer problem

The temperature distribution between bars 1 and 2 was calculated using the finite element method. The orange dot shown in Figure 4.27 corresponds to the temperature at a general location between bar 1 and bar 2. The variable h_L is an array containing 100 linearly distributed values ranging from 0 m to 0.05 m. The variable h_S is an array containing 100 linearly distributed values defined simply as 0.05 m minus the value of h_L . Using the values of h_L and h_S , the temperatures at the endpoints (T_L and T_S) and the thermal conductivities of the solid and liquid paraffin wax (k_L and k_S), the temperature distribution (T) between bar 1 and bar 2 can be estimated using the Equation 4.5 [121], and the results are presented in Figure 4.28.

$$T = \frac{\frac{k_L T_L}{h_L} + \frac{k_S T_S}{h_S}}{\frac{k_L}{h_L} + \frac{k_S}{h_S}} \quad (4.5)$$

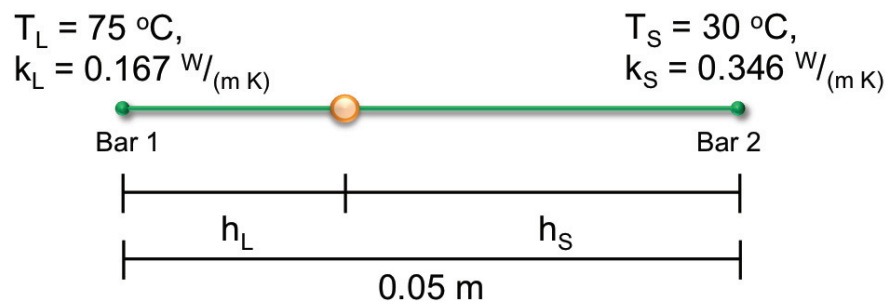


Figure 4.27 A diagram defining the lengths, temperatures, h_L and h_S , used in the finite element model calculations

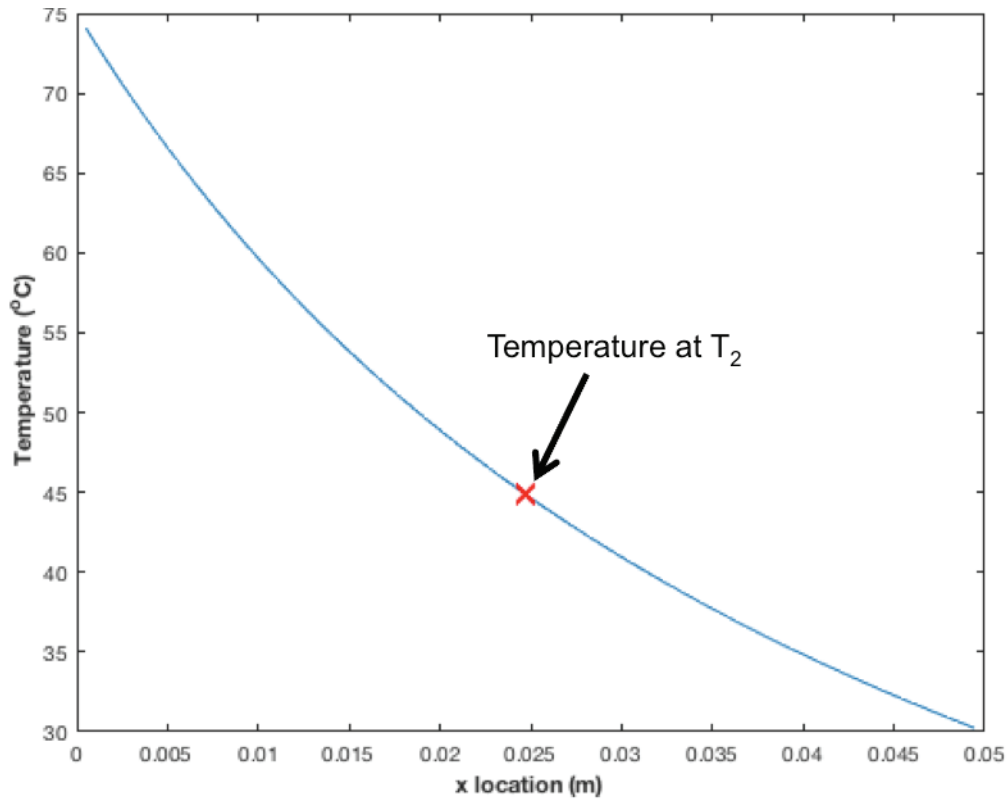


Figure 4.28 Temperature distribution between thermocouple bars 1 and 2 as determined from the finite element analysis of the one-dimensional heat transfer problem

The results of the finite element analysis of the one-dimensional heat transfer problem indicate that the temperature distribution between bars 1 and 2 when bar 1 is exposed to liquid wax and bar 2 is exposed to solid wax is non-linear. The temperature calculated at the midpoint between thermocouple bar 1 and thermocouple bar 2 is approximately 45 °C, which is 30 °C less than the average temperature of the thermocouples on bar 1 and only 15 °C warmer than the average of the thermocouples on bar 2. Figure 4.29 provides a comparison between the linear temperature estimation and the temperature distribution calculated via the 1D heat transfer problem.

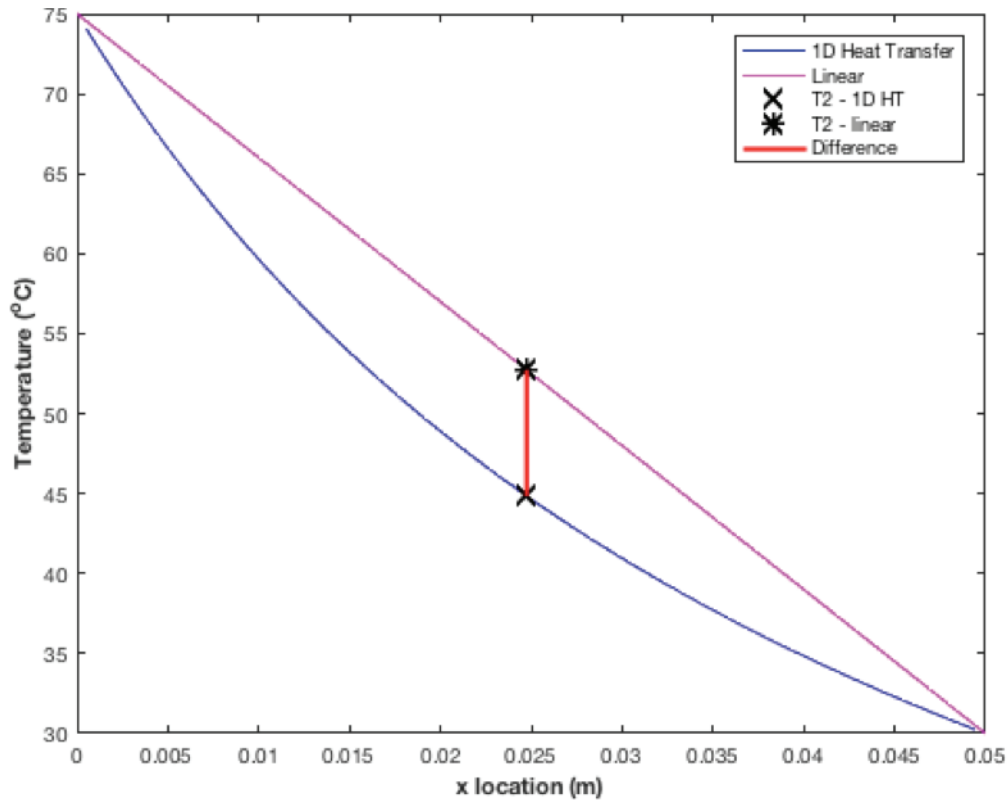


Figure 4.29 Comparison of the results obtained via the finite element analysis of the one-dimensional heat transfer problem and a linear distribution of temperatures between thermocouple bars 1 and 2.

Figure 4.29 indicates there is a 7.88 °C difference in temperature between the linear temperature estimate and the temperature distribution calculated via the one-dimensional heat transfer problem. Although the thermal conductivities in this one-dimensional heat transfer problem were not the thermal conductivities for the wax used in the present study, they do represent a material (paraffin wax) similar to the material used in this study (EcoSoya wax). Thus, it is reasonable to assume that the nonlinear temperature distribution obtained for the paraffin wax would be similar to the temperature distribution obtained for the EcoSoya wax. The results obtained from this heat transfer problem indicate that the temperature distribution as determined from the interpolant method described in section 4.2.5 does not capture the effects caused by the

different thermal conductivities for the solid and liquid wax. Based on these results, the melt temperature estimated from the speed of sound versus temperature plots for channels 2 through 4 in Figures 4.23 through 4.25, respectively, were likely overestimated by about 10 °C, which would then match the results obtained by Gregg’s DSC testing [105].

A comparison of the speed of sound versus temperature plots for channels 1 through 4 is provided in Figure 4.30. The results in Figure 4.30 represent the results

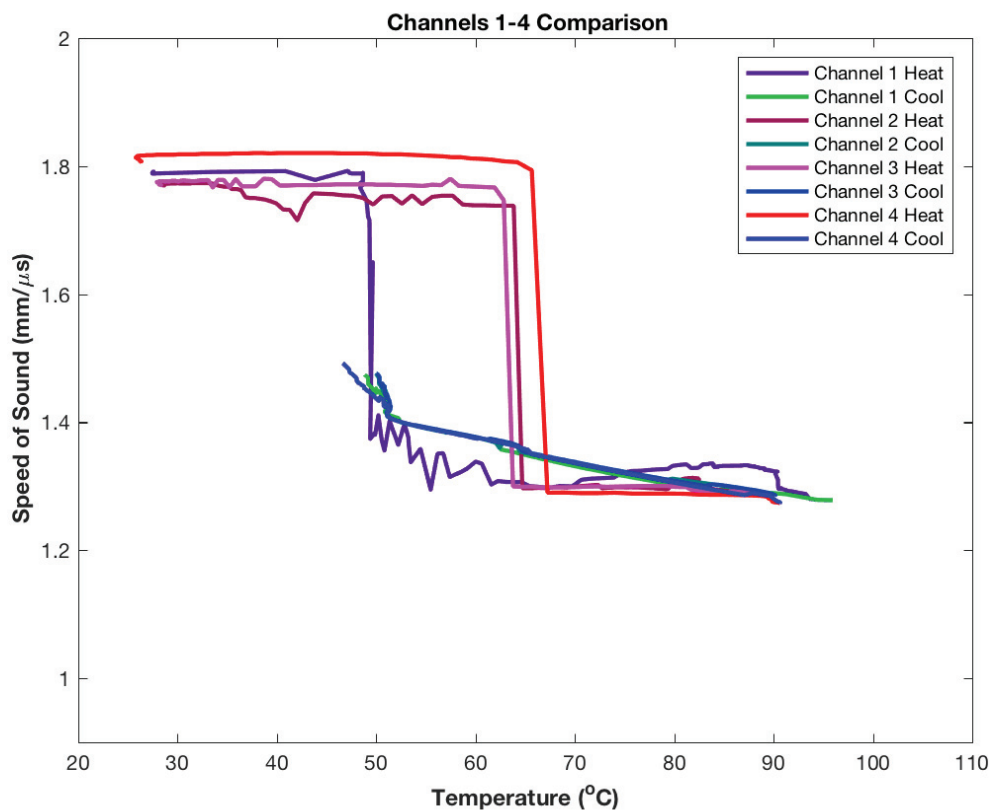


Figure 4.30 Comparison of the speed of sound versus temperature plots for channels 1 through 4. The heating portion of the curves is provided in the red and purple colors whereas the cooling portion of the curves (when the heater is off) is provided in the blue and green colors.

obtained throughout the entire experiment. The results obtained while the heater was on are plotted in red and purple while the results obtained while the wax was cooling are

plotted in blue and green. The heating and cooling portion of each channels data is denoted in the legend in the upper right corner of the graph.

A zoomed in portion of the graph corresponding to the transition from solid to liquid wax is provided in Figure 4.31. The results for channel 1 differ from the results obtained for channel 2 through 4 because the temperature estimated at channel 1 only used four thermocouples compared to the six thermocouples that were used for each of the remaining three channels. The transition from solid to liquid wax occurs within a 5 °C

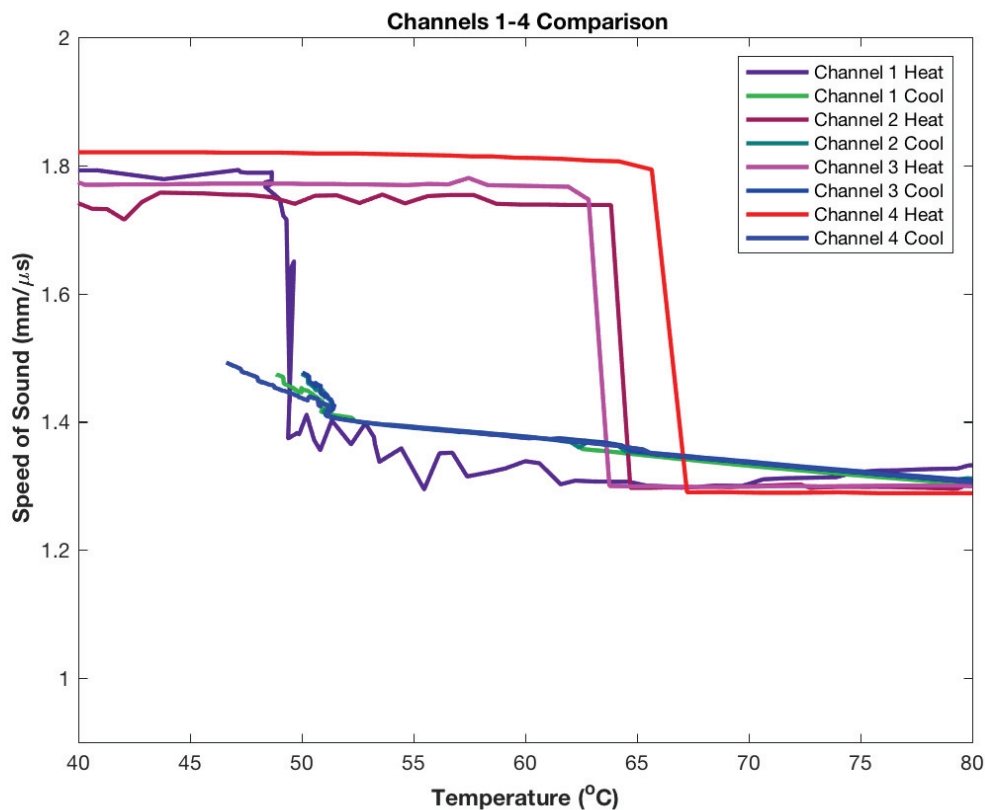


Figure 4.31 Speed of sound versus temperature where the axes have been reduced such that the material's transition from solid to liquid during the melting stage is highlighted by the near step change in speed of sound.

temperature range for channels 2 through 4 in Figure 4.31. Prior to the wax melting, there is a slight vertical variation amongst the speed of sound values for channels 1 through 4.

This variation in the solid speed of sound is likely caused by the difference in signal gain from A-scan to A-scan, the presence of voids in the solid wax, as well as the different physical phenomena occurring at each of the channels. For example, the A-scans for channels 1 through 4 at 24 minutes into the test are provided in Figure 4.32. At this point in the experiment, the wax along channel 1 has started to melt, and channels 3 and 4 are far away from the melt zone. The general shape of the signals at channels 1 through 4 appear rather unique from one another with channels 3 and 4 sharing the most similarity. Although the TOF appears similar to one another for each of these channels, it is different

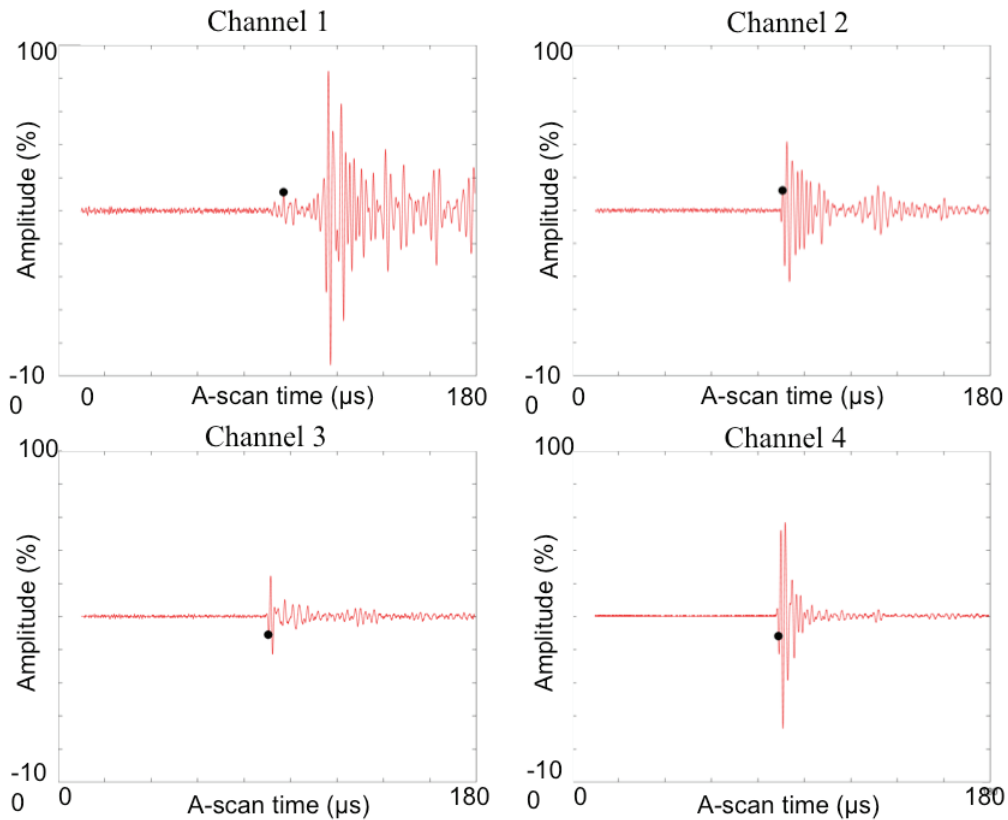


Figure 4.32 Comparison of the A-scans obtained for channels 1 through 4 at 24 minutes into the experiment.

for each of these channels, which led to the difference in the speed of sound as seen for the portion of the speed of sound plot corresponding to the solid wax. Even if the scans were normalized such that the peak of the ultrasound signal in each A-scan presented in Figure 4.32 were equal to one, the shape of these four A-scans likely would prevent the same TOF being determined for all four A-scans.

Considering that voids form within the wax as it cools, it is not unreasonable for the TOF to be slightly different from channel to channel while the wax is a solid. The speed of sound calculated when the wax is a liquid should be more consistent from channel to channel as no voids are present in the liquid wax, and once the wax is fully melted and the heater is turned off, the temperature throughout the box should be homogeneous. Figure 4.33 presents the comparison of the speed of sound versus temperature plot for channels 1 through 4 after the heater is turned off and the wax is allowed to cool. As seen in Figure 4.33, the speed of sound measurements compare well with one another across channels 1 through 4. Furthermore, Figure 4.34 shows that the shape of the A-scan for the liquid wax is much more consistent channel to channel and nearly the same TOF is obtained for each of the four channels at minute 169 in the experiment.

A comparison of the speed of sound versus temperature plots for channel 4 in each of the four experiments performed on the EcoSoya wax is presented in Figure 4.35, and a comparison of the cooling portion of these experiments is presented in Figure 4.36. The speed of sound for the solid wax varies by up to $0.1 \text{ mm}/\mu\text{s}$ between the four experiments, and the melt temperature as determined by the speed of sound versus

temperature plot varies considerably between the four tests with two of the tests apparently overestimating the melt temperature by 10 °C and two of the tests

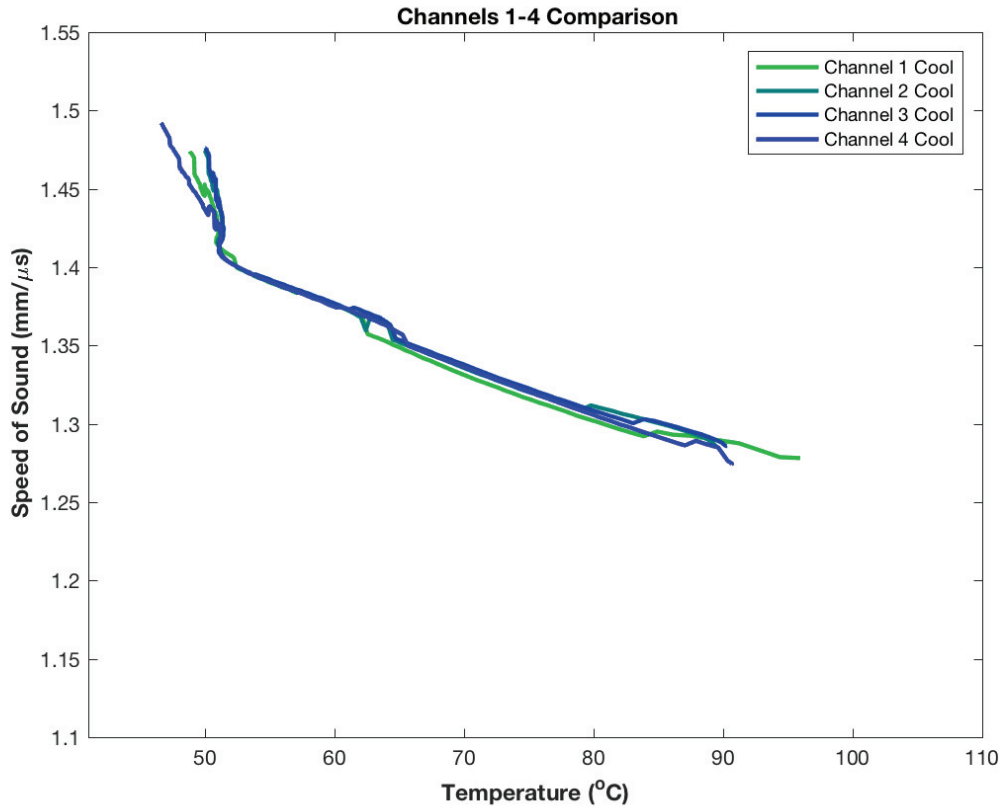


Figure 4.33 Speed of sound versus temperature as the material is cooling.

underestimating the melt temperature by 10 °C. However, as observed in Figure 4.36, the most similar aspect of the speed of sound versus temperature plot across all four tests is the inverse relationship between the speed of sound and temperature during the cooling portion of the experiment. Although the trend during the cooling portion of the experiment is similar across the four tests, the results are not identical from test to test even though the experimental setup was not changed between the tests. Future work may include working on a different method for comparing the results from multiple tests to one another, whether that includes plotting them with respect to a different metric or

normalizing each of the A-scan signals such that the peak in the A-scan is equal to an intensity of 100%.

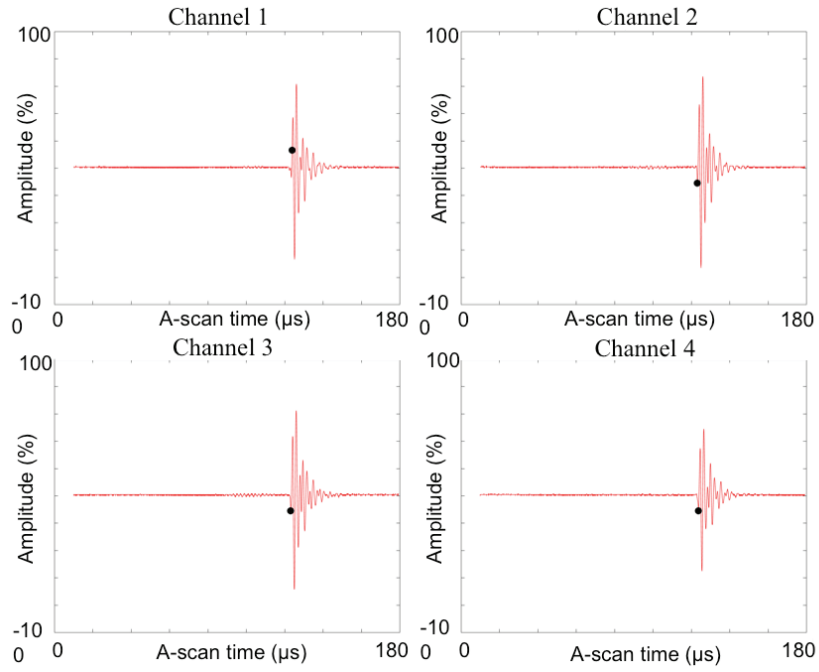


Figure 4.34 A-scans for channels 1 through 4 when the wax is liquid (at 169 minutes into the experiment)

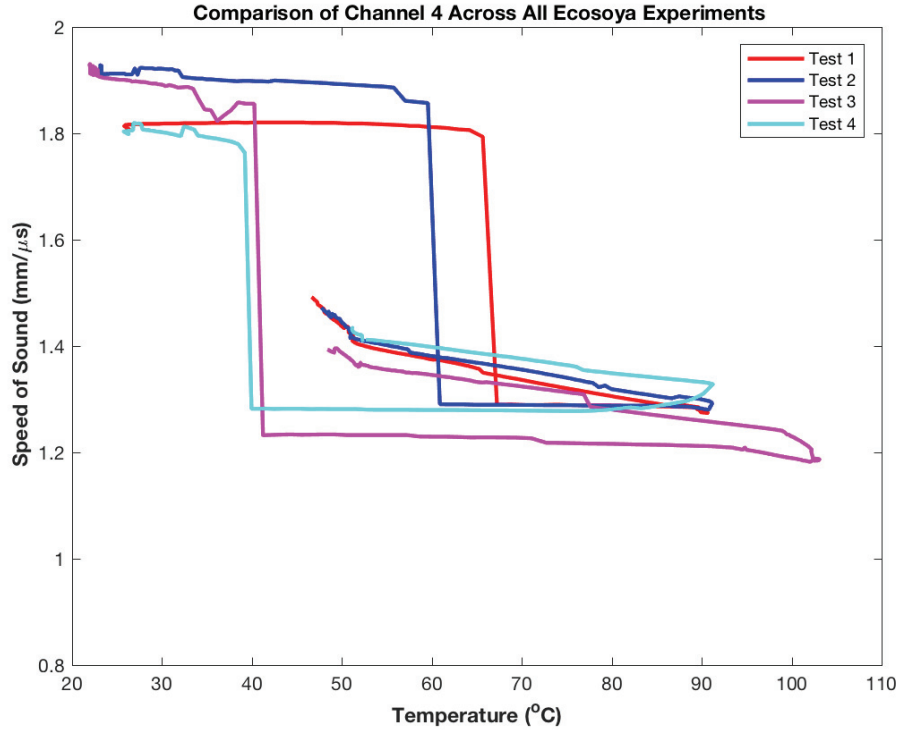


Figure 4.35 Comparison of the speed of sound versus temperature plots at channel 4 for all four of the Ecosoya experiments performed.

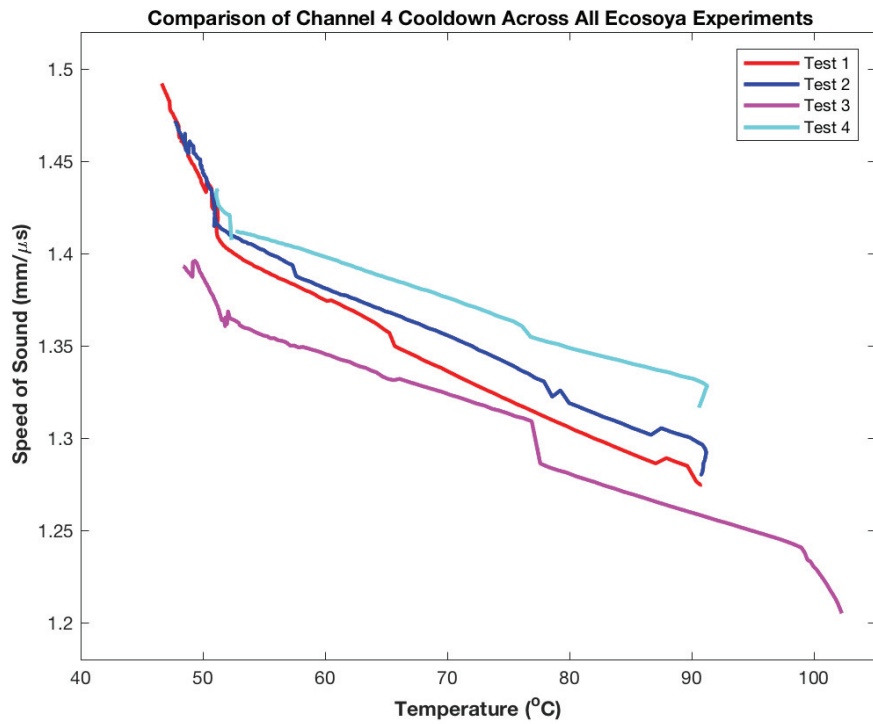


Figure 4.36 Comparison of the speed of sound versus temperature results for channel 4 in all of the Ecosoya tests as the material is re-solidifying.

4.2.7 Fast Fourier Transform Analysis of the A-scan Measurements

The final metric used for analyzing the results obtained in this study is a calculation of the Fast Fourier Transform (FFT) of the A-scan signal. Figures 4.37 and 4.38 show the FFT results for an A-scan signal associated with the solid wax and the liquid wax, respectively. Although the FFT results are similar to one another, the FFT for the A-scan of the liquid wax has a local minima near the operating frequency of the ultrasound probe whereas the FFT for the A-scan of the solid wax does not have this feature. Though minor compared to some of the details that can be obtained from the metrics previously described in section 4.2, the FFT of the A-scan signal may be another means by which to identify whether the EcoSoya wax is a solid or a liquid. Although this FFT analysis is capable of identifying the phase of the wax, it is ill suited for providing details about the temperature of the material.

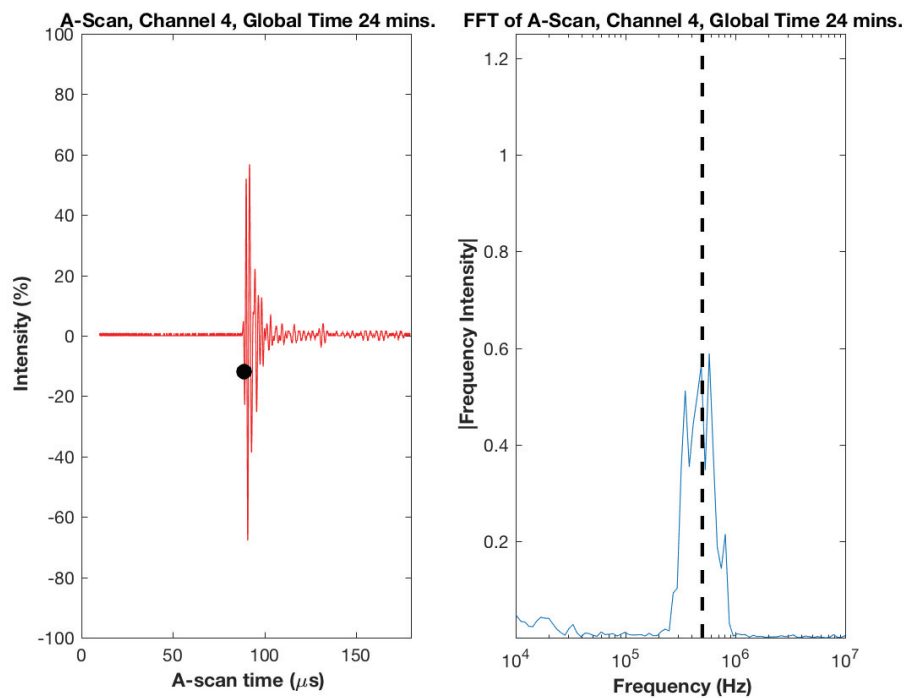


Figure 4.37 A-scan (left) and Fast Fourier Transform (right) results for solid EcoSoya wax at 24 minutes into the test.

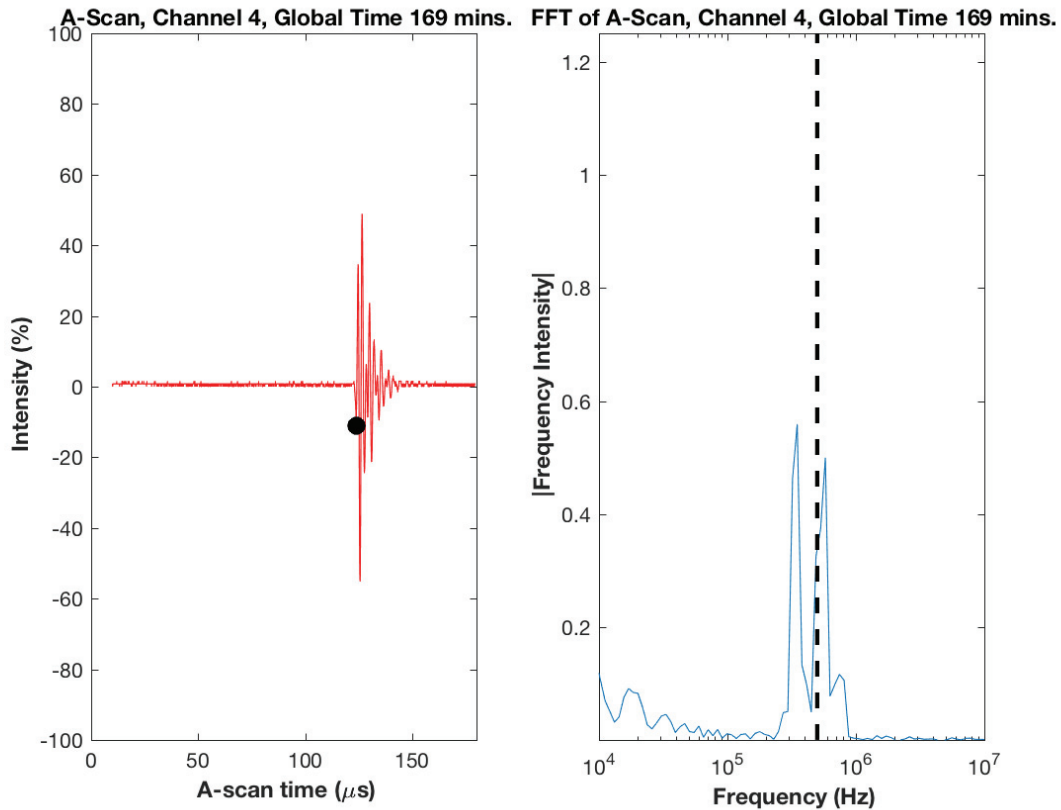


Figure 4.38 A-scan (left) and Fast Fourier Transform (right) results for liquid EcoSoya wax at 169 minutes into the test.

4.3 Machinist Wax – Small Acrylic Box

A second material, namely Rigidax machinist wax, was evaluated during this study. The machinist wax had increased porosity content and a different texture than the EcoSoya wax as observed in Figure 4.39. The EcoSoya wax was smooth in texture like a soy-based candle that may be used in one's household whereas the machinist wax had a coarse texture that looked like it was comprised of small spherical pellets similar to what one would see on a plate of caviar. The overarching goal of this experiment is to further examine the capabilities and potential limits of the ultrasound inspection technique proposed in the discussion of the EcoSoya experiment in section 4.2, and three facets can further describe this goal. First, the goal of the machinist wax experiment was to examine

a second material using the inspection technique described for the EcoSoya wax. Second, the porous machinist wax added another complexity to the inspection as the material's porosity increases the attenuation of the ultrasound wave making it more difficult for the wave to propagate across the container. Third, this experiment was performed with a slightly different experimental setup than the EcoSoya experiment since a smaller box was used to test the effects (or lack thereof) of the experimental geometry on the ultrasound data. The dimensions of this box and the placement of the transducers and thermocouples relative to the box dimensions will be discussed in section 4.3.1.

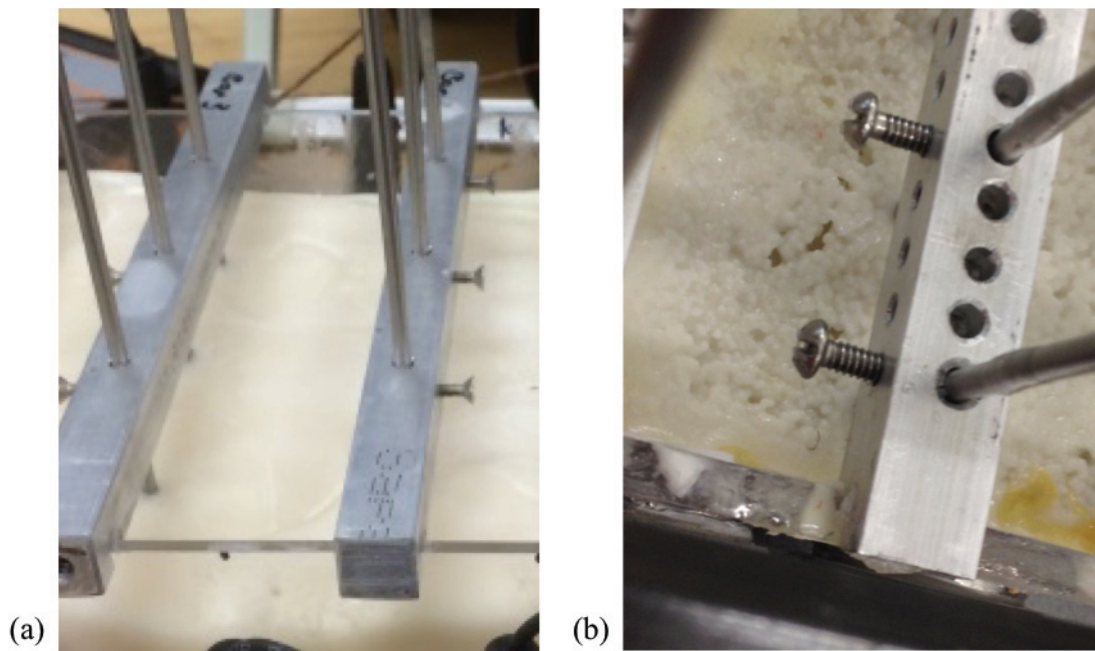


Figure 4.39 (a) The solid EcoSoya wax and (b) the solid machinist wax in their respective experimental setup configurations. The EcoSoya wax has a smoother texture than the pellet-like appearance of the machinist wax.

4.3.1 Machinist Wax Experimental Setup – Small Acrylic Box

As mentioned previously, the machinist wax experimental setup involved a different box geometry than that presented for the EcoSoya wax experiment. A top view

diagram of the experimental setup for the machinist wax box geometry is presented in Figure 4.40. The placement of the ultrasound probes relative to each other and to the box walls is presented in Figure 4.40. The box was manufactured using one-quarter inch thick acrylic material like that used in the manufacturing of the box for the EcoSoya experiment. The box was manufactured by employees at Sandia National Laboratories and was sent to Baylor University for testing related to this ongoing project. The placement of the thermocouples relative to the box geometry is presented in Figure 4.41. There is one less thermocouple bar than was presented in the EcoSoya wax experiment, and this difference is because of the reduced size of the box used in the machinist wax experiment. Unlike in the EcoSoya wax experimental setup, there is a thermocouple bar

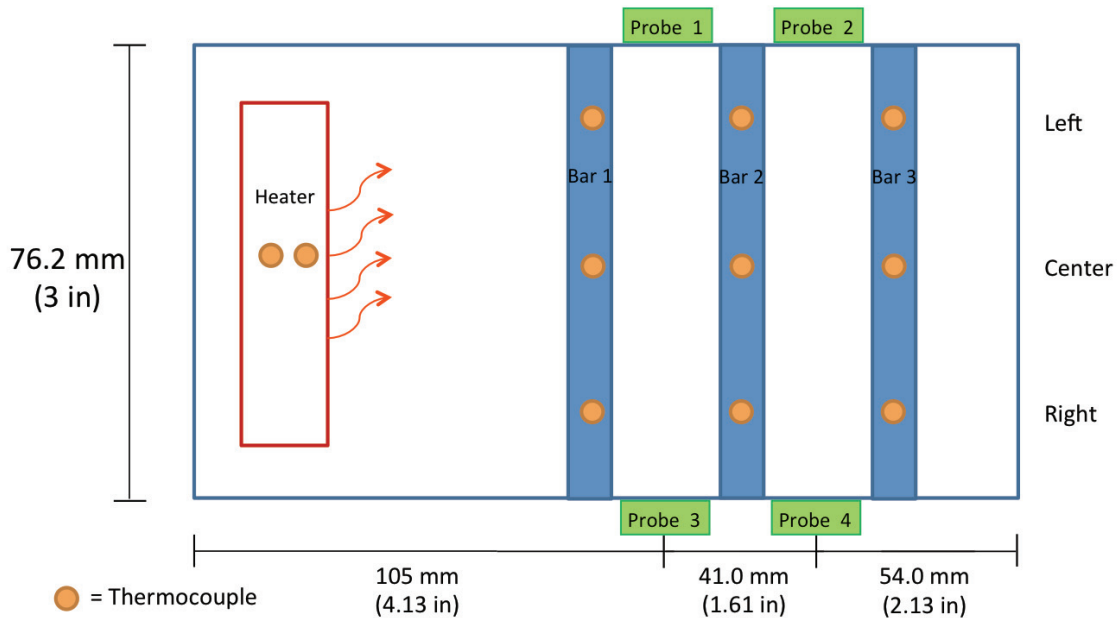


Figure 4.40 Drawing of the experimental setup of ultrasound probe placement for the machinist wax experiment with the small acrylic box. All dimensions are inner dimensions and do not include wall thickness.

heater block, two heating elements were placed in the heating block. Additionally, the aluminum heater block was 1"x2.5"x2.5" in size, which is larger than the block used in the EcoSoya experiment.

The thermocouples used in this experiment were not placed at the same depth relative to one another. Instead, when the heater was placed into the experimental setup, the machinist wax was allowed to continue melting. Having observed the behavior of this wax in previous experiments performed at Sandia National Laboratories, Mr. Moore and the author knew that the machinist wax did not melt as easily as the EcoSoya wax. Instead of melting to just below the heater block depth across the entire length and width

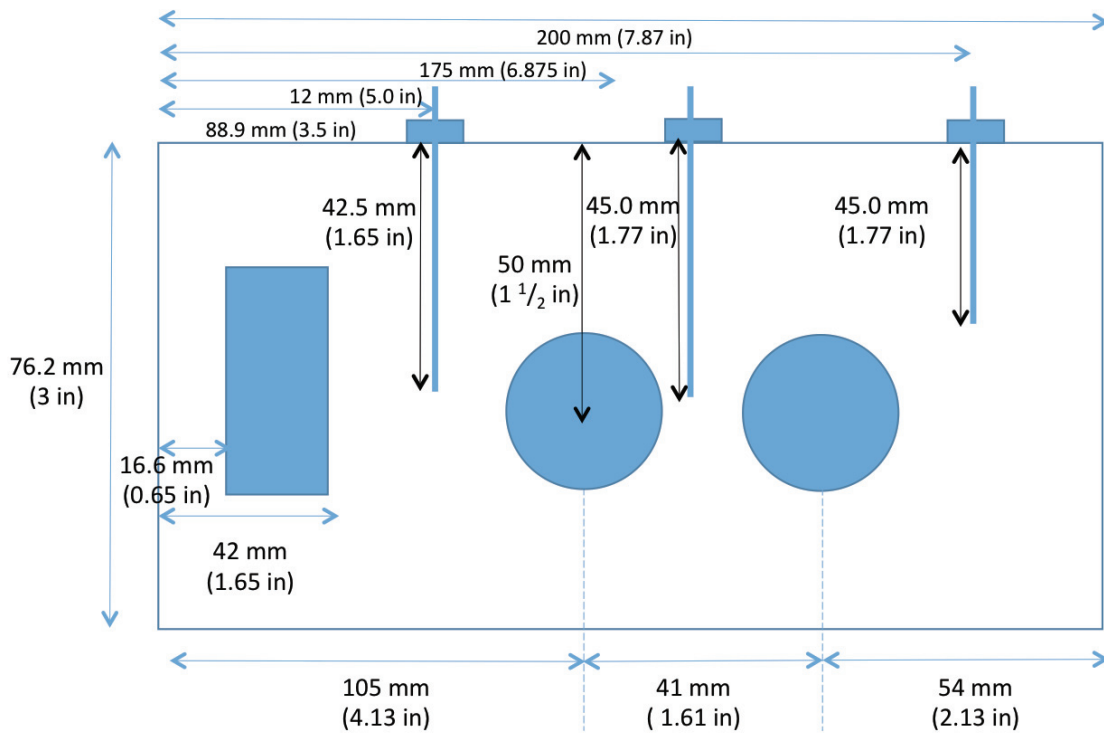


Figure 4.42 Side view of the experimental setup for the machinist wax experiment in the small acrylic box. All dimensions provided are inner dimensions and do not include the wall thickness. The rectangle represents the heater block and the circles represent transducers.

of the box as the EcoSoya wax had done, the machinist wax would likely exhibit a melting pattern such that the wax located furthest away from the heater may not melt during the experiment. Thus, during the manufacture of the experimental setup, the heater was turned on and the wax was allowed to melt across as much of the box as possible. Once the melt front appeared to stagnate, the thermocouples were placed in the box such that their depth was just higher than the remaining solid portion of the wax. It is interesting to note that the bar 2 thermocouples were placed 2.5 mm below the depth of the bar 1 thermocouples. This slight increase in depth further away from the heater block may have been caused by the presence of a void near the bar two thermocouples that filled with liquid wax upon the melt front propagating across this location. The thermocouples along bar 3, located farthest away from the heater block, are also the shallowest of the thermocouples used in this experiment because the liquid machinist wax was shallowest in this region.

In the machinist wax experiment, there were four channels monitored with two of these channels being the reciprocal of the other two channels as indicated in Figure 4.43. For example, channel 1 represents ultrasound probe 1 producing the incident ultrasound pressure wave while ultrasound probe 3 receives the wave once it has propagated across the width of the box. Channel 1b is the reciprocal of channel 1 such that probe 3 emits the incident wave while probe 1 receives the wave once it has propagated across the width of the box. Channels 2 and 2b are defined in a similar manner.

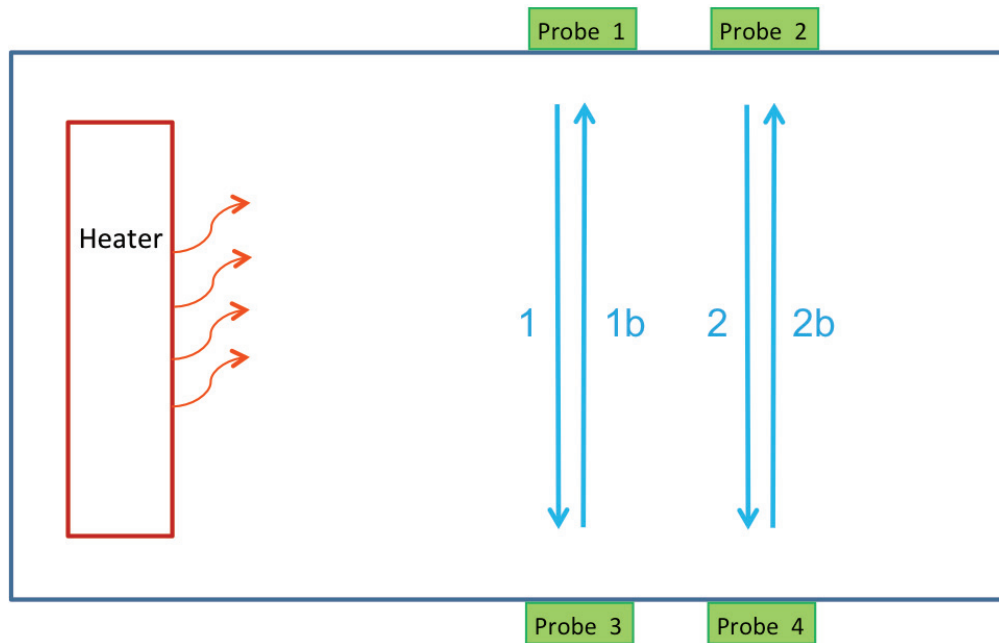


Figure 4.43 Channel listing for the experimental setup used with the machinist wax experiment in the acrylic box.

4.3.2 DSC Testing on Machinist Wax

Dynamic Scanning Calorimetry (DSC) testing was performed on the machinist wax to identify the melt temperature and re-solidification temperature of the material. As referenced in section 4.2.6, Gregg [83] completed a similar analysis for the EcoSoya wax in his masters thesis. The DSC equipment used for the experiment performed in this study is presented in Figure 4.44. The sample chamber has approximately the same diameter as a quarter. The machinist wax sample was hermetically sealed within one of the two aluminum T-zero pans as seen in the zoomed in image in Figure 4.44, and the second pan is an empty reference pan of the same type. Both pans are about the same size as a pencil eraser. A model Q20 DSC manufactured by TA Instruments was used for the experiment, and the test was performed in a nitrogen environment where nitrogen gas was pumped into the testing chamber at a rate of 20 milliliters per minute.

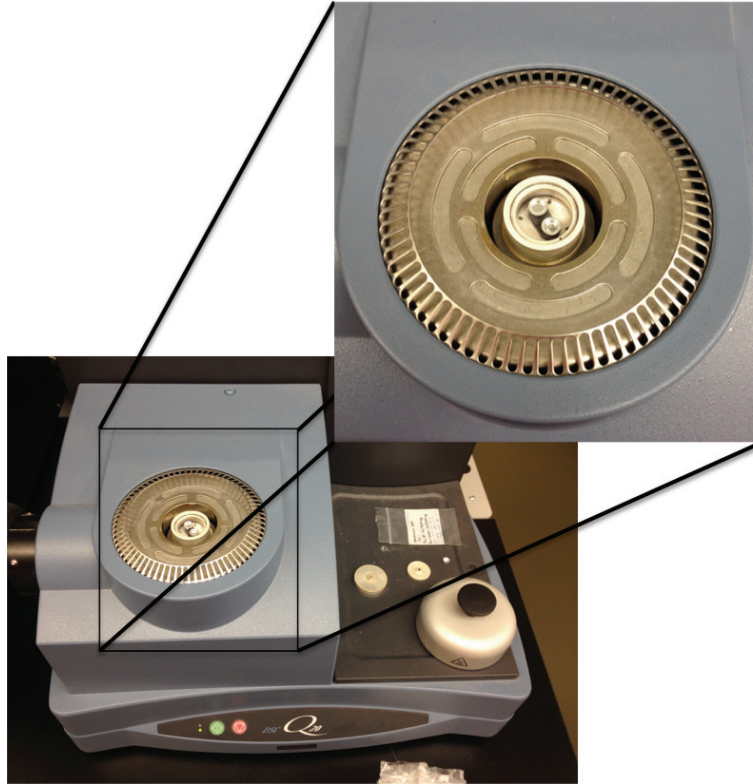


Figure 4.44 DSC experimental setup and chamber. The sample is located in one of the small pans in the zoomed in callout image.

A heat/cool/heat/cool procedure was performed on the machinist wax, and the results are presented in Figures 4.45 – 4.46. At the beginning of the experiment, the temperature in the sample chamber was reduced from room temperature down to 0°C and held in an isothermal state for five minutes. Then, the temperature of the chamber was increased to 150 °C at a rate of 1°C/min. Next, the temperature of the chamber was cooled back down to 0 °C at 1 °C/min, and then, the same heating and cooling cycle was performed again to complete the heat/cool/heat/cool test. After the test was completed, a second test was performed on a second sample, and the temperature rate used for increasing and decreasing the temperature inside of the chamber was 2 °C/min instead of 1°C/min. The results for each of the four legs of these two experiments are shown in

Figure 4.45, where the first heat, first cool, second heat and second cool portions of the experiment are each contained in their own subplot. The results from both tests are presented in each of the subplots in Figure 4.45 with the 1 °C/min test in blue and the 2 °C/min test in red.

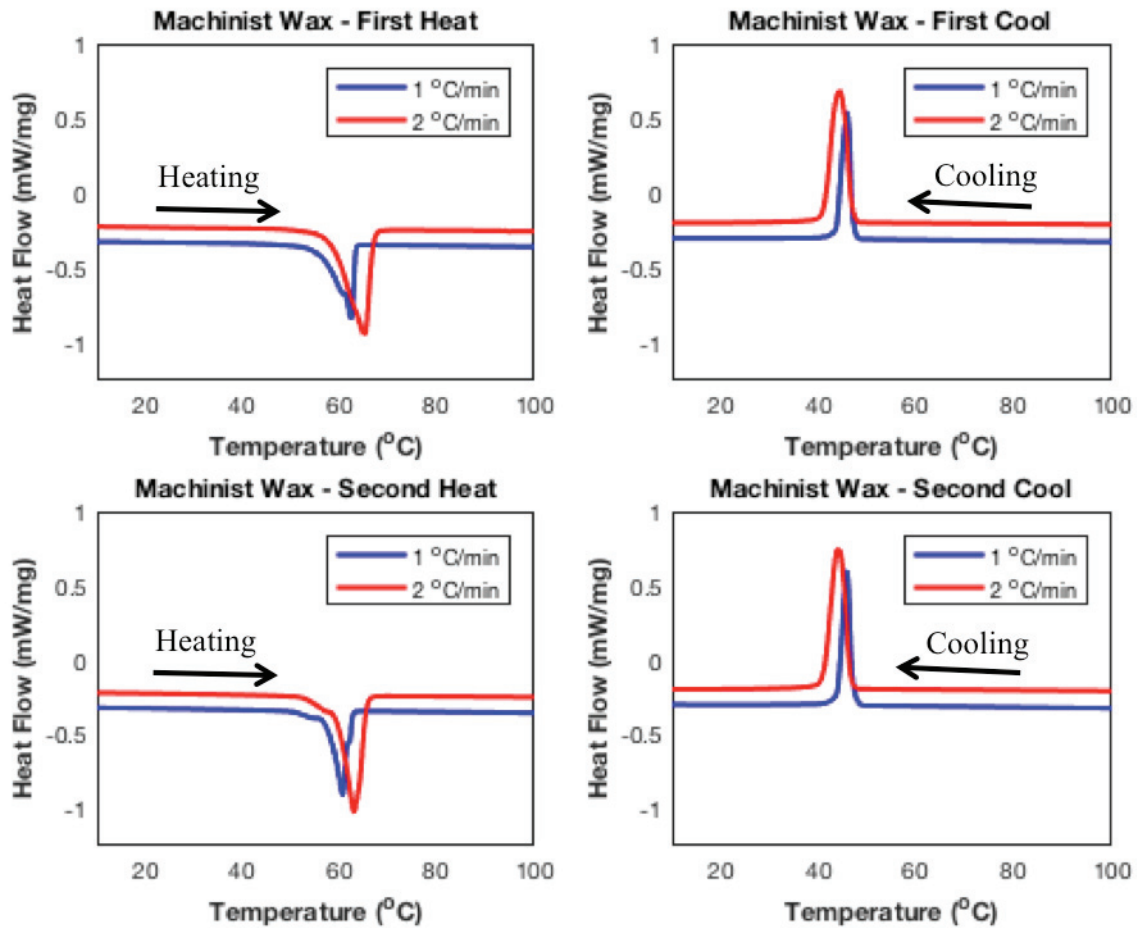


Figure 4.45 The DSC test results for the machinist wax for a heat/cool/heat/cool cycle where the blue line represents the temperature being varied by 1 °C/min and the red line corresponds to the temperature being changed by 2 °C/min.

The graphs presented in Figure 4.45 indicate that the results for the 1°C/min test and the 2 °C/min test are strikingly similar during the cool-down portions of the experiment, but there is a slight difference between the results obtained for the heating

portions of the two tests. Notice in the graph corresponding to the first heat in Figure 4.45 the minimum for the 2 °C/min test occurs at a temperature of approximately 66°C whereas the minimum for the 1 °C/min test occurs at a temperature of approximately 62 °C. Figure 4.46 presents the results from the full length of the experiment in one plot and highlights the melt temperature range as well as the re-solidification temperature for the machinist wax material.

The location of the melt temperature is a topic of discussion with respect to interpretation of DSC results. Some researchers define melt as the point at which the material begins to soften, which corresponds to the onset of the minimum location on the heating curve. Still other researchers define the melt as the minimum point on the curve while others define it as the upward trend of the trough. In the present study, the melt temperature will be defined as corresponding to the positive slope portion of the curve located directly after the minimum since the material should be fully liquid at that point. The melt temperature for each test is denoted by the dotted lines in Figure 4.46. The re-solidification temperature in this experiment is defined as the point in the cooling curve that marks the onset of the peak, and the orange dashed line in Figure 4.46 denotes this temperature. The horizontal axis in Figure 4.46 starts at 10 °C and ends at 100 °C. This temperature range was chosen for two reasons. First, the data obtained near the endpoints (0 °C and 150 °C) of the test was removed from the plot as there is approximately a 5 °C range where the measurements are not as stable due to the system's change from heating to cooling (or vice-versa). Second, the plot in Figure 4.46 was zoomed in to focus on the melt temperature range as well as the re-solidification temperature associated with the machinist wax.

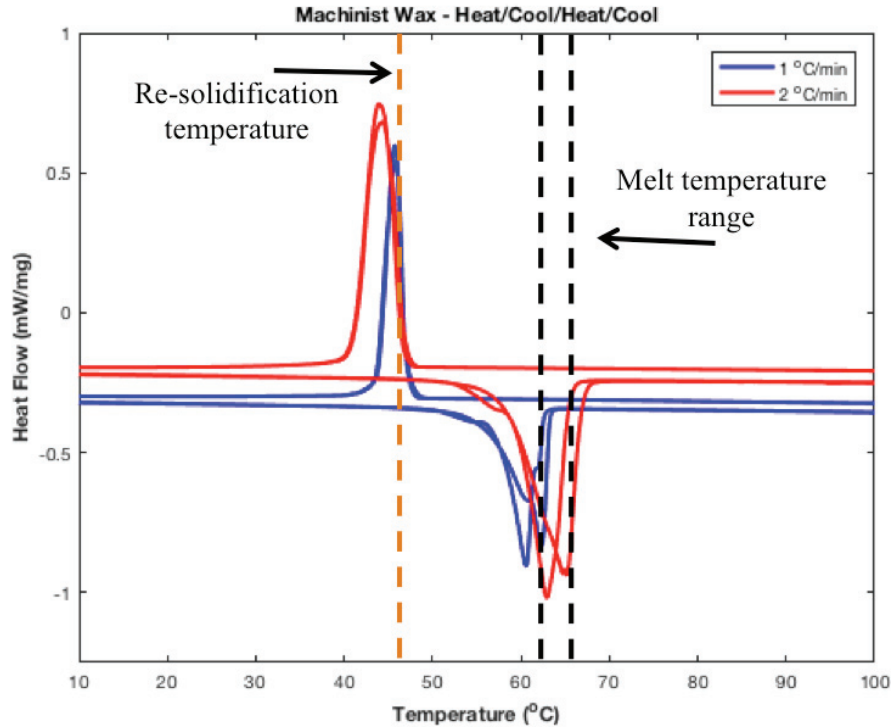


Figure 4.46 The DSC results for the heat/cool/heat/cool experiment performed in both the 1°C/min test (blue) and the 2 °C/min test (red).

The melting temperature is approximately 62 °C for the 1 °C/min temperature ramp and approximately 66 °C for the 2 °C/min temperature ramp as denoted by the black dashed lines in Figure 4.46. The re-solidification temperature for this material, which is denoted by the orange dashed line in Figure 4.46, is about 47 °C for both tests. Outside of the melting and re-solidification regions in Figure 4.46, another important observation from this graph is the near zero slope of the line for heat flow as a function of temperature. The slope of this line is related to the inverse of the heat capacity. Thus, the closer the slope is to zero, the higher the heat capacity of the material, which means it is more difficult to melt the material. Conversely, the larger the slope of this line, the lower the heat capacity of the material, which means it is easier to melt. A comparison of the DSC results for the machinist wax with those provided in Gregg’s thesis [83] shows that

the machinist wax is more difficult to melt than the EcoSoya wax, which confirms the observations made during the ultrasound experiments.

4.3.3 A-scan Measurements

An A-scan associated with the solid machinist wax is provided in Figure 4.47. In this figure, a wave signal is present near 42 μs , but the amplitude of this wave signal is near the same level as the noise in the signal. The signal gain at the time this A-scan was collected was 80 decibels. The A-scan signal associated with the solid machinist wax is considerably different than the A-scan signal associated with the solid EcoSoya wax as seen in Figure 4.7. This indicates that the ultrasound wave is not able to propagate through the machinist wax as easily as it did the EcoSoya wax.

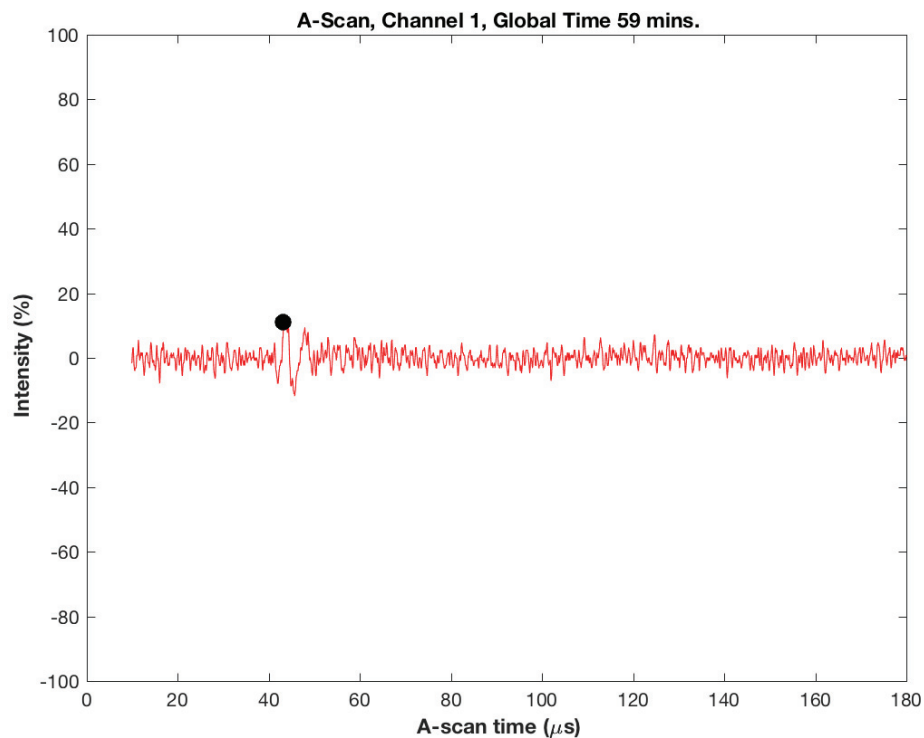


Figure 4.47 A-scan associated with the solid machinist wax 59 minutes into the test.

An A-scan corresponding to the liquid machinist wax is presented in Figure 4.48. This A-scan signal looks similar to the A-scan signal for the liquid EcoSoya wax as presented in Figure 4.8, but the TOF as indicated by the black dot is different between the two A-scans. The difference in the TOF between the EcoSoya experiment was caused by the difference in material and the difference in box geometry. The box used in the machinist wax experiment was one-half the width of the box used in the EcoSoya experiment, and the EcoSoya wax and the machinist wax have different speeds of sound. Both A-scans presented in Figure 4.47 and 4.48 were generated using the same Matlab code as was used in analyzing the EcoSoya wax experiment data.

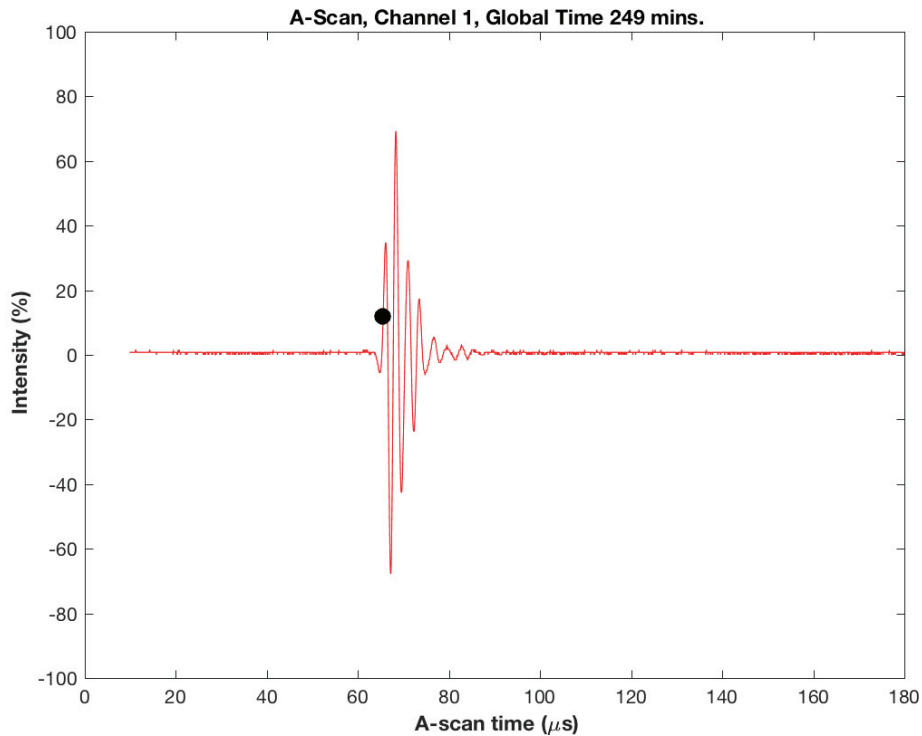


Figure 4.48 A-scan associated with the liquid machinist wax at 249 minutes into the machinist wax melt test.

4.3.4 B-scan Results

The B-scan obtained from the channel 1 data is presented in Figure 4.49, where channel 1 is located closest to the heater block. Although channel 1 is located only 2.5 inches away from the front surface of the heater block, the machinist wax takes nearly 110 minutes to fully melt along this probe channel, which corresponds to the observation from the DSC testing in Section 4.3.3 that the high heat capacity of the machinist wax makes it more difficult to melt. Figure 4.50 presents the B-scan for channel 1 along with a few markings to assist in the explanation of what can be gleaned from the graph.

First, the region of the B-scan corresponding to the solid wax is highlighted by the leftmost black oval. The amplitude of the ultrasound signal in this region of the B-scan is

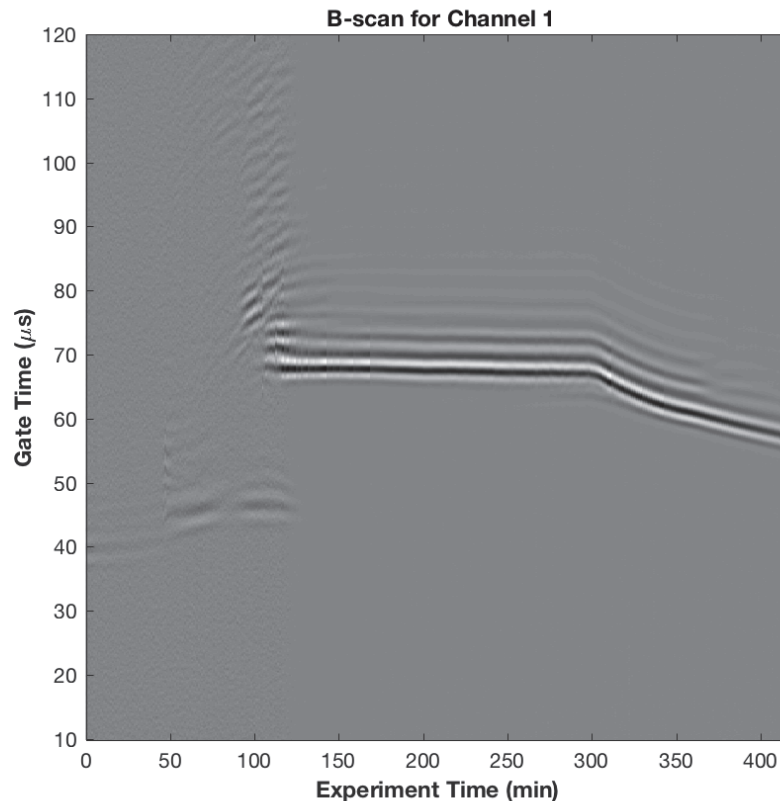


Figure 4.49 B-scan for channel 1 data

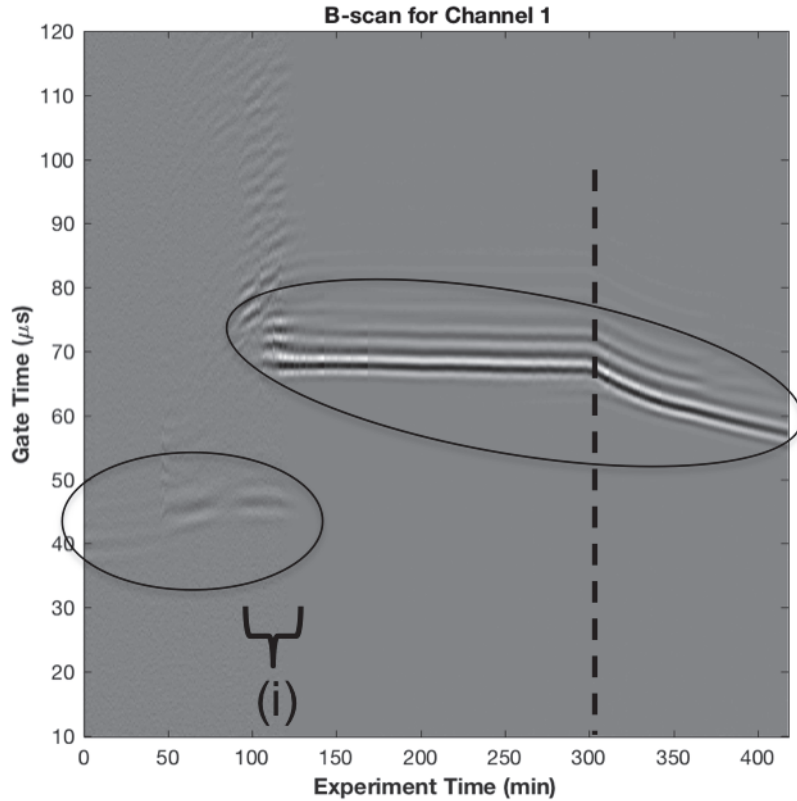


Figure 4.50 B-scan for channel 1 data with specific the solid and liquid portions of the experiment highlighted by ovals, the transition from solid to liquid highlighted by (i) and the dashed line indicating the heater was turned off.

weak because, as seen in the A-scan in Figure 4.47, the wave's amplitude in the A-scan is near that of the signal noise. However, it is important to note that even though the signal amplitude is low and the wave is near the same amplitude as the noise, the presence of this signal can still be located on the B-scan image. The rightmost oval corresponds to the liquid signal as it continues to heat while the melt front propagates toward channel 2 and as the wax begins to re-solidify after the heater is turned off. The portion of the B-scan indicated by the bracket labeled '(i)' highlights the transition of the machinist wax from a solid to a liquid material. As evidenced by the signals seen in the B-scan, the region marked by the bracket has both the solid wax and liquid wax signals present at the same

moment in time. By 125 minutes, the signal is solely that of the liquid machinist wax. The black dashed line in Figure 4.50 marks the heater being turned off at 299 minutes.

Although the times at which some of the notable events occurred, such as melt and the heater being turned off, differ between the EcoSoya and the machinist wax tests, there are similarities in the B-scans for the two materials. The same Matlab code was used to generate the B-scans for both experiments, and the process for visually interpreting the results was the same. For example, the portions of the graph corresponding to the solid and liquid wax as well as the transition region and the point at which the heater was turned off in each of the experiments can all be determined from the B-scan plots.

4.3.5 Speed of Sound Calculations and Results

The speed of sound for the machinist wax data was calculated using Equation 4.4, where the speed of sound is the thickness of the wax divided by the time spent within the wax. Since the wall thickness was the same as that used in the EcoSoya experiment, the time the ultrasound wave spent within the walls was the same as that calculated in Equation 4.1, and thus, the time spent within the wax can be calculated as in Equation 4.2. Since the speed of sound calculations followed the same formulae as those described for the EcoSoya experiment, the focus of this section is on speed of sound plots for each channel as well as the comparison of the speed of sound obtained from channels 1 and 2.

4.3.5.1 Speed of Sound Results. The speed of sound for channel 1 is presented in Figure 4.51. This figure was generated using the same approach as in the EcoSoya experiment, but with a signal threshold of 30%. Notice the speed of sound plot provided

in Figure 4.51 has no points located between approximately 0 and 90 minutes during the test. The lack of points between 0 and 90 minutes was caused by the signal amplitude being less than the signal threshold in which case the TOF was saved as a ‘NAN’ in Matlab, where ‘NAN’ stands for ‘not a number’ and serves as an empty location within an array of numbers. The speed of sound results for channel 2 are presented in Figure 4.52, and this figure was generated using the same signal threshold and data analysis process as was performed for the EcoSoya wax data and analysis of channel 1 of the machinist wax data.

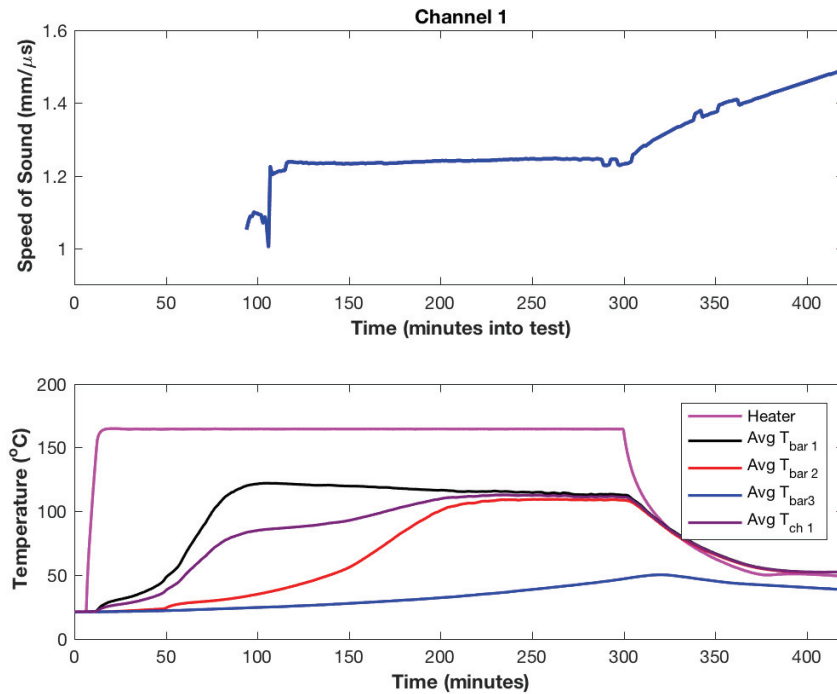


Figure 4.51 Speed of sound (top) and temperature as measured by thermocouples for data collected at channel 1, which is closest to the heater block.

The same lack of data points as was previously mentioned can also be seen in Figure 4.52. There was a lack of speed of sound points between 0 and approximately 250 minutes during the experiment as the ultrasound signal through the solid machinist wax

was below the signal threshold. The observations from Figures 4.51 and 4.52 indicated that the analysis approach might need to be changed slightly for the machinist wax. The first step was to identify what was happening to the ultrasound signal during the time period when no speed of sound points are available (due to the TOF being defined as a NAN).

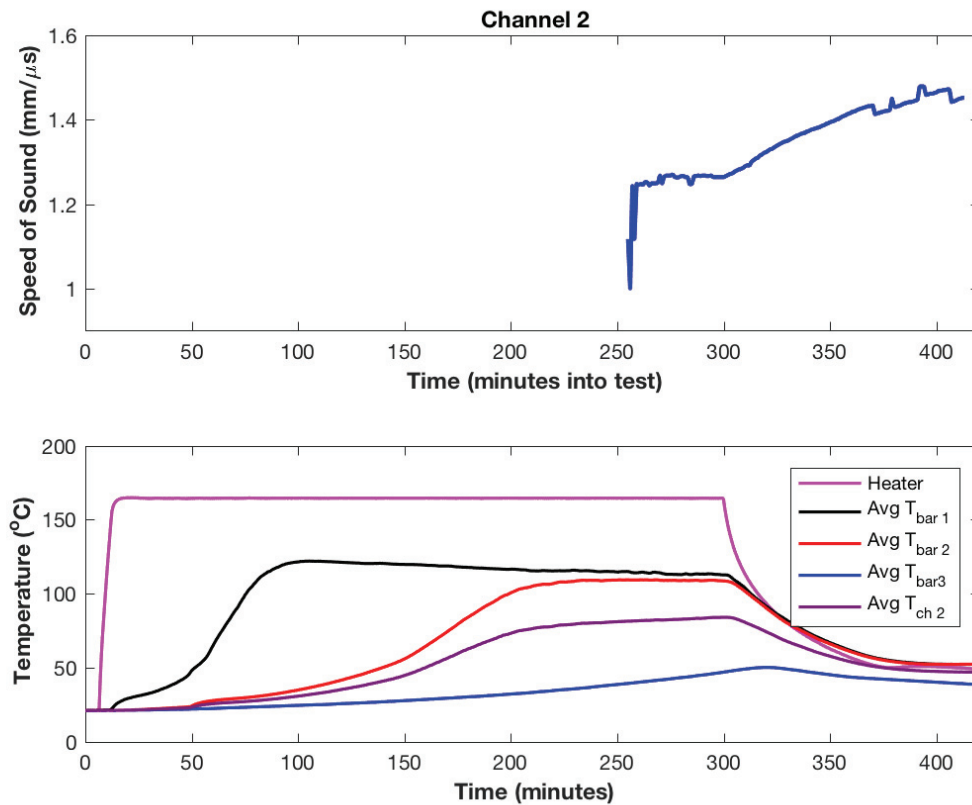


Figure 4.52 Speed of sound (top) and temperature as measured by thermocouples for data collected at channel 2, which is farthest from the heater block.

The A-scans presented in Figure 4.53 show the ultrasound signal and the changes in the identified TOF for channel 1 between minutes 27 and 38. Throughout this time period, the ultrasound signal is near the same amplitude level as the signal noise. Thus, deciphering between the ultrasound signal and the electrical noise is nearly impossible. Such a distinction between the signal and the noise cannot be simply determined via

threshold methods as both are at the same amplitude, which makes the signal indistinguishable from the rest of the A-scan via thresholding methods. The black dot indicating the signal threshold value in Figure 4.53 is the same as the threshold that was used during the EcoSoya wax analysis. Clearly, none of the A-scan images in Figure 4.53 have a signal amplitude near 30%, which was the threshold used for calculating the speed of sound values, but furthermore, only half of the A-scan in Figure 4.53 have signals that are at or above the 10% signal threshold indicated by the black dot. Again, with the signal amplitude near the same amplitude as the signal noise, the signal threshold method cannot distinguish between the signal and the noise.

Notice in Figures 4.53(a) and 4.53(c) the TOF has identified a point in the A-scan that meets the 10% threshold limit, but does not necessarily correspond to the ultrasound signal. Conversely, in minutes 29 and 38 the A-scan contained no points that were equal to or greater than the signal threshold of 10% signal intensity. From this observation, the author hypothesized that if a lower threshold were used in an effort to capture more data points corresponding to the ultrasound signal propagating through the solid wax, the program would be unable to distinguish between the noise and the ultrasound signal, and the resulting speed of sound plot would be chaotic as the TOF would be different A-scan to A-scan. Thus, the author chose to use a higher signal threshold, in this case 30%, to provide a cleaner speed of sound plot. Using the higher threshold value, there is no speed of sound information provided for the solid wax, which again shows the importance of using the B-scan image for data interpretation since there is evidence of the solid wax signal in the B-scan that is difficult to capture using the threshold method for identifying the TOF for the speed of sound calculations.

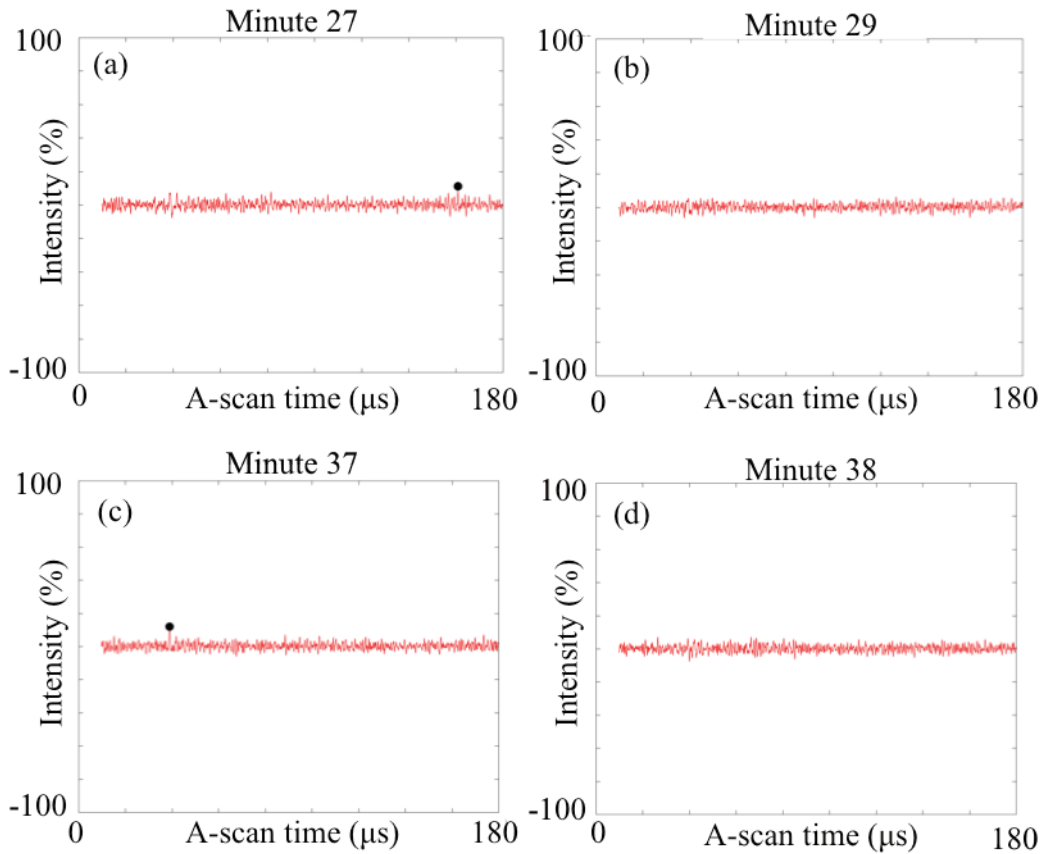


Figure 4.53 A-scans for the machinist wax along channel 1 at minutes (a) 27, (b) 29, (c) 37 and (d) 38.

Using a threshold of 30% signal intensity, the TOF was identified for the A-scans, and the speed of sound was calculated as previously described. The results for the speed of sound calculations for channels 1 and 2 using the 30% signal threshold are presented in Figure 4.54. While the machinist wax was solid, the signal amplitude was lower than the 30% signal threshold, and thus, no speed of sound calculations are available for the time period when the machinist wax was solid. Once the machinist wax melted, the difficulties in identifying TOF were removed, and a smooth speed of sound curve was obtained as seen in Figure 4.54.

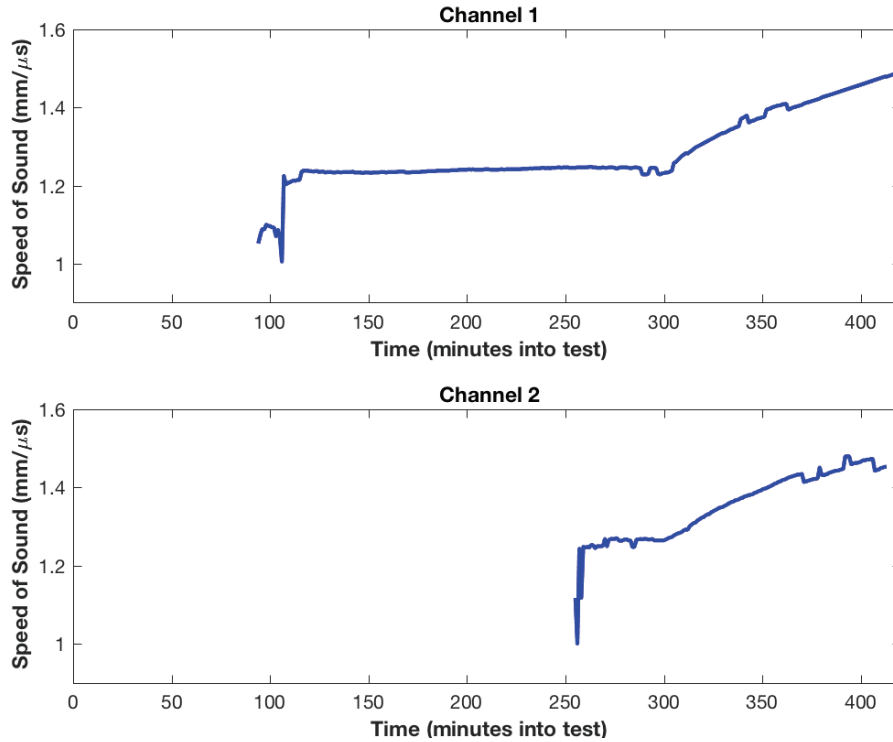


Figure 4.54 Speed of sound results for channel 1 (top) and channel 2 (bottom) when a 30% signal threshold was used to determine the TOF.

From the speed of sound plots presented in this section for the machinist wax, the following information may be ascertained. The machinist wax posed increased difficulty when trying to capture the speed of sound prior to melting the material. The same methods used for calculating the speed of sound for the EcoSoya wax were applied to the machinist wax, and although the equations did not change, the TOF measurements played a key role in the speed of sound plots containing regions with no speed of sound data points. The regions without data points in the speed of sound plots for the machinist wax corresponded to A-scans not having a signal above the threshold.

The transition from solid to liquid machinist wax can be determined from the speed of sound plots presented in Figure 4.51 and 4.52. Once the machinist wax melted, the smooth, continuous curve appeared in the speed of sound graph and corresponded to

the signal amplitude increasing above 30% and ultrasound wave propagating through the liquid machinist wax. After the heater was turned off, the wax began to cool, and the speed of sound began to increase.

4.3.5.2 Comparison of Speed of Sound Results for Machinist Wax. As in the EcoSoya wax experiments, the reciprocal channels were monitored for this machinist wax experiment. The speed of sound results for channels 1 and 1b are presented in Figure 4.55. Again, there was no TOF values obtained while the machinist wax was solid since the signal amplitude was not equal to or greater than the signal amplitude threshold. Once the machinist wax had melted (near 120 minutes), the results from channels 1 and 1b were indistinguishable from each other, and since the machinist wax was liquid, there were no longer any voids present in the material.

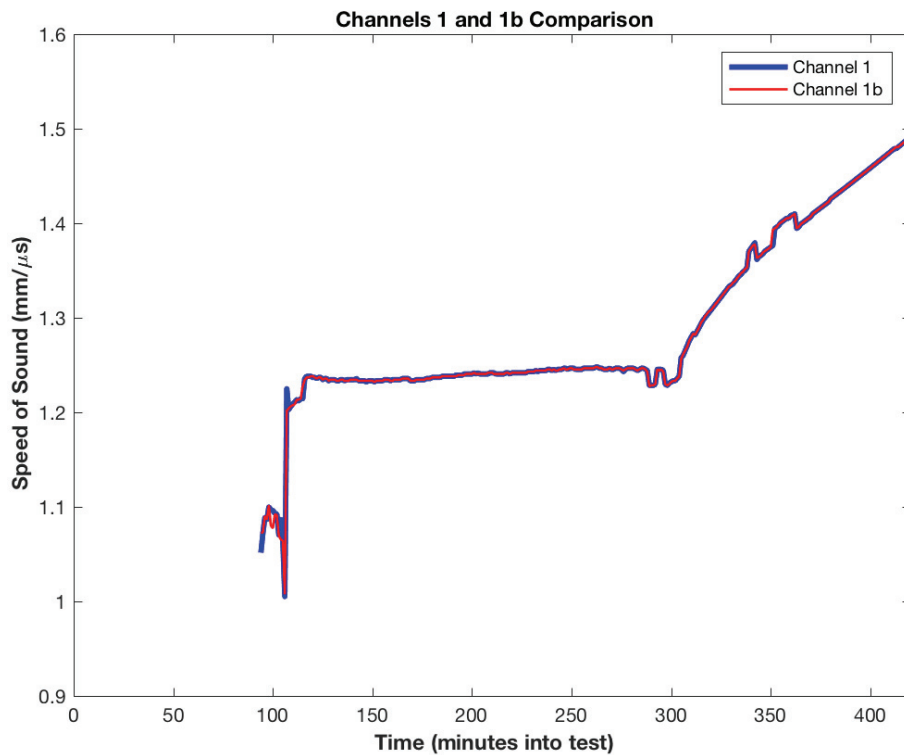


Figure 4.55 Comparison of the speed of sound results for channels 1 and 1b.

Although the speed of sound plots for the machinist wax did not provide details related to the solid wax portion of the experiment as compared to the speed of sound plots generated for the EcoSoya wax data, the speed of sound for channels 1 and 2 in the machinist wax experiment were compared to one another and provided some additional useful information as seen in Figure 4.56. The results obtained for channel 1 were plotted in blue whereas the results for channel 2 were plotted in red in Figure 4.56. The results in Figure 4.56 show the approximate time at which the machinist wax melted at channel 1 was 120 minutes whereas the approximate time at which the machinist wax melted at channel 2 was 260 minutes. It took the melt front 140 minutes to propagate the 41 millimeters from the center point of the probes in channel 1 to the center point of the probes in channel 2. This observation further supports the results obtained from the DSC testing regarding the high heat capacity associated with the machinist wax.

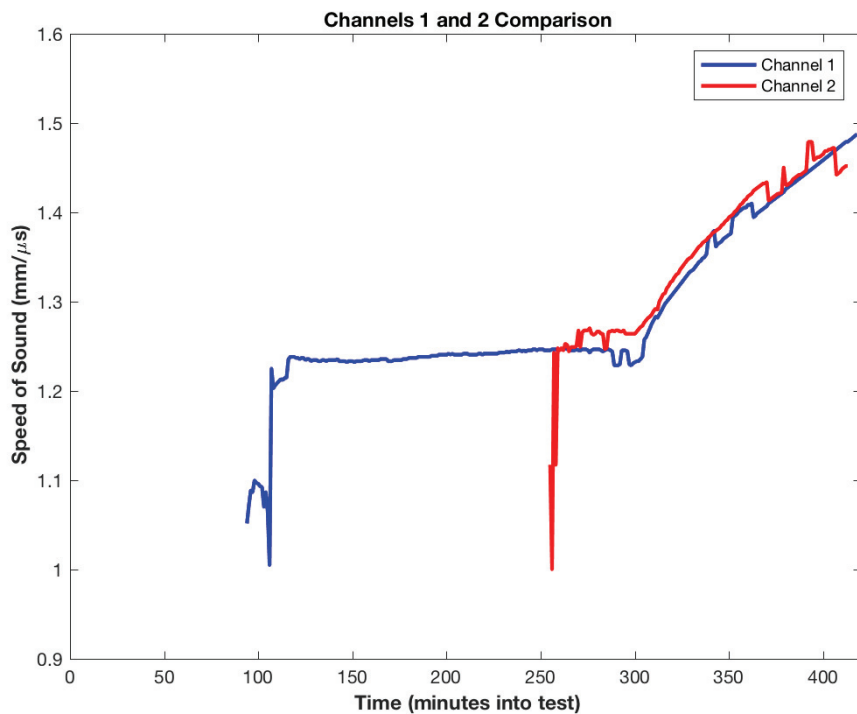


Figure 4.56 Comparison of the speed of sound results for channels 1 (closest to the heater block) and 2 (farthest from the heater block).

4.3.6 Temperature Corrections

As in the EcoSoya experiment, the temperature along the probe channel was estimated so a comparison between the speed of sound and temperature along the probe channel may be performed. The same temperature estimation technique used in section 4.2.5 was used for estimating the temperature along the probe channels in the machinist wax experiment. The graph of the temperatures as measured via the thermocouples in the experiment is presented in Figure 4.57. The heater block temperature, the average temperature along each thermocouple bar and the average temperature among all thermocouples located on thermocouple bars are represented in Figure 4.57.

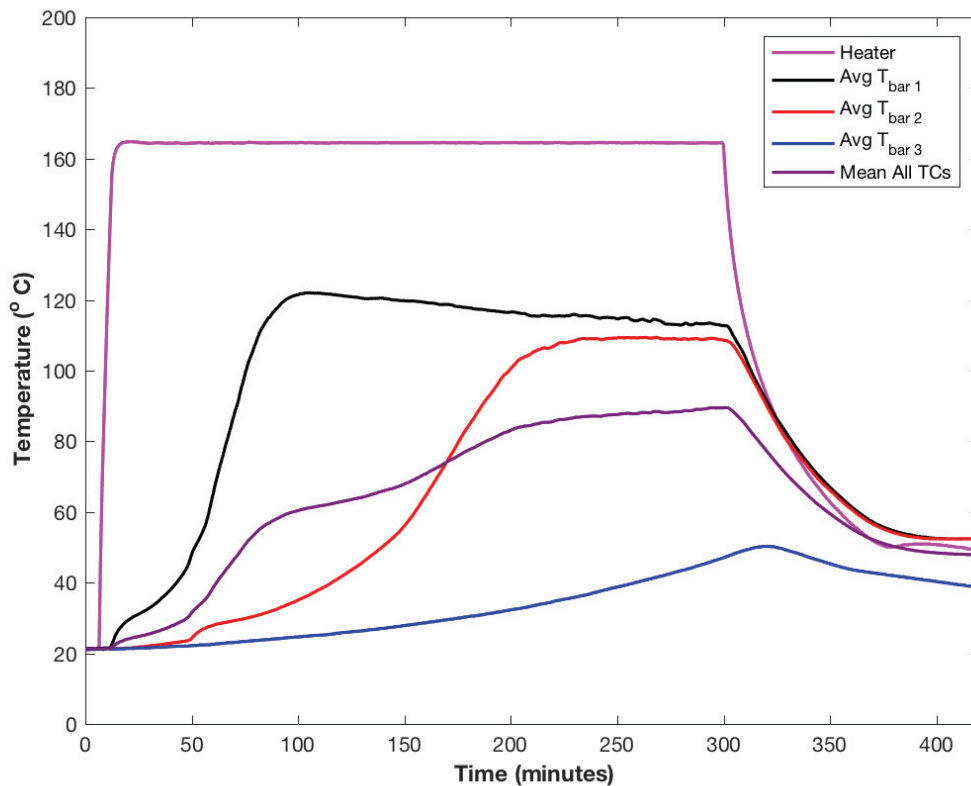


Figure 4.57 Temperature values as obtained from thermocouple measurements throughout the experiment.

The diagram presented in Figure 4.58 identifies the location of the thermocouple estimations along the probe channel along with their spacing relative to the remaining components within the experimental setup. The orange circles denote the actual thermocouples just as they were in the experimental setup diagrams presented earlier in

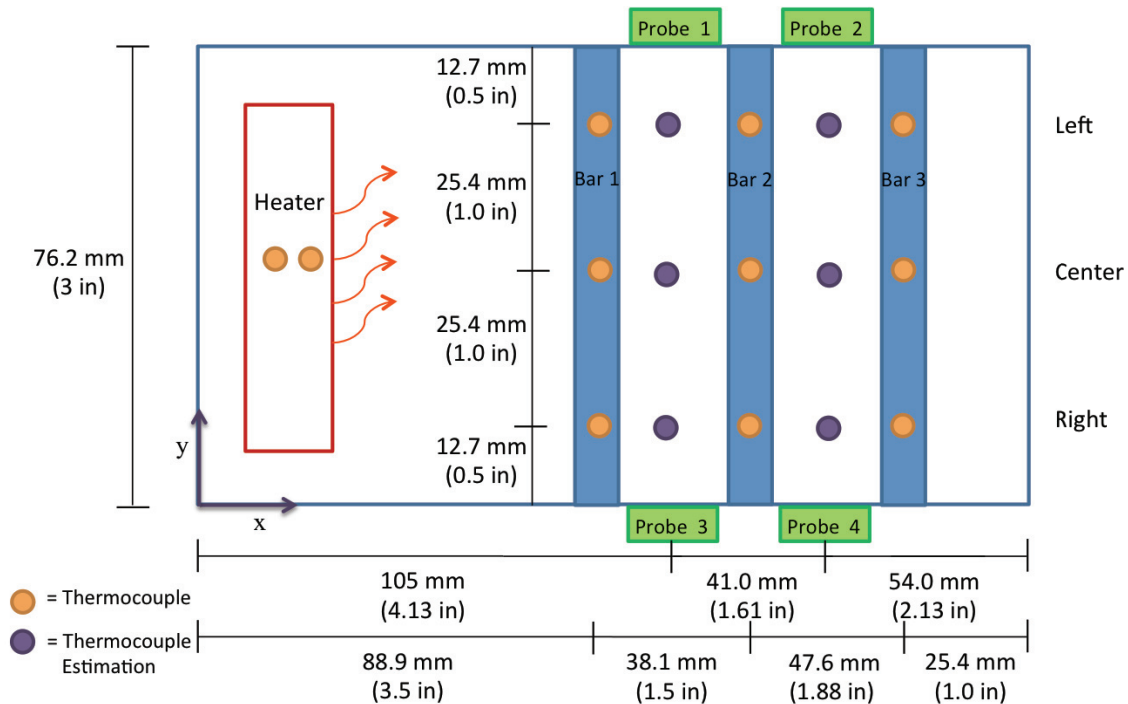


Figure 4.58 Diagram of the temperature estimation locations relative to the probe channels as well as the remaining components in the experimental setup

this chapter, and the purple circles denote the thermocouple estimations. Three thermocouple estimations were performed along the probe channel in an effort to mimic the thermocouple bars located on either side of the probe channel. Then, the average of the three thermocouples estimates along each probe channel was calculated. The results of the average thermocouple estimation at each probe channel 1 and probe channel 2 are presented in Figure 4.59.

The temperature estimation results were used for plotting the speed of sound versus temperature plots as will be described in the next section. However, recall from the one-dimensional heat transfer problem that was considered previously, the thermal conductivity of the material affects the temperature distribution along the x-axis, where the x-axis is defined as in Figure 4.58. After performing a literature search, the author

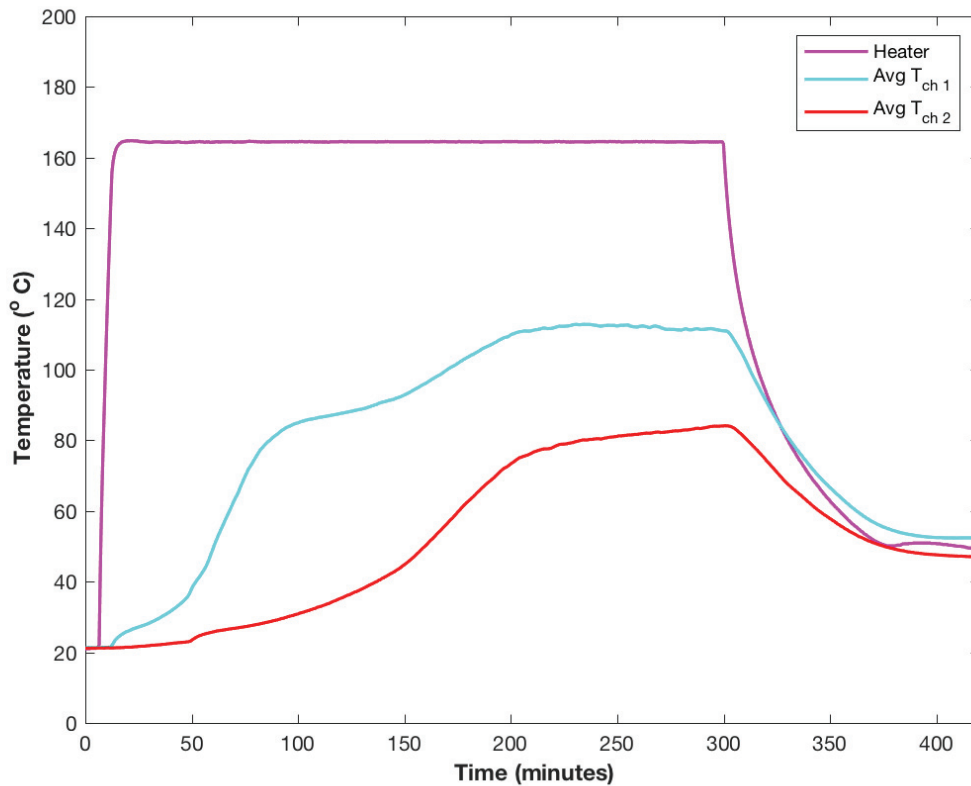


Figure 4.59 The average temperature estimates obtained for the ultrasound probe path at channels 1 and 2 in the experimental setup.

was unable to find published values for the thermal conductivity of the machinist wax; however, based on the results of the one-dimensional heat transfer problem for the EcoSoya wax, similar results would be expected for this experiment as well. Thus, the calculated temperature estimations were likely an overestimate of the actual temperature along the probe channels.

4.3.7 Correlation between Speed of Sound and Temperature

The results of the speed of sound versus temperature plots are presented in Figures 4.60 and 4.61 for channels 1 and 2, respectively. These graphs were created using the 30% signal intensity threshold. Thus, in the results presented for channel 1 in Figure 4.60, there is no speed of sound values associated with the solid wax portion of the experiment. The transition from solid to liquid machinist wax as determined from

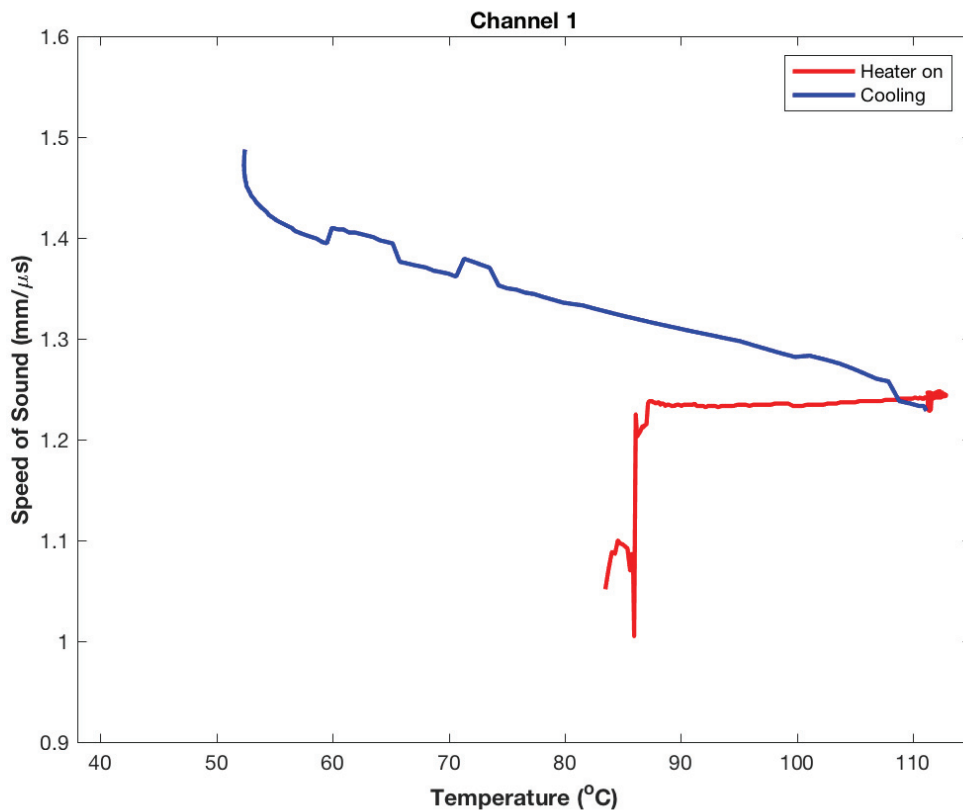


Figure 4.60 Speed of sound versus temperature plot for channel 1.

Figure 4.60 occurred at a temperature of about 87 °C, which is higher than the melt temperature range as identified by the DSC testing by approximately 21 °C. The large difference in melt temperature as determined from the speed of sound versus temperature plot and the DSC results was likely caused by the thermal conductivity of the machinist

wax as well as the material's high heat capacity. The machinist wax's high heat capacity means that the material is difficult to melt. As evidenced by the melt front taking 140 minutes to propagate from channel 1 to channel 2, the machinist wax along channel 1 was still solid when the material at the thermocouples on bar 1 had melted. The author knows the material along channel 1 was still solid at the time that the wax along thermocouple bar 1 was liquid because she monitored the entire test and watched the melt flow propagation across the box. Thus, the calculated temperature estimations are overestimations of the actual temperature along the probe channel, and future work could include identifying the thermal conductivity of the solid and liquid machinist wax for use in the one-dimensional heat transfer problem, which could potentially provide more accurate temperature estimations.

The speed of sound versus temperature results for channel 2 are presented in Figure 4.61. The interpretation of these results is similar to that provided for the channel 1 results; however, the liquid machinist wax along channel 2 did not get as warm as the liquid machinist wax along channel 1. The maximum estimated temperature of the liquid wax along channel 1 was about 112 °C, whereas the maximum estimated temperature of the liquid wax along channel 2 was about 85 °C. Since the machinist wax has a high heat capacity, the temperature gradient across the experimental setup was expected.

The speed of sound versus temperature results for channels 1 and 2 are compared in Figure 4.62. The portions of the experiments corresponding to the heater being on were plotted in the red and purple colors whereas the cooling portions of the experiments were plotted in the blue and green colors.

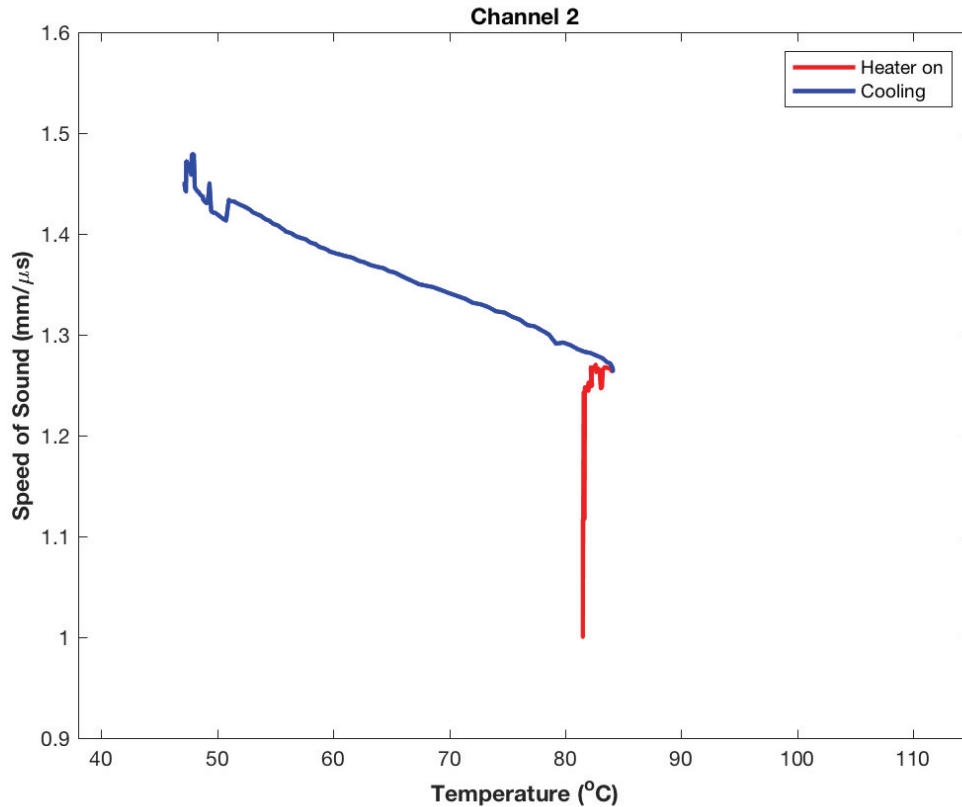


Figure 4.61 Speed of sound versus temperature plot for channel 2.

Since the temperature of the machinist wax along the two channels was drastically different (by almost 30 °C) when the heater was turned off, the cool-down portion of the speed of sound versus temperature graph was different for the machinist wax experiment than it was for the EcoSoya wax experiment. The results from channels 1 through 4 in the EcoSoya wax experiment nearly laid on top of one another whereas the results from the machinist wax experiment did not. Figure 4.63 presents the cool-down portion of the speed of sound versus temperature plot with a narrower vertical axis to highlight the similarities and differences for the results along channels 1 and 2. The results for channel 1 and channel 2 begin to converge with one another as the machinist wax cools, but once the temperature of the wax reaches approximately 55 °C, the slope of the speed of sound versus temperature line for both channel 1 and channel 2 increases in magnitude. From

55 °C until the end of the test, the results from the two channels diverge slightly from one another. The change in the slope of the cool-down curve corresponds to the onset of the re-solidification of the machinist wax. As determined from the DSC testing the temperature at which the material begins to re-solidify is 45 °C, which is 10 °C less than the estimated temperature of re-solidification as determined from the speed of sound versus temperature graph in Figure 4.63.

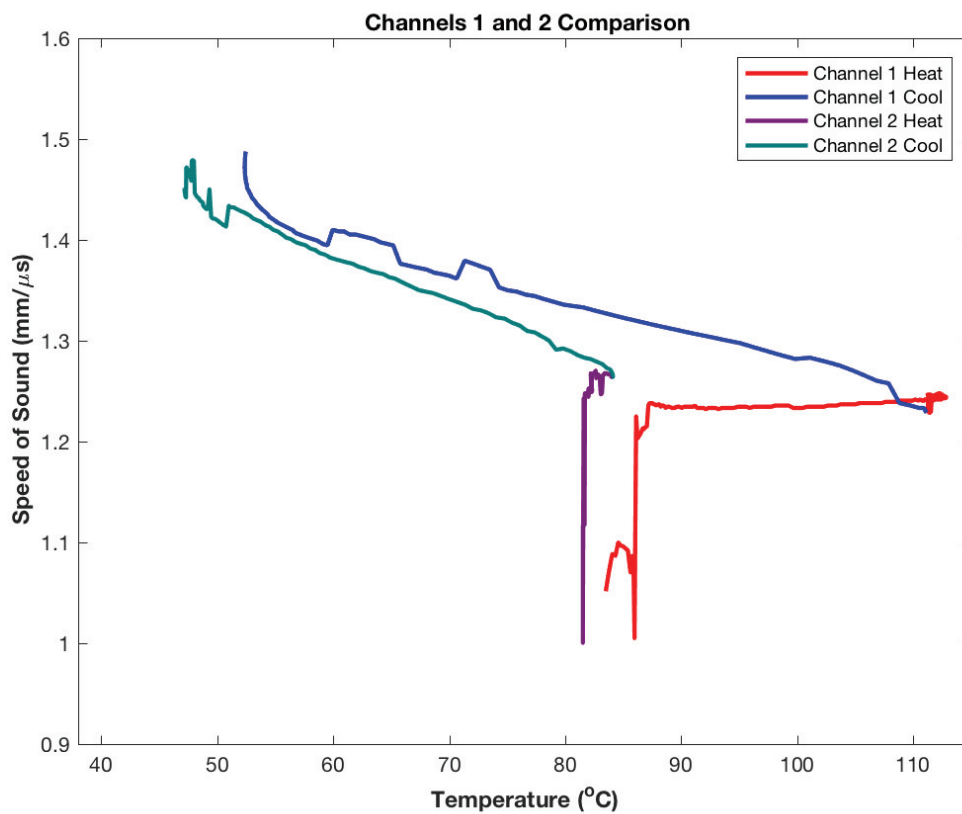


Figure 4.62 Comparison of the speed of sound versus temperature plot for channel 1 and channel 2. The red and purple lines represent the heater being on during each test whereas the blue and green lines correspond to the cooling portion of each experiment.

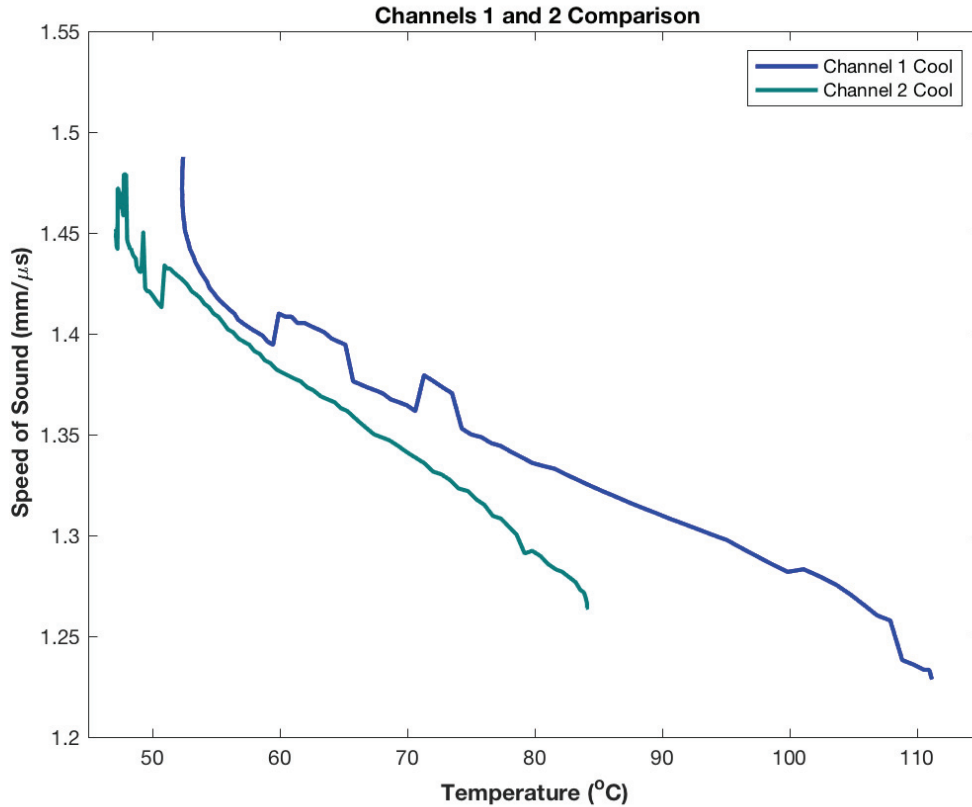


Figure 4.63 Comparison of the speed of sound versus temperature results for channels 1 and 2 as the machinist wax cools.

4.3.8 Fast Fourier Transform Analysis of the A-scan Measurements

A Fast Fourier Transform (FFT) of the A-scan signal was calculated for each A-scan collected throughout the experiment. A figure representative of the results obtained for when the machinist wax was solid is presented in Figure 4.64, and a figure representative of the results obtained after the machinist wax had melted is presented in Figure 4.65. The FFT results for the A-scan signal associated with the solid machinist

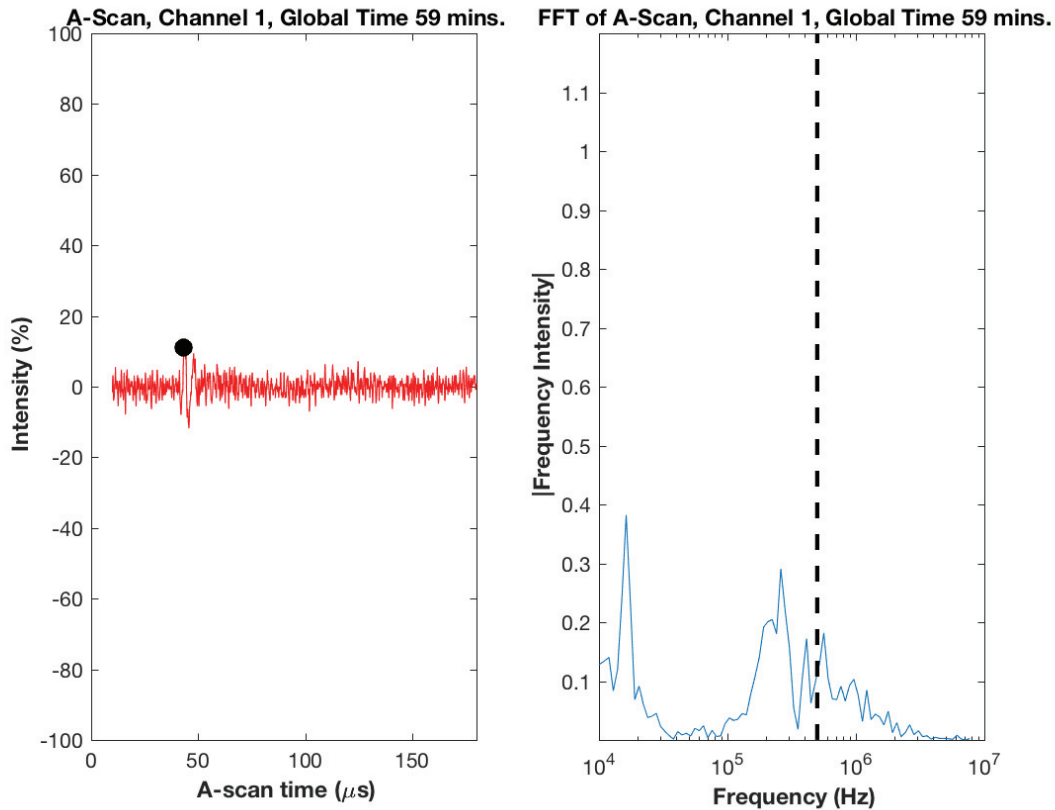


Figure 4.64 A-scan (left) and Fast Fourier Transform (right) results for solid machinist wax at 59 minutes into the test.

wax was dominated by the frequency of the signal noise, which was approximately 15 kHz instead of the 0.5 MHz operating frequency of the ultrasound probe. There was a local maximum in the FFT plot in Figure 4.64 near 0.2 MHz that corresponds to the ultrasound wave propagating through the machinist wax.

The FFT results presented in Figure 4.65 for the A-scan corresponding to the liquid machinist wax were dominated by the ultrasound wave propagating through the liquid machinist wax rather than by the signal noise. However, the presence of the signal noise can still be observed near the 10 kHz range. The peak frequency intensity in the FFT plot occurs at approximately 0.35 MHz, which is near the 0.5 MHz operating frequency of the ultrasound probe.

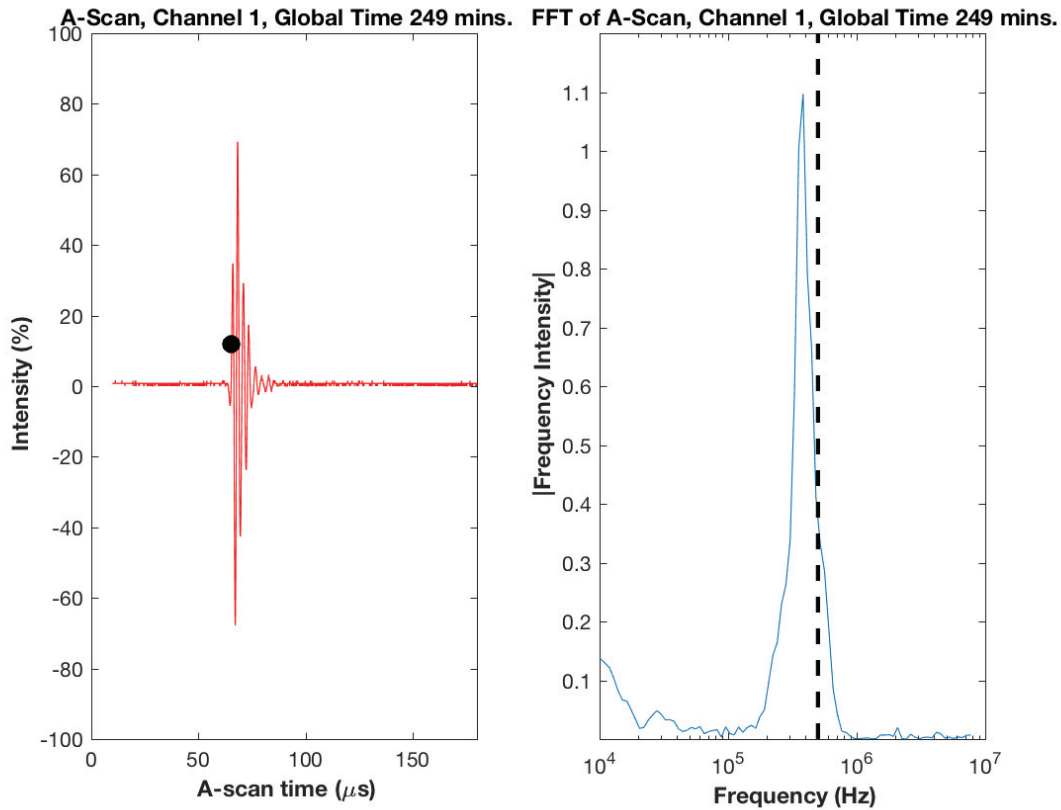


Figure 4.65 A-scan (left) and Fast Fourier Transform (right) results for liquid machinist wax at 249 minutes into the test.

The focus of the FFT plots obtained for the machinist wax experiment is the identification of the frequencies associated with the signal noise, and the frequency intensity of the signal noise relative to the frequency intensity of the ultrasound wave signal. Since the A-scan signal is different for the solid machinist wax as compared to that for the solid EcoSoya wax, the FFT was able to assist the inspector in confirming that the A-scan for the solid machinist wax contained signal noise in addition to the ultrasound signal. For example, the FFT presented in Figure 4.64 for the solid machinist wax indicated the frequency intensity of the signal noise was higher than the frequency intensity of the ultrasound signal. The opposite is true for the liquid machinist wax as the ultrasound wave signal has a higher frequency intensity than the signal noise.

4.4 Machinist Wax Experimental Results – Small Steel Box

Another experiment was performed using the machinist wax in a different experimental setup configuration. Since the machinist wax was a difficult material to melt, the box used in this experiment was manufactured using steel instead of acrylic. In general, metals are better thermal conductors than plastics, and the idea behind this experimental setup was to use the box to assist with heating the material. Also, this experimental setup prevents the user from being able to monitor the melt front propagation from the side of the container and limits the viewing of the experiment to the top of the container.

This experiment was performed by Mr. Moore and Ms. Nelson at Sandia National Laboratories, and they kindly sent the experimental data to the author for post-processing and analysis. The results from this experiment will be compared with those from the machinist wax experiment performed at Baylor University.

4.4.1 Machinist Wax Experimental Setup – Small Steel Box

A digital drawing of the experimental setup used for this test is presented in Figure 4.66 and was provided by Sandia National Laboratories. The box was manufactured using 1/16th inch steel, and the interior dimensions of the box were 3”x5”x4”. The ultrasound probes were identical to the ones used in the experiments described in sections 4.2 and 4.3. The ultrasound probes labeled 1 and 3 were placed 38.1 millimeters (1.5 inches) from the edge of the wall, meaning the centerline of the ultrasound probe was located along the centerline of the 76.2 millimeters (3 inches) wide box wall. Similarly, ultrasound probes 2 and 4 were each placed along the centerline of

the 127 millimeters (5 inches) long wall. Each of the ultrasound probes were adhered to the box using Loctite Super Gel adhesive as in the previous experimental configurations.

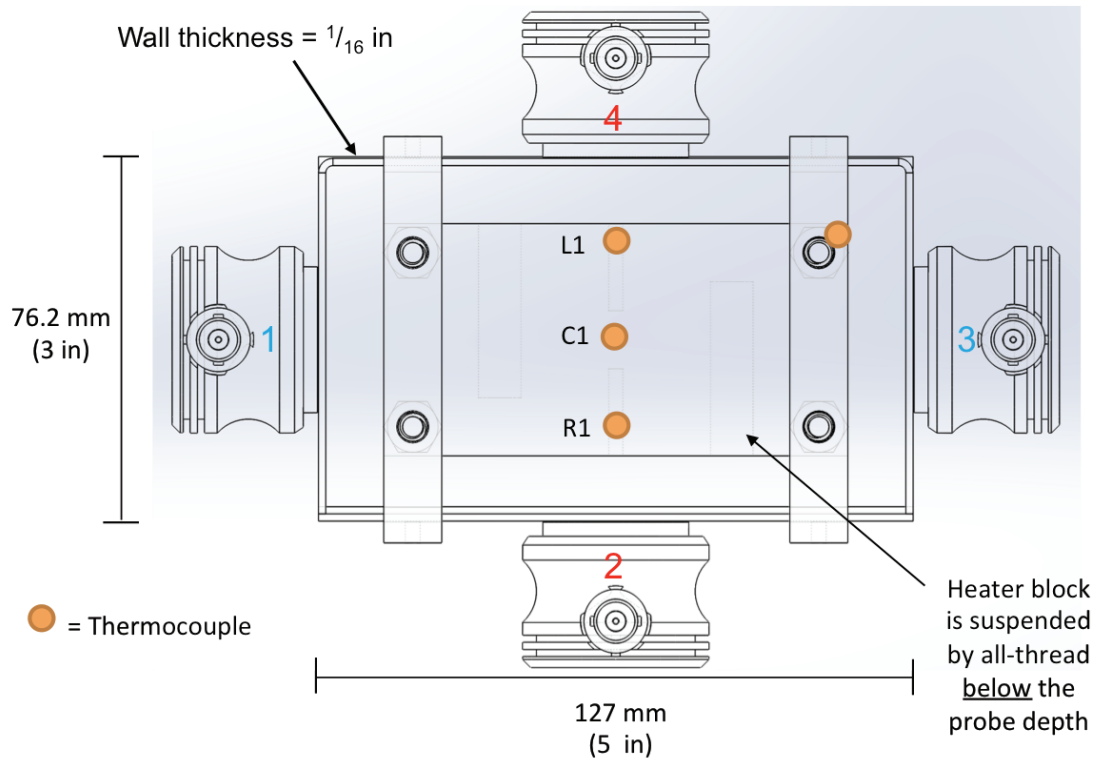


Figure 4.66 Top view of the experimental setup for the machinist wax experiment in the steel box. The digital drawing was provided by Sandia National Laboratories.

Four thermocouples were used for monitoring and recording the temperature data throughout the experiment. One of the thermocouples was located directly on top of the heater block, and this thermocouple is shown in the upper right corner of Figure 4.66. The remaining three thermocouples were placed in the direct line of sight of the ultrasound probes. These three thermocouples located in the center of the box had a smaller diameter than those used in the previous experiments and were acoustically transparent to the ultrasound probes meaning they did not interfere with the wave

propagation across the width of the box. Thus, no temperature corrections were necessary for determining the temperature along the probe channel.

A three-dimensional diagram of the box is presented in Figure 4.67 with the ultrasound wave propagation paths indicated by the red and blue lines. The heater was located near the bottom of the steel box and was suspended by threaded rods that were attached to the same type of aluminum bars that held thermocouples in prior experiments. As indicated in the diagram provided in Figure 4.68, the heater was placed at a depth below the ultrasound probes to avoid interfering with the ultrasound wave propagation throughout the experiment.

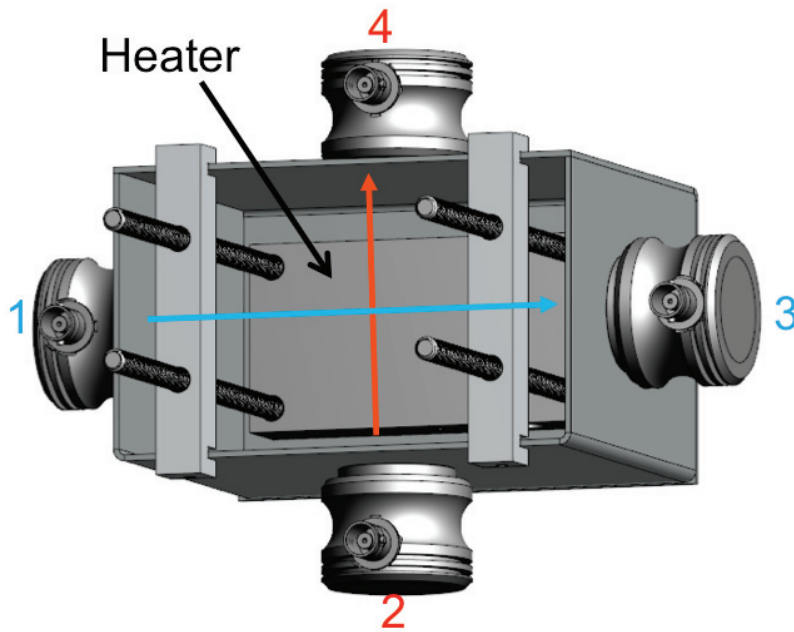


Figure 4.67 Three-dimensional representation of the steel box experimental setup used for this experiment. The digital drawing was provided by Sandia National Laboratories.

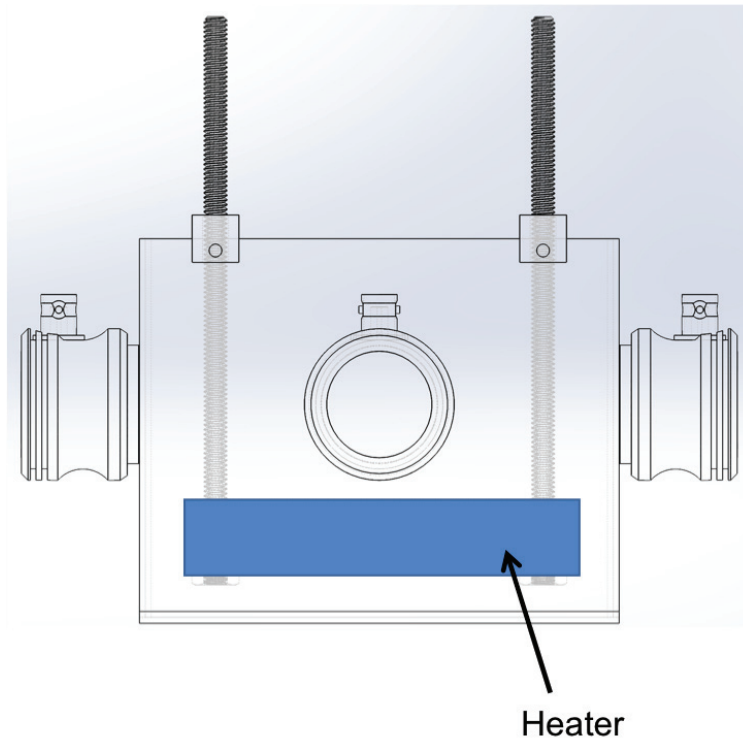


Figure 4.68 Side view diagram of the experiment, which highlights the location of the heater relative to the ultrasound probes. The digital drawing was provided by Sandia National Laboratories.

The channel diagram for this experiment is shown in Figure 4.69. Channels 1 and 2 are labeled in Figure 4.69 where channel 1 consists of probe 1 transmitting the incident ultrasound wave and probe 3 receiving the signal once it has propagated across the length of the box. Channel 2 consists of probe 2 transmitting the incident ultrasound wave and probe 4 receiving the signal once the wave has propagated across the width of the box. Unlike the previous experiments, the data from the reciprocal channels was not collected. For example, data was collected for ultrasound probe 2 transmitting the incident ultrasound wave while ultrasound probe 4 received the signal after it propagated across the width of the box, but the case for ultrasound probe 4 transmitting the ultrasound wave and probe 2 receiving the transmitted signal was not considered in this experiment.

Results from the prior tests presented in sections 4.2 and 4.3 indicated that the results obtained from reciprocal channels matched well with the results for the original channel. The focus of the present experiment is on the ultrasound data obtained for wave propagation across the narrow portion of the box as well as the ultrasound data obtained for wave propagation across the long portion of the box.

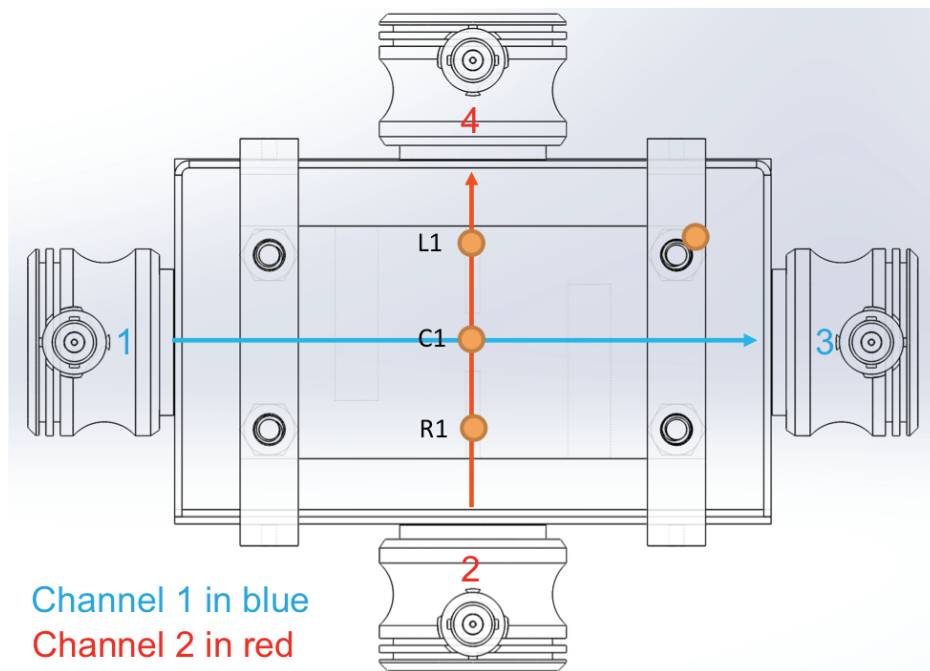


Figure 4.69 Channel listing for the ultrasound probes used in the machinist wax experiment with the steel box. The digital drawing was provided by Sandia National Laboratories.

A photograph of the experimental setup is provided in Figure 4.70. In this image, the heater was turned on, and the machinist wax was beginning to melt by the heater. The melted wax began propagating upward along the all-thread and began to flow across the top surface of the machinist wax. The placement of the thermocouples is highlighted in Figure 4.70, and as seen in the figure, the melted machinist wax moved across the surface

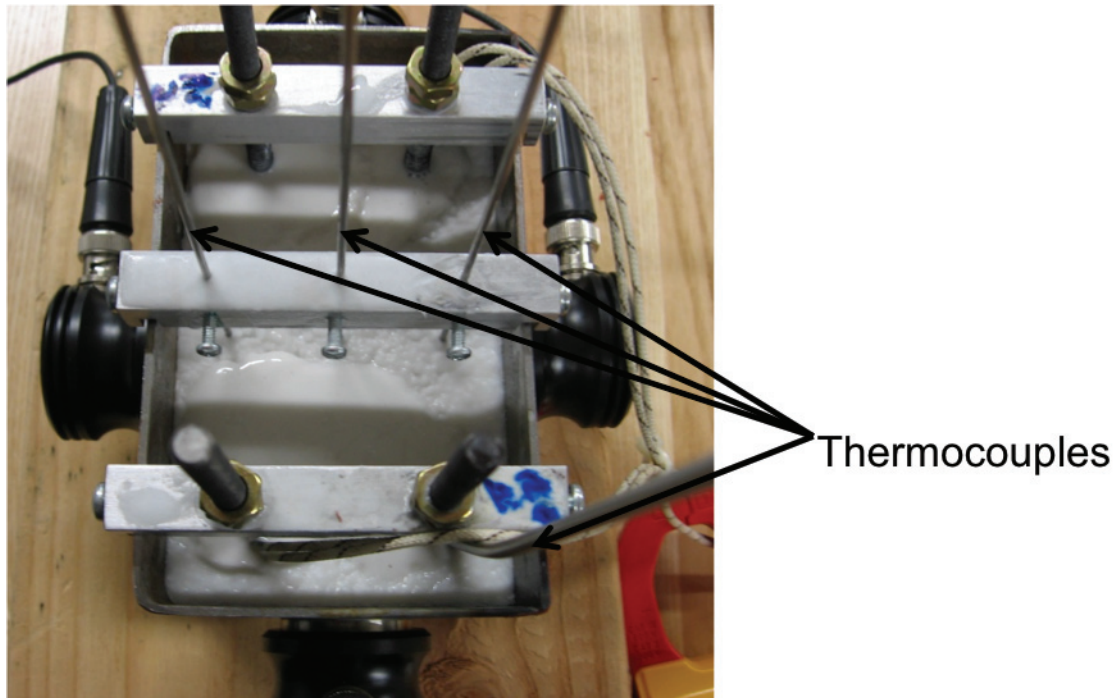


Figure 4.70 Photograph taken of the experimental setup. The melted wax is propagating upward along the all-thread and across the top surface of the wax. This photograph was provided by Sandia National Laboratories

toward the thermocouples located in the middle of the box. Considering the experimental setup included a larger heater, the thermocouples were located above the heater, and heat rises, the temperatures measured throughout this experiment were higher than those measured in previous experiments.

4.4.2 A-scan Measurements

A-scans representative of the signal propagating through solid machinist wax and through liquid machinist wax along channel 2 are presented in Figures 4.71 and 4.72. The A-scan results are presented for channel 2 since channel 2 had the ultrasound wave propagate through the same thickness of machinist wax as the experiment performed at Baylor University. The A-scan signal for the solid machinist wax was considerably different than any of the A-scans presented for the solid materials thus far. Unlike the A-

scan obtained for the solid machinist wax in the experiment performed with the acrylic box, the A-scan obtained for the solid wax during the experiment performed with the steel box has strong signal amplitude. However, the shape of the signal does not correspond to the wave propagating through the wax material. Instead, a quick calculation using the speed of sound equation (Eq 4.3) confirmed that the A-scan signal

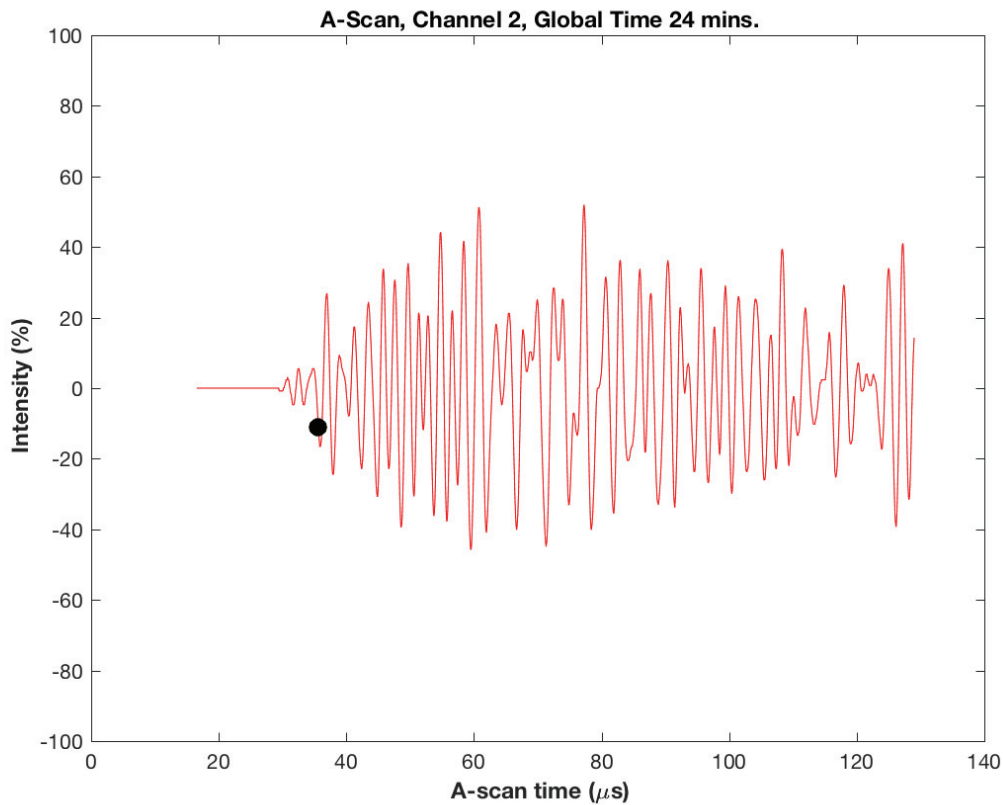


Figure 4.71 A-scan for the solid machinist wax at 24 minutes into the experiment.

captured during the time period before the machinist wax melted actually corresponded to the wave propagating along the surface of the steel box. This topic will be further discussed in section 4.4.3.

An A-scan that corresponds to the liquid machinist wax along channel 2 is provided in Figure 4.72. The A-scan for the liquid machinist wax is similar to the A-scan

obtained for liquid wax in the machinist wax experiment with the acrylic box. Thus, the A-scan results were affected by the material selection for manufacturing the box because the portion of the ultrasound wave that propagated through the wax lost so much of its signal strength (likely due to the porosity and attenuative nature of the machinist wax) that that portion of the signal was overpowered by the signal propagating along the box wall, which did not lose much of its signal strength. Then, as the wax melted, the porosity of the material decreased and the ultrasound wave did not lose as much of its signal strength as it propagated across the width of the box.

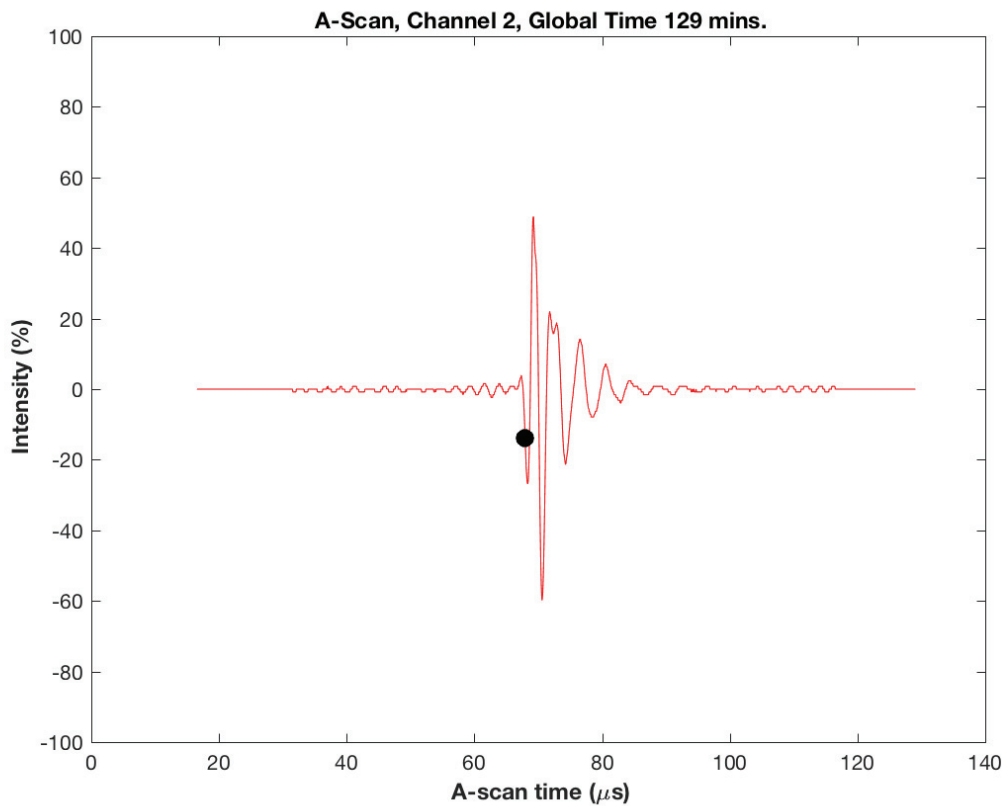


Figure 4.72 A-scan for the liquid machinist wax at 129 minutes into the experiment.

4.4.3 B-Scan Results

The B-scan plot for channel 1 is presented in Figure 4.73 with further explanations and specific features highlighted in Figure 4.74, and the B-scan plot for channel 2 is presented in Figure 4.75. Throughout the first approximately 70 minutes of the experiment and from 280 minutes to the end of the experiment, the A-scan and B-scan are dominated by the portion of the ultrasound wave propagating along the steel wall rather than through the wax as highlighted by sections (i) and (ii) in Figure 4.74,

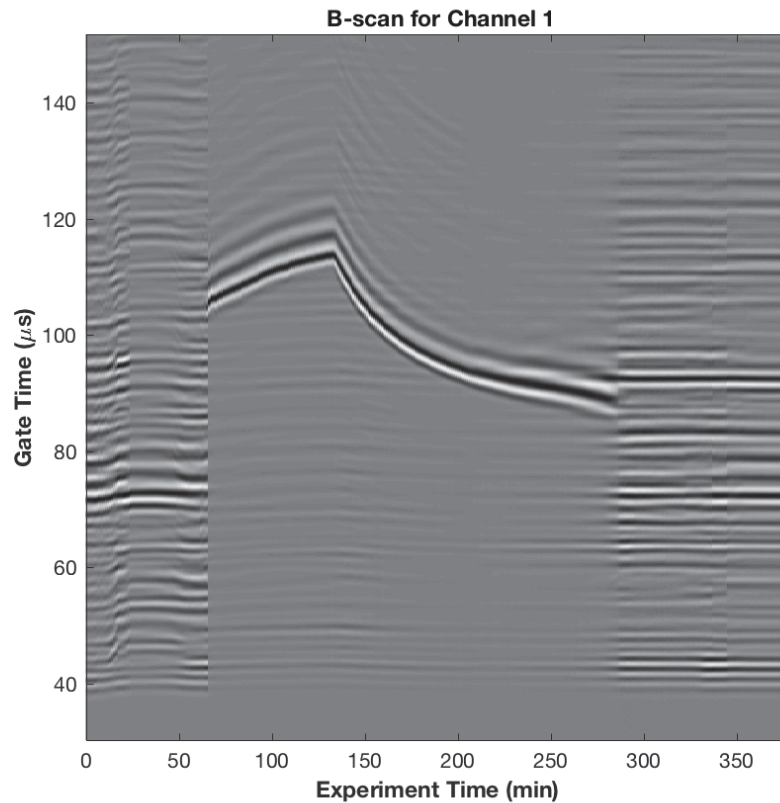


Figure 4.73 B-scan for channel 1

respectively. The data in-between 70 minutes and 280 minutes corresponds to liquid machinist wax, and once the heater was turned off at 135 minutes (denoted by the dashed black line in Figure 4.74), the liquid machinist wax began to re-solidify. This same

analysis also applies to the interpretation of the B-scan for channel 2 as seen in Figure 4.75. For the purposes of focusing of the data related to the machinist wax rather than propagating along the box wall, the remainder of the discussion about the machinist wax experiment with the steel box will no longer include the data from the first 70 minutes of the experiment or from 280 minutes to the end of the experiment.

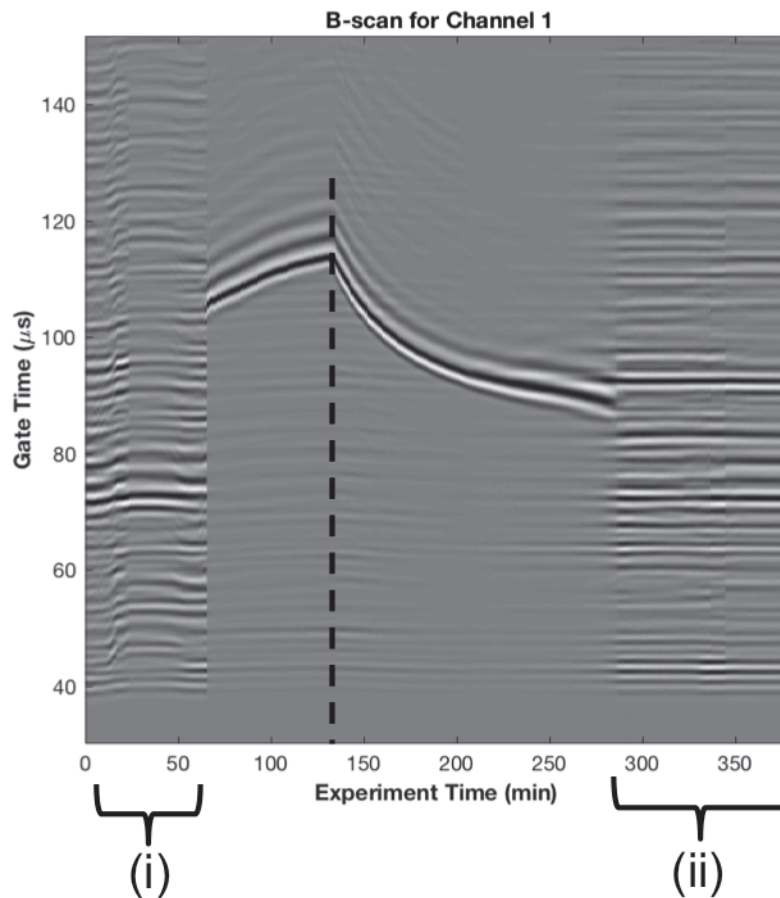


Figure 4.74 Explaining the B-scan for channel 1 by highlighting important features

4.4.4 Speed of Sound Calculations and Results

The speed of sound of the machinist wax was calculated using the same equation and Matlab program as what was used during the EcoSoya data analysis. Since the wall thickness was one-sixteenth of an inch instead of one-quarter of an inch and the wall was

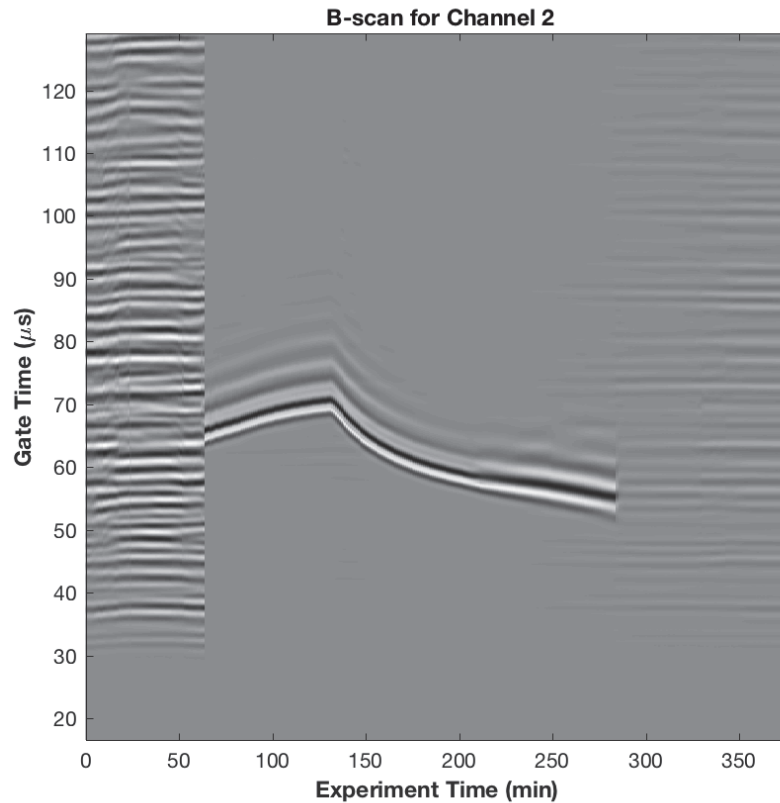


Figure 4.75 B-scan for channel 2

a different material than in each of the prior tests, the time required for the ultrasound wave to propagate through the thickness of the steel wall was calculated using equation 4.1. Then, the time the ultrasound wave spent propagating through the machinist wax was determined using equation 4.2, and finally, the speed of sound for the machinist wax was calculated using equation 4.4. The results of the speed of sound calculations for channels 1 and 2 and the comparison between channels 1 and 2 will be discussed in the following two subsections.

4.4.4.1 Speed of sound results for small steel box experiment. The results from calculating the speed of sound for the machinist wax using the same signal threshold (10% signal intensity) as for the EcoSoya wax are presented in Figures 4.76 and 4.77 for

channels 1 and 2, respectively. The results in Figure 4.77 for channel 2 indicate a smooth curve throughout the time period of interest in the experiment. The results for the speed of sound calculations along channel 1 contained step discontinuities. Figure 4.78 compares the speed of sound graph with the B-scan and provides a visual explanation of how the step changes in the speed of sound graph were obtained. The signal highlighted

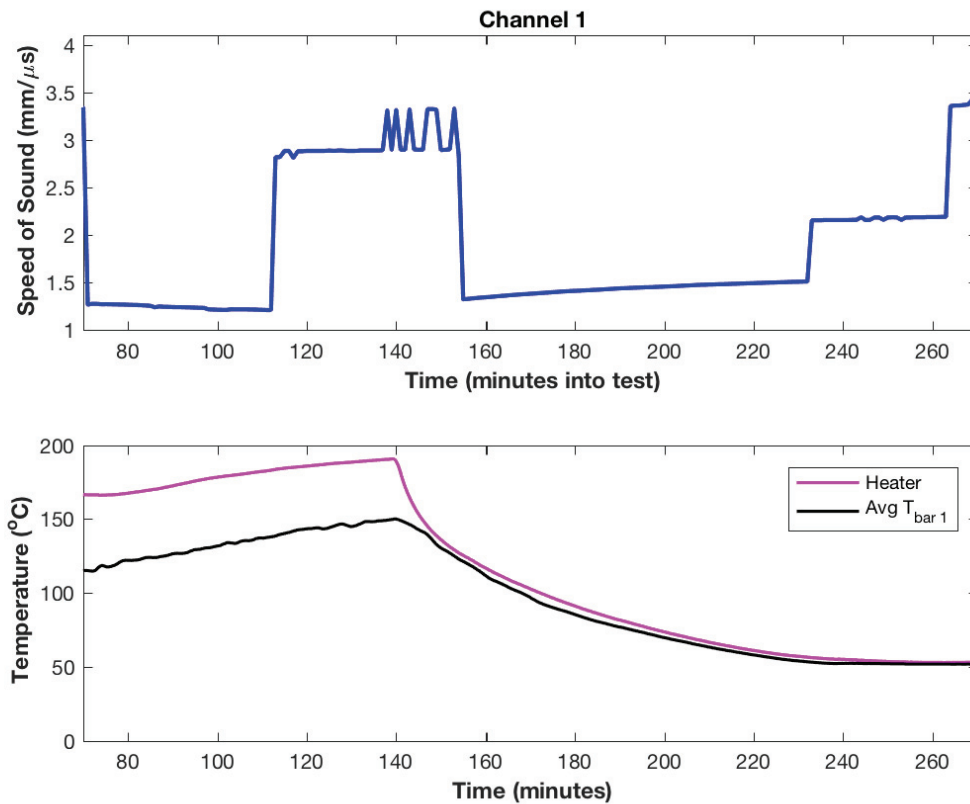


Figure 4.76 Speed of sound calculations for channel 1

in the black oval on the B-scan corresponds to the TOF that was used while calculating the speed of sound at channel 1 over that same time period. This signal corresponded to the wave propagating along the box wall, and since the signal intensity threshold was at 10%, if the wall signal should increase above that threshold, which it did, then that will be the time location used for identifying the TOF. This TOF issue appears to only affect

channel 1, so to address this issue, a 20% signal intensity threshold value will be used when evaluating the signal at channel 1. The results obtained for channel 1 using the higher signal intensity threshold value are presented in Figure 4.79. Since the plot no longer requires such a large vertical axis, the speed of sound versus time plots were re-plotted for both channel 1 and channel 2 in Figures 4.79 and 4.80, respectively.

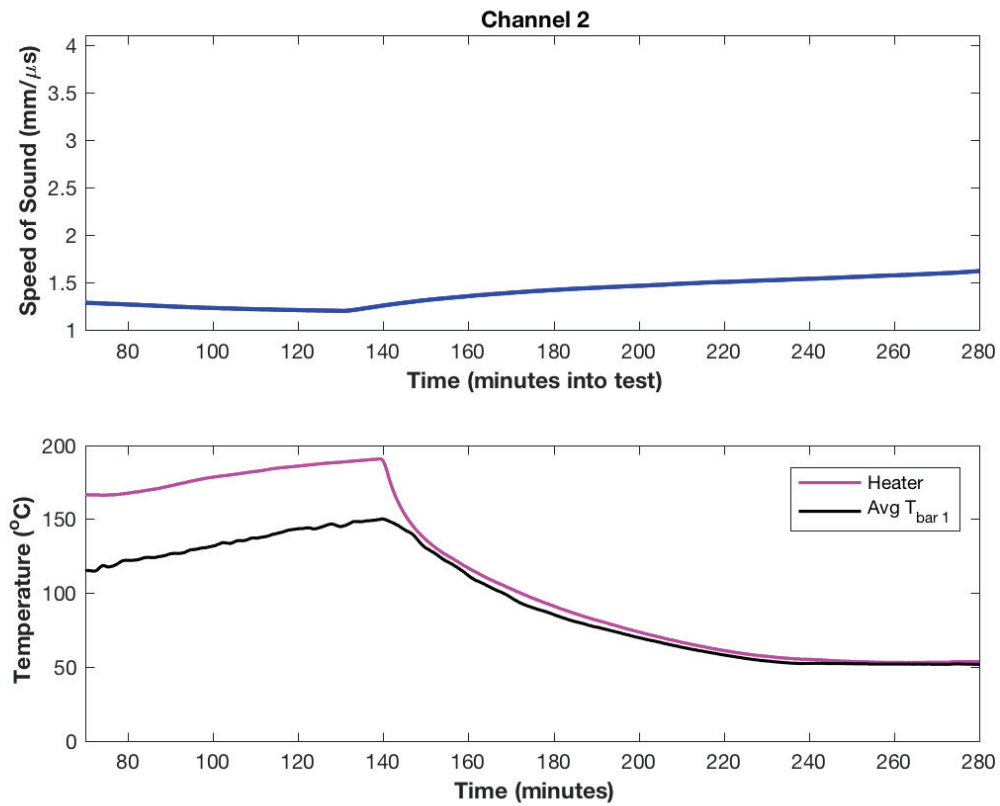


Figure 4.77 Speed of sound calculations for channel 2

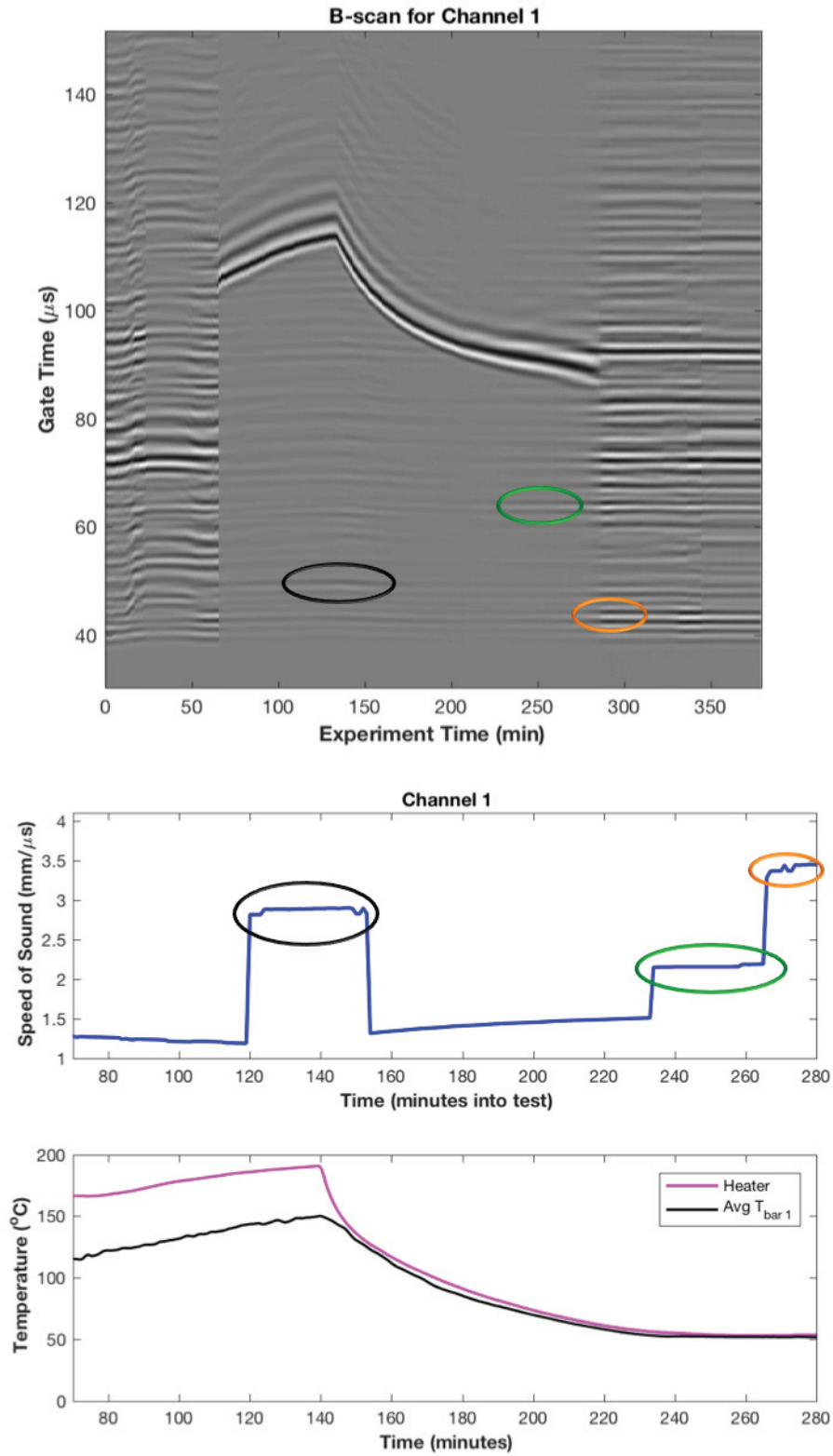


Figure 4.78 Explaining the discontinuities in the speed of sound graph (bottom) by comparing it with the B-scan (top).

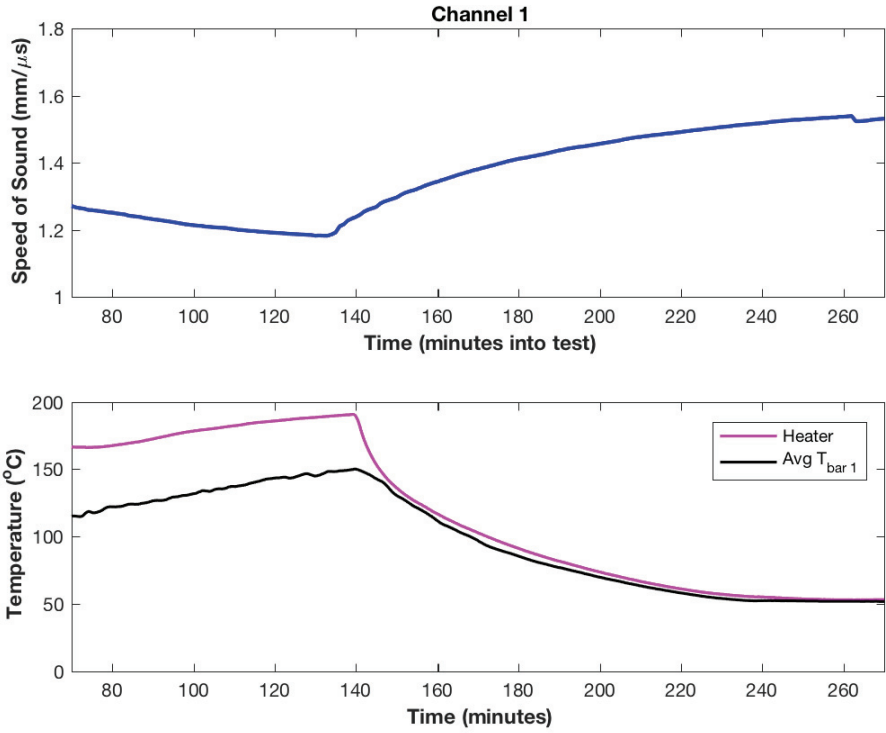


Figure 4.79 The speed of sound versus time plot (top) and temperature versus time plot (bottom) for channel 1 using a higher signal intensity threshold

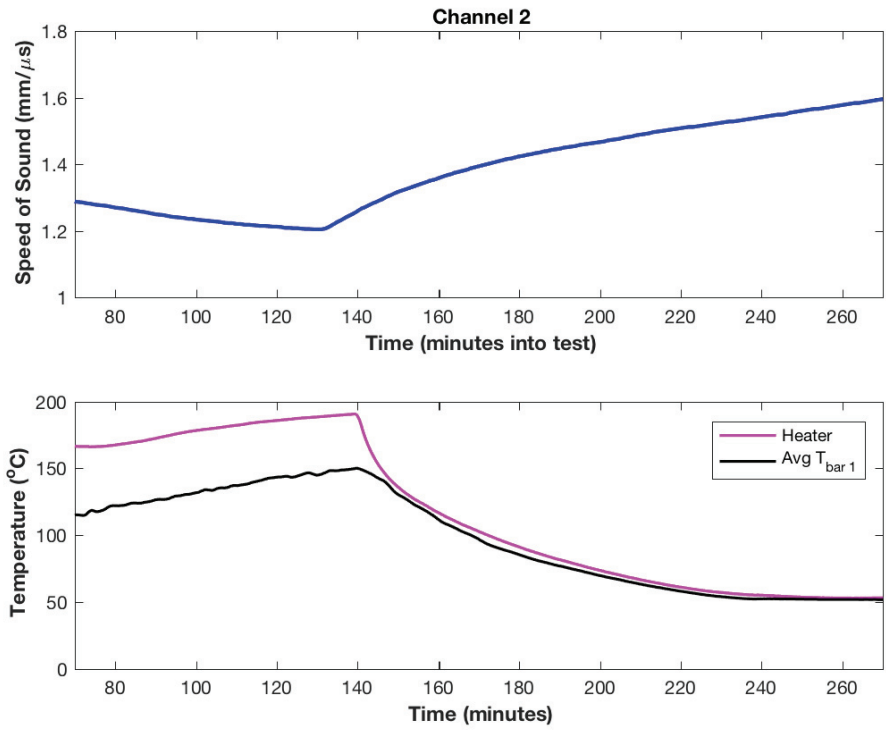


Figure 4.80 Speed of sound versus time plot (top) and temperature versus time plot (bottom) for channel 2 with the modified vertical axis

4.4.4.2 *Comparison of the speed of sound results.* The calculated speed of sound measurements for channels 1 and 2 are compared with one another in Figure 4.81. The results for channels 1 and 2 are very similar to one another with the percent difference in the speed of sound measurements being less than 2% throughout the experiment with the exception being in the last 10 minutes of the test as seen on the horizontal axis.

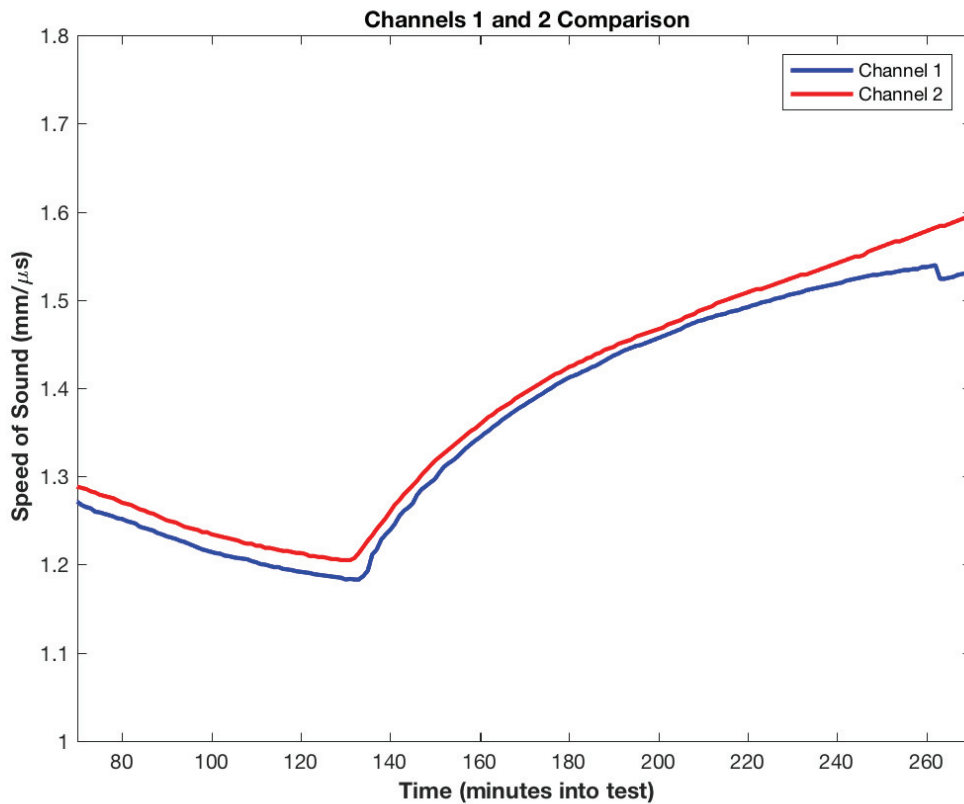


Figure 4.81 Comparison between the speed of sound for channels 1 and 2.

4.4.5 *Correlation between Speed of Sound and Temperature*

The speed of sound versus temperature plots for channels 1 and 2 of this experiment are presented in Figures 4.82 and 4.83. The red portion of the curve corresponds to the heater being on whereas the blue portion of the curve corresponds to the heater being off and the wax cooling. Recall from the discussion of the B-scan plots

in section 4.4.3 that the portion of the ultrasound data presented in figures subsequent to that section consists of data only from 70 minutes to 270 minutes during the experiment. Thus, in Figure 4.82 the start of the heating portion of the curve shows the temperature of the wax was already about 112 °C, and the melting temperature of the machinist wax cannot be determined from the graph. When the heater was turned off, the wax was approximately 145 °C, which is considerably warmer than the maximum temperature obtained using the acrylic box experimental setup at Baylor where the maximum temperature attained during that experiment was approximately 115 °C.

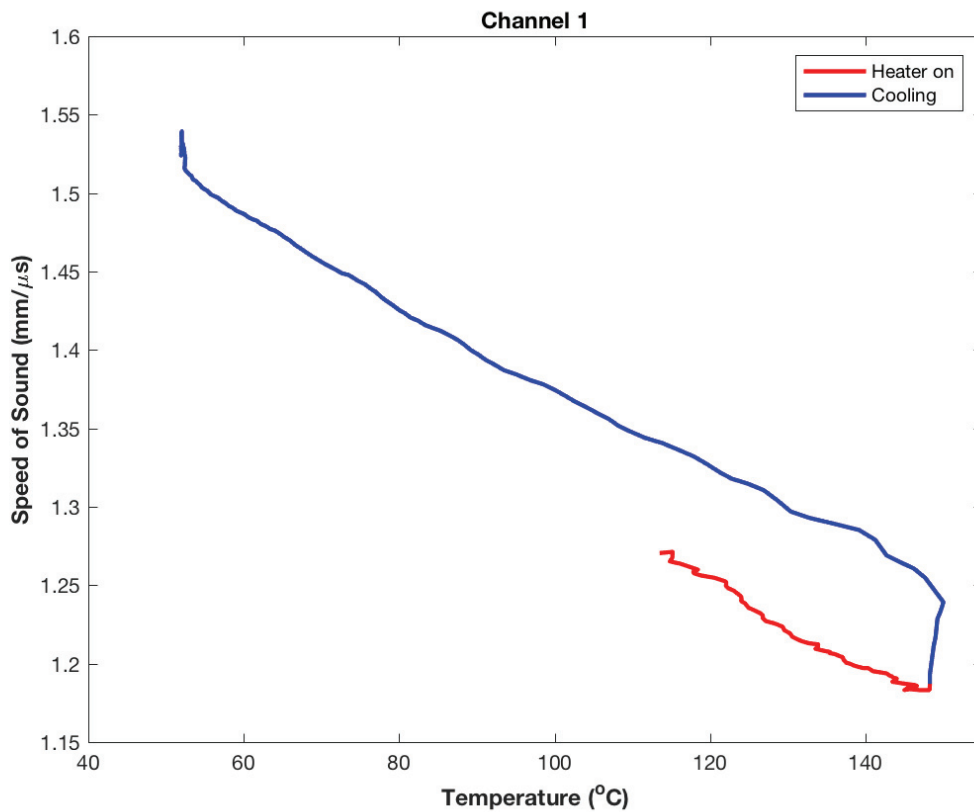


Figure 4.82 The speed of sound versus temperature plot for channel 1. The red curve corresponds to the heater being on whereas the blue curve represents the heater being turned off and the machinist wax cooling.

The speed of sound versus temperature results obtained for channels 1 and 2 exhibit similar trends, and at approximately 50 °C, the slope of the line in both figures changes drastically to an almost infinite slope. For further comparison purposes, the results for channels 1 and 2 were plotted on the same graph in Figure 4.84. The portions of the graph corresponding to the heater being on are shown in red and purple whereas the cooling portions of the curves are plotted in blue and green. The results obtained for these two channels are nearly identical to one another with one of the channels appearing to have been a vertical translation of the other channel's results. The calculations were

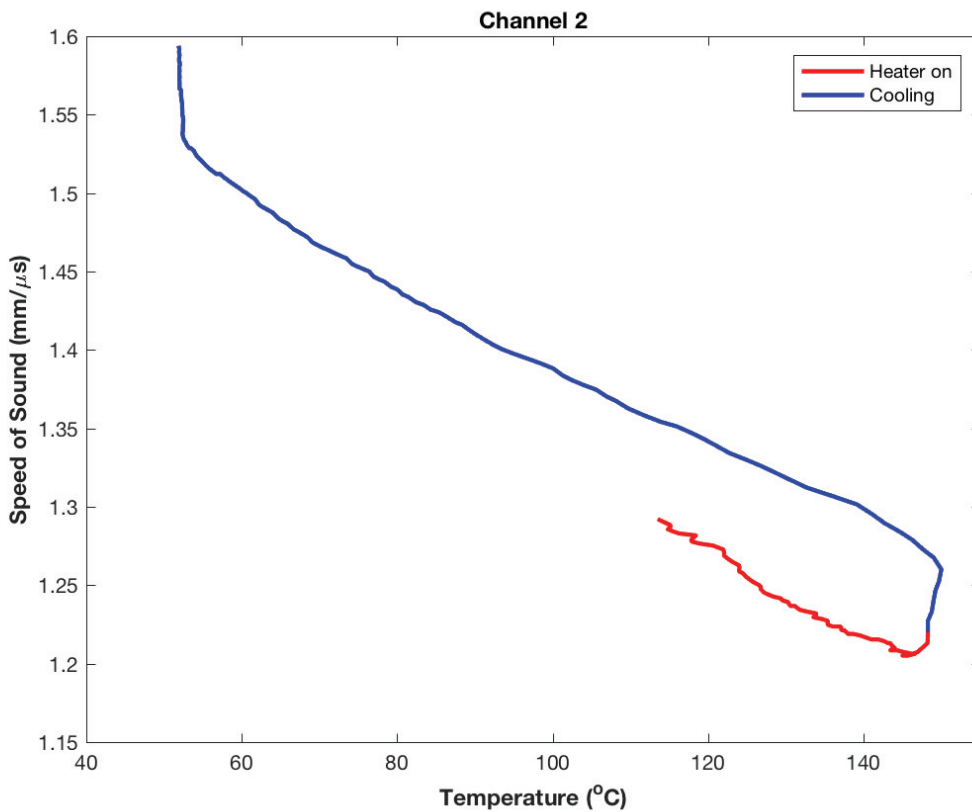


Figure 4.83 The speed of sound versus temperature plot for channel 2. The red curve corresponds to the heater being on whereas the blue curve represents the heater being turned off and the machinist wax cooling.

performed using the dimensions of the box as provided in the manufacturing drawings. The author thought there might have been a chance that the actual box turned out to have slightly different dimensions than in the drawing. After performing a short study in Matlab that investigated the effect of small changes in the box width, the author found that by increasing the channel 1 width by 1 millimeter or decreasing the channel 2 width by 1 millimeter, the results actually did lie on top of one another as seen in Figure 4.85.

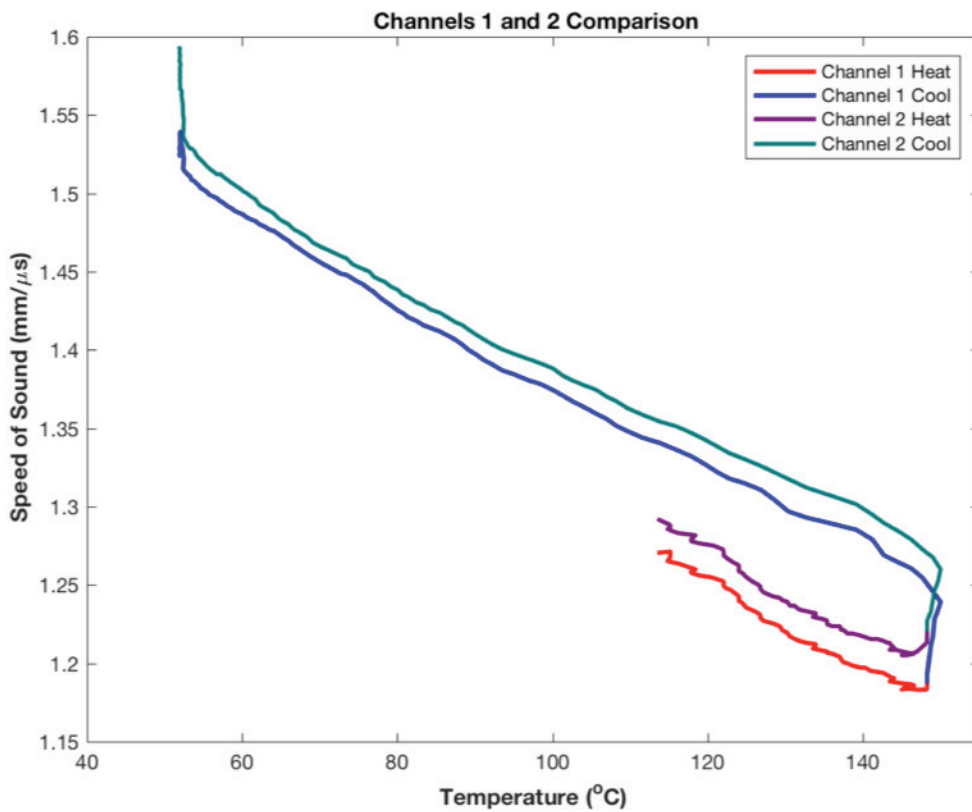


Figure 4.84 Comparison of the speed of sound versus temperature plots for channels 1 and 2

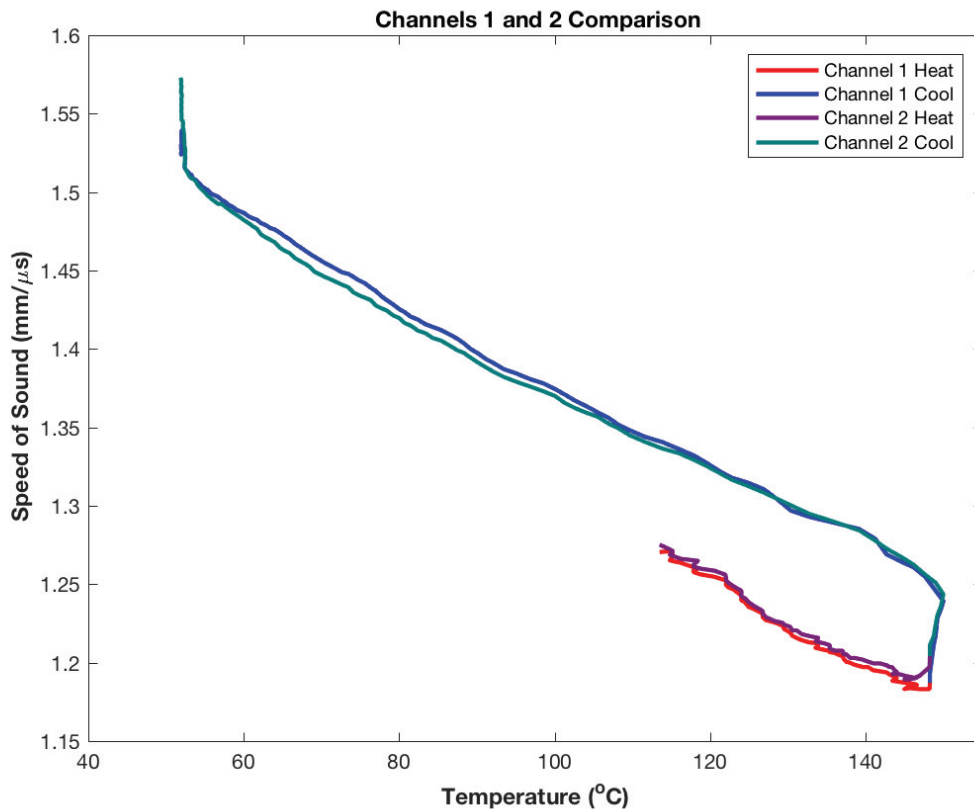


Figure 4.85 Comparison of the speed of sound versus temperature plots for channels 1 and 2 where the box width across channel 2 was decreased by 1 millimeter.

A comparison of the results obtained across all of the machinist wax experiments was performed, and the results are provided in Figure 4.86. Two of the experiments were performed at Baylor University using the acrylic box experimental setup while the third experiment was performed using the steel box experimental setup at Sandia National Laboratories. The test corresponding to the experiment performed with the steel box can clearly be identified by its high temperature measurements. The slope of the cooling portion of each of the three experiments appears to be the same, and each of the three experiments show a change in slope near 50 °C in the cooling portion of the experiment. The heating portion of the experiment cannot be compared between the acrylic box setup

and the steel box setup except to say the A-scan signal in the steel box setup is dominated by the ultrasound wave propagating along the box wall rather than through the thickness of the wax during the heating portion of the experiment. Both of the experiments performed with the acrylic box show the transition from solid to liquid wax occurring at nearly the same temperature, even though this temperature was an overestimation of the temperature along the probe channel as discussed in section 4.3.7.

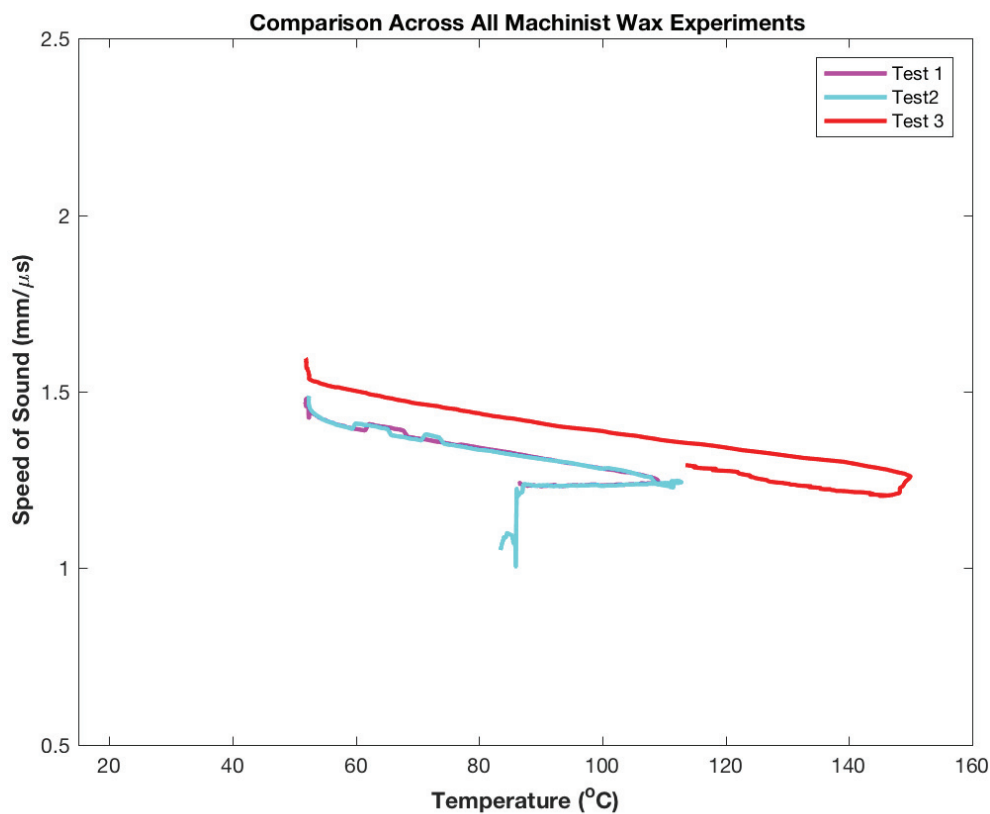


Figure 4.86 Comparison of the speed of sound versus temperature results for channel 1 in the experiments performed at Baylor University and channel 2 in the experiment performed at Sandia National Laboratories.

4.4.6 Fast Fourier Transform Analysis of the A-scan Measurements

The Fast Fourier Transform for a signal during the heating of the machinist wax and during the liquid machinist wax portion of the experiment are presented in Figures

4.87 and 4.88, respectively. The A-scan signal in Figure 4.87 and its corresponding FFT plot are dominated by the ultrasound wave propagating along the box wall rather than through the machinist wax. The peak frequency intensity in the FFT plot occurs at the operating frequency of the probe, which is to be expected since the ultrasound wave does not experience much attenuation when traveling through the metal. The lower frequency intensities ranging from approximately 0.2-0.4 MHz correspond to the ultrasound signal propagating through the machinist wax. This observation is confirmed by the analysis of the FFT plot in Figure 4.88, which corresponds to the liquid machinist wax. The peak

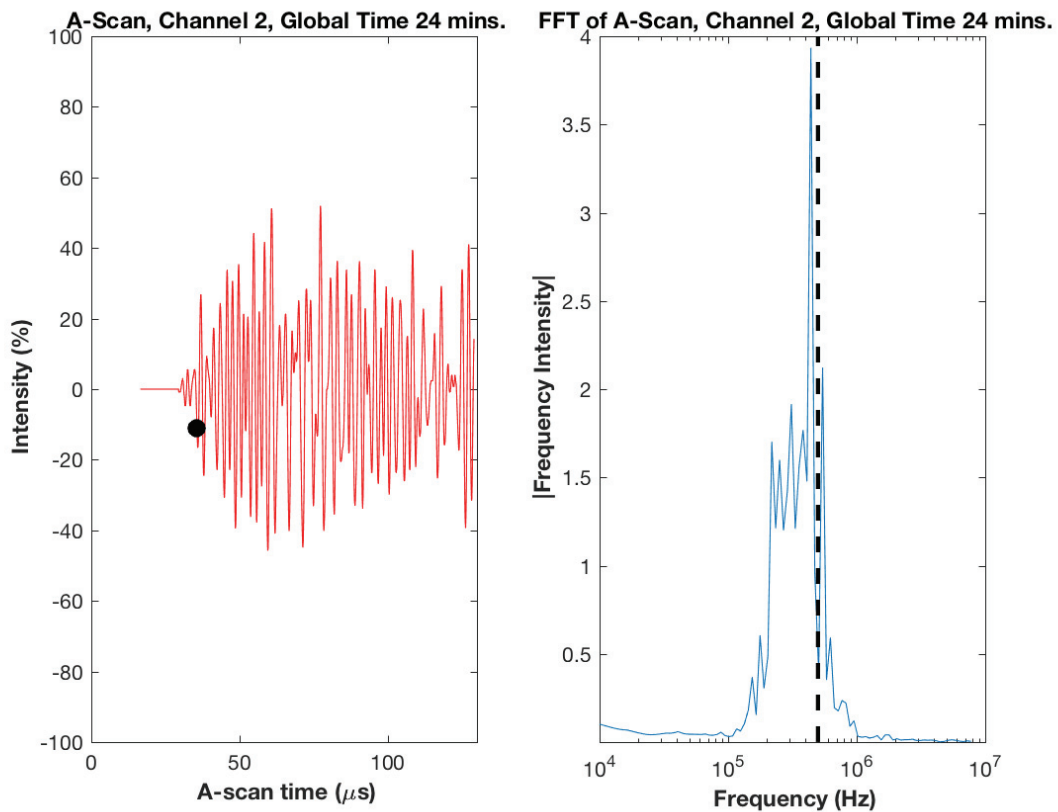


Figure 4.87 A-scan (left) and Fast Fourier Transform (right) results for solid machine wax at 24 minutes into the test.

frequency intensity no longer occurs at the operating frequency of the probe (0.5 MHz), but rather, the peak frequency intensity occurs near 0.2 MHz with local maxima occurring within the range of 0.3-0.5 MHz.

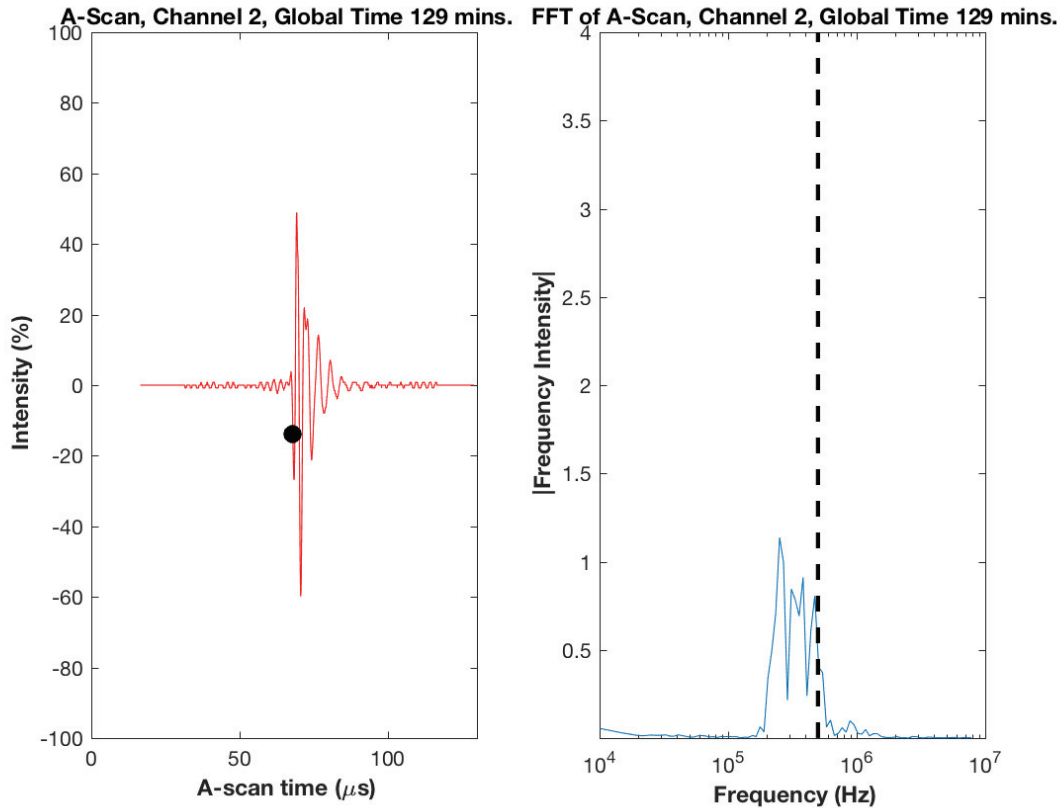


Figure 4.88 A-scan (left) and Fast Fourier Transform (right) results for liquid machine wax at 129 minutes into the test.

4.5 Conclusions and Future Work

The purpose of the experiments presented in this chapter was to develop an ultrasound through transmission technique for identifying the phase of a material and to start correlating the ultrasound results to the temperature of the material. Future work will involve identifying the reliability of the temperatures as determined from the ultrasound data. The proposed non-invasive and non-destructive ultrasound technique could be

applied to the food and drink industry where the temperature of different ingredients and fluids must be monitored for recipe and food health purposes as well as in the oil and gas industry where the curing of the cement used for creating tie-backs could be monitored.

The goal of the present section is to summarize the findings from the different experiments presented throughout this chapter and to identify areas where future work may be performed. The experiments performed in this study considered two different wax materials, two different placements of the heater relative to the ultrasound probes, and three different experimental setup configurations. Sections 4.5.1 through 4.5.3 will compare and contrast the results from each of the tests with respect to these considerations. Section 4.5.4 will contain a discussion of potential areas of future work for this project.

4.5.1 Comparison of Results for Different Materials

Two different materials were considered in this study, namely EcoSoya wax and a machinist wax called Rigidax. These materials were chosen because they could be melted with a heater and re-solidify via conductive and convective heat transfer in a room temperature environment. Furthermore, these two materials attenuate the ultrasound signal as the ultrasound wave propagates across the width of the box. Although both of these materials were a type of wax, they were quite different from one another both in appearance and with respect to their thermal properties. Figure 4.39 showed the striking difference in the physical appearance of the two materials with the EcoSoya wax having a smooth surface with few if any voids present along the surface of the wax and the machinist wax appearing to have a pellet-like texture with several voids visible on the surface of the material.

The EcoSoya wax melted easily across the length and width of the acrylic box used in the experiment. As the melt front progressed across the box in the EcoSoya experiments, sub-surface voids were identified, as bubbles would float to the top surface, and in some cases, the void was about as large as a golf ball. As indicated by a comparison of the slope of the DSC results obtained for the EcoSoya wax (which was presented in Gregg's masters thesis [83]) and the machinist wax (presented in this dissertation), the EcoSoya wax had a lower heat capacity than the machinist wax. Thus, according to the DSC results, the EcoSoya wax should have been easier to melt than the machinist wax, and the experiments performed for this study confirmed those results.

The machinist wax was more difficult to melt than the EcoSoya wax. It took about the same amount of time for the EcoSoya wax to melt across the full length and width of the large acrylic box as it took the machinist wax to melt at the first probe channel nearest the heater block. Furthermore, the heater block in the EcoSoya experiment was at a lower temperature than in the machinist wax experiment. Although the machinist wax posed difficulties in the beginning of the experiment, once the machinist wax melted, the behavior of the material was similar to that of the EcoSoya wax: it melted, then it slowly started to re-solidify. During the beginning of the machinist wax experiment, the machinist wax was in contact with the walls of the box, so water was not needed to couple the machinist wax to the walls of the box like it was in the EcoSoya experiment. However, the machinist wax was very porous in its solid form, and the strength of the ultrasound signal decreased significantly while propagating through the thickness of the machinist wax. The amplitude associated with the ultrasound signal propagating through the thickness of the solid machinist wax in the acrylic box was near

the same amplitude as the signal noise. While the machinist wax was being heated, there were some A-scans collected throughout the experiment where the ultrasound signal seemed to disappear completely as if it had been attenuated so much that it could not propagate through the thickness of the machinist wax.

From a data analysis perspective, the analysis approach was nearly identical for both materials. However, the signal intensity threshold for identifying the TOF played a bigger role in the machinist wax data analysis as the amplitude of the ultrasound signal was near that of the signal noise. Thus, the signal intensity threshold needed to be increased to avoid capturing a lot of signal noise.

Both materials chosen for this study were useful for testing the ultrasound approach to monitoring phase and temperature of the material. The fact that the two materials were different from one another, with respect to porosity, heat capacity and texture, assisted in proving the applicability of the technique to multiple materials.

4.5.2 Comparison of Results with Respect to Heater Placement

In the EcoSoya experiments and the machinist wax experiments inside of the acrylic box, the heater was placed at one end of the box, and the wax was melted from one end of the box to the other. For the machinist wax experiment with the steel box, the heater was placed near the bottom of the box and below the height of the ultrasound probes. Thus, the machinist wax was melted from underneath. Since the heater extended across the majority of the length and width of the steel box, it likely provided a more uniform melt of the machinist wax. However, from photographs taken during the early part of the experiment, the liquid machinist wax propagated upward along the all-thread

rods that held the heater in place, and then, it would flow across the top surface of the machinist wax.

Analysis of the data obtained in all of the experiments, the A-scan, B-scan and speed of sound plots were able to indicate the phase change of the material regardless of heater placement relative to the other components in the experimental setup. The speed of sound versus temperature plots also proved to be similar to one another regardless of heater block placement, as seen in the comparison of the speed of sound versus temperature plots for the machinist wax in Figure 4.86 where similar trends are identified across all three machinist wax experiments.

4.5.3 Comparison of Results with Respect to Experimental Setups

Throughout this study three different experimental setups were used with a different experimental setup presented in section 4.2.1 (large acrylic box), 4.3.1 (small acrylic box), and 4.4.1 (small steel box). The purpose of using multiple experimental setups was to identify which portions, if any, of the experiment and the data analysis were geometry dependent.

The experiment proved to be geometry independent in many respects. For example, the material melted across the length and width of the box regardless of the size of the box. Although the machinist wax took longer to melt, this was caused by the material's increased heat capacity as compared to the EcoSoya wax.

Although the geometry of the box did not affect the melting or re-solidifying of the wax, the material chosen for manufacturing the box did affect the experiment. For example, the steel box used in the machinist wax experiment described in section 4.4 was a better heat conductor than the acrylic box used in the machinist wax experiment

described in section 4.3. The machinist wax melted more quickly in the steel box than it did in the acrylic box. However, the steel box did have its drawbacks. While the machinist wax was solid, the signal intensity of the ultrasound wave propagating through the thickness of the wax was less than the signal intensity of the ultrasound wave propagating along the walls of the steel box. Thus, the A-scans collected at the beginning of the experiment in the steel box were dominated by the signal intensity of the ultrasound wave propagating along the box walls rather than through the machinist wax. This same phenomenon was not observed with the acrylic box. Instead, the signal intensity of the ultrasound wave propagating through the machinist wax dominated the A-scan signal rather than the signal intensity of the ultrasound wave propagating through the acrylic box walls.

With respect to the data analysis performed in Matlab, the geometry impacted the analysis in two ways. First, the dimensions used in the analysis program needed to be updated depending on the experimental setup being used. This change was required to ensure the calculations were correct. No other changes to the Matlab code were necessary for the experiments performed within the acrylic boxes. There was a second change required in the Matlab program for the experiment performed using the steel box. As mentioned in section 4.4.3, the A-scan was dominated by the signal corresponding to the ultrasound wave propagating along the walls of the steel box for the first 70 minutes of the experiment and from 270 minutes until the end of the experiment. To keep the focus of the data analysis solely on the material of interest, namely the machinist wax in that experiment, the first 70 minutes of data and the data from 270 minutes until the end of the experiment were removed from figures involving the speed of sound calculations.

The different experimental geometries and setups used in the experiments performed in this study had relatively minor effects on the measured results. The experimental setup that had the largest impact on the results was the steel box used in the machinist wax experiment detailed in section 4.4. This observation about the effects of geometry and experimental setup with respect to the measured results is promising as it indicates the potential for this ultrasound technique to be successfully applied to a variety of experimental geometries.

4.5.4 Future Work

Although this study considered multiple materials and experimental geometries, there are areas where future work could be performed. For example, all of the configurations used in this study were rectangular. It would be interesting to see how a different geometry, such as a cylindrical pipe that may be used for transporting fluids in an oil and gas application, would affect the ultrasound measurements.

The temperature estimations along the probe channels in sections 4.2.5 and 4.3.6 were performed using a scatteredInterpolant method in Matlab, and these were proven via the one-dimensional heat transfer study to be overestimating the temperature along the probe channel. Future work may consider identifying the thermal conductivity of the solid wax and the thermal conductivity of the liquid wax. Then, use the thermal conductivities along with the one-dimensional heat transfer problem to identify a better estimation of the temperature along the probe channel.

Another area that may be included in future work is considering different materials. For example, would a thermoplastic behave in a similar manner as the wax? Some materials that may be considered are polypropylene, ABS, and a thermoset resin.

The interesting aspect of monitoring the thermoset resin would be monitoring the exothermic reaction as the polymer chains crosslink with one another as the thermoset cured. However, the thermoset resin experiment would be irreversible and would require manufacturing a new experimental setup for each experiment performed.

Finally, all of the experiments performed in this study looked at through transmission ultrasound data. Future work may consider looking at pulse echo ultrasound data to identify where the melt front is located, or the data could potentially be used for identifying how much of the material located perpendicular to the probe is solid and how much is liquid. Pulse echo ultrasound methods monitor the reflection of the ultrasound wave off materials with different densities. Since the solid and liquid material have different densities, the pulse echo method may be able to detect how much of the material is solid and how much is liquid by monitoring the reflections as the wave propagates across the width of the box. For example, Figure 4.89 shows an instance during the experiment for EcoSoya wax where channel 1 had a region of solid wax followed by liquid wax followed by more solid wax between the two ultrasound probes.

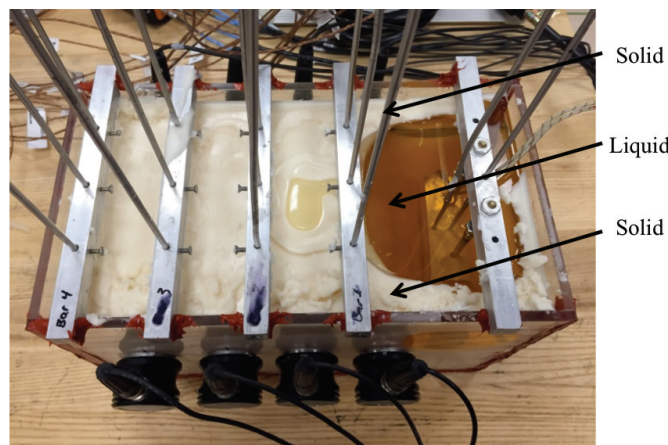


Figure 4.89 The ultrasound wave along channel 1 in an EcoSoya wax experiment encounters a solid wax region followed by a liquid wax region followed by another solid wax region.

CHAPTER FIVE

Oblique Incidence, Through Transmission Ultrasound Method for Inspecting Carbon Fiber Reinforced Laminated Composites

5.1 Introduction

The present study focused on the ultrasound inspection of a carbon fiber reinforced laminated composite using an oblique incident through transmission ultrasound technique. The carbon fiber reinforced laminated composite was manufactured by the project sponsor, Sandia National Laboratories, using an 8 harness satin carbon fiber fabric preimpregnated with UF 3352 TCRTM resin. The ultimate goal of the overall project is to identify the elastic constants for the bulk laminate using a nondestructive ultrasound technique. The measured C-scan results would be compared with the predicted wave propagation as generated by a mathematical model. The scientific contribution of the present study is the development of the oblique incident through transmission ultrasound technique that gives the inspector a better idea of how the wave propagates through the laminated composite. The study begins by looking at the results obtained while scanning an isotropic, homogeneous aluminum plate and then progresses to discuss the results obtained for the laminated composite of interest. The time of flight obtained for the longitudinal wave in the C-scan measurements was confirmed via calculations as will be discussed in the presentation of the data. Perturbations in the experimental parameters, such as varying the orientation of the pulser and the receiver as well as inspection of different laminate thicknesses, are also presented and discussed throughout this chapter.

The proposed inspection technique has applications in industries, such as the automotive and aerospace industries, where fiber reinforced laminated composites are increasingly being incorporated into products like the Boeing 787 and the BMW i8 seen in Figure 5.1. The increased use of such materials has spurred the need for technological developments in the area of nondestructive inspection to accurately identify defects and to characterize the fiber reinforced laminated composites. The proposed oblique incidence through transmission ultrasound technique is the first step in a project whose goal is to identify the material's elastic constants. The desire to nondestructively identify the material's elastic constants is derived from the necessity of knowing whether or not the material has the desired mechanical properties. For example, the technique could be used for quality assurance inspections once a part has been manufactured or it could be used for inspecting a part that has been in service for an extended period of time to determine whether or not it can still perform at the desired level of strength.



Figure 5.1 BMW i8 present at the 2015 Society of Plastics Engineers Automotive Composites Conference and Exhibition in Novi, Michigan. Photo by author.

5.2 Experimental Setup and Snell's Law Calculations for Aluminum Plate

The present study used an oblique incident through transmission ultrasound setup with two spherically focused ultrasound probes. Both of the ultrasound probes used in the study had an operating frequency of 5 MHz and a focal length of 50.8 millimeters (2 inches). A gimbal was attached to each probe, and the two ultrasound probes were oriented at the same angle (θ_1) in the through transmission setup as seen in Figure 5.2. For inspection of the aluminum plate the value of θ_1 was 5° . Since the focal length of each probe is 50.8 millimeters, the probes are placed such that their focal points align, and a ruler was used to verify the two probes were 102 millimeters apart from each other.

Then, the orientation of the receiver was increased to θ_2 as seen in Figure 5.3. For the inspection of the aluminum sample, the value of θ_2 was 14° . The value of θ_2 was chosen based on previous experiments performed by the author [68] where inspections with a variety of pulser and receiver orientations were performed to identify the desired experimental setup to obtain a C-scan that displayed a clear separation of the ultrasound wave components as they exited the material. Further discussion of this study will be presented in section 5.4.

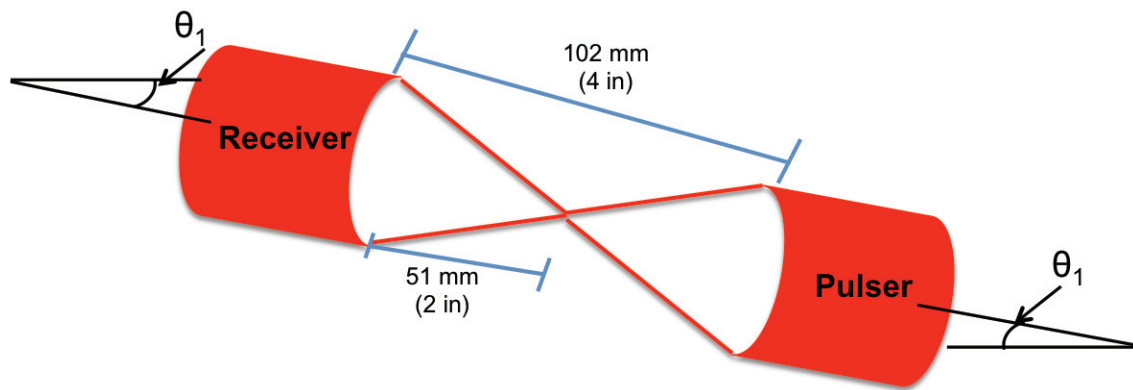


Figure 5.2 Side view diagram of experimental setup.

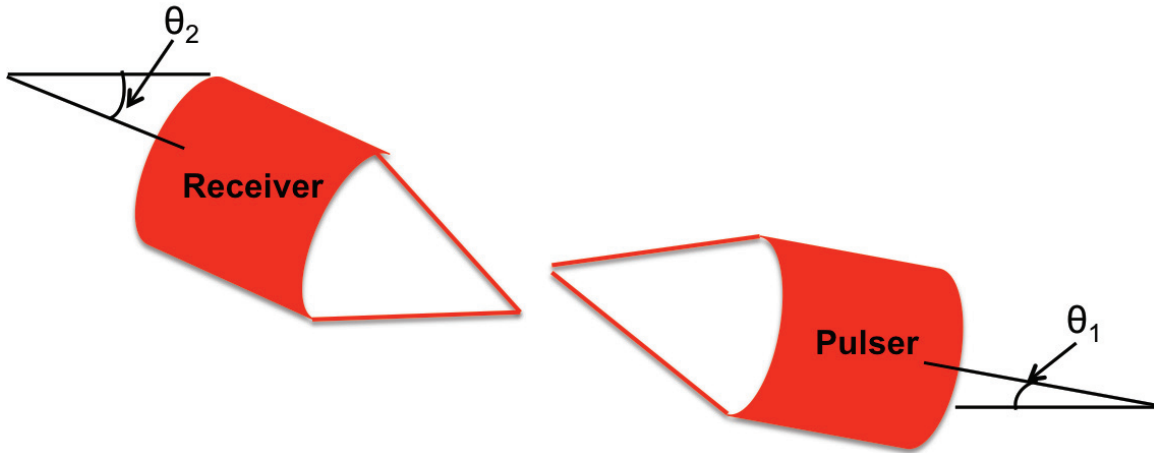


Figure 5.3 The receiver was rotated to a new angle relative to the horizontal axis.

Once the receiver orientation was changed from 5° to 14° as seen in Figure 5.3, the distance between the two pulsers changed. For the purposes of calculating the time of flight (TOF), which is the time required for the ultrasound wave to propagate through the thickness of the sample, the new distance between the pulser and receiver must be identified. The TOF calculation will be used later in this section for confirming the measured results are reasonable. Figure 5.4 presents a zoomed-in diagram showing the geometric effects of changing the orientation of the receiver. The receiver oriented at 5° is represented by the red receiver in Figure 5.4, and the receiver orientated at 14° is represented by the blue receiver. The ‘O’ in Figure 5.4 represents the center of rotation in the gimbal that controls the orientation of the receiver. From the center of rotation, O, to the tip of the ultrasound probe is 76.2 millimeters (3 inches), and this value is defined as d . The horizontal component of d for each of the receiver orientations is presented in Figure 5.4. For the receiver oriented at 14° , the horizontal length component is defined as

$$d_{14} = d\cos(14^\circ) \quad (5.1)$$

and the horizontal length component for the receiver oriented at 5° is defined as

$$d_5 = d\cos(5^\circ) \quad (5.2)$$

The difference between the horizontal length components of the two receiver orientations is represented by the term Δl , which is defined as

$$\Delta l = d_5 - d_{14} \quad (5.3)$$

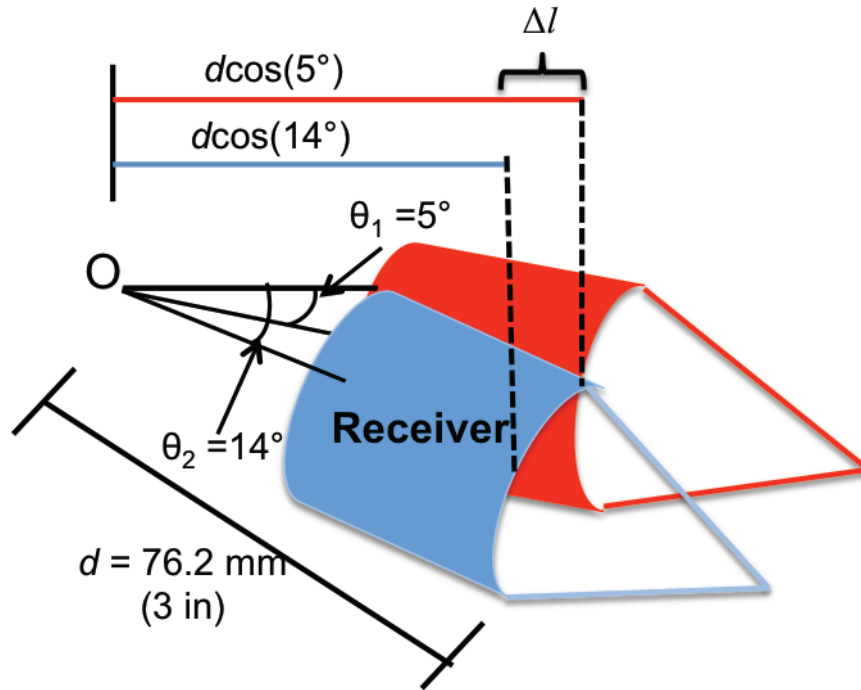


Figure 5.4 The receiver orientation was changed from 5 degrees to 14 degrees relative to the horizontal axis.

The horizontal components determined from equations 5.1 through 5.3 can then be related to the rest of the experimental setup as seen in Figure 5.5. The horizontal distance between the pulser oriented at 5° and the receiver oriented at 5° is given as the horizontal component of the triangle drawn in Figure 5.5. Using the 102 millimeter distance between the two probes and the orientation of the pulser (5°), the length of the base of the triangle can be calculated using simple trigonometry as seen in Figure 5.5. Then, the base of the triangle that connects the pulser to the receiver is defined as seen in

Figure 5.6. Using trigonometry, the distance between the pulser and the receiver oriented at 14° is defined by h and is calculated as

$$h = \frac{(102\text{mm}) \cos(5^\circ) + \Delta l}{\cos(5^\circ)} \quad (5.4)$$

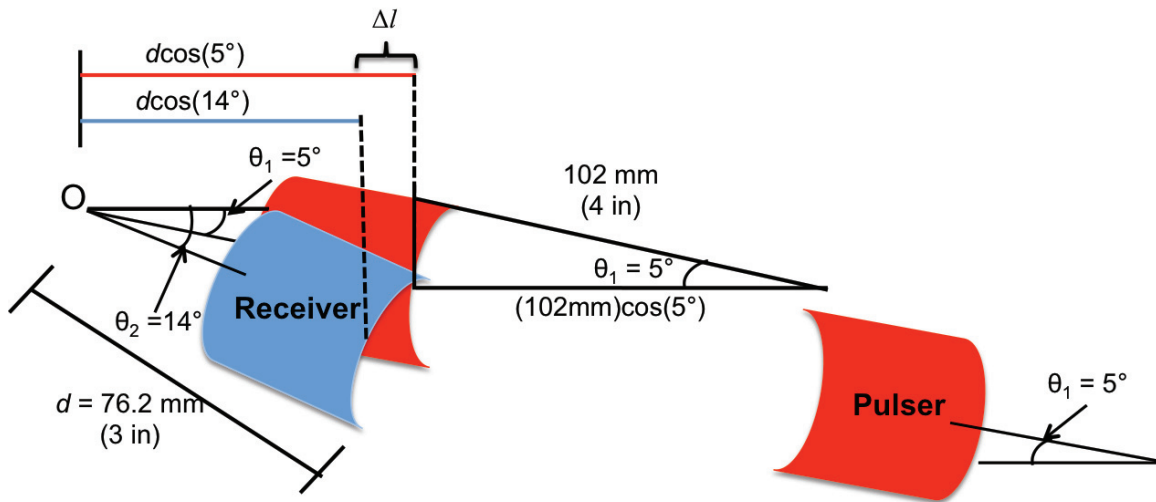


Figure 5.5 The geometry of the pulser relative to the different receiver probe angles.

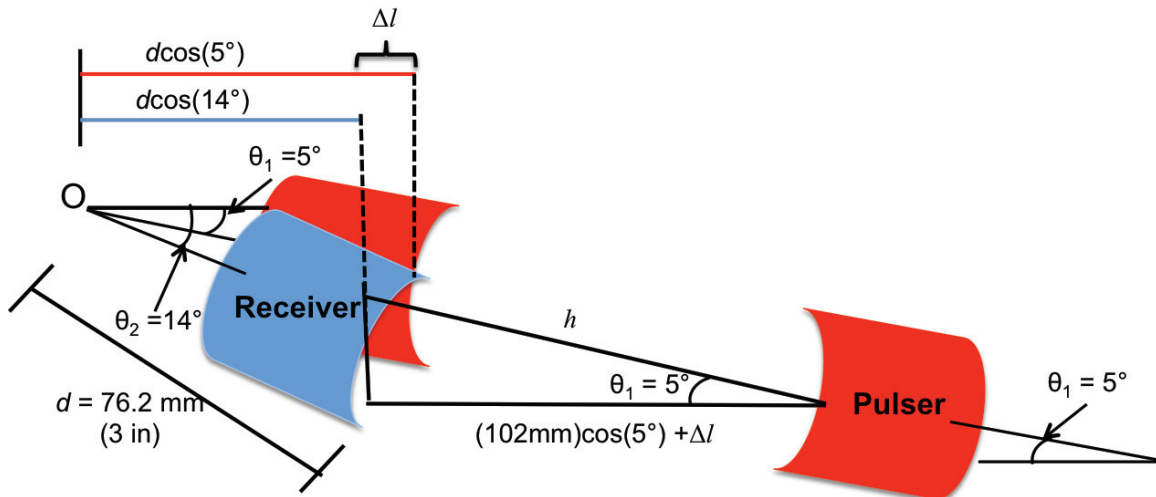


Figure 5.6 A visual representation of the geometry defining the distance in water between the pulser at 5° orientation and the receiver at 14° orientation.

Once the distance h between the pulser ($\theta_1 = 5^\circ$) and the receiver ($\theta_2 = 14^\circ$) was calculated, the aluminum sample was placed at the midpoint between the pulser and the receiver as seen in Figure 5.7. Photographs taken of the experimental setup in the laboratory are presented in Figures 5.8 and 5.9, where Figure 5.8 presents a top view and Figure 5.9 presents a side view of the experimental setup.

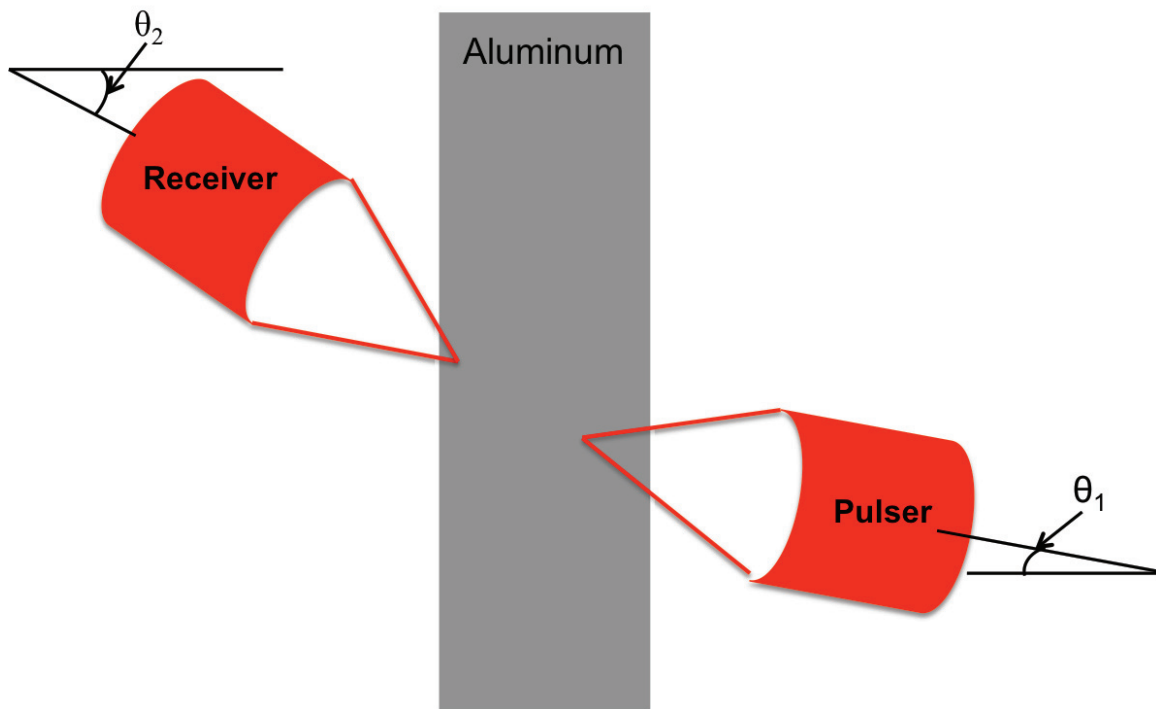


Figure 5.7 Experimental setup with the aluminum sample placed between the pulser and receiver ultrasound probes.

As the incident, longitudinal ultrasound wave exits the pulser, the wave propagates through the water until it reaches the surface of the aluminum sample. Then, the incident ultrasound wave splits into a longitudinal wave and a shear wave as the ultrasound wave continues to propagate through the thickness of the aluminum. The time required for each of the two waves to propagate through the thickness of the aluminum is dependent on the longitudinal wave velocity and shear wave velocity associated with the

material. The longitudinal wave velocity for aluminum is $6.32 \text{ mm}/\mu\text{s}$, and the shear wave velocity for aluminum is $3.04 \text{ mm}/\mu\text{s}$ [116].

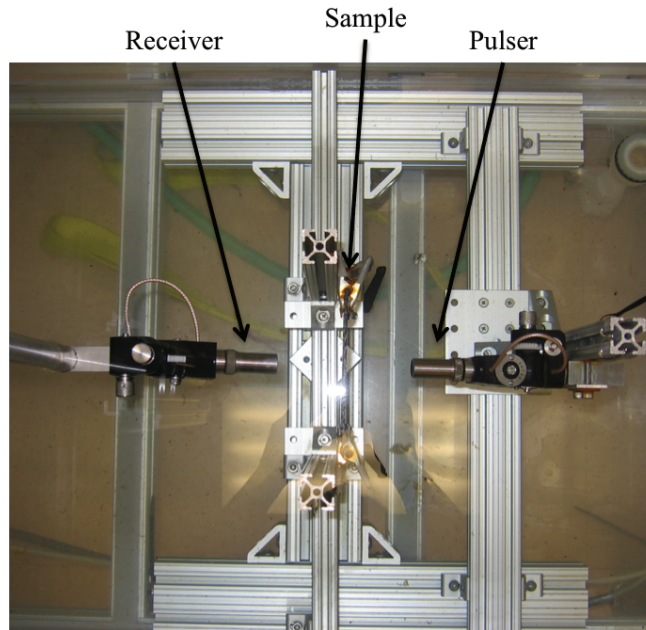


Figure 5.8 Top view photograph of the experimental setup configuration.

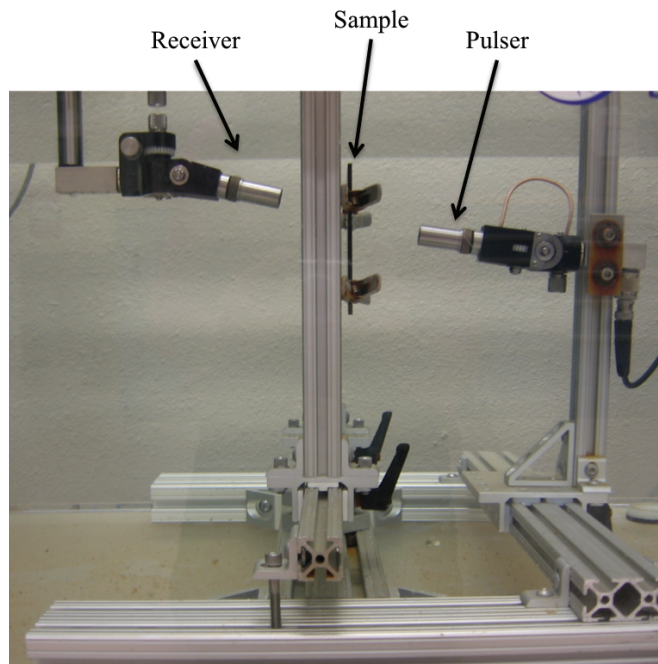


Figure 5.9 Side photograph of the experimental setup configuration.

In the experiment, the ultrasound wave entered the aluminum sample at an oblique incident angle, and Snell's Law can be used to calculate the angle of refraction for both the longitudinal wave and the shear wave propagating through the aluminum. Snell's Law is a mathematical approach for describing the relationship between the incident and refracted wave [63]. Snell's Law is defined as

$$\frac{\sin\theta_I}{\sin\theta_R} = \frac{c_I}{c_R} \quad (5.5)$$

where θ_I is the angle of the incident wave (defined as θ_1 in Figure 5.7), θ_R is the angle of the refracted wave, c_I is the speed of sound for the material in which the wave originates, and c_R is the speed of sound of the second material into which the wave propagates.

The diagram in Figure 5.10 shows θ_1 as the angle of the incident wave, and knowing the shear wave velocity for aluminum (c_S) and the longitudinal wave velocity for water ($c_W = 1.48 \text{ mm}/\mu\text{s}$ [116]), the angle of refraction for the shear wave propagating through the aluminum sample is calculated using Snell's Law as

$$\theta_S = \sin^{-1} \left(\frac{c_S}{c_W} \sin(\theta_1) \right) \quad (5.6)$$

A similar calculation may be performed for the longitudinal wave propagating through the thickness of the aluminum as seen in equation 5.7

$$\theta_L = \sin^{-1} \left(\frac{c_L}{c_W} \sin(\theta_1) \right) \quad (5.7)$$

where the subscript 'L' corresponds to the values associated with the longitudinal wave propagating through the aluminum sample. The diagram provided in Figure 5.11 depicts the angles associated with the longitudinal wave propagating through the thickness of the aluminum plate. Using the previously defined values of the different sound velocities and the angle of the incident wave, the angle of refraction for the shear wave (θ_S) was

calculated to be 10.4° , and the angle of refraction for the longitudinal wave (θ_L) was calculated to be 22.0° . Once the longitudinal and shear waves propagated through the thickness of the aluminum, the waves propagated into the water and toward the receiver where the wave signals were captured and stored to the computer for further analysis. Since water can only sustain longitudinal waves [63], the shear wave experienced a mode-conversion back to a longitudinal wave as it entered the water. The angle at which the waves refracted into the water as they exited the aluminum was the same as the angle of the incident wave. Figure 5.12 depicts the shear wave and longitudinal wave propagation relative to one another inside of the aluminum sample. The figure is a diagram and the angles are not to scale; however, Figure 5.12 demonstrates that the shear wave propagates through the aluminum at a shallower angle than the longitudinal wave.

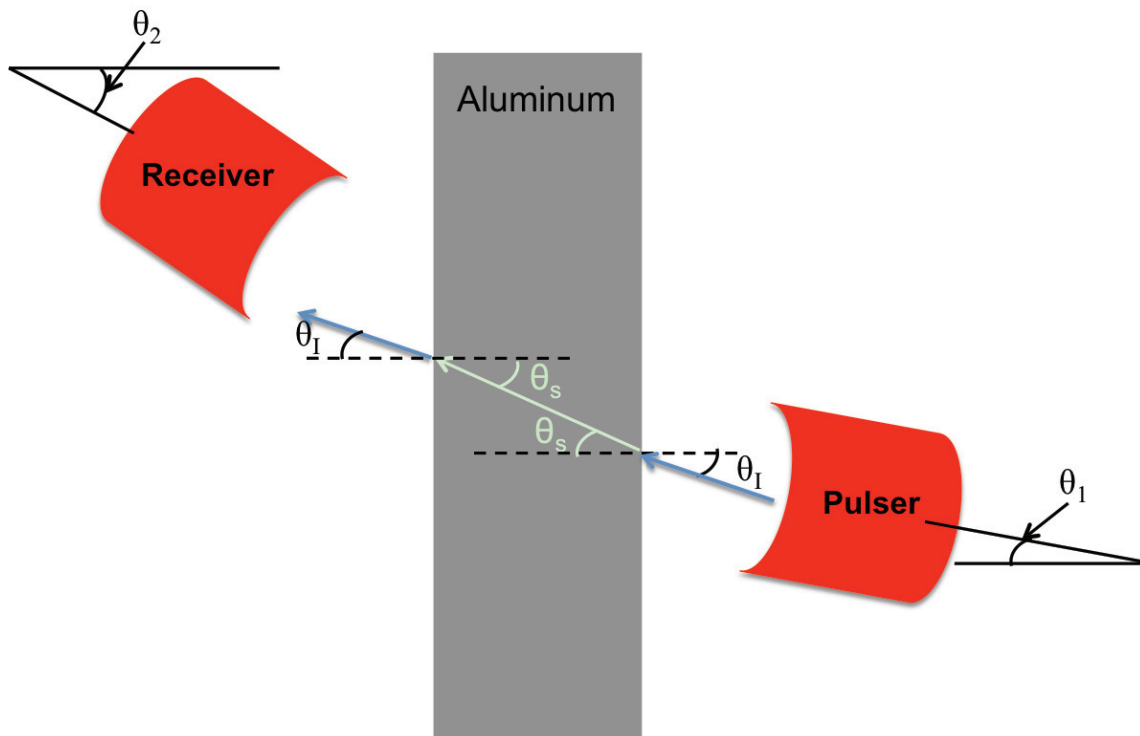


Figure 5.10 Graphical depiction of the components used in Snell's Law calculations for the shear wave propagating through the aluminum.

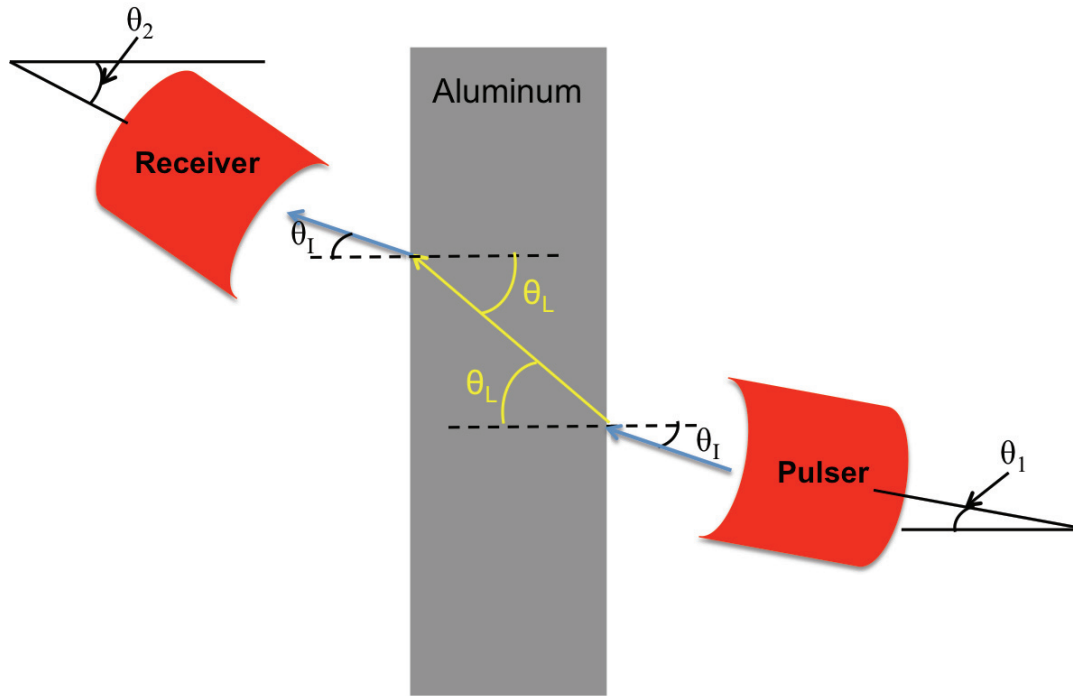


Figure 5.11 Diagram of the components used in the Snell's Law calculations for the longitudinal wave propagating through the thickness of the aluminum sample.

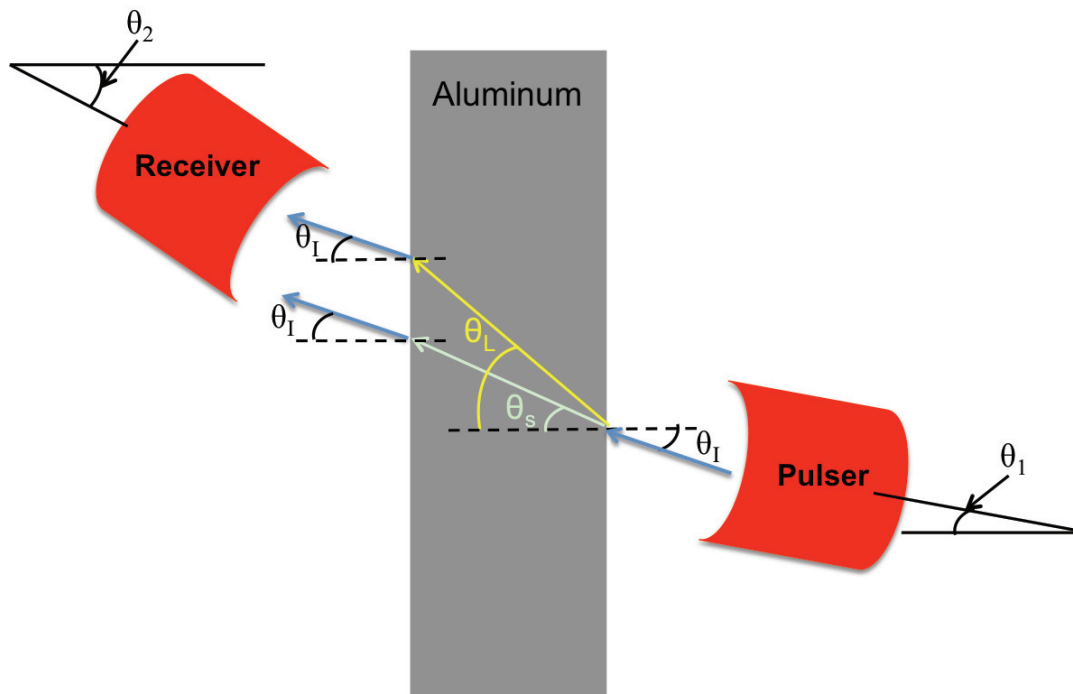


Figure 5.12 Diagram of the components used in the Snell's law calculations for both the longitudinal and shear waves. The diagram shows the shear and longitudinal wave relative to one another within the sample.

Using the Snell's Law calculations from equations 5.6 and 5.7 and the geometry of the experimental setup, the time of flight (TOF) for the longitudinal wave and the shear wave propagating through the aluminum can be determined. Since the ultrasound waves propagate through the water at the same angle regardless of whether it is before or after the wave has propagated through the aluminum thickness, the total time spent traveling through the water can be calculated as

$$h_W = h - \frac{t_{AL}}{\cos(5^\circ)} \quad (5.8)$$

where h_W is the total distance the wave traveled in the water, h is the total distance between the pulser and the receiver as determined from equation 5.4, and t_{AL} is the thickness of the aluminum plate (13.2 mm). The total distance the waves travel in the water is 90.3 millimeters (3.56 in). The time required for the waves to propagate through this distance of water is determined using the TOF equation where the distance traveled is divided by the speed of sound of the medium, in this case water, as seen in equation 5.9.

$$TOF_W = \frac{h_W}{c_W} \quad (5.9)$$

The calculated value of TOF_W is 61.3 μ s. Next, the time required for the shear wave to propagate through the thickness of the aluminum is calculated using the angle of refraction as determined from equation 5.6 and the thickness of the aluminum plate. The total distance the shear wave traveled in the aluminum, h_S , is defined as

$$h_S = \frac{t_{AL}}{\cos(\theta_S)} \quad (5.10)$$

and the time the shear wave spent traveling in the aluminum (TOF_S) is given by

$$TOF_S = \frac{h_S}{c_S} \quad (5.11)$$

The calculation for the time required for the longitudinal wave to propagate through the aluminum plate can also be calculated using equations 5.10 and 5.11 with the terms with a subscript ‘S’ being replaced by terms with a subscript ‘L’. The results from equations 5.10 and 5.11 indicate that the shear wave takes 4.42 μs to propagate through the aluminum whereas the longitudinal wave takes 2.26 μs to propagate through the aluminum. The total TOF for the ultrasound signal to propagate from the pulser to the receiver can be determined for the shear wave and the longitudinal wave that propagate through the aluminum. The total TOF in the water and the aluminum is calculated using equation 5.12.

$$TOF_{STOT} = TOF_W + TOF_S \quad (5.12a)$$

$$TOF_{LTOT} = TOF_W + TOF_L \quad (5.12b)$$

where TOF_{STOT} refers to the total time of flight for the wave to propagate through the water and the shear wave to propagate through the aluminum and TOF_{LTOT} is the total time of flight for the wave to propagate through the water and the longitudinal wave to propagate through the aluminum. The value of TOF_{STOT} was 65.7 μs , and the value of TOF_{LTOT} was 63.6 μs . These TOF values as calculated from equation 5.12 will be compared with the measured C-scan results to ensure the reasonableness and accuracy of the measurements.

5.3 C-scan Measurement Results for the Aluminum Plate

Ultrasound C-scan measurements were performed on the aluminum plate using a Mistras UPK-T36 ultrasound immersion system. The system contained a pulser, an x, y, and z translation system, and UTwin software to control the system and store and post-process the data. As discussed in section 5.2, the orientation of the two ultrasound probes

were manually controlled using gimbals as were seen in the experimental setup photos in Figures 5.8 and 5.9. The C-scan results for the aluminum plate are presented in Figure 5.13 where the vertical and horizontal axes are in units of inches. The color bar provided in Figure 5.13 corresponds to the maximum signal amplitude captured in the A-scan.

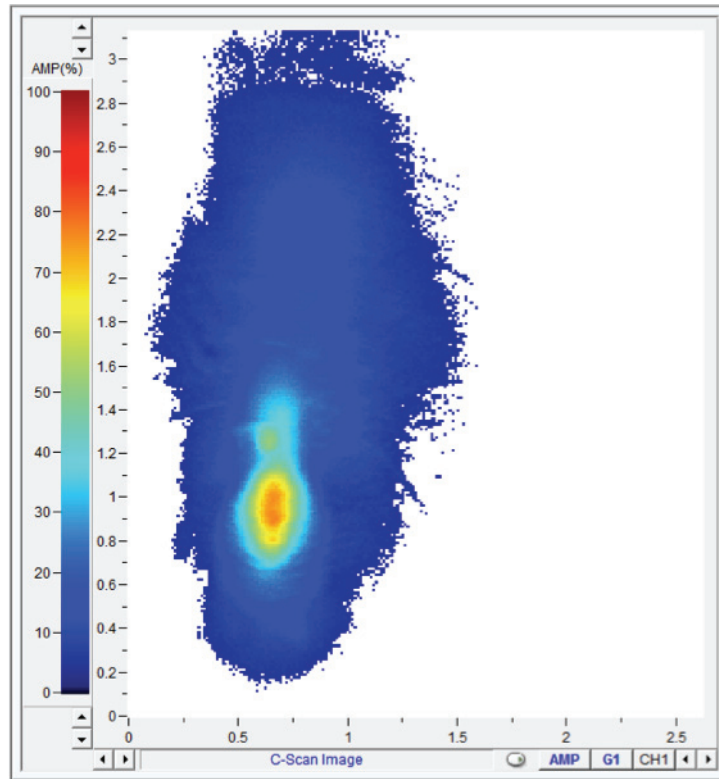


Figure 5.13 C-scan results for the aluminum plate.

Figure 5.14 highlights the longitudinal wave's A-scan signal as identified in the C-scan image. The A-scan shown in Figure 5.14 is known to be the longitudinal wave for two reasons. First, the shape of the wave is characteristic of the longitudinal wave having a rapid increase in the signal amplitude followed by an exponential decay in the signal amplitude. Second, the TOF for the onset of the longitudinal wave compares well with the calculated TOF_{LTOT} from equation 5.12b in section 5.2. The measured TOF was 63.5

μs whereas the calculated TOF_{LTOT} was $63.6 \mu\text{s}$. These results compare well with one another and confirm that the A-scan signal shown in Figure 5.14 was the longitudinal wave that propagated through the aluminum.

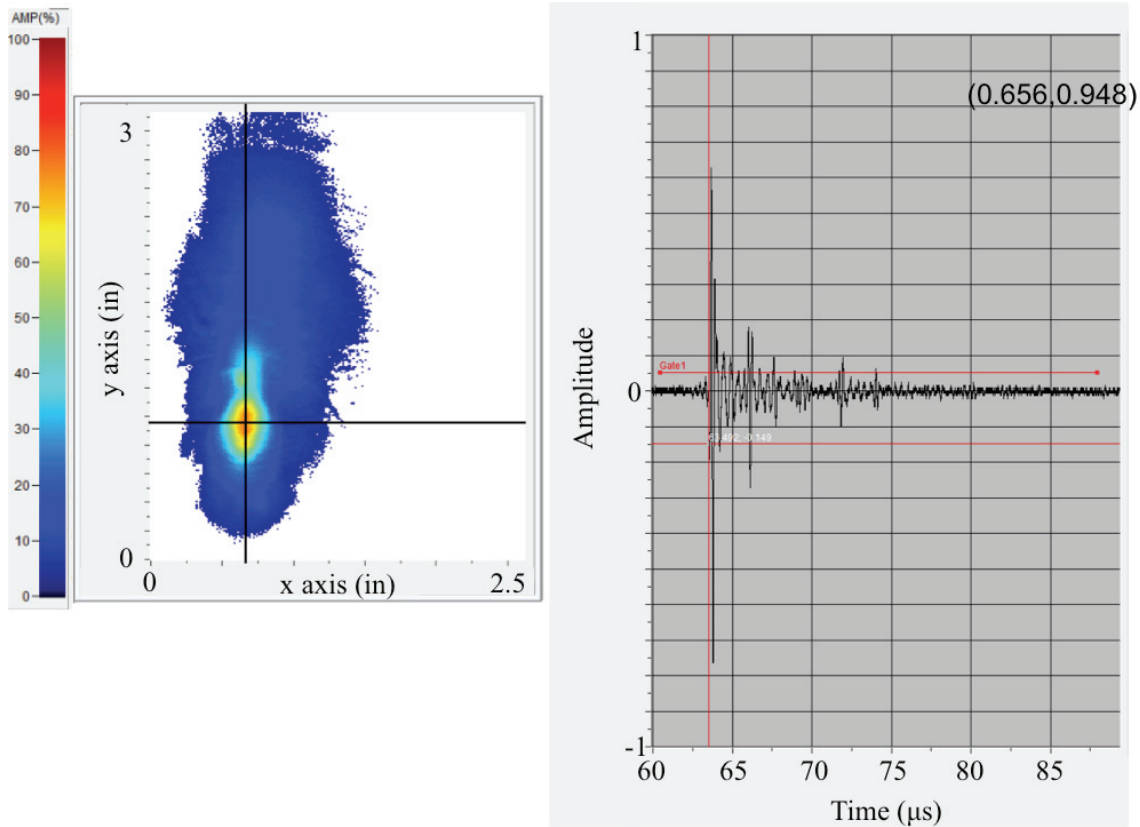


Figure 5.14 C-scan and A-scan signal comparison

The identification of the shear wave propagating through the aluminum was more difficult to confirm. A graph of the energy reflection and transmission coefficients as a function of angle of incidence was located in literature for longitudinal and shear waves propagating through an aluminum sample immersed in water [122]. From the plot of the energy transmission coefficients for the longitudinal and shear waves with an angle of incidence of 5° , approximately 30% of the longitudinal wave's energy is transmitted across the water-aluminum boundary whereas approximately 2% of the shear wave's

energy is transmitted across the water-aluminum boundary. The same energy percentages occur when the waves propagate across the aluminum-water boundary. Thus, by the time the longitudinal and shear waves arrive at the receiving probe, 9% of the longitudinal wave's energy has propagated all the way to the receiver whereas only 0.04% of the shear wave's energy made it to the receiver. With the longitudinal wave having 225 times more energy arriving at the receiver than the shear wave, the shear wave signal was likely lost in the noise of the A-scan signal, and the shear wave's reflections within the aluminum probably experienced some convolution with the longitudinal wave's signal. The main contribution from this section is confirmation of the proper identification of the longitudinal wave's TOF value as compared to the calculated value from section 5.2. Now that the experimental setup and identification of the longitudinal wave have been confirmed for the aluminum sample, the following section will apply this oblique incidence through transmission ultrasound technique to a carbon fiber reinforced laminated composite.

5.4 C-scan Inspection of Carbon Fiber Reinforced Laminated Composites

The oblique incidence through transmission ultrasound technique was also applied to the inspection of carbon fiber reinforced laminated composites. Unlike the isotropic, homogeneous aluminum sample that was studied in section 5.3, the laminated composite is nonhomogeneous and anisotropic with the degree of anisotropy being dependent on the laminate stacking sequence. For the purpose of this study, all of the laminates were manufactured by our project sponsor, Sandia National Laboratories, using 8 harness satin woven carbon fiber fabric that was preimpregnated with UF 3352 TCRTM resin. Figure 5.15 depicts the weave pattern seen in an 8 harness satin fabric. The blue

arrow pointing downward along the diagonal of the fabric square highlights the trend observed in the weave, namely the fiber tows in the warp direction lay atop one tow in the weft direction after propagating underneath 7 tows in the weft direction.

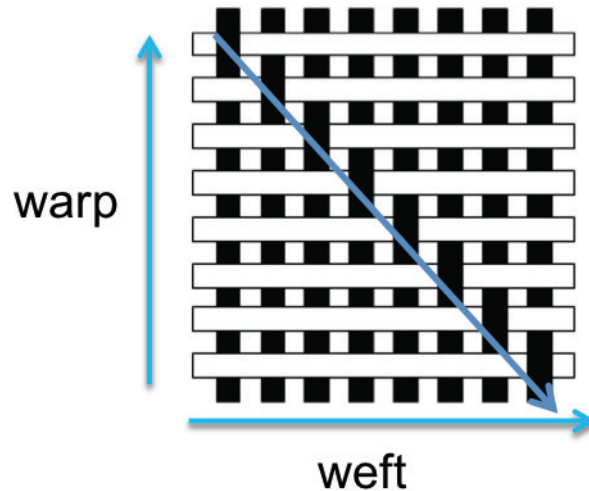


Figure 5.15 Diagram of 8 harness satin woven fabric.

The experimental setup used for the inspection of carbon fiber reinforced laminated composites was identical to that used for the inspection of the aluminum sample in section 5.3. As in the previous section, a shear wave and a longitudinal wave are predicted to propagate through the thickness of the laminate based on the laminate's shear wave velocity, the laminate's longitudinal wave velocity and Snell's Law. Snell's Law and TOF calculations were also performed for the carbon fiber reinforced laminated composites, and the longitudinal and shear wave velocities for the laminated composites were measured and published by Dorado and Moore [123]. The TOF calculations indicated that the shear wave's total TOF (through the water and the composite) was 70.6 μs , and the longitudinal wave's total TOF was 69.4 μs . These results will be compared with the measured C-scan results in section 5.4.1.

5.4.1 Oblique Incidence Through Transmission C-scan Results

The C-scan results for an 8 ply carbon fiber reinforced laminated composite manufactured using the aforementioned prepreg material and stacking sequence are presented in Figure 5.16. As compared to C-scan results for the aluminum plate in Figure 5.13, the C-scan results obtained for the carbon fiber reinforced laminated composite do not span as much area in the y direction. For example, the C-scan results for the aluminum sample spanned a y axis of 3 inches whereas the C-scan results for the composite laminate span approximately 1.1 inches along the y axis. Similar to the C-scan

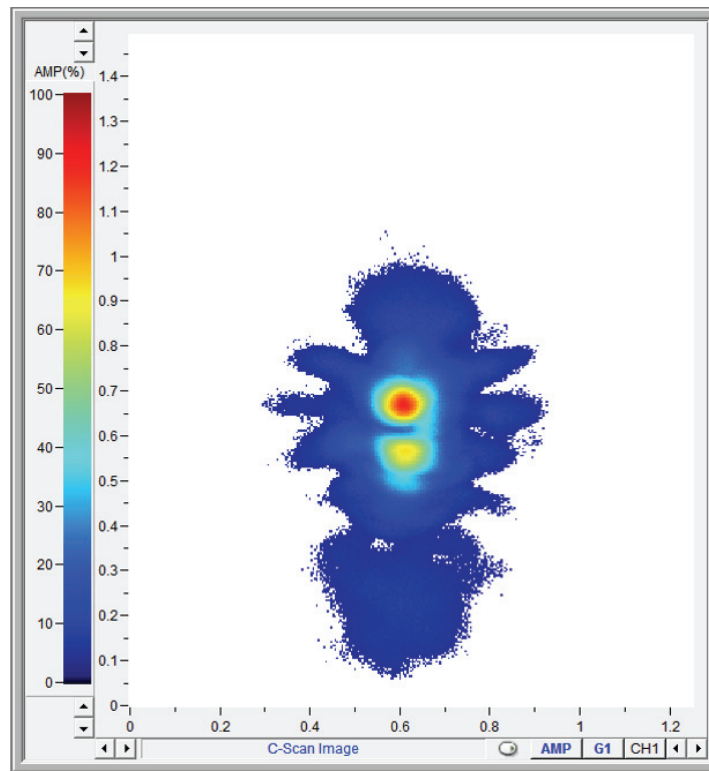


Figure 5.16 C-scan for oblique incidence through transmission ultrasound wave propagating through an 8 ply carbon fiber reinforced laminated composite

for the aluminum plate, the C-scan for the composite is symmetric about the centerline of the ultrasound data. Unlike the C-scan for the aluminum plate, the longitudinal wave in

the C-scan for the laminated composite appears to have a double peak with high amplitude signals. Figure 5.17 confirms the similarity in the A-scan signal shape for these two high amplitude regions of the C-scan located at (0.608 in, 0.675in) and (0.608 in, 0.561 in). The A-scan corresponding to the highest amplitude region at (0.608 in, 0.675 in) has a TOF of 69.9 μs , which compared well with the TOF calculated for the longitudinal wave (69.4 μs) in section 5.3.

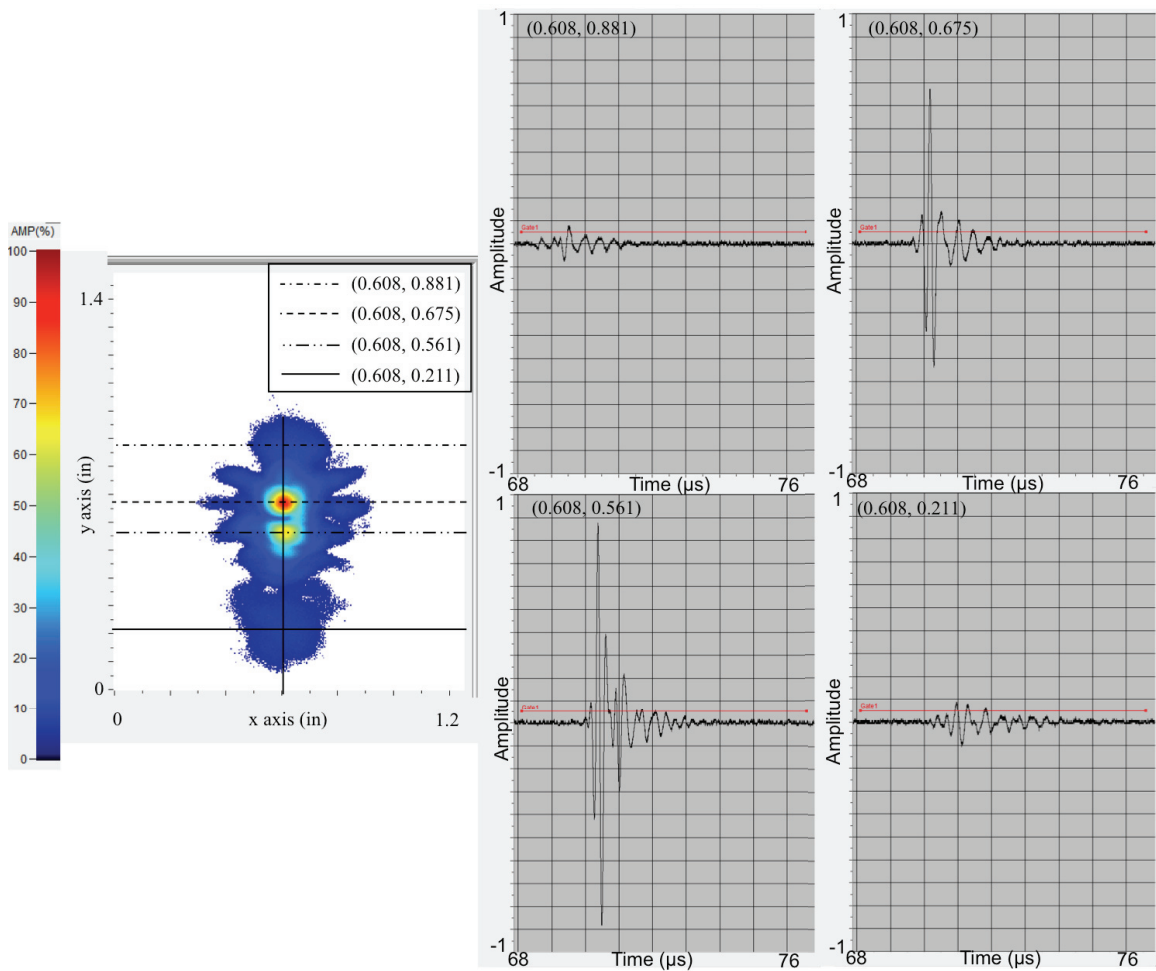


Figure 5.17 Comparing the A-scans to locations on the C-scan for the inspection of an 8 ply carbon fiber reinforced laminated composite

Additionally, in Figure 5.17 the A-scan signal is evaluated at a couple of other locations in the C-scan to identify more information about the signal shape. As observed from the A-scans at locations (0.608 in, 0.881 in) and (0.608 in, 0.211 in), the structure of the wave in these two A-scans are similar. Furthermore, based on review of literature, these two regions appear to represent the side lobes associated with the ultrasound wave propagating through the thickness of the laminate. Side lobes are formed when a portion of the wave energy exits the probe in an outward direction different than the focused direction of the probe. For additional information about side lobes and ultrasound beam profiles, the reader is encouraged to seek Newberry's dissertation [1].

Using the C-scan shown in Figure 5.17, a gate was placed around the portion of the ultrasound signal that corresponded to the wave propagating through the thickness of the laminated composite. Then, a Fast Fourier Transform analysis was performed on the gated region of each A-scan. After calculating the FFT for the gated portion of the A-scan signal, the frequency intensity of the 5 MHz component was stored for each (x,y) location in the C-scan, and a surface plot was generated using an in-house custom Matlab program. Figure 5.18 presents the surface plot of the intensity of the 5 MHz component of the FFT calculation for each A-scan, where the calculated intensity values were normalized with respect to the maximum intensity observed in the C-scan area. The graph shown in Figure 4.18 is similar to the predicted wave field patterns observed in Figure 35 of Newberry's dissertation [1].

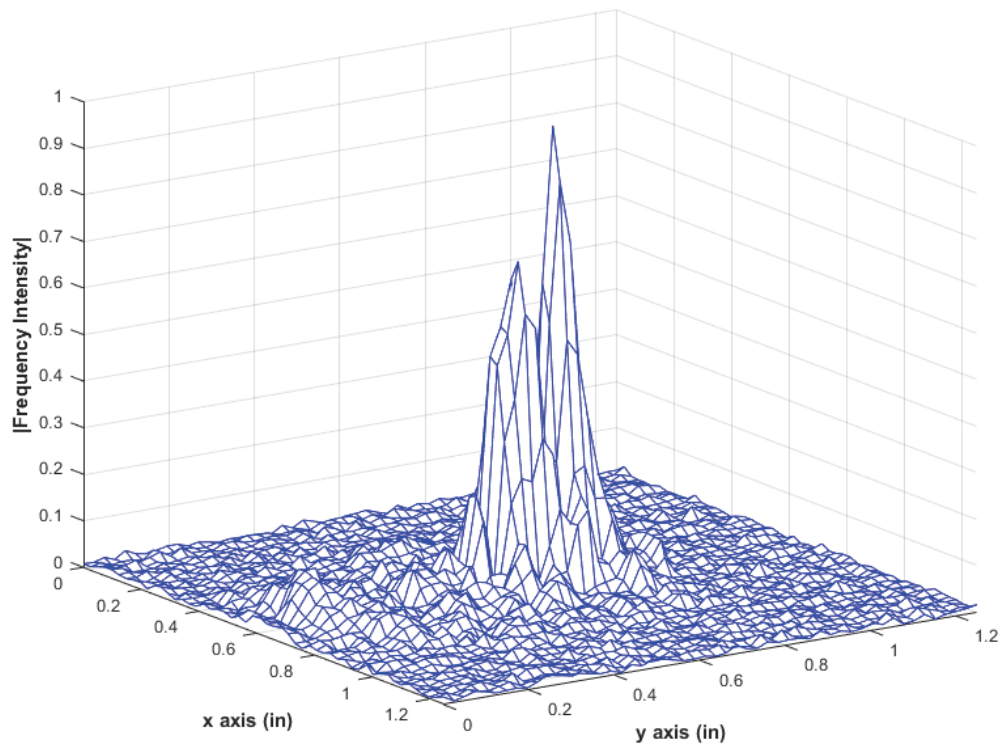


Figure 5.18 Frequency intensity plot corresponding to the 5 MHz component of the FFT analysis performed on each A-scan from the C-scan provided in Figure 5.17.

The author hypothesizes that these side lobes observed in the C-scan are more sensitive to changes in the material properties than the main longitudinal portion of the wave. Thus, when applying this oblique incidence through transmission measurement technique to determine the elastic constants of a sample, as is the overarching goal of the project related to this chapter, the side lobes of the wave may provide a more sensitive method for comparing the wave displacement calculations to the measured results. However, only comparison with the mathematical model will be able to prove this hypothesis, and as mentioned in the introduction in section 5.1, the focus of this chapter is on the experimental component of the project. The mathematical model will be discussed in the Future Work section of chapter 6.

5.4.2 Varying the Incident Angle

The same oblique incident through transmission ultrasound technique was applied to the 8 ply laminated composite, but the pulser orientation was changed from 5° to 10° while the orientation of the receiver remained a constant 14° . The goal of this study was to identify via experiments how the C-scan image would change when the orientation of the pulser was changed. For example, would the side lobes appear to spread further apart or closer together? A comparison of the C-scan results for the two scenarios is presented in Figure 5.19. The leftmost C-scan corresponds to the pulser being at 5° orientation and the receiver being at 14° , whereas the rightmost C-scan corresponds to a pulser orientation of 10° and a receiver orientation of 14° . The C-scan results appear to span less vertical distance in the C-scan obtained when the pulser orientation was 10° .

Additionally, the side lobe regions appear to have moved closer to the longitudinal wave

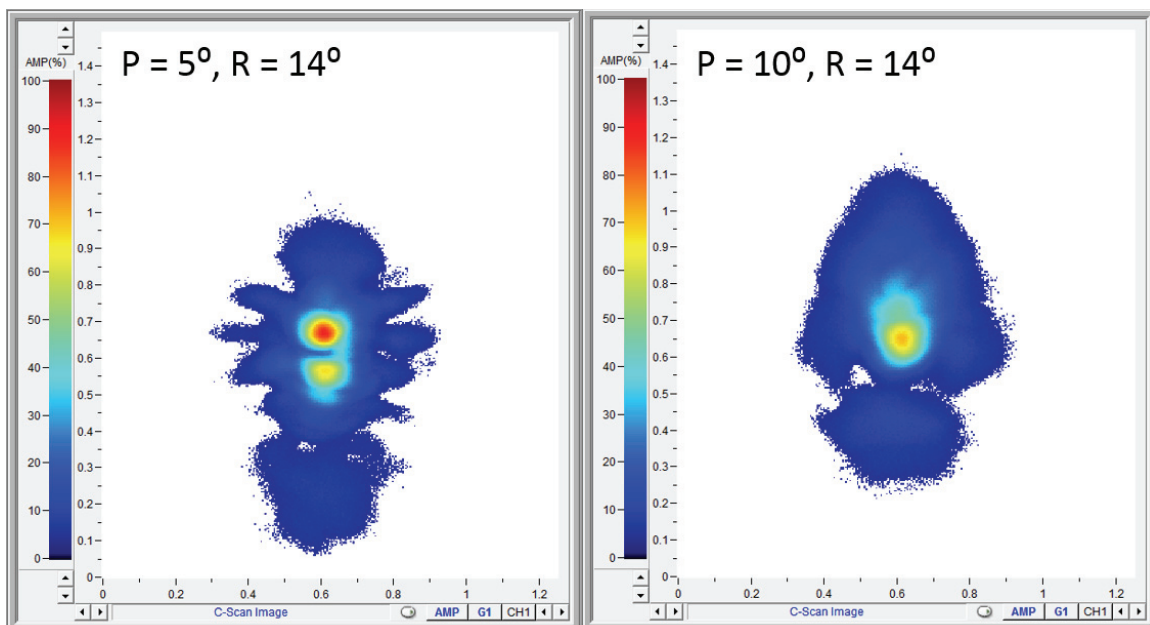


Figure 5.19 C-scan results for varying the incident angle for the ultrasound wave (by varying the orientation of the pulser relative to the sample surface normal)

(as indicated by the high amplitude region) for the C-scan obtained when the pulser is oriented at 10° . For the C-scan results obtained with the pulser at 5° , the C-scan appears to have more information about the scattering of the ultrasound wave based on the small lobes extending outward from the longitudinal wave region.

5.4.3 Varying the Receiver Angle

A similar study was performed on the 8 ply laminated composite by keeping the pulser at a constant orientation of 10° and varying the receiver orientation. The C-scan images provided in Figure 5.20 present results for receiver orientations of 14° (left) and 18° (right). Similar to the results presented in Figure 5.19, the shape of the C-scan results in Figure 5.20 appear to differ between the two scans while the scan whose difference between the pulser and receiver angle is greatest appears to provide more information about the scatter of the ultrasound wave as it propagated through the laminated composite. The C-scan results for the pulser oriented at 10° and the receiver oriented at 18° were similar in shape and signal distribution to those obtained when the pulser was at 5° and the receiver was at 14° in Figure 5.19. In general, the same observations from varying the pulser orientation (section 5.4.2) can be made from varying the receiver orientation (section 5.4.3).

5.4.4 Rotating the Sample Relative to the Ultrasound Probes

This third study sought to better understand how rotating the sample relative to the ultrasound probes would vary the measured results. As seen in Figure 5.21, the 8 ply laminated composite started at an orientation of 0° relative to the z axis, where the z axis is parallel to the thickness of the laminate. Based on the definitions of the x and y axes in

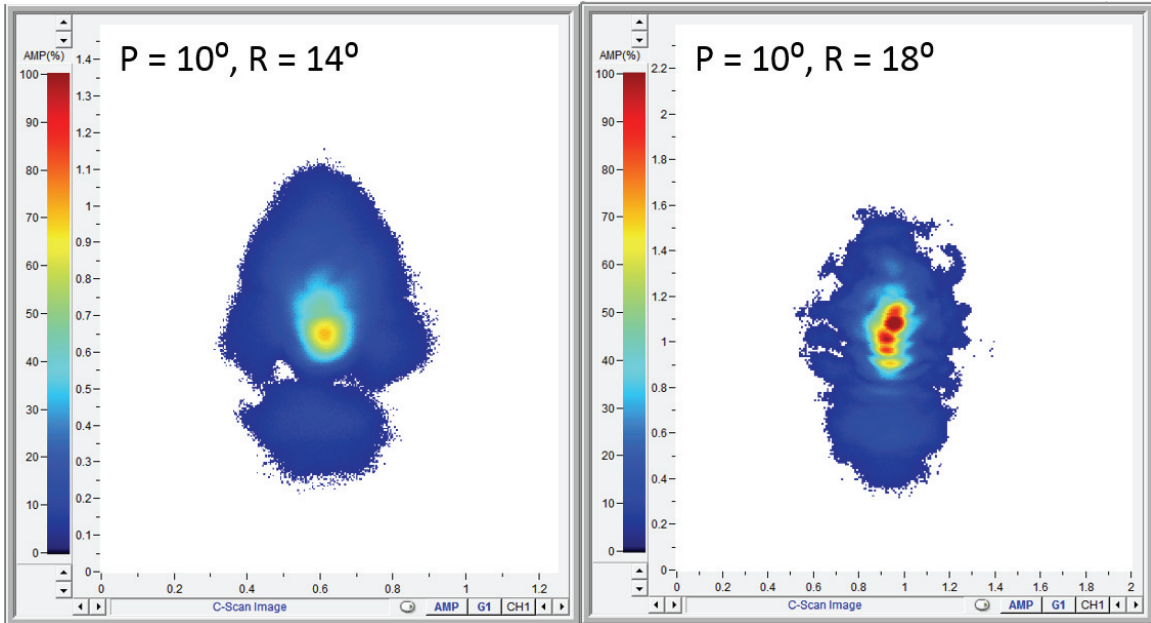


Figure 5.20 C-scan results for varying the angle of the receiving probe relative to the sample surface normal

the C-scan shown in Figure 5.21, the z axis would be coming out of the page. To obtain the second C-scan in Figure 5.21, the sample was rotated 45° about the z axis, and to obtain the third C-scan in Figure 5.21, the sample was rotated 90° about the z axis. The three C-scans presented in Figure 5.21 share many similarities including the same location of the longitudinal wave, approximately the same span along the y axis and along the x axis., and similar locations for the side lobes. One difference to note amongst the three C-scan figures is the slight variation in the extremities of the C-scan. For example, the side lobe located above the longitudinal wave for the rightmost C-scan in Figure 5.21 has much smaller signal amplitude than the topmost side lobe in either of the other two C-scans.

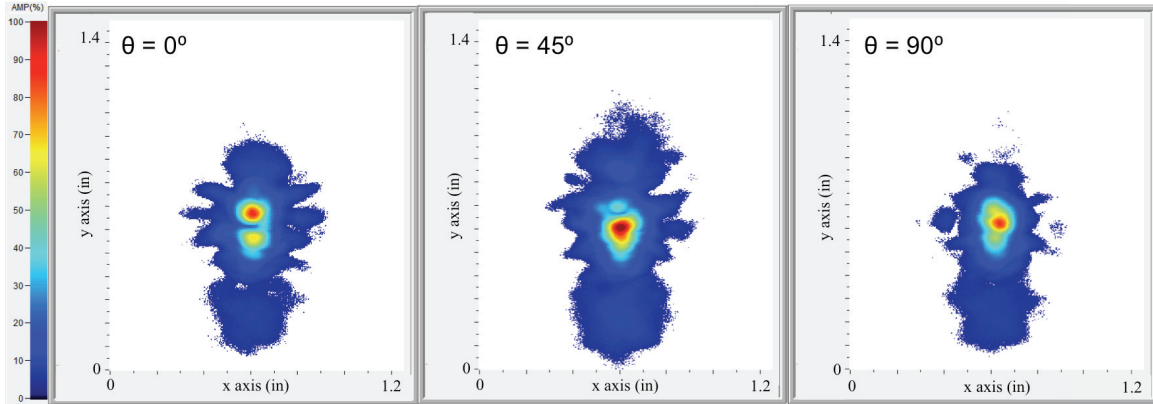


Figure 5.21 C-scan results for rotating 8 ply laminate sample with respect to the z axis

5.4.5 C-Scan Results Obtained for Different Laminate Thicknesses

The studies performed thus far in the present chapter have dealt with varying the orientation of different components within the experimental setup and observing how such changes affect the C-scan measurements. The present study looks at the results obtained for a 2 ply, 4 ply, 8 ply and 16 ply laminated carbon fiber reinforced composite. Please note the vertical axis on the 2 ply laminate results ranges from 0 to 1.75 inches and its horizontal axis ranges from 0 to 1.45 inches. The vertical axis for the remaining three C-scans in Figure 5.22 ranges from 0 to 2.3 inches and the horizontal axis ranges from 0 to 2 inches. The C-scans for each of the four laminates exhibit the side lobes that were discussed in section 5.4.1. Additionally, each of the four C-scans indicates a strong longitudinal wave signal; however, the high amplitude region on the 8 ply and 16 ply laminates appears to have multiple peaks where the longitudinal wave is expected to be located. Likely, the presence of multiple peaks near this location was caused by the increased thickness of the laminates as compared to the other two laminates. With the ultrasound wave propagating along the fabric weave, the ultrasound wave experiences more scatter in a thicker composite than it would in a thinner composite. Thus, the

longitudinal wave region on the C-scan appears as though it has many high amplitude peaks caused by the scattering of the wave as it propagated through the material. Future work performed with the mathematical model would assist in addressing this hypothesis.

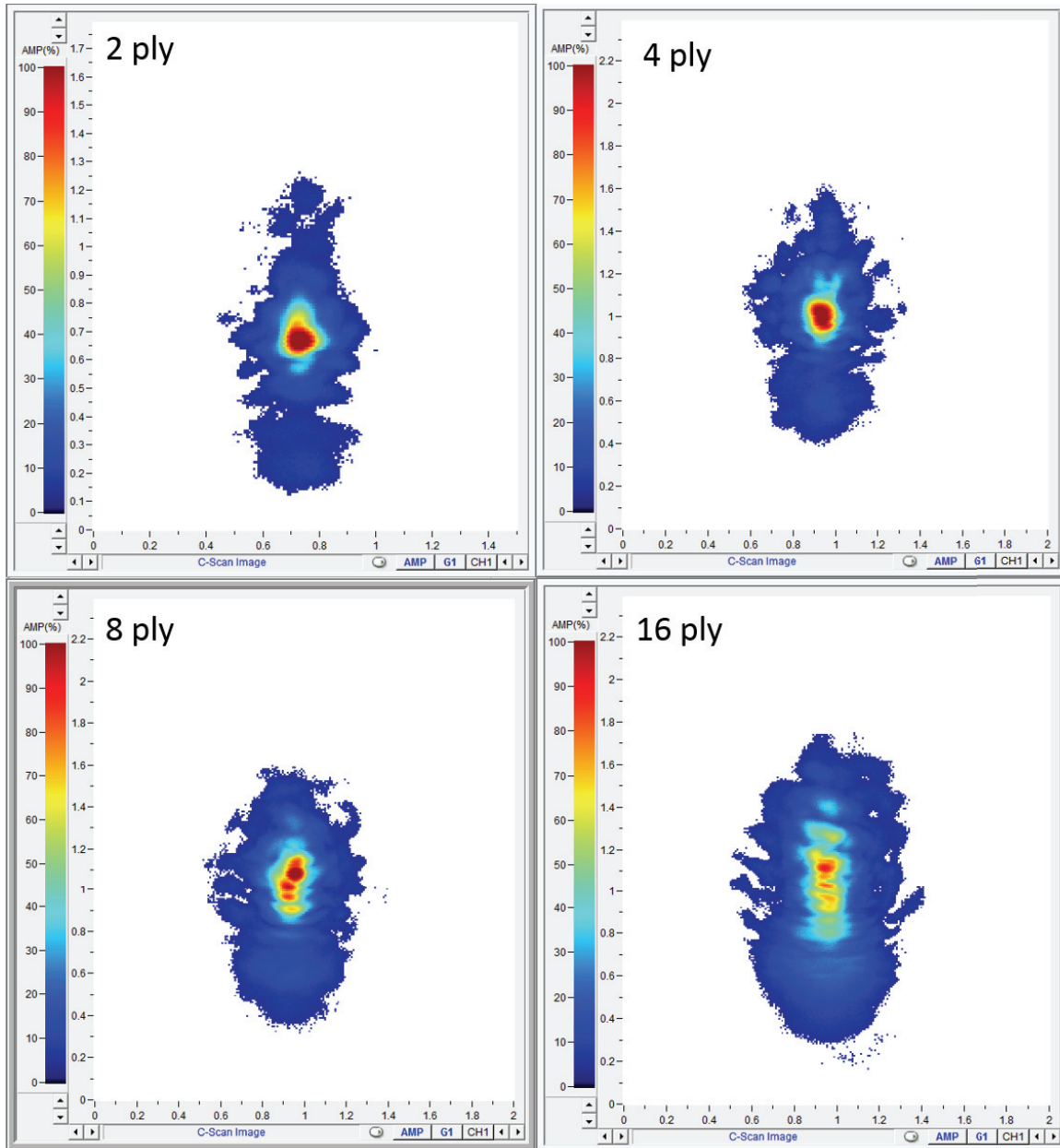


Figure 5.22 C-scan results obtained for 2, 4, 8, and 16 ply laminated composites with the pulse oriented at 10° and the receiver oriented at 18°

The spread of the C-scan results along the x axis appears to increase for increasing number of plies as well, which is expected based on the same argument as previously stated. As the wave propagates through thicker composites, the wave experiences a greater amount of diffraction, and subsequently, the wave spreads outward thus leading to a C-scan measurement that covers more of the x and y axes than it does for thinner fiber reinforced laminated composites.

5.5 Summary and Future Work

The purpose of the present study was to develop an oblique incident through transmission ultrasound technique for capturing the wave and how it diffracts as it propagates through the thickness of a laminated composite. Section 5.2 and 5.3 discussed the experimental setup and its application to the inspection of an aluminum plate. Based on the comparison of the calculated and measurement TOF for the longitudinal wave, the experimental technique applied in the present study provided reasonable results since the calculated and measured TOF values were nearly identical.

The oblique incident through transmission ultrasound technique was then applied to a carbon fiber reinforced laminated composite, the C-scan results were analyzed, and the calculated TOF for the longitudinal wave was compared with the measured TOF. Again, the calculated and measured longitudinal wave's TOF compared well with one another, which further supported the reasonableness of the measured results in the present study. The multiple experimental setup perturbations examined in section 5.4 provided insight as to how the pulser and receiver orientations affect the collected C-scan data. When the pulser and receiver are near the same orientation, the side lobes are located closer to the longitudinal wave than they are when the pulser and receiver are oriented

about 10° different than one another. The orientation of the composite laminate sample used in the present study relative to the z axis did not significantly alter the collected C-scan data. For example, the three C-scans shown in Figure 5.21 had similar features and minor differences from one another even though the laminate underwent 45° and 90° rotation relative to the z axis.

The final perturbation of the experiment involved inspecting different laminate thicknesses ranging from 2 plies to 16 plies. Based on the C-scan measurements, the thicker the laminate, the increased amount of wave scatter as the ultrasound wave propagates through the sample thickness. Thus, the C-scans corresponding to the 8 and 16 ply laminates appear to cover a wider range on the x and y axes of the plot. Furthermore, the longitudinal wave observed in the C-scans for the 2 and 4 ply laminates appeared to be concentrated in a small region that had high signal amplitude. For the 8 and 16 ply laminates, the longitudinal wave was still associated with the high amplitude region of the C-scan, but the region was larger than that observed for the 2 and 4 ply laminates. The increased wave scatter as the wave propagated through the thicker fiber reinforced laminated composites caused this increase in the size of the longitudinal wave region in the C-scan measurement.

The side lobes observed in the collected ultrasound data are unusual aspects of the C-scans captured using this ultrasound technique. Future work including comparison of the measured results with those predicted via a mathematical model will assist in addressing the hypothesis that the sensitivity of the side lobes to changes in material properties may assist in determining the elastic constants associated with a sample. A

discussion of the proposed mathematical model to be pursued in future work is provided in Chapter Six.

CHAPTER SIX

Conclusions and Future Work

6.1 Conclusions

As industries continue to incorporate larger amounts of composite materials into their product lines, there is an increasing need for nondestructive testing methods to guarantee these materials are capable of operating at required level of performance. A variety of nondestructive testing methods have been developed in the past 35 years in an attempt to address the growing needs of industry. The present dissertation contributed to this cause by presenting ultrasound methods for the inspection of the bondline between a laminated composite and a metal plate, regardless of which material is facing the transducer. Additionally, a through transmission ultrasound method presented in this dissertation for monitoring the phase and temperature of a material as it was exposed to both heating and cooling conditions, and an oblique incidence through transmission ultrasound method was presented as the first step in a larger project that seeks to identify the elastic constants of a laminated composite as well as learn how the ultrasound wave scatters as it propagates through a laminated composite. The conclusions drawn from each of these three studies are presented in sections 6.1.1 through 6.1.3.

6.1.1 Conclusions from the Bondline Analysis Study

The goal of the bondline analysis study was to identify the presence (or lack thereof) of a bond between a carbon fiber reinforced laminated composite and an aluminum plate. Two ultrasound pulse echo methods were applied to the inspection of

this sample: a contact transducer method and a spherically focused immersion transducer methods. For each ultrasound method applied in this study, the sample was inspected from both the carbon fiber reinforced laminated composite side as well as from the aluminum plate side. The purpose of inspecting the sample from both sides was to simulate a real world environment where a technician may not have access to both sides, and with paint covering the surface of the material, the inspector may not be able to identify whether the composite side or the aluminum side is facing the ultrasound transducer.

Both the contact probe and the spherically focused immersion probe were able to correctly identify the location of bonded and unbonded locations between the laminated composite and the aluminum plate, but the spherically focused immersion probe provided a better improved spatial resolution of 0.04 inches. Although the ultrasound wave lost more energy as it propagated through the laminated composite as compared to propagating through the aluminum plate, the location of unbonded regions between the two materials were successfully identified in this study. The sample of interest in this study included three different laminate thicknesses, and the inspection method was successfully applied to each of the three laminate thicknesses. One of the novel aspects of this study was the inspection of the bondline between dissimilar materials. As mentioned in the literature review, many of the previous studies focused on the bondline inspection between similar materials, such as two aluminum plates or two composite laminates. The bond between dissimilar materials in this study required the inspector to have an understanding of the difference in wave propagation when inspecting a laminated composite versus aluminum. The laminated composite attenuates the ultrasound signal

more quickly and also scatters the ultrasound signal more so than the aluminum. Thus, signal interpretation on such a sample can be more difficult.

The identification of the presence or absence of a bondline between the carbon fiber reinforced laminated composite and the aluminum plate was also performed via the Fast Fourier Transform analysis of the ultrasound data. From the FFT analysis, the frequency intensity can be used to identify whether a certain A-scan location is associated with a bonded location or an unbonded location. For example, an unbonded location has higher frequency intensity than a bonded location.

6.1.2 Phase and Temperature Monitoring of Highly Attenuative Materials via a Through Transmission Ultrasound Method

The second scientific contribution of the present work involved monitoring phase and temperature during the heating and cooling of two highly attenuative wax materials using a through transmission ultrasound technique. The two materials were studied independently of one another meaning that studies were performed on the EcoSoya soy-based wax prior to conducting experiments on the Rigidax machinist wax. Ultrasound transducers were placed along each of the long sides of the rectangular boxes holding the wax of interest such that the transducers on one side of the box were aligned with the transducers on the other side of the box. Thermocouple data was collected throughout the experiment using an array of thermocouples placed throughout the length and width of the box. The ultrasound data was collected using TD PocketScan software and was exported to Matlab for further analysis.

During the analysis, a variety of plots were generated for each channel including: the A-scan for each minute in time, the B-scan, the plot of the speed of sound versus

time, the plot of speed of sound versus temperature and an FFT analysis of each A-scan. From comparison of the A-scan figures generated for data throughout the test, the increase in the time of flight is observed as the wax material melts and a decrease in the time of flight is observed as the wax begins to re-solidify. The B-scan image is one of the most useful images generated from the ultrasound data because it presents data from throughout the experiment, shows the pronounced change in time of flight as the material changes phases from solid to liquid and vice versa, and shows details related to the ultrasound signal as the material transitions from a solid to a liquid, which is a feature not easily observed in the other analysis images. The speed of sound versus time graphs show the decrease in the speed of sound as the wax melts as well as the gradual increase in the speed of sound as the wax begins to re-solidify. The speed of sound versus temperature plots show the relationship between the measured speed of sound and temperature. Although the temperatures used in these plots were captured via the thermocouple measurements, by obtaining the relationship between the speed of sound and temperature with these plots, future experiments may be able to predict the temperature of the material by referencing these speed of sound versus temperature plots.

6.1.3 Conclusions from the Oblique Incidence Through Transmission Ultrasound Study

The final study in this dissertation focused on an oblique incidence through transmission ultrasound inspection of carbon fiber reinforced laminated composites. This study is the first prong in a two prong project that relates measured C-scan results to wave displacements calculated using a mathematical model based on the work of Newberry [1]. The experimental measurements obtained and presented in Chapter Five indicate how the wave scatters as it propagates through the laminated composite as well

as the location of side lobes of the ultrasound signal relative to the location of the longitudinal wave. The time of flight for the measured longitudinal wave was confirmed via time of flight calculations. Throughout the study presented in Chapter Five, a variety of the experimental parameters were studied including varying the pulser orientation, varying the receiver orientation, varying the rotation of the sample about the z axis (which is along the thickness of the composite laminate), and inspecting different laminate thicknesses.

In general, similar trends are observed throughout each of the C-scan inspections performed. When the pulser and receiver are closer to the same orientation angle, the side lobes appear to be located closer to the main portion of the longitudinal wave, but the further apart the pulser and receiver orientation angles, the further the side lobes appear to be from the main longitudinal wave location. As discussed in Newberry's dissertation [1], the anisotropy of the material affects the shape of the side lobes. The present author hypothesizes that these side lobes may be more sensitive to changes in the material's elastic constants than the main portion of the longitudinal wave, and would thus assist in providing more accurate results when seeking to determine the material's elastic constants via comparison with the mathematical model. However, to prove this hypothesis is correct, the mathematical model must be fully operational and the second prong of this larger project must be completed. Thus, the results of this hypothesis are proposed in section 6.2.3 as future work related to this project.

6.2 Future Work

Although a significant amount of work has been performed on each of the three studies presented in this dissertation, there are areas where future work may be pursued in

each of these projects. The following subsections will describe some of the proposed areas for future work along with a discussion on how these may be accomplished.

6.2.1 Future Work – Bondline Analysis Project

The bondline analysis study involved the inspection of a 4 ply, an 8 ply and a 12 ply laminated composite bonded to an aluminum plate. There are two areas of future work that are proposed with respect to this project. First, the thicker the composite, the more difficult it is for the ultrasound wave to propagate through the part thickness. Future work may consider thicker laminates as potential applications in the automotive and aerospace industries may require the use of laminates with an increased number of plies. Another area for future research is the bondline inspection of a curved sample comprised of the composite laminate and aluminum plate. The results presented in this dissertation dealt with a flat sample, but many real world applications involve parts that are not flat.

6.2.2 Future Work – Ultrasound Technique for Monitoring Material Phase and Temperature During Heating and Cooling

In Chapter Four of this dissertation, the phase and temperature of two different wax materials were analyzed using ultrasound data coupled with thermocouple data. From the results, the phase of the material can easily be identified by a variety of graphs, as previously discussed, and the temperature of the material has been related to the speed of sound values. Future work on this project may include applying this inspection technique to additional materials, such as polymers or a wax that has had glass microspheres mixed into the material. The glass microspheres in the later example would potentially scatter the ultrasound wave and pose a new and interesting research problem that could be addressed.

Future work may also be performed by looking at the derivatives of the speed of sound versus temperature plot and the speed of sound versus time plot. Such analysis may provide the user with additional information like a drastic change in slope related to the cooling portion of the experiment, such as when the material has reached the gel-like stage.

6.2.3 Future Work - Oblique Incidence Through Transmission Ultrasound Inspection Technique for Laminated Composites

The oblique incidence through transmission ultrasound inspection of the carbon fiber reinforced laminated composites provided the inspector with an idea of how the wave scatters as it propagates through the composite as well as where the side lobes are located relative to the longitudinal wave. The author has hypothesized that the side lobes may be more sensitive to changes in the material properties than the longitudinal wave and may be better able to assist in determining the elastic constants of the laminated composite when comparing the results to the mathematical model. The advised future work on this project is the completion of the mathematical model. The proposed mathematical model is based on the mathematical model developed by Newberry [1] in his dissertation. The model for this project would compare the time of flight for the peak wave displacement with the measured time of flight for the peak wave displacement. The mathematical model as described in Newberry's dissertation [1] is also described in the proceeding sections.

6.2.3.1 Calculating the sound pressure field in water. The initial sound pressure wave is defined as

$$p_o(x, y) = \begin{cases} p^* e^{\left(\frac{jk}{2}\right)\left(\frac{x^2+y^2}{f}\right)} & \text{if on probe face} \\ 0 & \text{elsewhere} \end{cases} \quad (6.1)$$

where $p_o(x, y)$ is the initial pressure at the probe face with respect to spatial coordinates x and y , p^* is the initial pressure of the wave, k is the wavenumber, and f is the focal length of the ultrasound probe.

Next, calculate the pressure field in the water, $p(x, y, z)$, as

$$p(x, y, z) = \sum_{m=0}^{\infty} \sum_{n=0}^{\infty} G_{mn} \Phi_{mn}(x, y, z) \quad (6.2)$$

where G_{mn} are constant coefficients defined as

$$G_{mn} = \left(\frac{1}{w_x(0)w_y(0)\pi 2^{m+n-1} m! n!} \right) \int_{-\infty}^{\infty} \int_{-\infty}^{\infty} p_o(x, y) \Phi_{mn}(x, y, 0) dy dx \quad (6.3)$$

where $w_x(0)$ and $w_y(0)$ refer to the initial beam widths in the x and y directions, respectively. Since the ultrasound probe is circular $w_x(0) = w_y(0)$ for this study. The term $\Phi_{mn}(x, y, 0)$ represents the scalar wave equation for time harmonic disturbances at $z = 0$ (the probe face) and is defined as

$$\Phi_{mn}(x, y, 0) = e^{\left(\frac{-jk}{2}\right)\left[\frac{x^2}{q_x(0)} + \frac{y^2}{q_y(0)}\right]} H_m \left[\frac{\sqrt{2}}{w_x(0)} x \right] H_n \left[\frac{\sqrt{2}}{w_y(0)} y \right] \quad (6.4)$$

where H_m and H_n represent the m^{th} and n^{th} order Hermite polynomials that are evaluated at the points indicated within the square brackets and $q_x(0)$ and $q_y(0)$ represent the wave's radius of curvature in the x and y directions.

From equation 6.2, the remaining term on the right hand side of the equation, $\Phi_{mn}(x, y, z)$, represents the scalar wave equation and is defined as

$$\Phi_{mn}(x, y, z) = \sqrt{\frac{w_x(0)w_y(0)}{w_x(z)w_y(z)}} e^{-jkz} e^{j[(2m+1)\psi_x(z)+(2n+1)\psi_y(z)]} \quad (6.5)$$

$$e^{-\left(\frac{jk}{2}\right)\left[\frac{x^2}{q_x(z)} + \frac{y^2}{q_y(z)}\right]} H_m\left[\frac{\sqrt{2}}{w_x(z)}x\right] H_n\left[\frac{\sqrt{2}}{w_y(z)}y\right]$$

where $w_x(z)$ and $w_y(z)$ are the beam widths defined as

$$w_x(z) = \left[\frac{-\lambda_z}{\pi \text{Im}\left(\frac{1}{q_x(z)}\right)} \right]^{1/2} \quad (6.6a)$$

$$w_y(z) = \left[\frac{-\lambda_z}{\pi \text{Im}\left(\frac{1}{q_y(z)}\right)} \right]^{1/2} \quad (6.6b)$$

with the terms $q_x(z)$ and $q_y(z)$ defined as

$$q_x(z) = q_x(0) + z \quad (6.7a)$$

$$q_y(z) = q_y(0) + z \quad (6.7b)$$

The terms $\psi_x(z)$ and $\psi_y(z)$ in equation 6.5 represent the difference in phase angle from the initial phase angle to that associated with coordinate z , which are defined as

$$\psi_x(z) = \frac{1}{2} [\angle q_{x0} - \angle q_x(z)] \quad (6.8a)$$

$$\psi_y(z) = \frac{1}{2} [\angle q_{y0} - \angle q_y(z)] \quad (6.8b)$$

The pressure field in the water is calculated from the ultrasound probe face until the wave enters the sample of interest. For this study, the sample of interest is a carbon fiber reinforced laminated composite. As was discussed in relation to Snell's Law, a portion of the incident ultrasound wave refracts into the sample as a longitudinal wave, a portion of the incident ultrasound wave refracts into the sample as a shear wave, and the remaining portion of the incident ultrasound wave reflects off of the surface of the sample. The following subsection will describe the equation needed to calculate the refracted waves.

6.2.3.2 Calculating the transmission of the wave from the water into the sample.

As the ultrasound wave approaches the sample surface, part of the wave refracts into the sample, and the remainder of the wave reflects back toward the transducer. The $q_x(z)$ and $q_y(z)$ values from the location just prior to entering the sample will be used in the following equations for calculating the $q_x(z)$ and $q_y(z)$ for the transmitted wave. Let subscript 'T' refer to quantities associated with the transmitted wave and subscript 'I' refer to quantities associated with the incident wave (the wave that propagated through the water). Equations 6.9a and 6.9b define the transmitted values of $q_x(z)$ and $q_y(z)$.

$$\left(\frac{1}{q_x}\right)_T = \left(\frac{S_w \cos^2(\psi_{cf}) \cos^2(\phi_w)}{S_{cf} \cos^2(\psi_w) \cos^2(\phi_{cf})}\right) \left(\frac{1}{q_x}\right)_I - \frac{\cos^2 \psi_{cf} \left((S_w/S_{cf}) \cos(\theta_w) - \cos(\theta_{cf}) \right)}{B_x \cos^2(\phi_{cf})} \quad (6.9a)$$

$$\left(\frac{1}{q_y}\right)_T = \left(\frac{S_w}{S_{cf}}\right) \left(\frac{1}{q_y}\right)_I - \frac{\left(\frac{S_w}{S_{cf}}\right) - 1}{B_y} \quad (6.9b)$$

where the terms with a subscript 'w' refer to quantities associated with the water and terms with a subscript 'cf' correspond to quantities for the carbon fiber reinforced

laminated composite. The S terms in equations 6.9a and 6.9b represent the slowness values for the water and the carbon fiber reinforced laminated composite. Since two waves propagate through the composite (a longitudinal wave and a shear wave), equations 6.9a and 6.9b must be evaluated twice, once for each wave propagating through the laminate. The terms B_x and B_y represent the radius of the interface between the two materials.

Equations 6.9a and 6.9b represent the general case of transmitting a wave across the boundary between two materials, and the second term on the right hand side of each of these two equations accounts for the curvature of the boundary surface. If the boundary is flat, as is the case in the present study, then equations 6.9a and 6.9b simplify to the following

$$\left(\frac{1}{q_x}\right)_T = \left(\frac{S_w \cos^2(\psi_{cf}) \cos^2(\phi_w)}{S_{cf} \cos^2(\psi_w) \cos^2(\phi_{cf})}\right) \left(\frac{1}{q_x}\right)_I \quad (6.10a)$$

$$\left(\frac{1}{q_y}\right)_T = \left(\frac{S_w}{S_{cf}}\right) \left(\frac{1}{q_y}\right)_I \quad (6.10b)$$

6.2.3.3 Performing the Christoffel analysis. Knowing the density (ρ) of the carbon fiber reinforced laminated composite and estimating the stiffness tensor for the bulk laminate (C_{ijkl}), the phase velocity (v_p) and polarization directions (d_k) for the laminate can be calculated using the Christoffel equation as

$$(C_{ijkl} \tau_i \tau_l - \rho v_p^2 \delta_{jk}) \widehat{d}_k = 0 \quad (6.11)$$

where τ_i represents the propagation direction associated with the ultrasound wave and δ_{jk} is the Kronecker delta. Equation 6.11 is of the same form as an eigenvalue problem (see

e.g., equation 6.12) where the phase velocities (v_p) are equal to the eigenvalues (λ) and the polarization directions are equal to the eigenvectors.

$$|\mathbf{A} - \lambda\mathbf{I}| = 0 \quad (6.12)$$

The Christoffel analysis is repeated for a variety of wave propagation directions, and the results of the analysis are used for creating a slowness surface. The slowness is defined as the inverse of the phase velocity. From the slowness surface, perform a regression near the direction where the wave is propagating and obtain the values of the constants S_o and A through E in the following equation.

$$\left(\frac{k}{\omega}\right) \cong S_o + A\left(\frac{k_x}{\omega}\right) + B\left(\frac{k_y}{\omega}\right) + C\left(\frac{k_x}{\omega}\right)^2 + D\left(\frac{k_x}{\omega}\right)\left(\frac{k_y}{\omega}\right) + E\left(\frac{k_y}{\omega}\right)^2 \quad (6.13)$$

where k is the slowness, k_x is the slowness in the x -direction and k_y is the slowness in the y -direction. This analysis will be performed twice; once for each the longitudinal wave and the shear wave propagating through the laminate composite. The constants S_o and A through E will be used in the following section while calculating the wave displacement within the laminated composite.

6.2.3.4 Calculating the wave displacement within the sample. Using the values of $q_x(z)$ and $q_y(z)$ as calculated in equations 6.10a and 6.10b for the transmitted wave as the incident values (q_{x0} and q_{y0}) for the propagation within the laminate, calculate the wave displacement $u(x, y, z, t)$ for the ultrasound wave using Equation 6.14.

$$\underline{u}(x, y, z, t) = \sum_{m=0}^{\infty} \sum_{n=0}^{\infty} G_{mn} \underline{u}_{mn}(x, y, z, t) \quad (6.14)$$

where G_{mn} are the same constant coefficients as defined in equation 6.3 and $\underline{u}_{mn}(x, y, z, t)$ is the wave displacement corresponding to the m^{th} and n^{th} order Hermite polynomial with $\underline{u}_{mn}(x, y, z, t)$ defined as

$$\begin{aligned} \underline{u}_{mn}(x, y, z, t) = & \hat{d}^i(0,0)u_o \sqrt{\frac{w_{x0}w_{y0}}{w_x(z)w_y(z)}} e^{(j\omega_o(t-S_o z))} \\ & e^{j[(2m+1)\psi_x(z)+(2n+1)\psi_y(z)]} \\ & e^{\left\{\frac{-j\pi[(x+Az)^2+(y+Bz)^2]}{\lambda_z \left[\frac{1}{q_x(z)} + \frac{1}{q_y(z)} \right]}\right\}} \end{aligned} \quad (6.15)$$

where $w_x(z)$ and $w_y(z)$ are as defined in equations 6.6a and 6.6b, respectively, $\psi_x(z)$ and $\psi_y(z)$ are as defined in equations 6.8a and 6.8b, respectively, and $q_x(z)$ and $q_y(z)$ are defined as

$$q_x(z) = q_{x0} + \left(\frac{\Lambda_x}{\lambda_z}\right)z \quad (6.16a)$$

$$q_y(z) = q_{y0} + \left(\frac{\Lambda_y}{\lambda_z}\right)z \quad (6.16b)$$

where the terms Λ_x and Λ_y are defined as

$$\Lambda_x = \frac{2\pi}{\omega_o S_o} (1 - CS_o) \quad (6.17a)$$

$$\Lambda_y = \frac{2\pi}{\omega_o S_o} (1 - ES_o) \quad (6.17b)$$

At this point, all of the values needed to compute the wave displacement in equation 6.14 are known. To compare the model with the experimental results, the author would propose bringing the ultrasound data from the time domain into the frequency domain using the FFT so that the measured results may be compared to the calculated results for the 5 MHz frequency content alone rather than for all frequencies exhibited by

the ultrasound probe. The measured results and the results calculated from the mathematical model would be normalized such that the peak value is one and the minimum value is negative one. Then a comparison of the wave displacement from the mathematical model to the measured results may be performed. If the measured and calculated results do not match one another, the elastic constants used in the model will be perturbed and the model calculations will be performed again until the measured and calculated results match one another, at which point the elastic constants of the material have been determined. Again, this is the future work proposed on the oblique incidence through transmission ultrasound inspection project, and there will likely be some additional items that will need to be addressed as the model is being written. However, section 6.2.3 has attempted to provide a good explanation of the author's interpretation of how to incorporate the model into this two-prong oblique incident through transmission project.

APPENDICES

APPENDIX A

Additional Results from Bondline Inspection

A.1 Contact Transducer Results

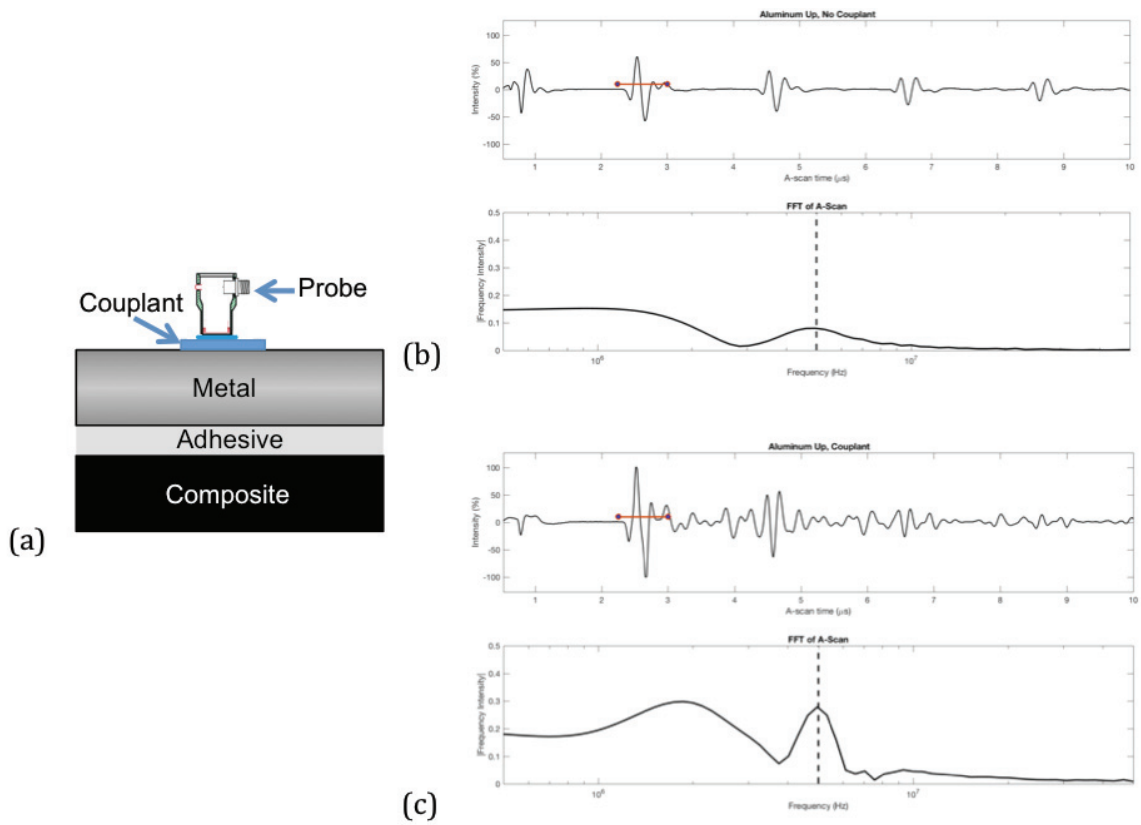


Figure A.1 (a) Contact transducer inspection of aluminum-to-composite bondline for 4 ply laminate region. Results for (b) no couplant and (c) couplant between the two adherends.

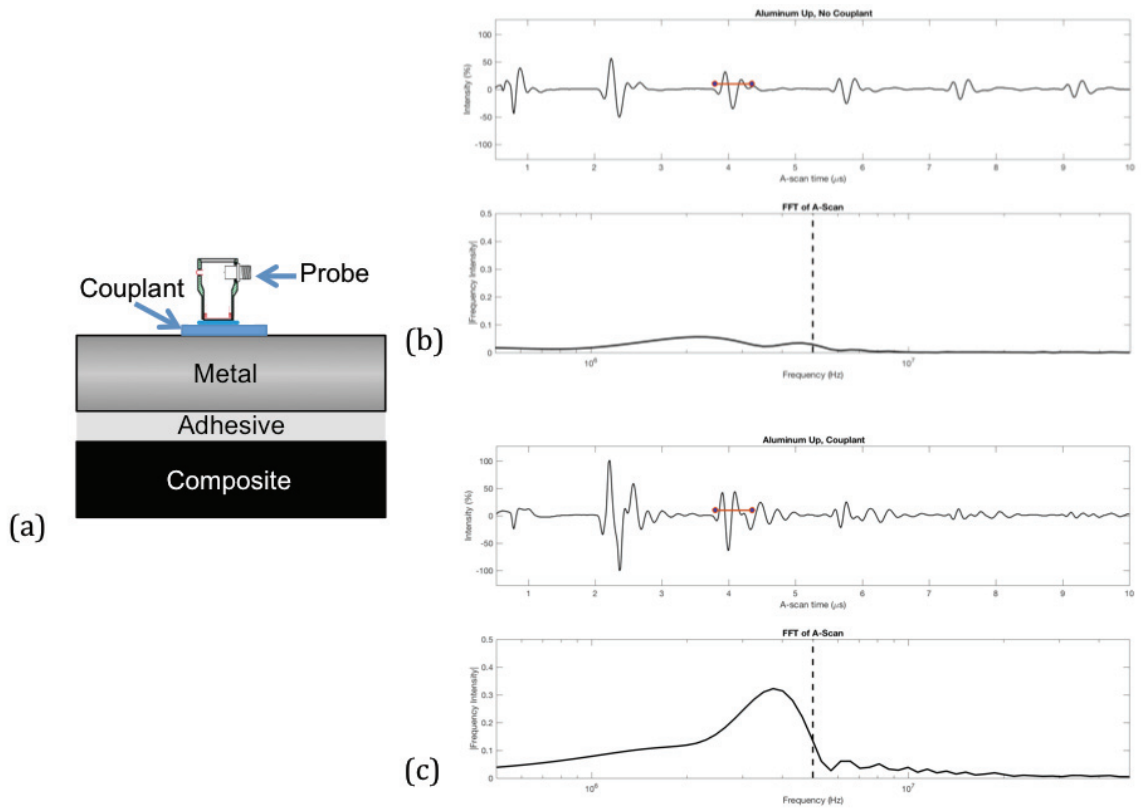


Figure A.2 (a) Contact transducer inspection of aluminum-to-composite bondline for 8 ply laminate region. Results for (b) no couplant and (c) couplant between the two adherends.

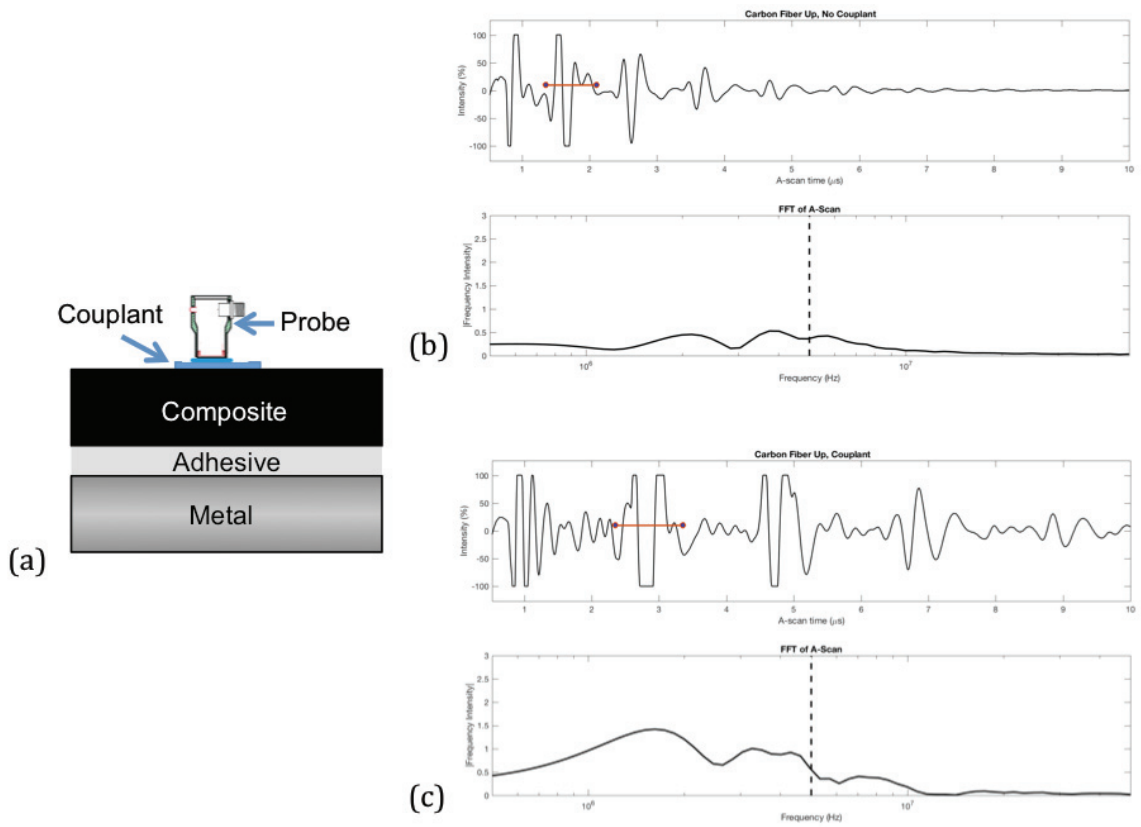


Figure A.3 (a) Contact transducer inspection of composite-to-aluminum bondline for 4 ply laminate region. A-scan (top) and FFT (bottom) results for (b) no couplant and (c) couplant between the two adherends.

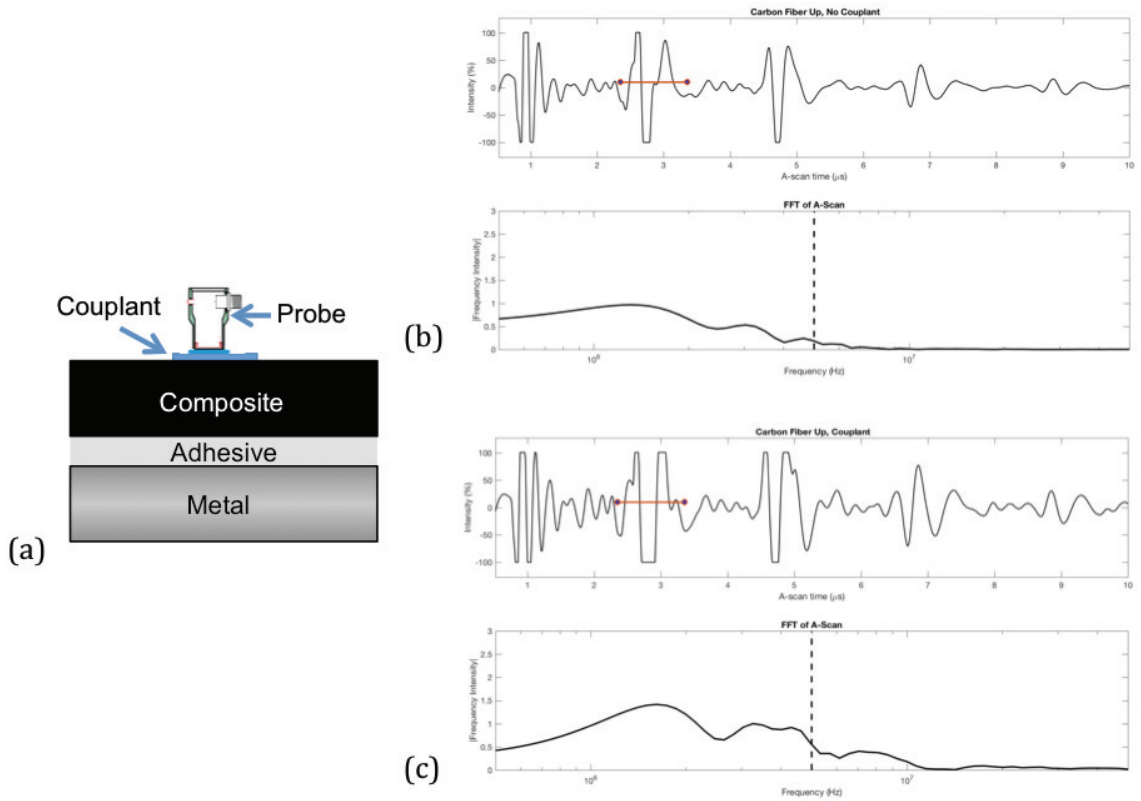


Figure A.4 (a) Contact transducer inspection of composite-to-aluminum bondline for 8 ply laminate region. Results for (b) no couplant and (c) couplant between the two adherends

A.2 Immersion Inspection Results

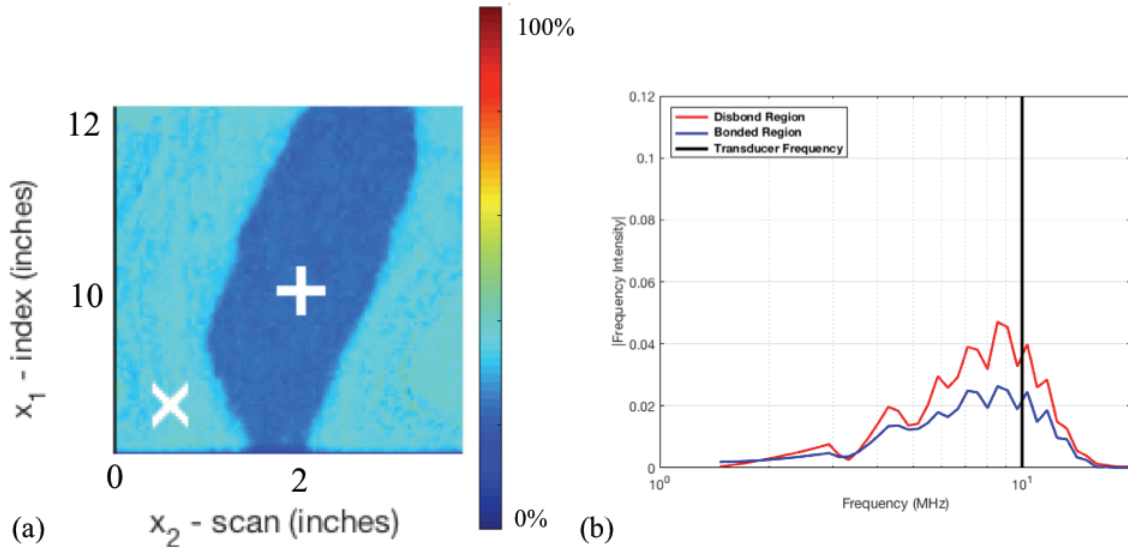


Figure A.5 (a) C-scan image of the bondline at the aluminum-to-composite interface for the 4 ply laminate region of the co-cured sample inspected with the immersion ultrasound method. (b) FFT results for the gated region of the A-scan corresponding to the bondline.

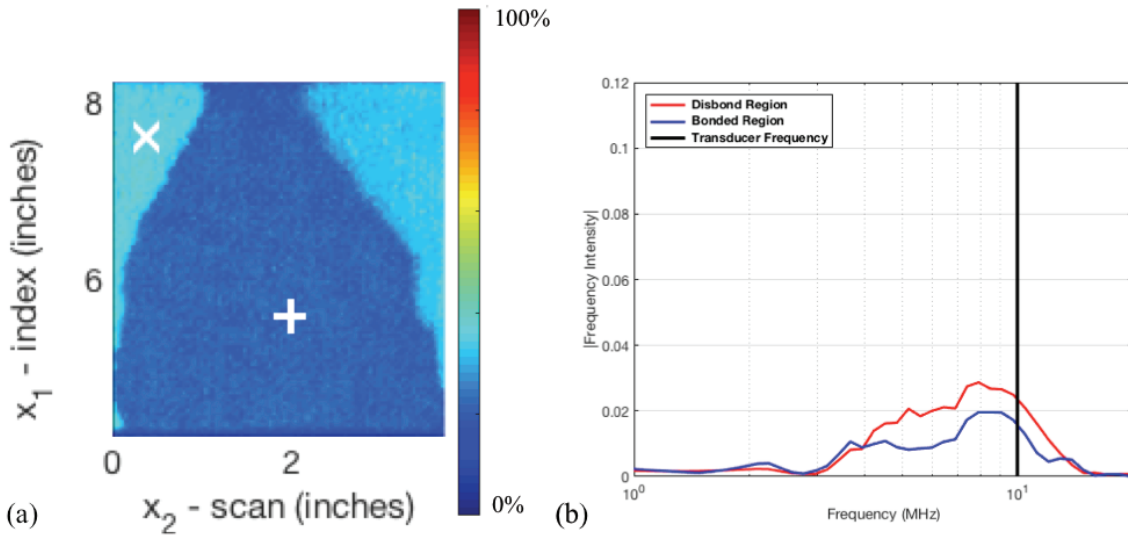


Figure A.6 (a) C-scan image of the bondline at the aluminum-to-composite interface for the 8 ply laminate region of the co-cured sample inspected with the immersion ultrasound method. (b) FFT results for the gated region of the A-scan corresponding to the bondline

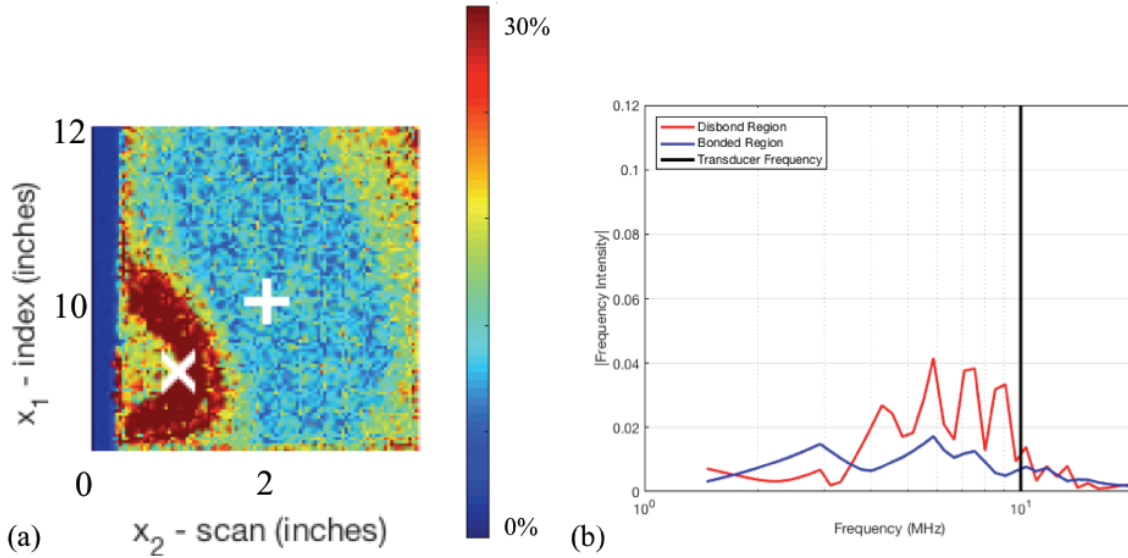


Figure A.7 (a) C-scan image of the bondline at the composite-to-aluminum interface for the 4 ply laminate region of the co-cured sample inspected with the immersion ultrasound method. (b) FFT results for the gated region of the A-scan corresponding to the bondline

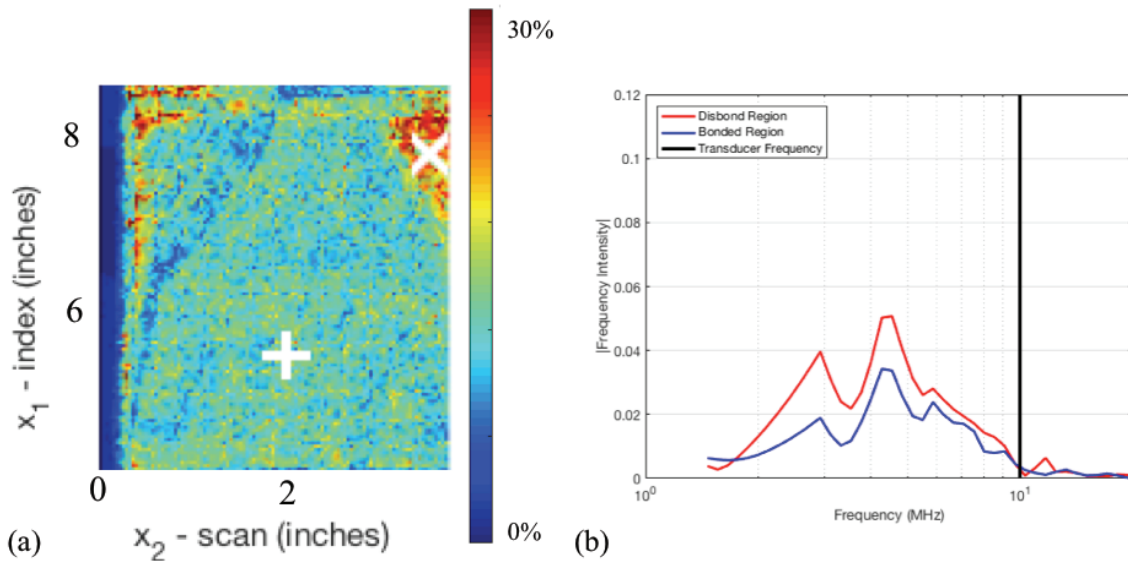


Figure A.8 (a) C-scan image of the bondline at the aluminum-to-composite interface for the 8 ply laminate region of the co-cured sample inspected with the immersion ultrasound method. (b) FFT results for the gated region of the A-scan corresponding to the bondline

APPENDIX B

Results from Additional Wax Experiments

B.1 Results from EcoSoya Experiment Two

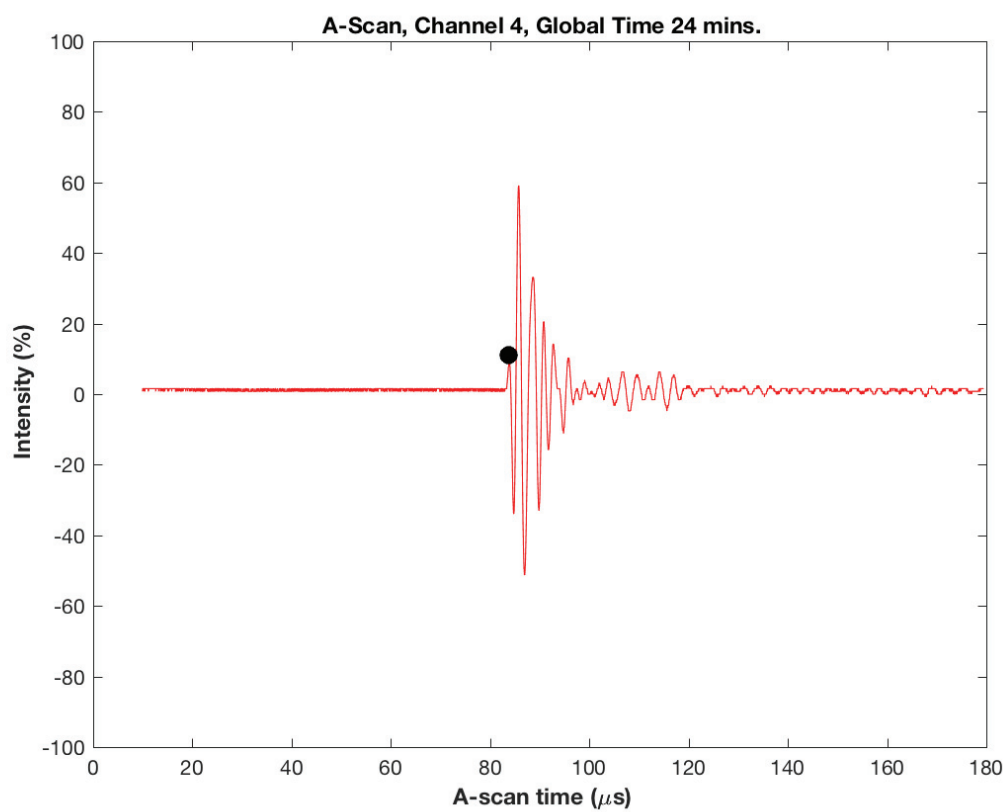


Figure B.1 A-scan signal associated with the solid EcoSoya wax. The black dot indicates the first point that meets or exceeds the amplitude threshold.

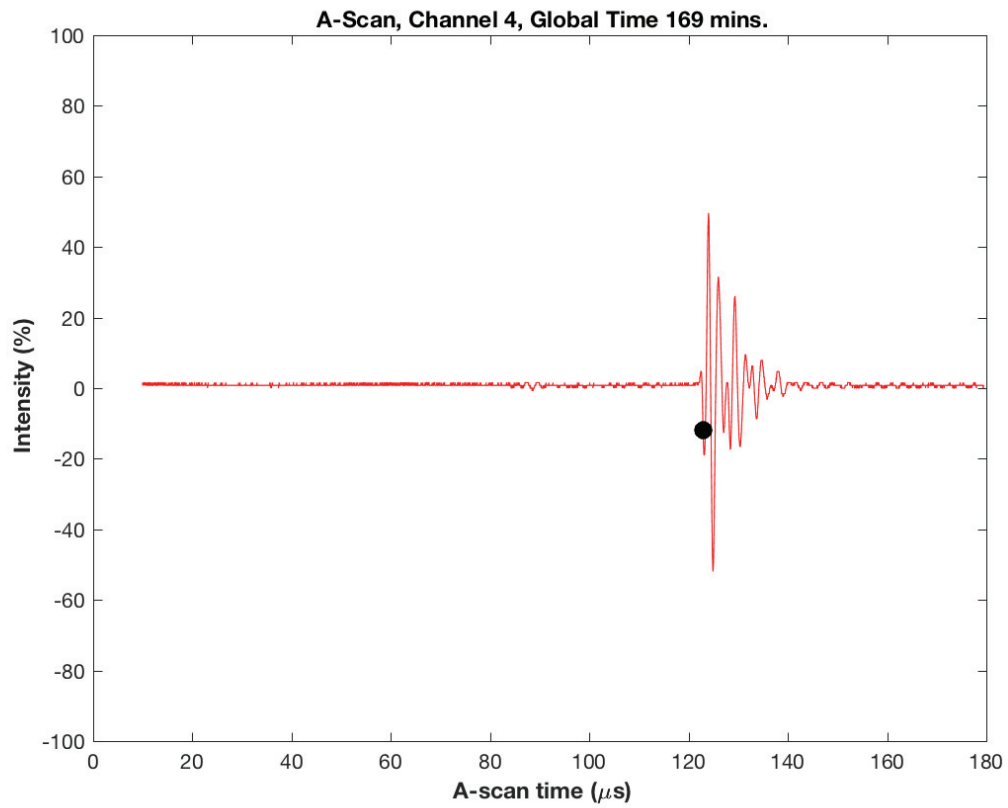


Figure B.2 A-scan signal associated with the liquid EcoSoya wax. The black dot indicates the first point that meets or exceeds the amplitude threshold.

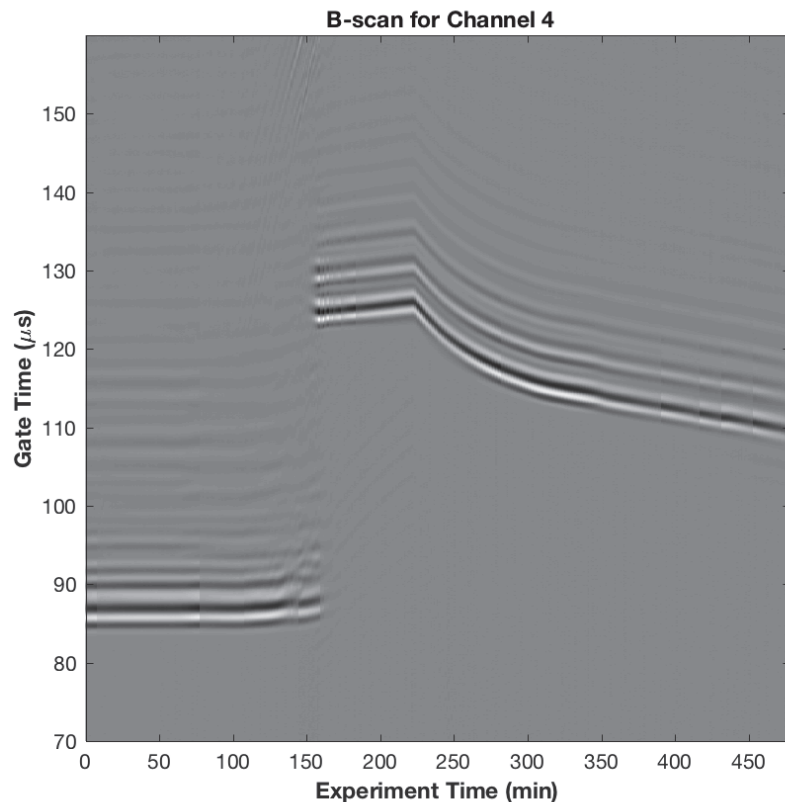


Figure B.3 B-scan for channel 4, which is located farthest away from the heater.

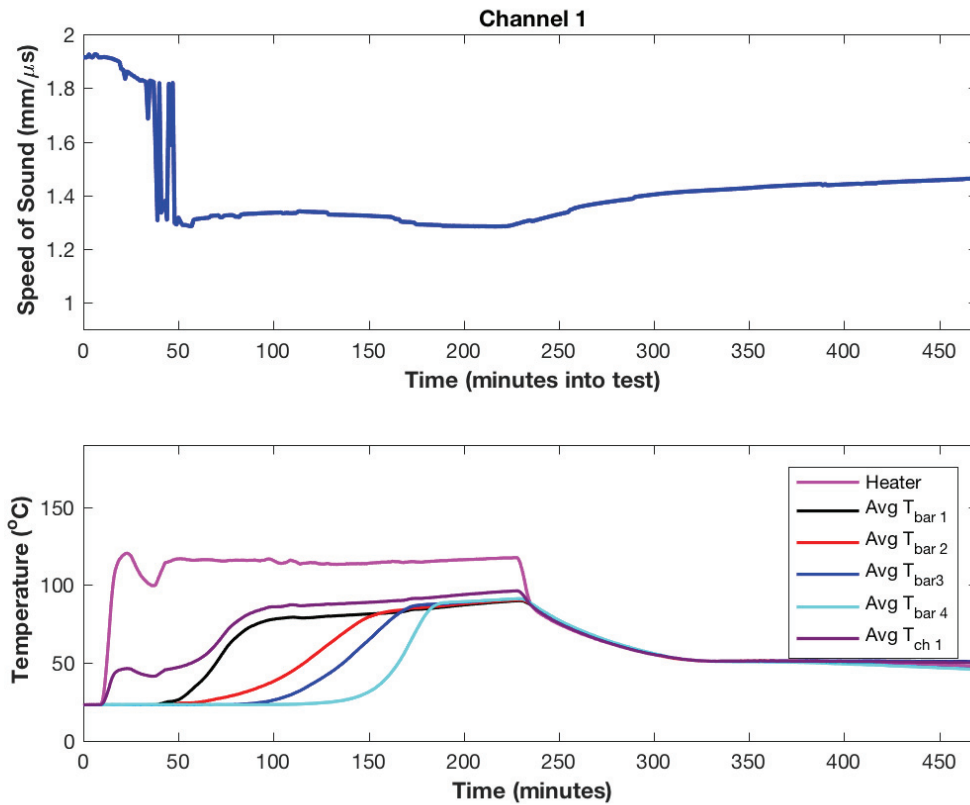


Figure B.4 The speed of sound for channel 1 (top), which is located closest to the heater, and the temperature measured via thermocouples throughout the experiment (bottom).

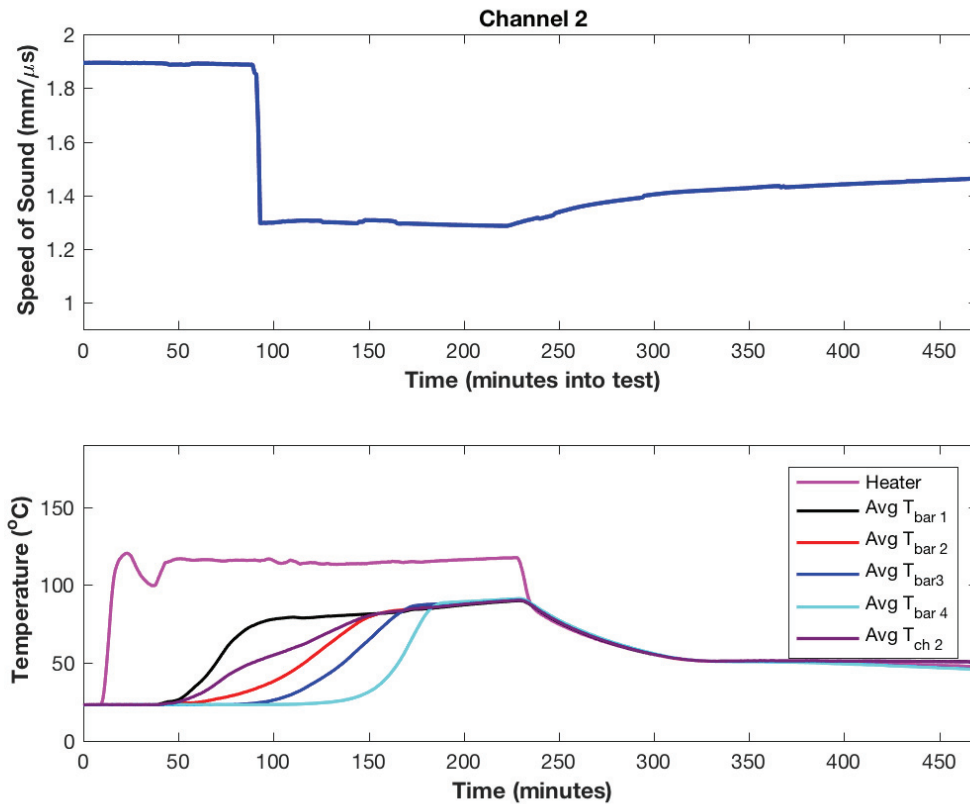


Figure B.5 The speed of sound for channel 2 (top), and the temperature measured via thermocouples throughout the experiment (bottom)

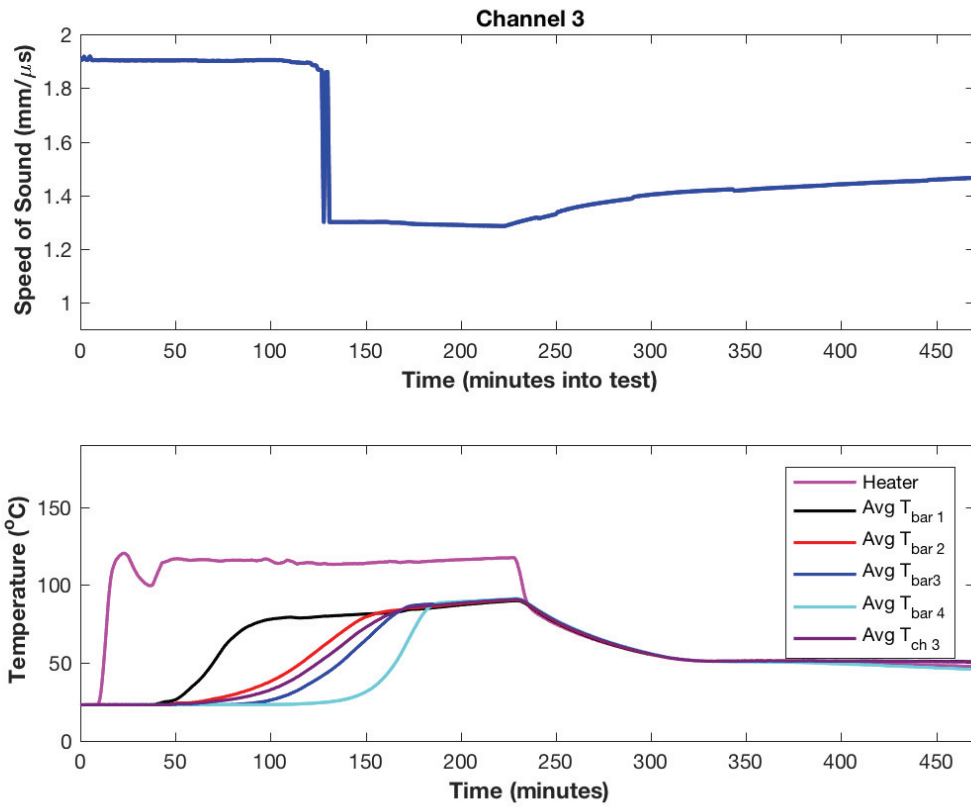


Figure B.6 The speed of sound for channel 3 (top), and the temperature measured via thermocouples throughout the experiment (bottom)

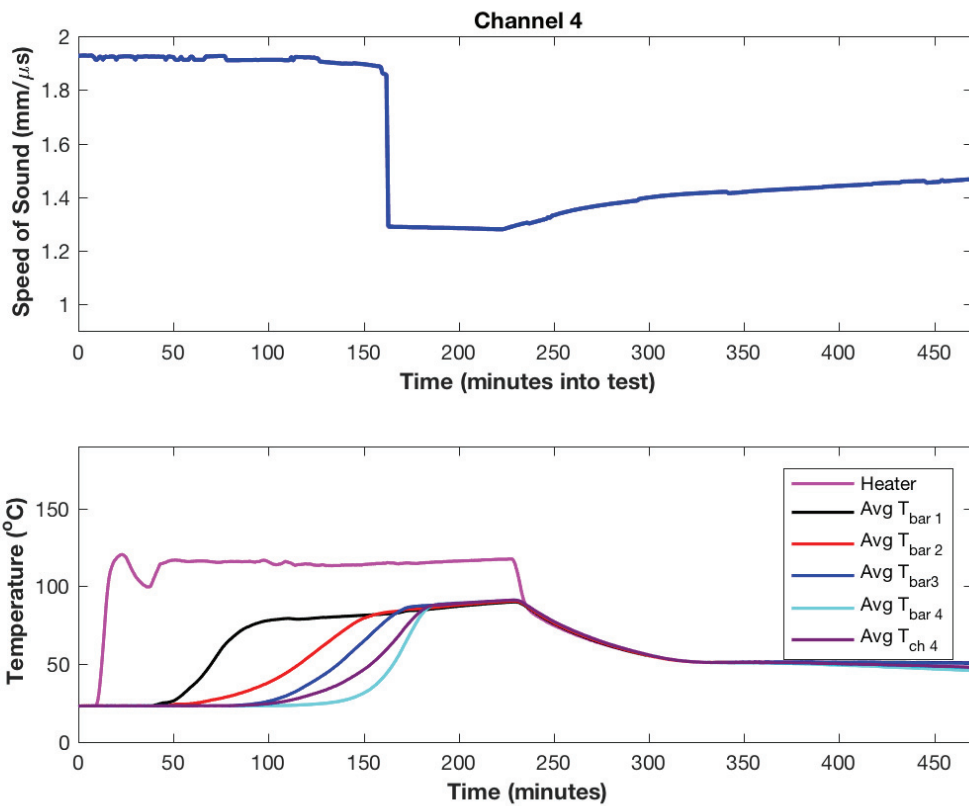


Figure B.7 The speed of sound for channel 4 (top), and the temperature measured via thermocouples throughout the experiment (bottom)

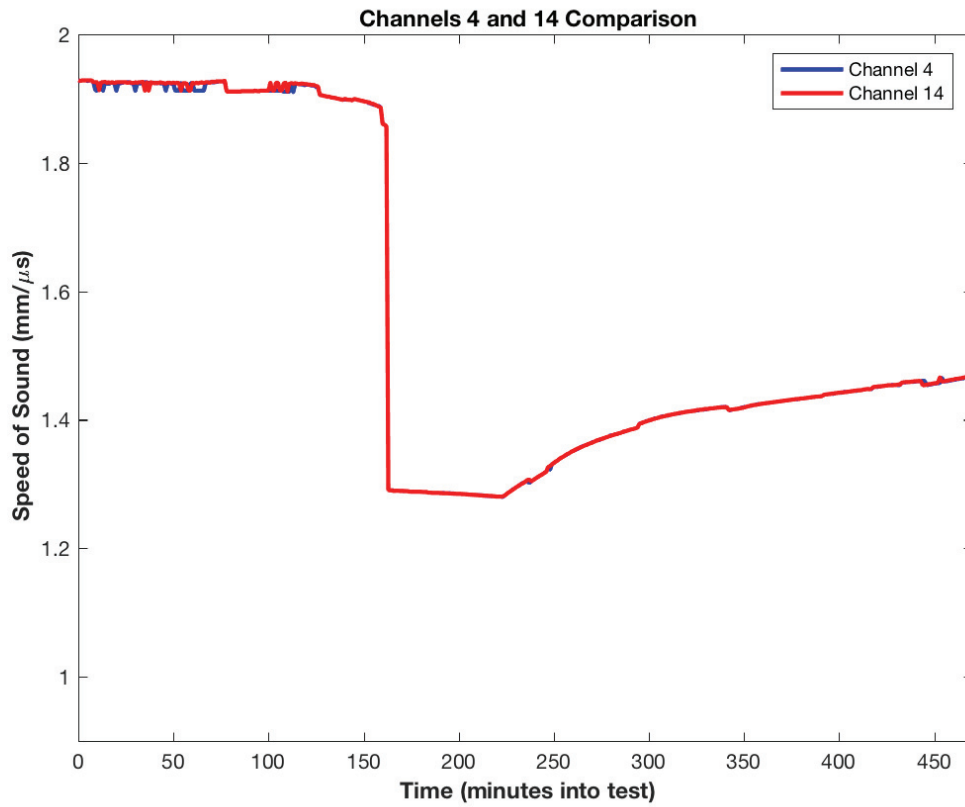


Figure B.8 Comparing the calculated speed of sound for channels 4 and 14.

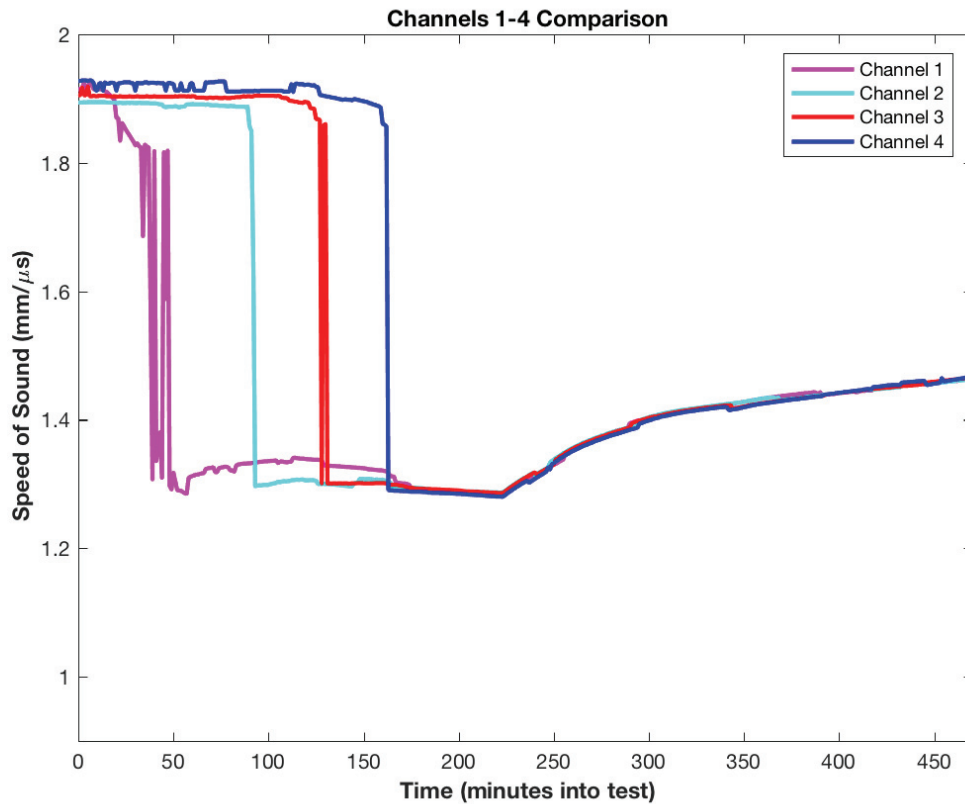


Figure B.9 Comparing the calculated speed of sound for channels 1 through 4.

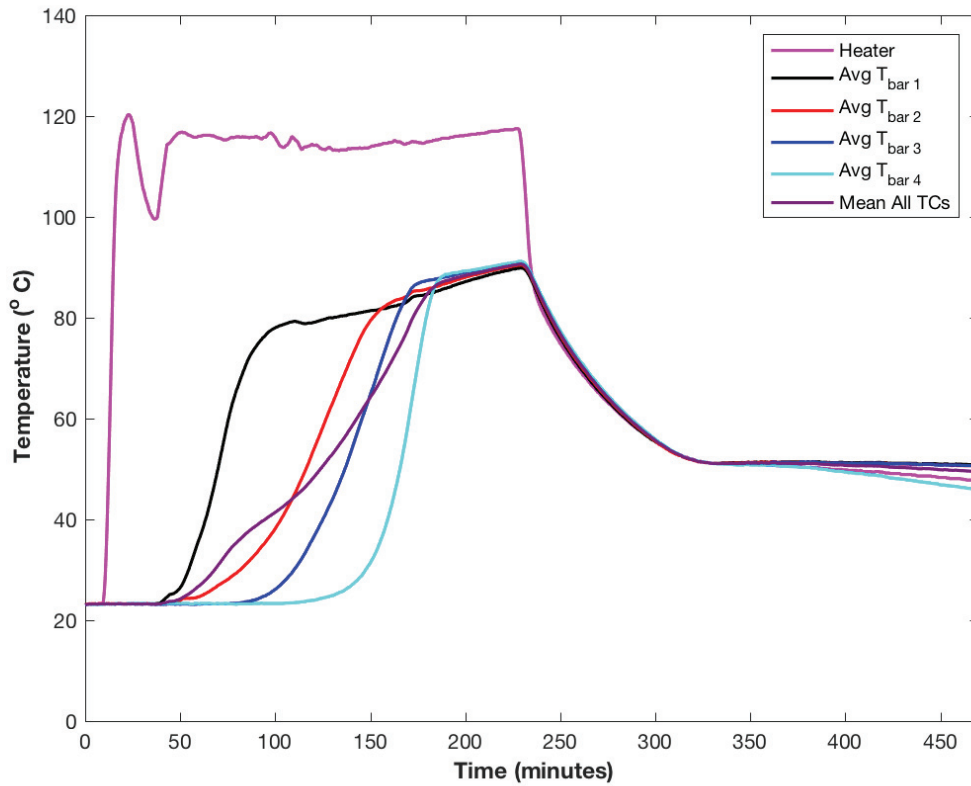


Figure B.10 The temperature throughout the experimental setup as monitored by the thermocouples. The average temperature for each bar of thermocouples has been included in this image along with the temperature at the heater block.

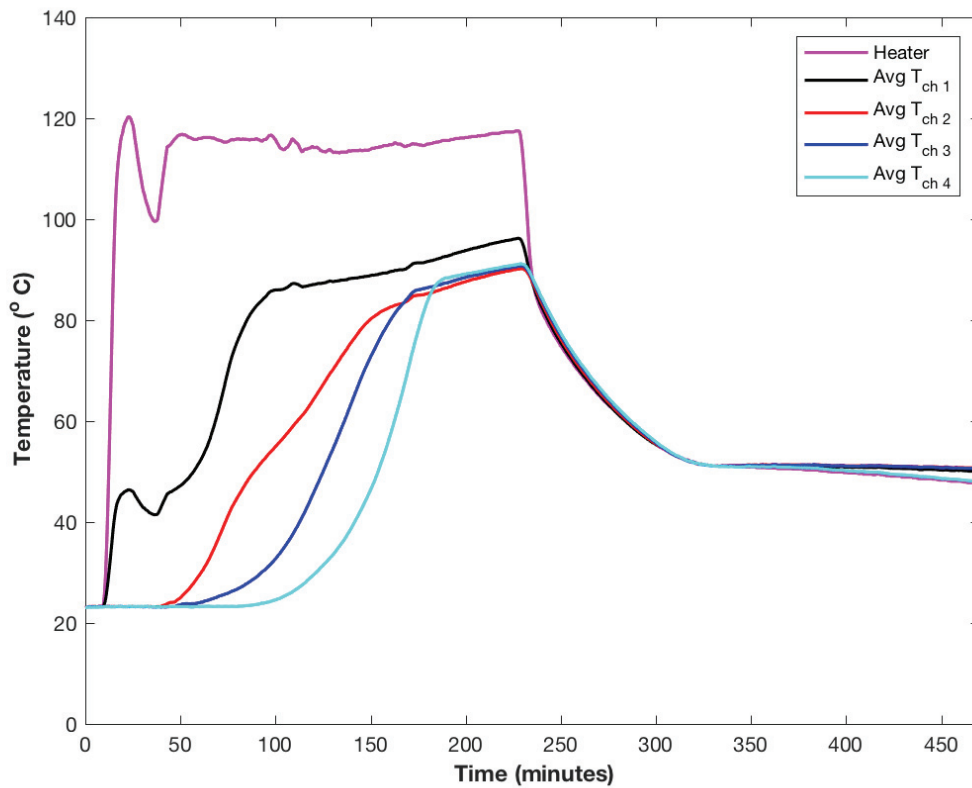


Figure B. 11 The temperatures calculated along the ultrasound probe path for channels 1 through 4.

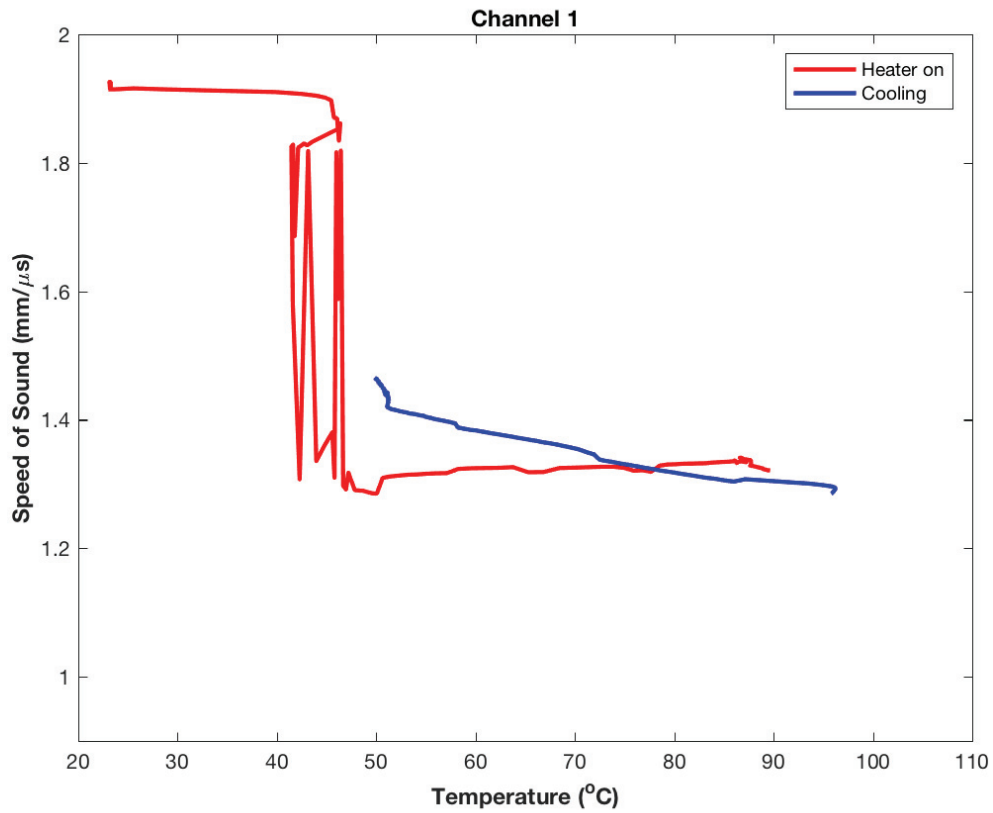


Figure B.12 The speed of sound versus temperature for channel 1, which is located closest to the heater block.

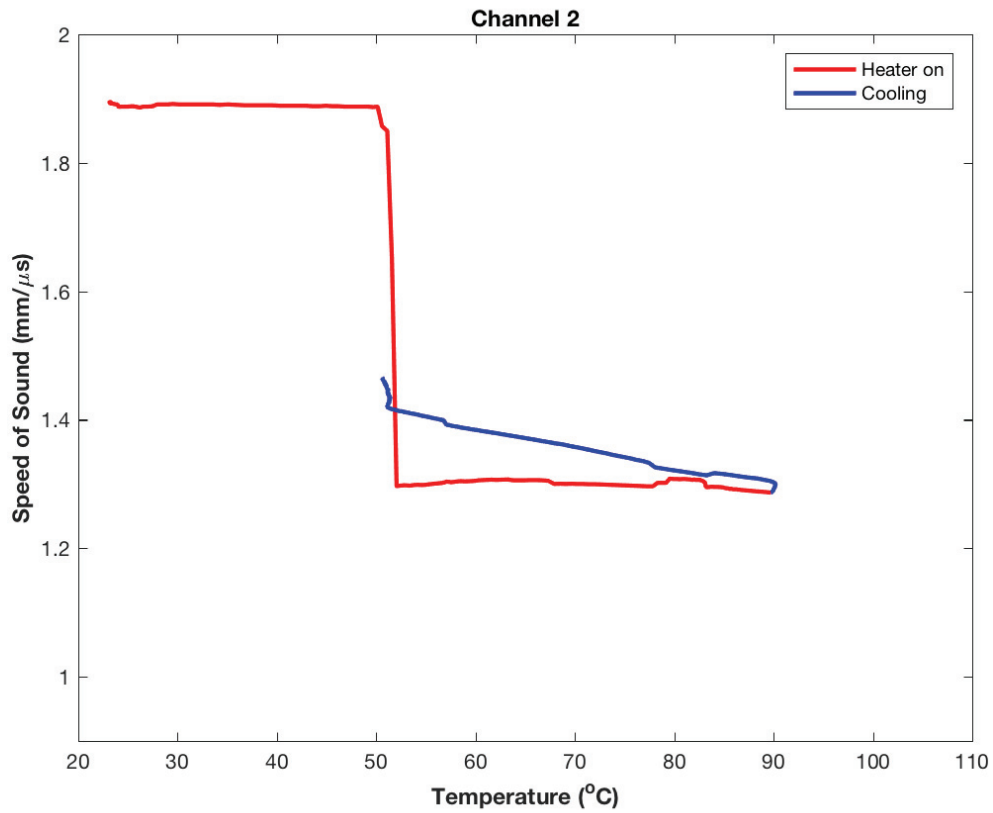


Figure B.13 The speed of sound versus temperature at channel 2.

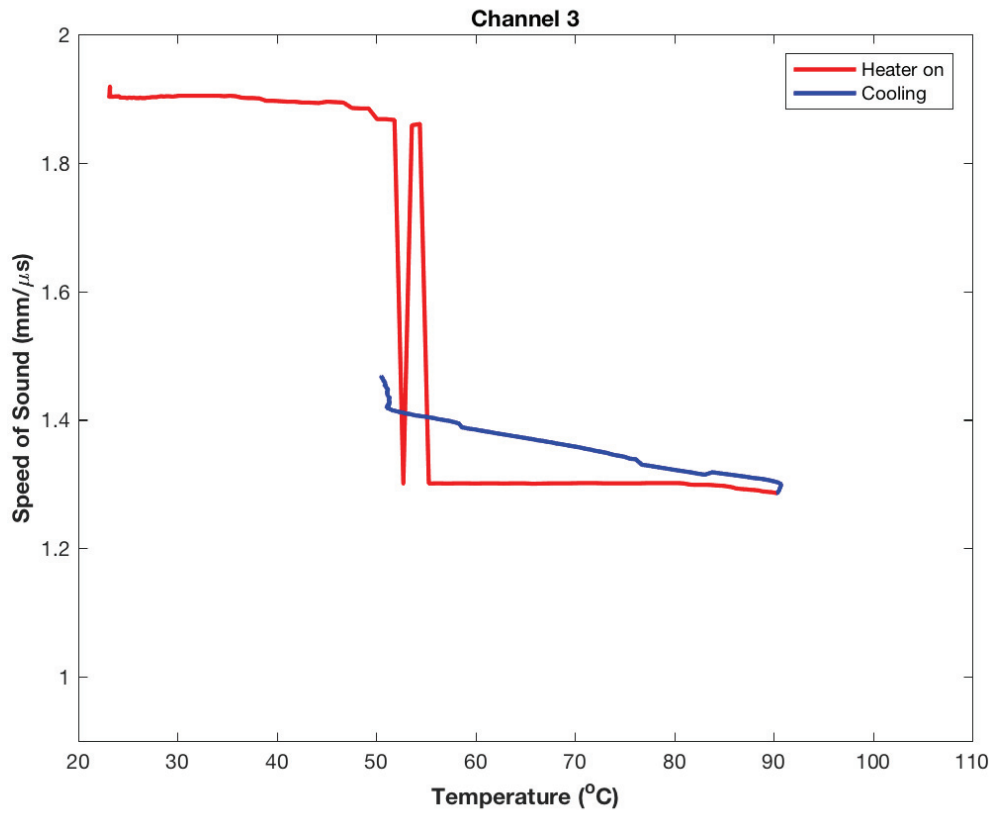


Figure B.14 The speed of sound versus temperature at channel 3.

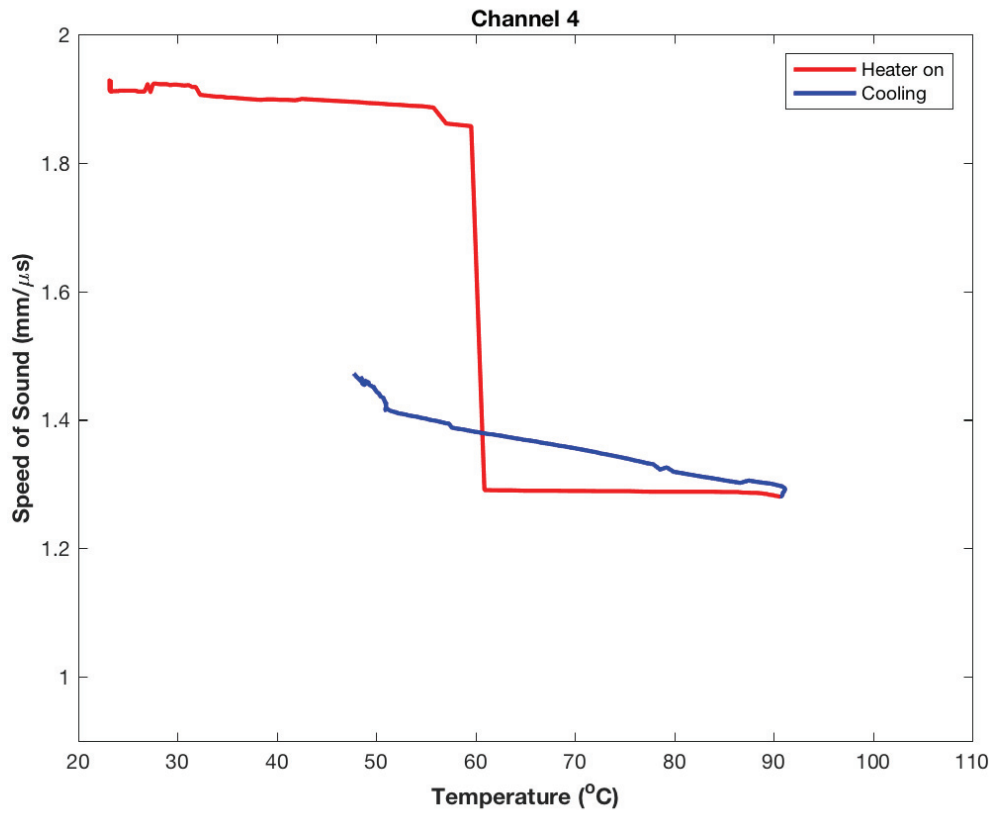


Figure B.15 The speed of sound versus temperature at channel 4.

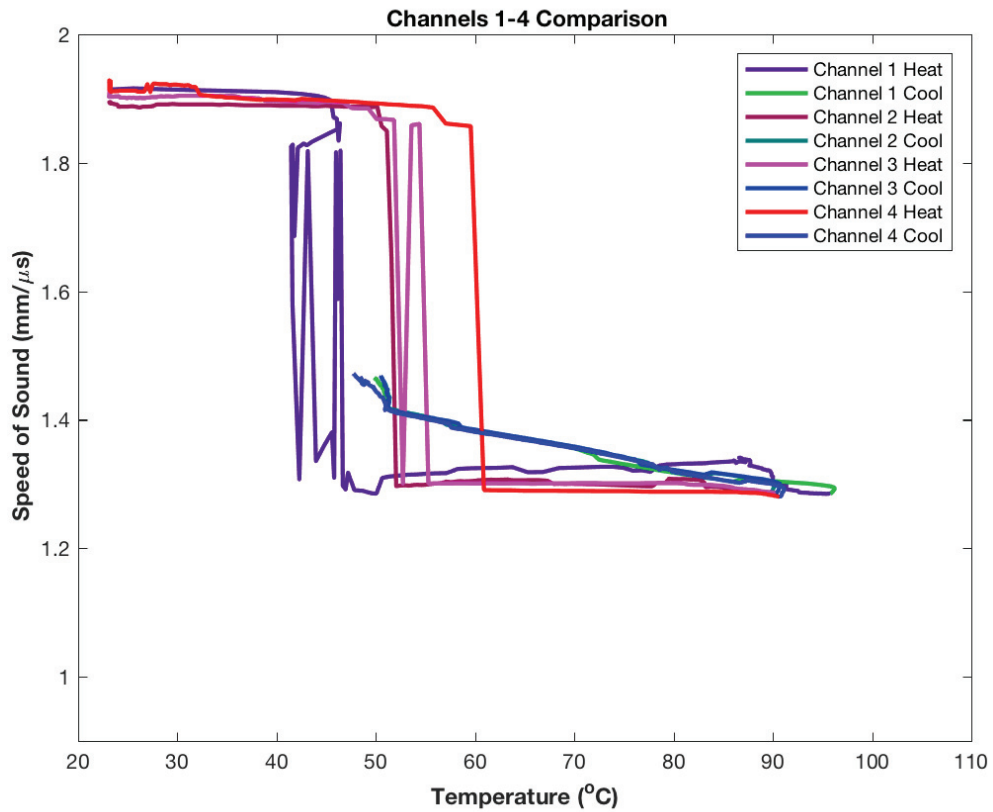


Figure B.16 Comparison of the speed of sound versus temperature plots for channels 1 through 4. The heating portion of the curves is provided in the red and purple colors whereas the cooling portion of the curves (when the heater is off) is provided in the blue and green colors

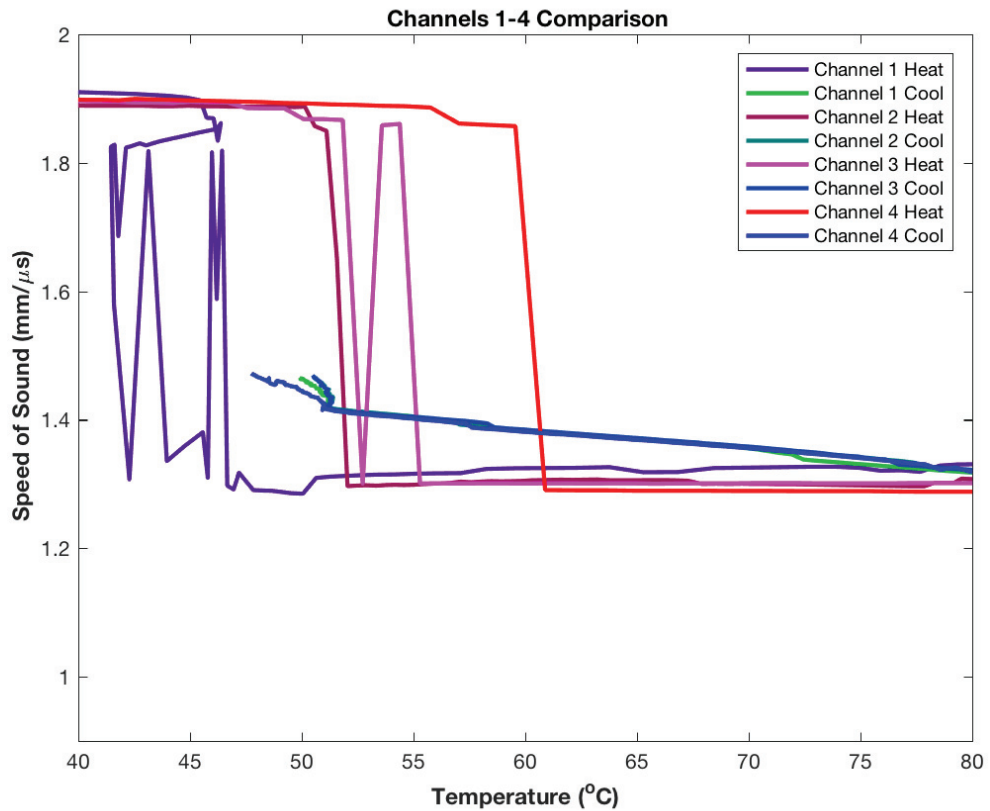


Figure B.17 Speed of sound versus temperature where the axes have been reduced such that the material's transition from solid to liquid during the melting stage is highlighted by the near step change in speed of sound.

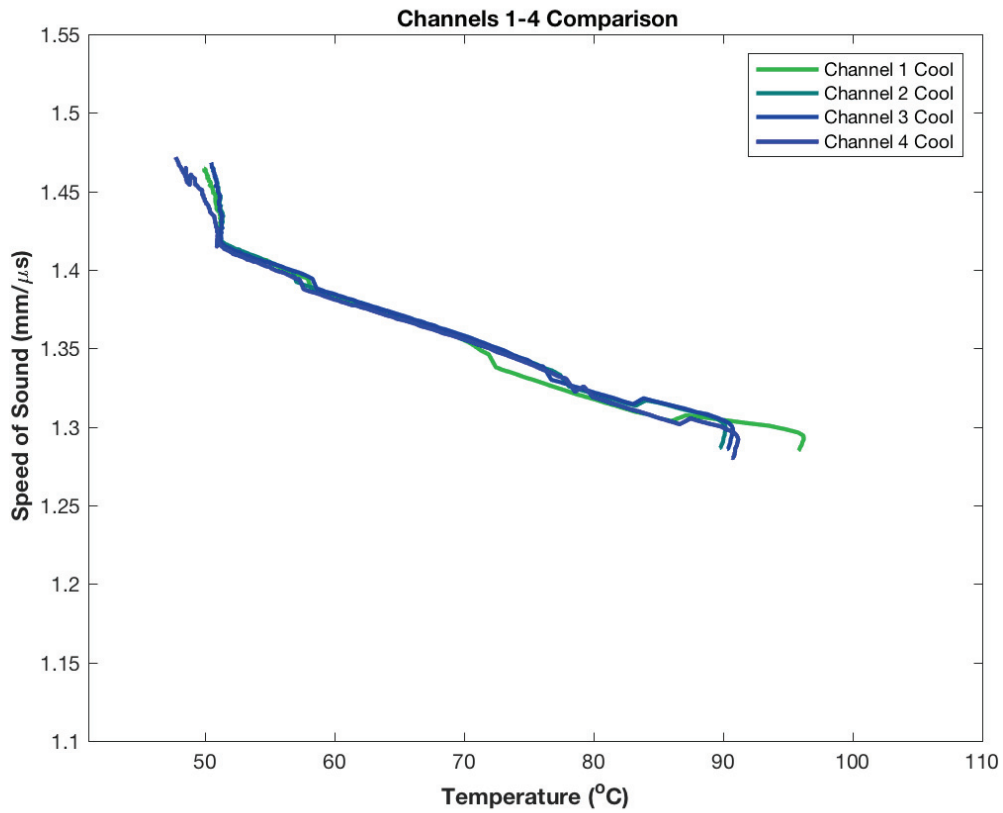


Figure B.18 Speed of sound versus temperature as the material is cooling.

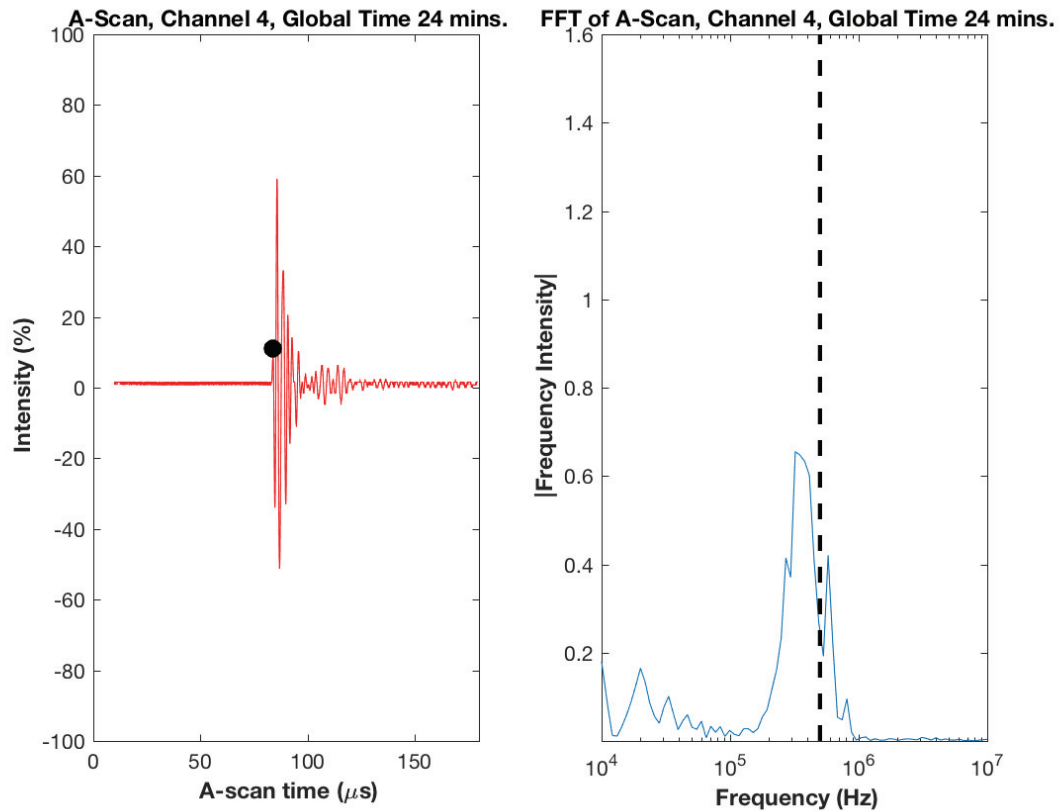


Figure B.19 A-scan (left) and Fast Fourier Transform (right) results for solid EcoSoya wax at 24 minutes into the test.

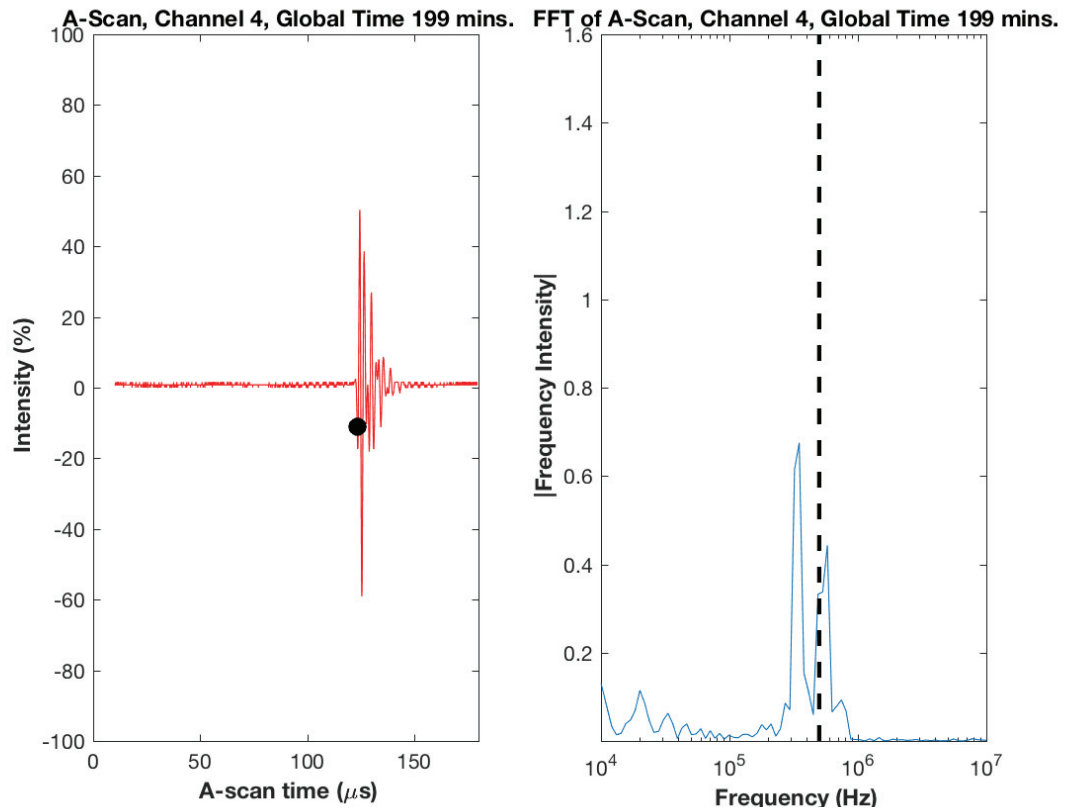


Figure B.20 A-scan (left) and Fast Fourier Transform (right) results for liquid EcoSoya wax at 199 minutes into the test.

B.2 Results from EcoSoya Experiment Three

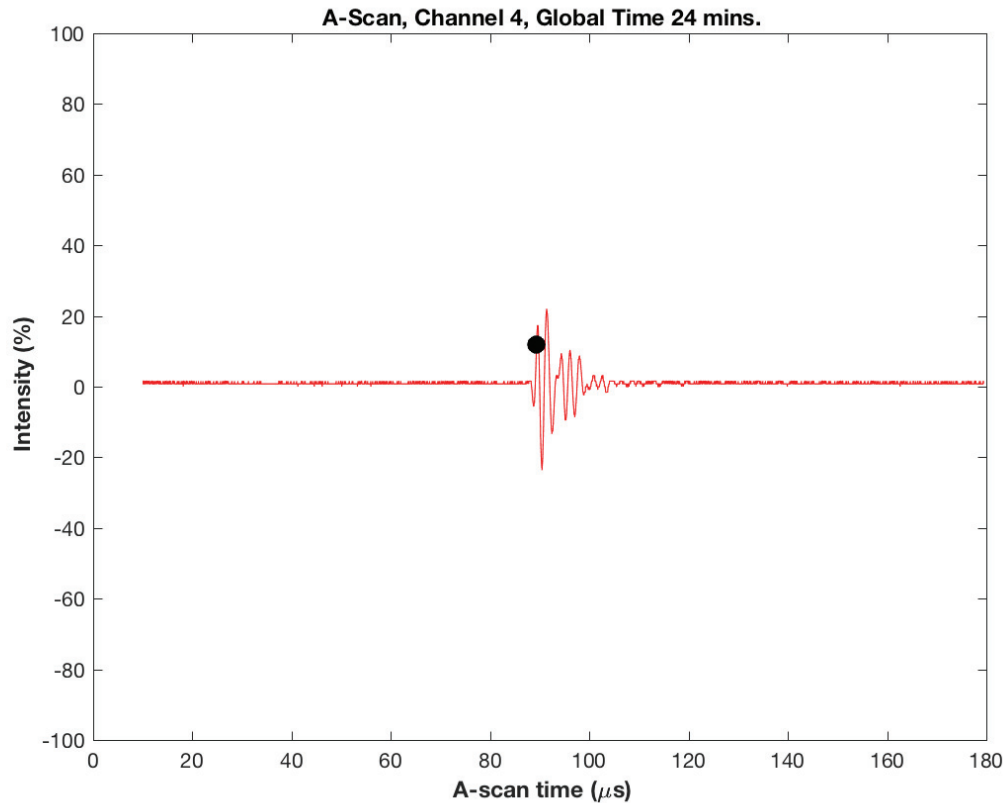


Figure B.21 A-scan signal associated with the solid EcoSoya wax. The black dot indicates the first point that meets or exceeds the amplitude threshold.

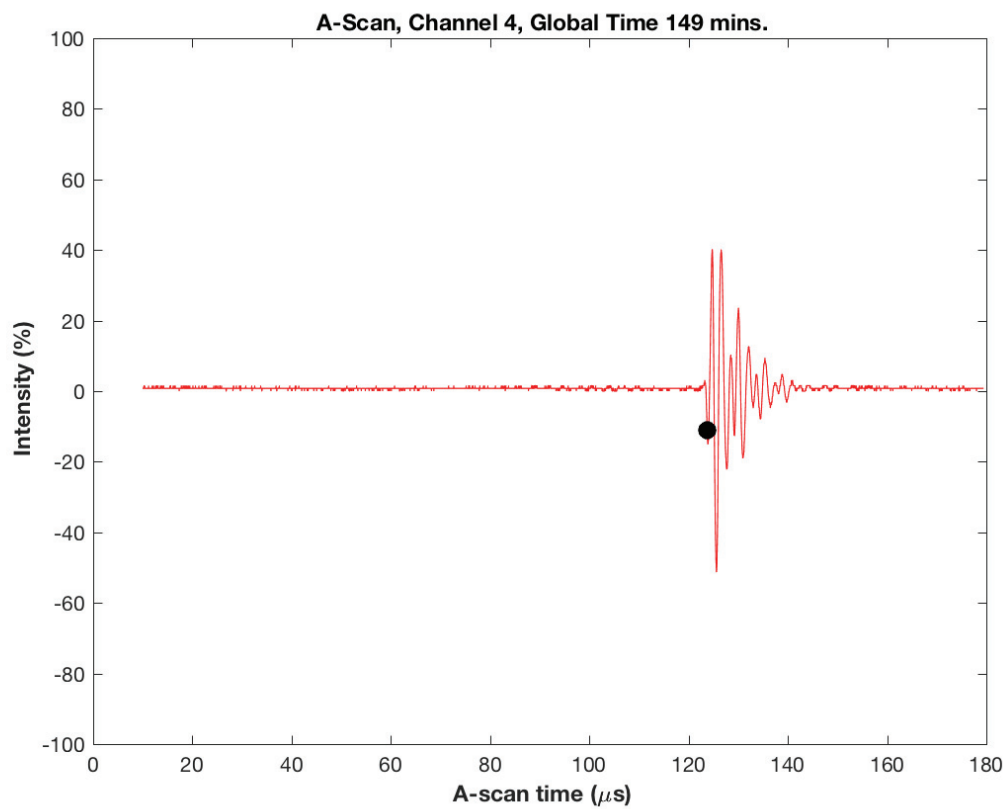


Figure B.22 A-scan associated with the liquid EcoSoya wax. The black dot indicates the first point that meets or exceeds the amplitude threshold.

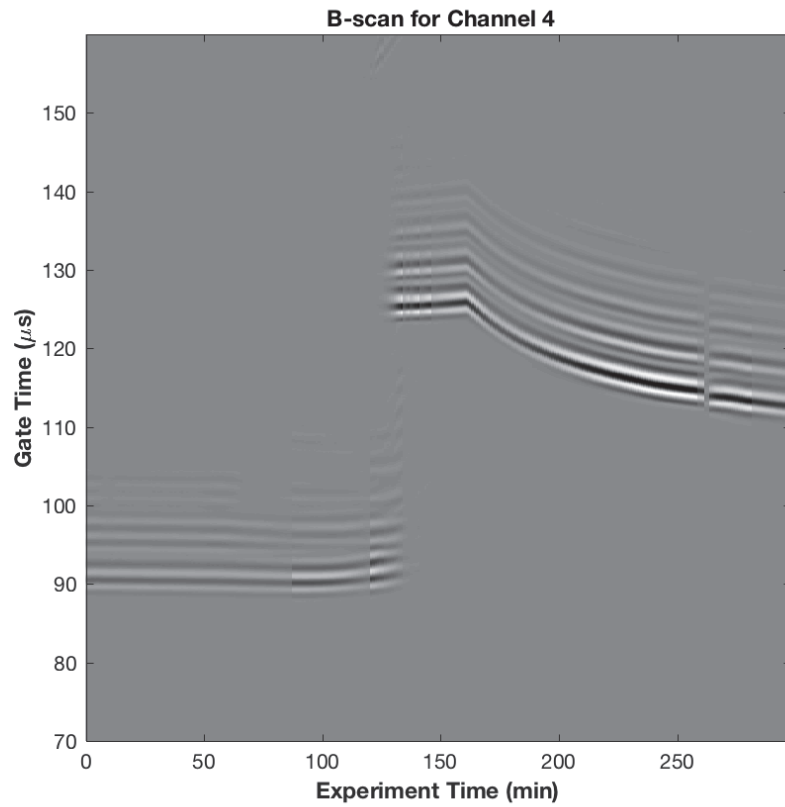


Figure B.23 B-scan for channel 4, which is located farthest away from the heater.

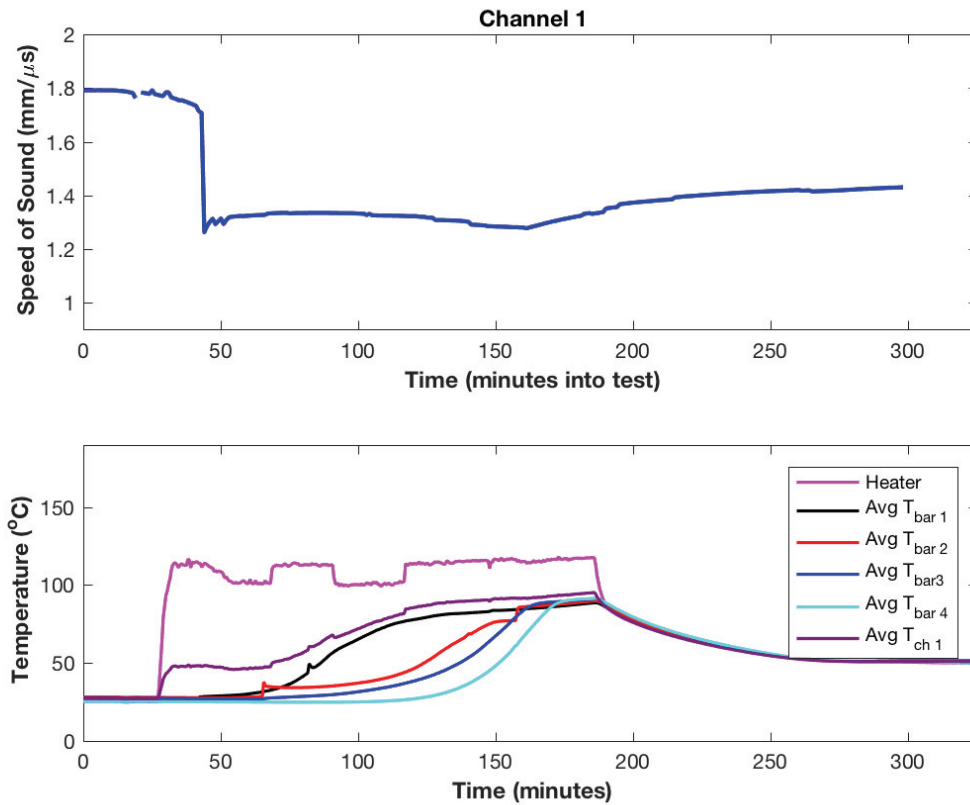


Figure B.24 The speed of sound for channel 1 (top), which is located closest to the heater, and the temperature measured via thermocouples throughout the experiment (bottom).

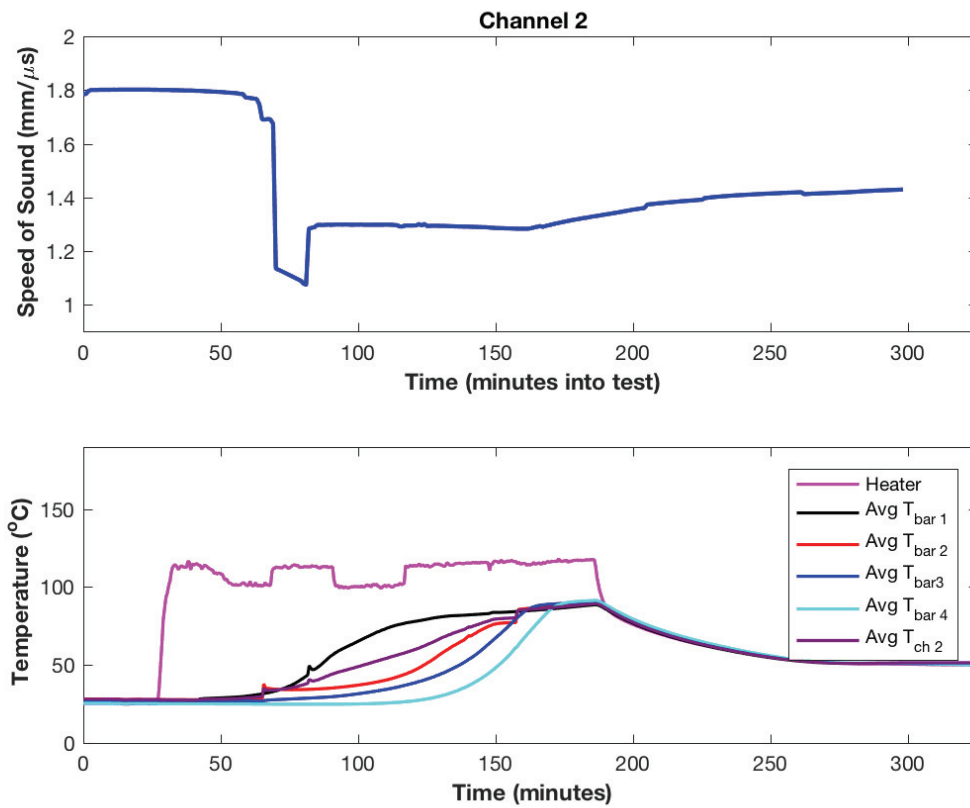


Figure B.25 The speed of sound for channel 2 (top), and the temperature measured via thermocouples throughout the experiment (bottom).

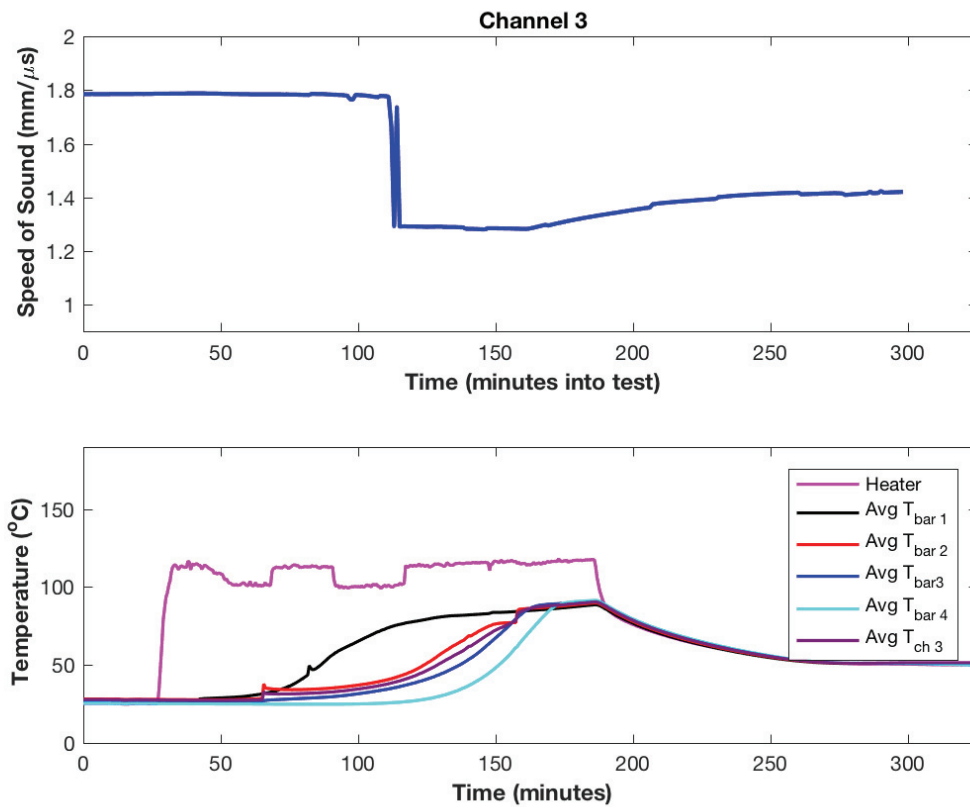


Figure B.26 The speed of sound for channel 2 (top), and the temperature measured via thermocouples throughout the experiment (bottom).

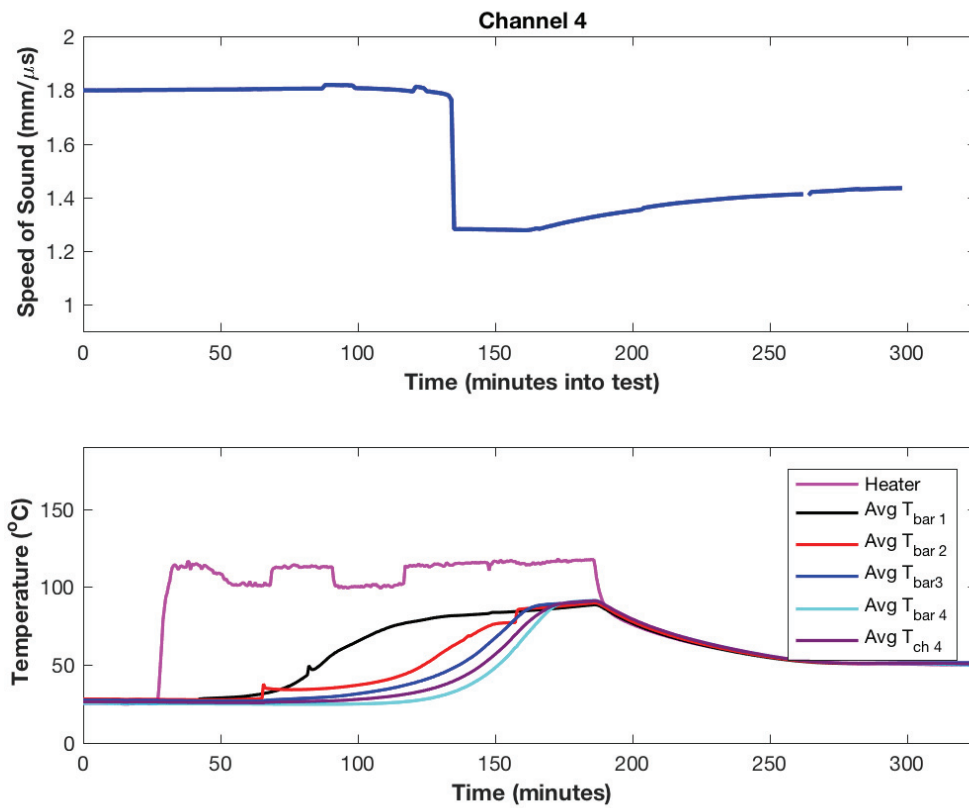


Figure B.27 The speed of sound for channel 4 (top), and the temperature measured via thermocouples throughout the experiment (bottom).

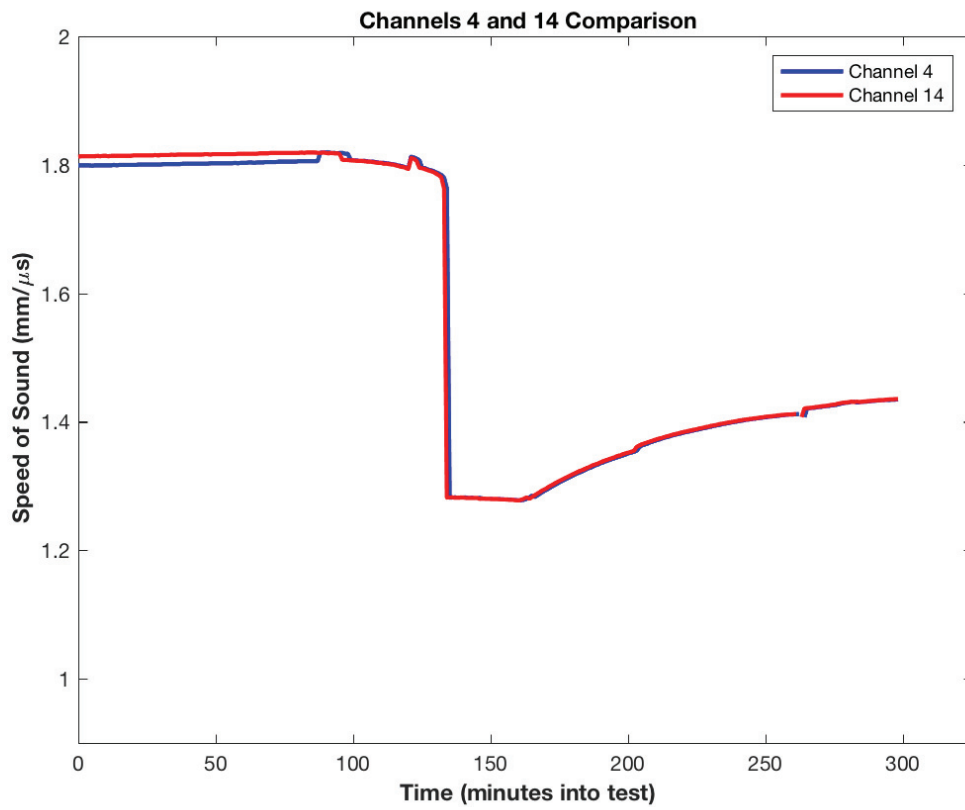


Figure B.28 Comparing the calculated speed of sound for channels 4 and 14.

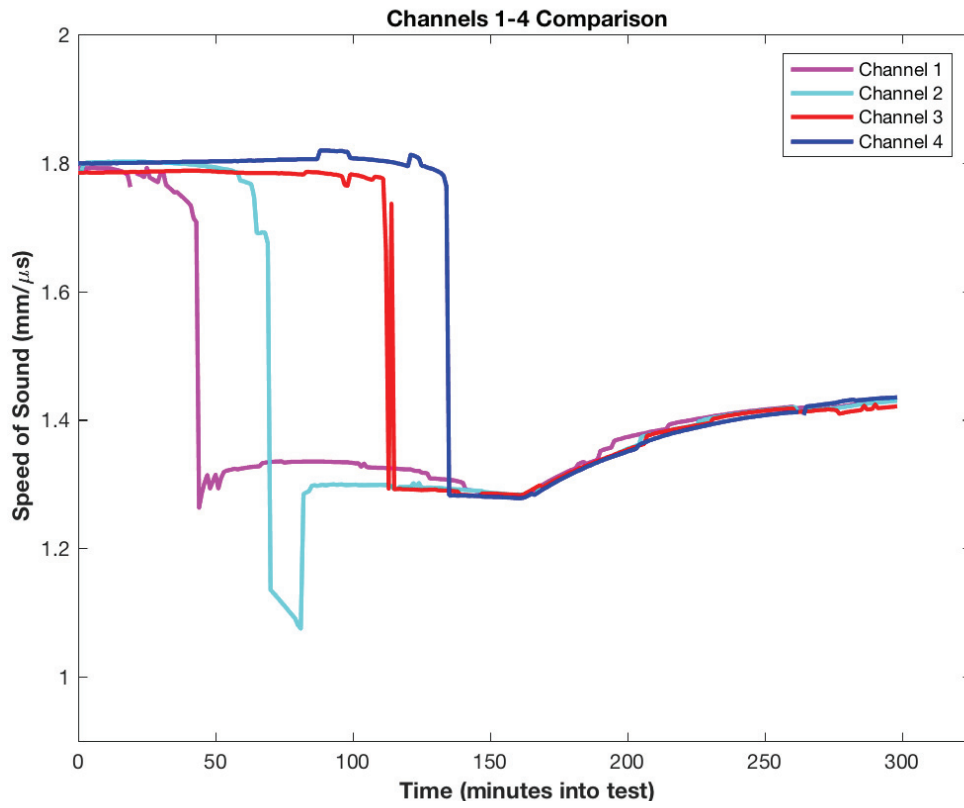


Figure B. 29 Comparing the calculated speed of sound for channels 1 through 4.

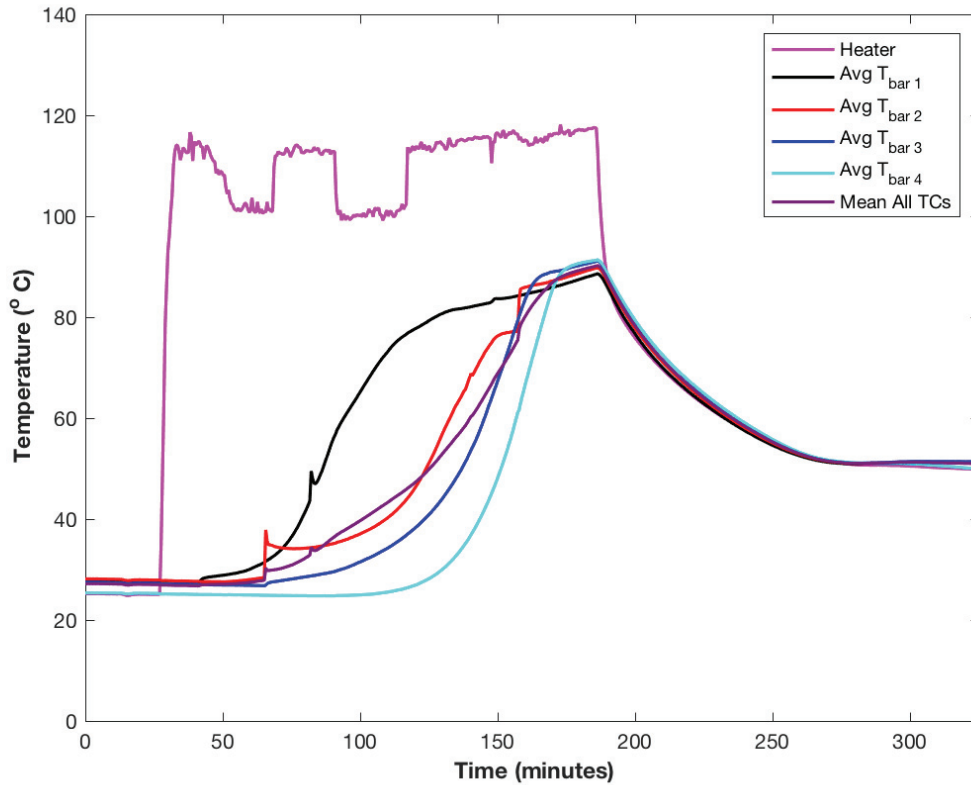


Figure B.30 The temperatures throughout the experimental setup as monitored by the thermocouples. The average temperature for each bar of thermocouples has been included in this image along with the temperature at the heater block.

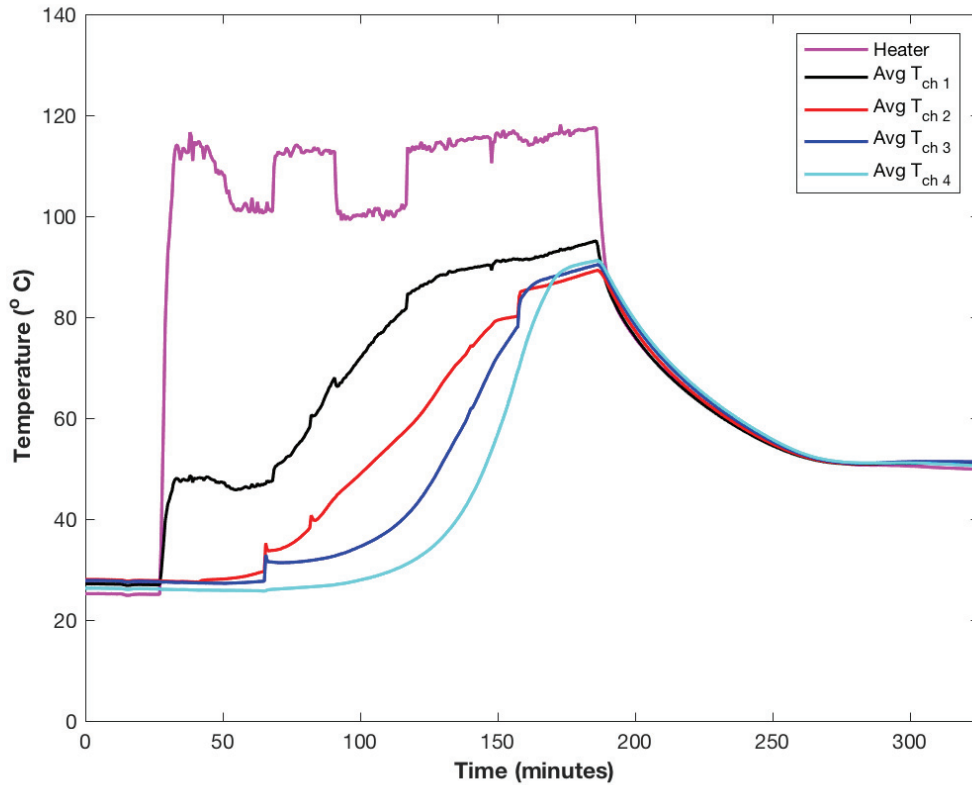


Figure 3.31 The temperatures calculated along the ultrasound probe path for channels 1 through 4.

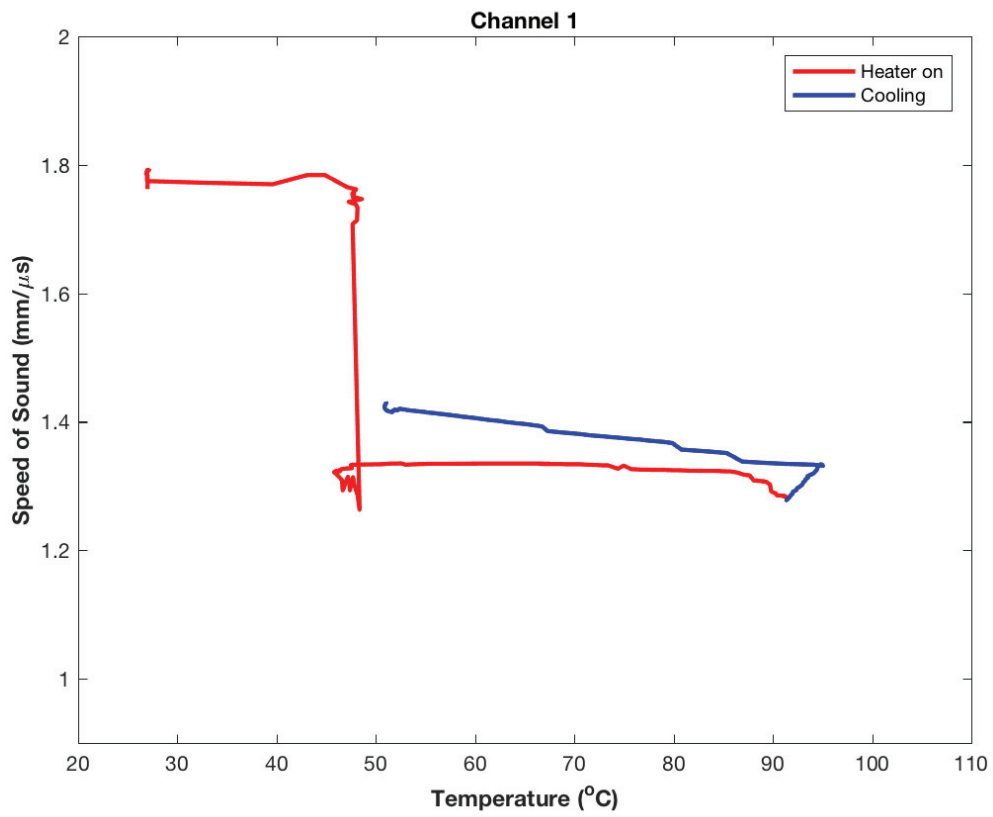


Figure B.32 The speed of sound versus temperature for channel 1, which is located closest to the heater block.

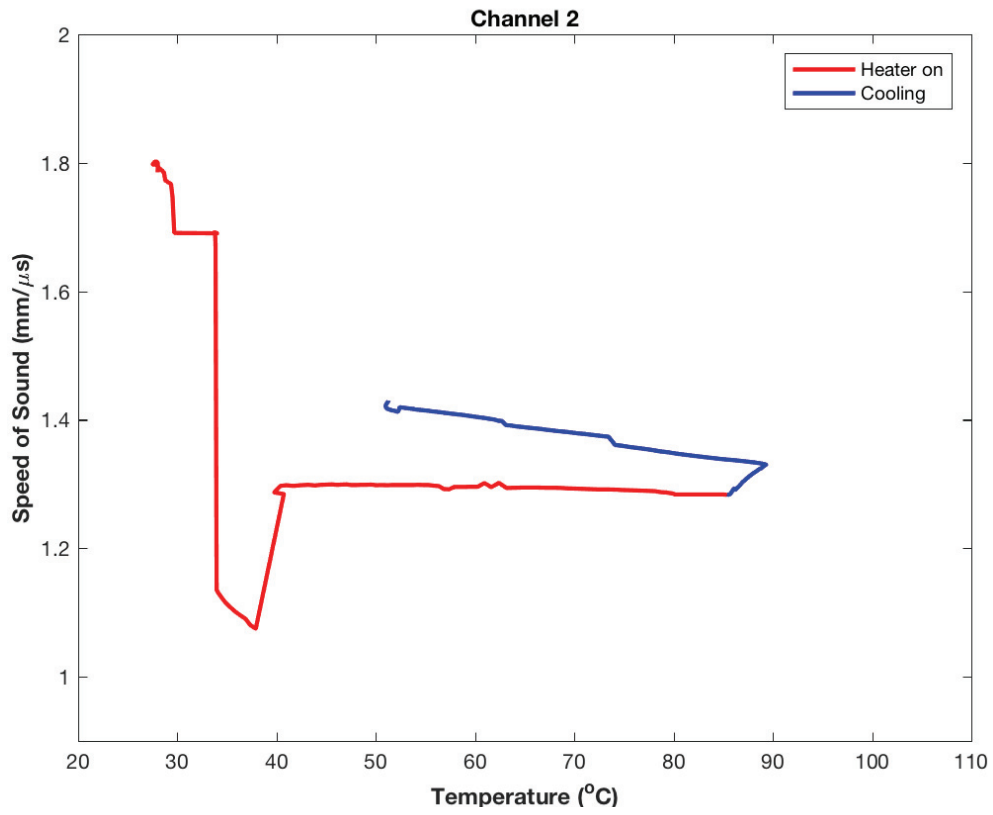


Figure B.33 The speed of sound versus temperature for channel 2.

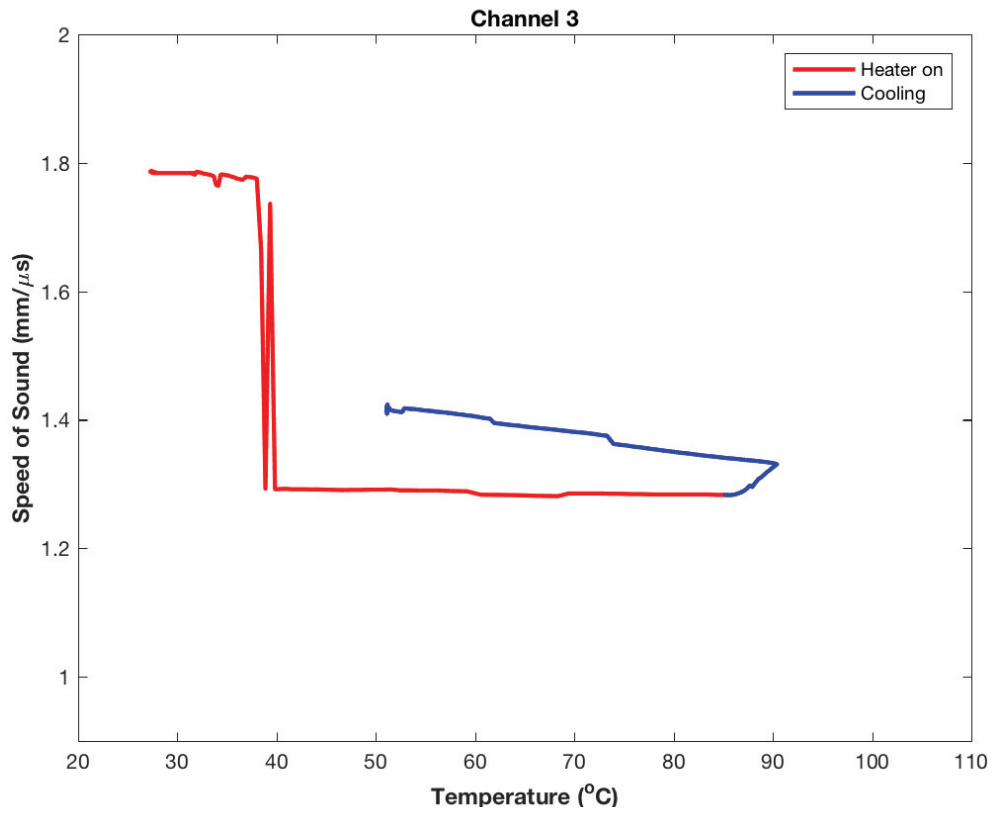


Figure B.34 The speed of sound versus temperature for channel 3.

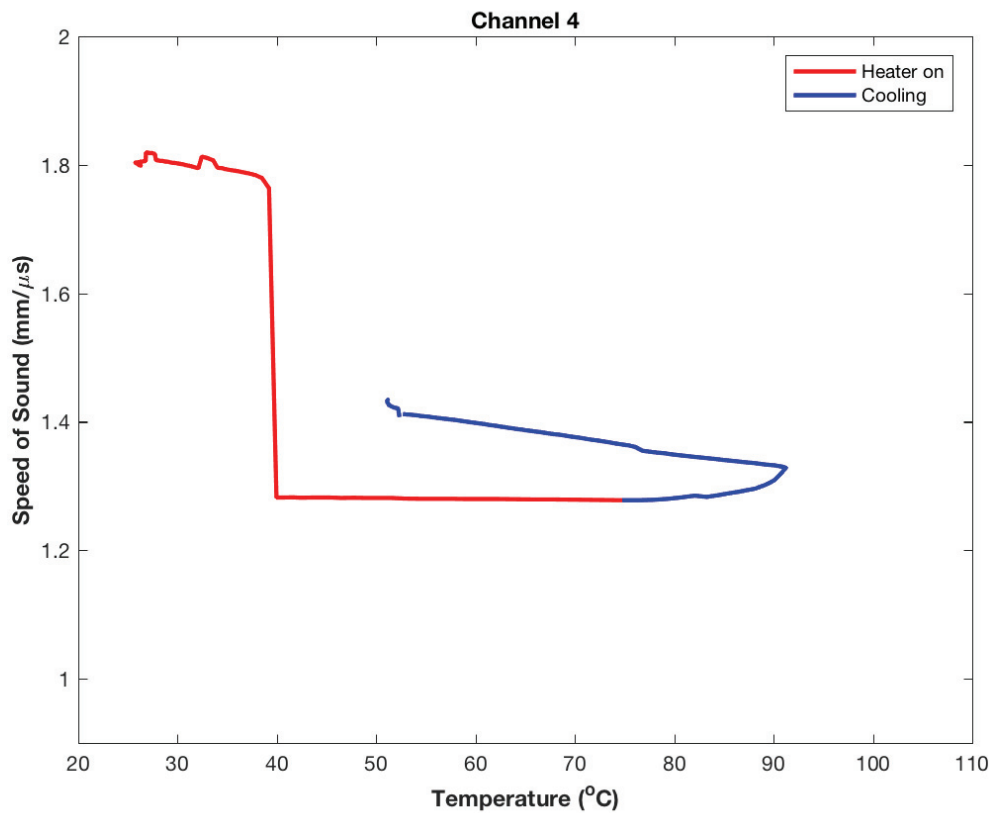


Figure B.35 The speed of sound versus temperature for channel 4.

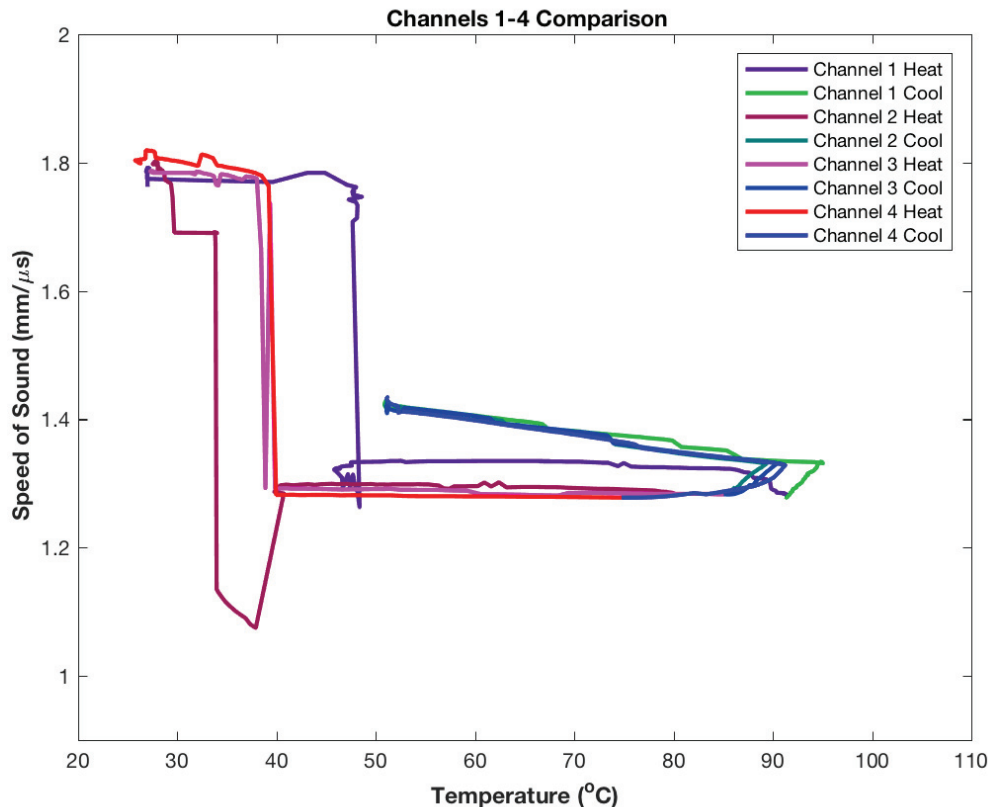


Figure B.36 Comparison of the speed of sound versus temperature plots for channels 1 through 4. The heating portion of the curves is provided in the red and purple colors whereas the cooling portion of the curves (when the heater is off) is provided in the blue and green colors.

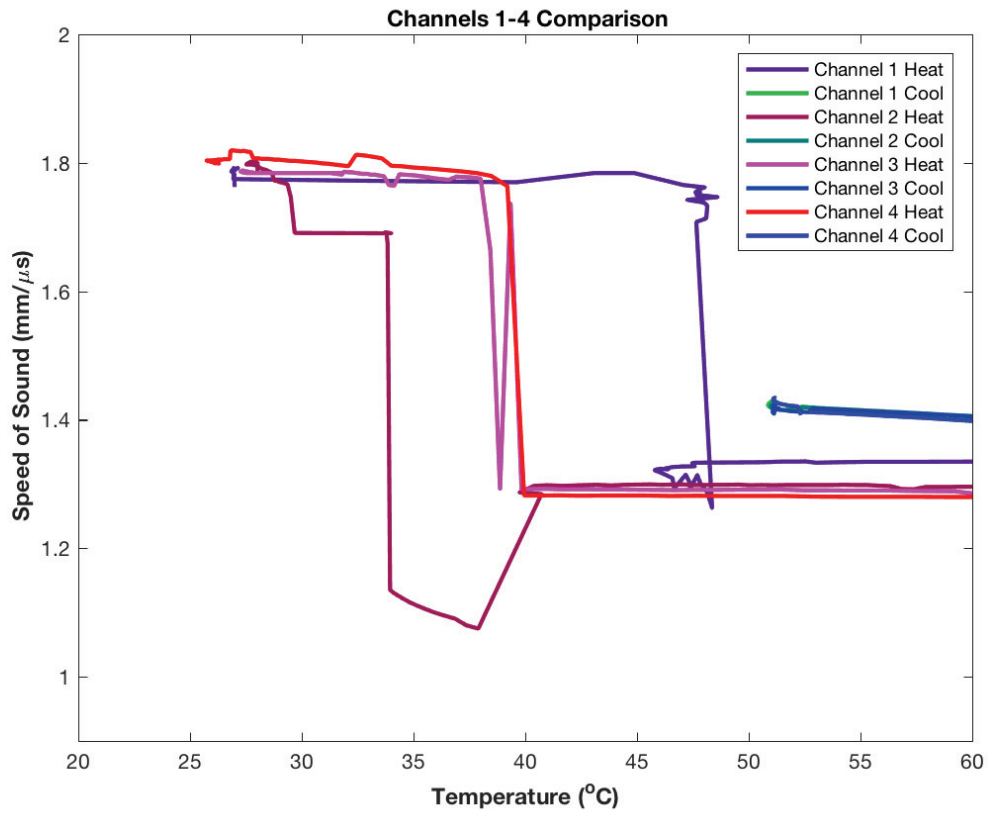


Figure B.37 Speed of sound versus temperature where the axes have been reduced such that the material's transition from solid to liquid during the melting stage is highlighted by the near step change in speed of sound

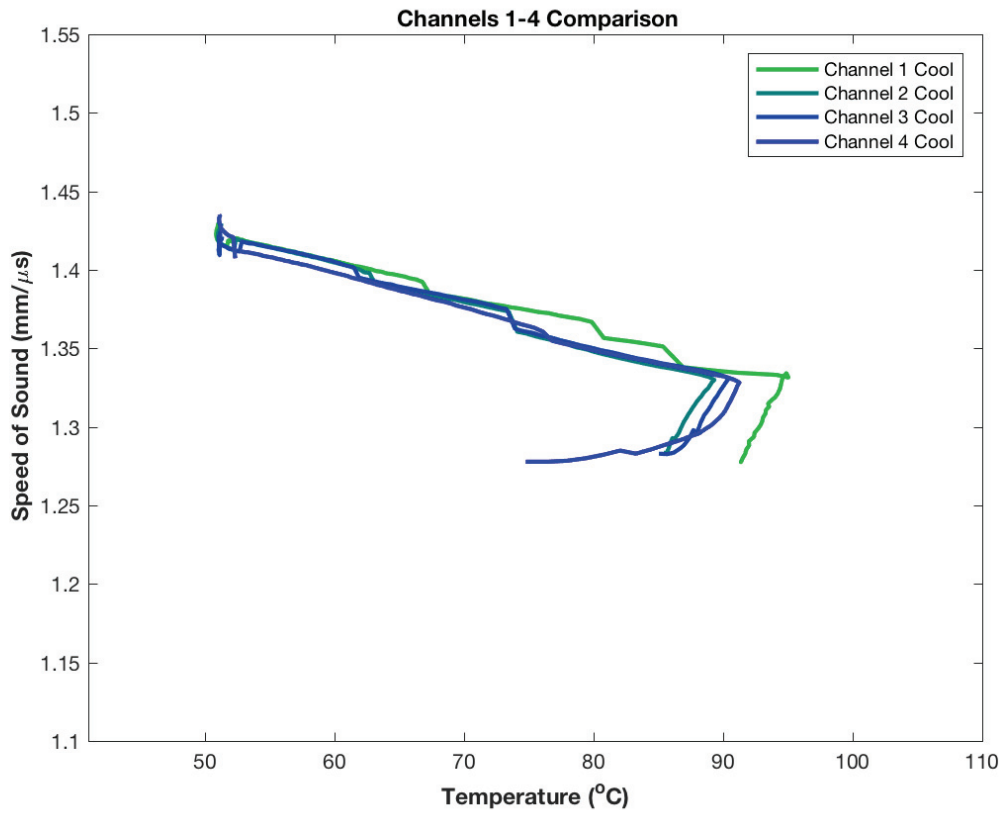


Figure B.38 Speed of sound versus temperature as the material is cooling.

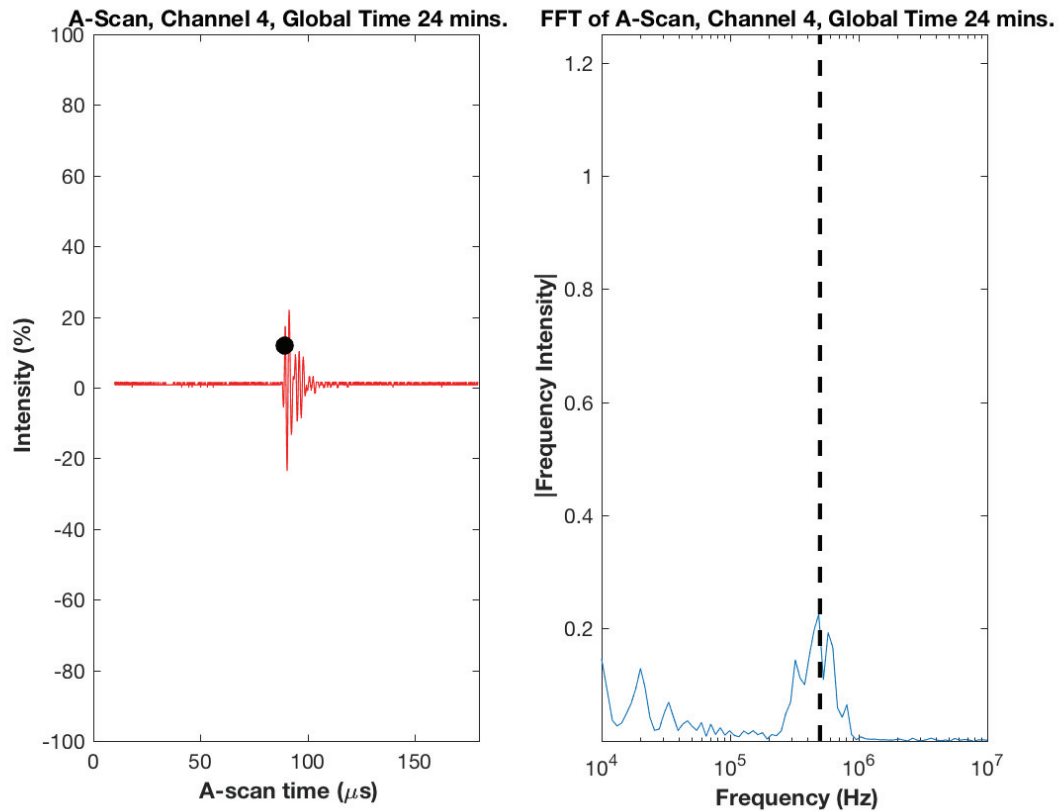


Figure B.39 A-scan (left) and Fast Fourier Transform (right) results for solid EcoSoya wax at 24 minutes into the test.

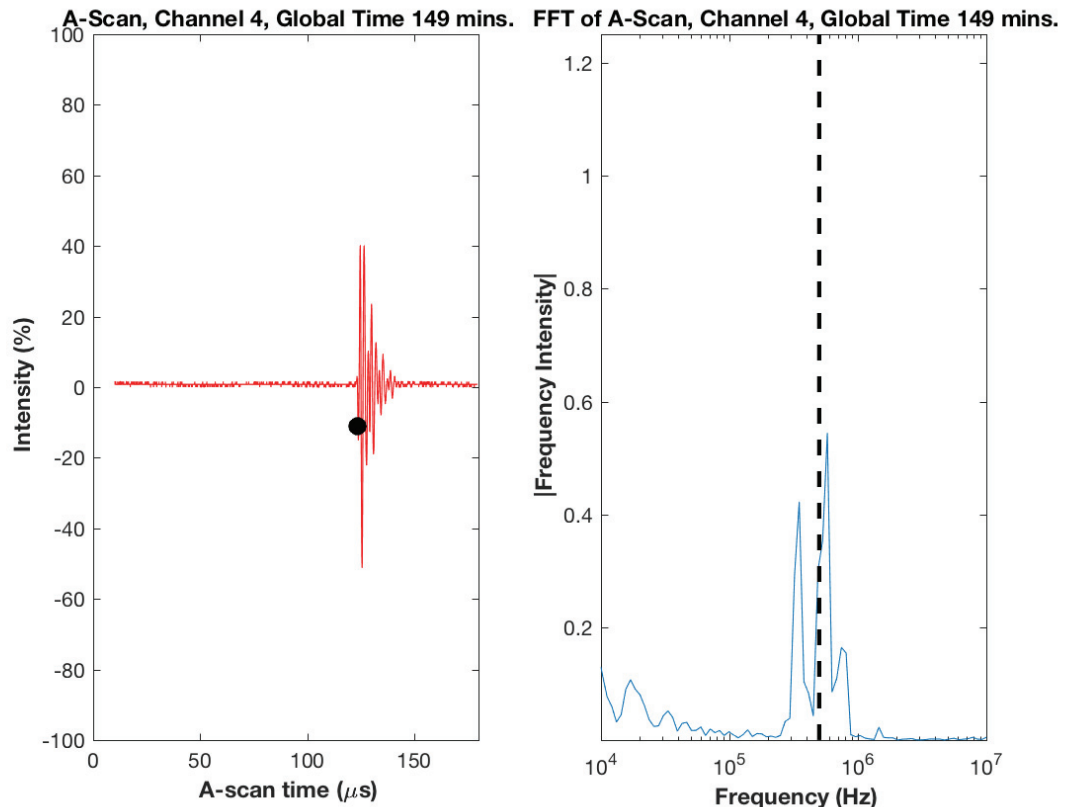


Figure B.40 A-scan (left) and Fast Fourier Transform (right) results for liquid EcoSoya wax at 149 minutes into the test.

B.3 Results from EcoSoya Experiment Four

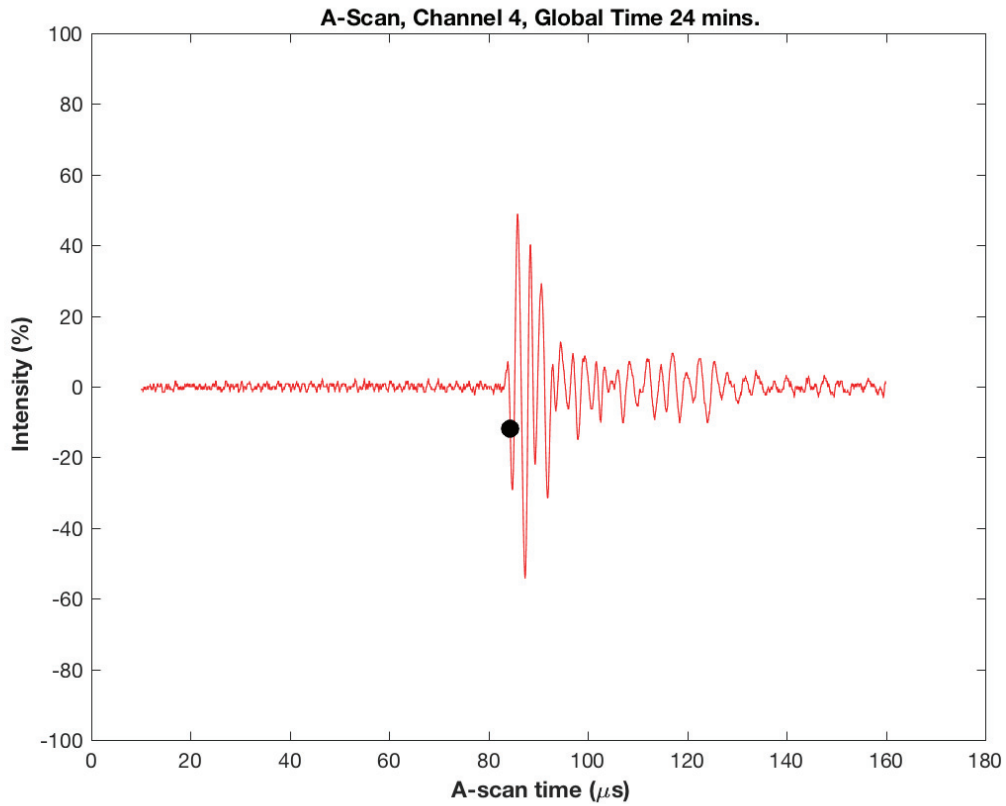


Figure B.41 A-scan signal associated with the solid EcoSoya wax. The black dot indicates the first point that meet or exceeds the amplitude threshold.

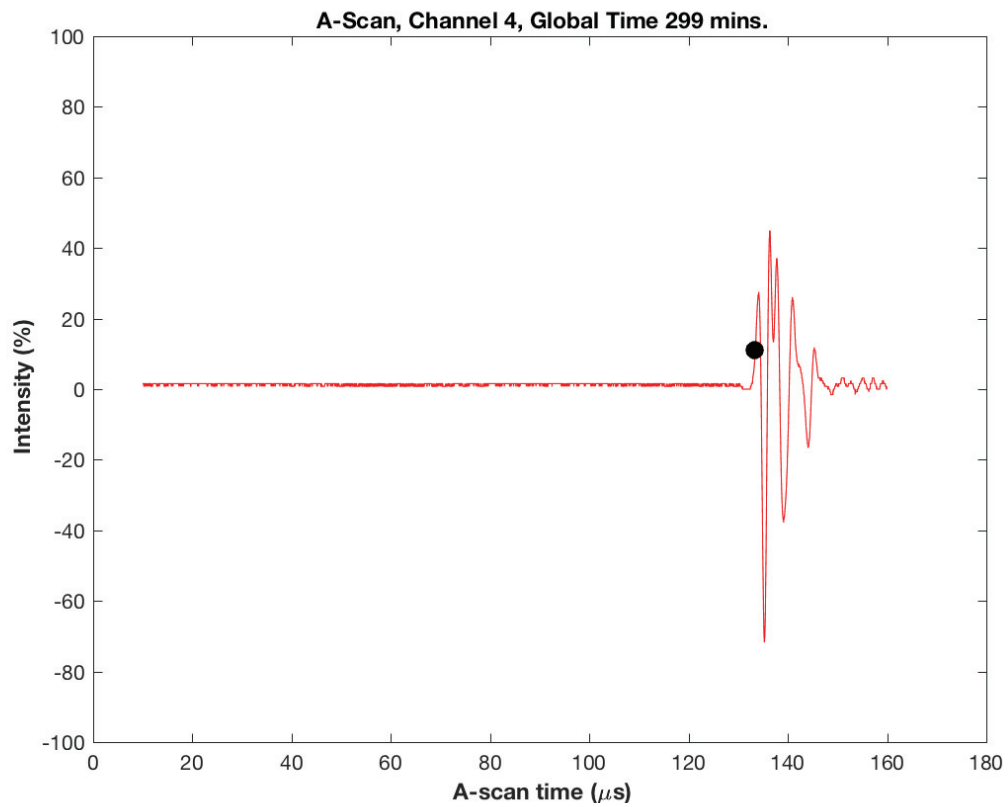


Figure B.42 A-scan signal associated with the liquid EcoSoya wax. The black dot indicates the first point that meets or exceeds the amplitude threshold.

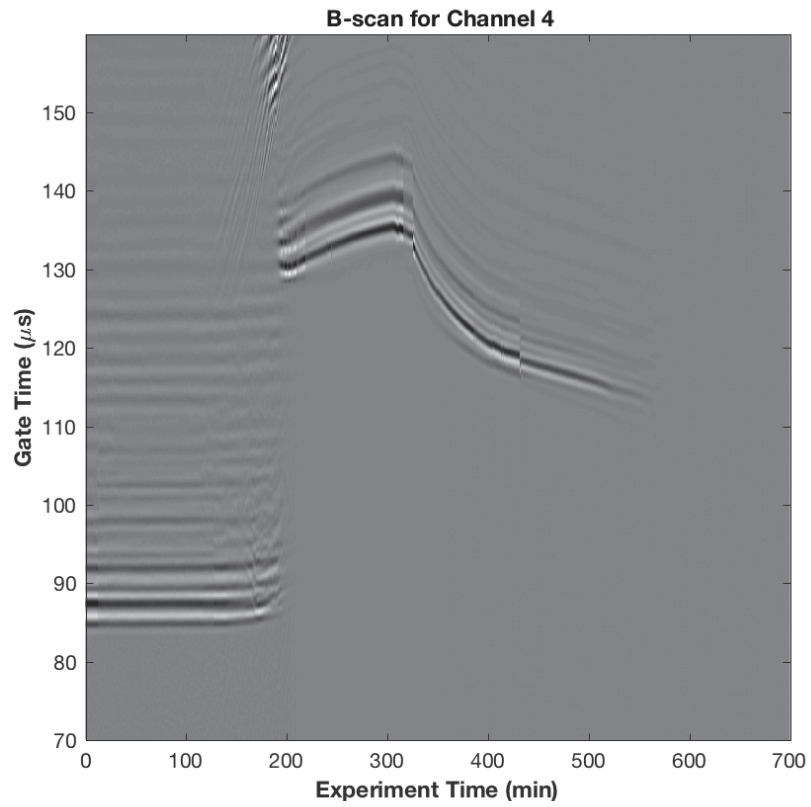


Figure B.43 B-scan for channel 4, which is farthest way from the heater.

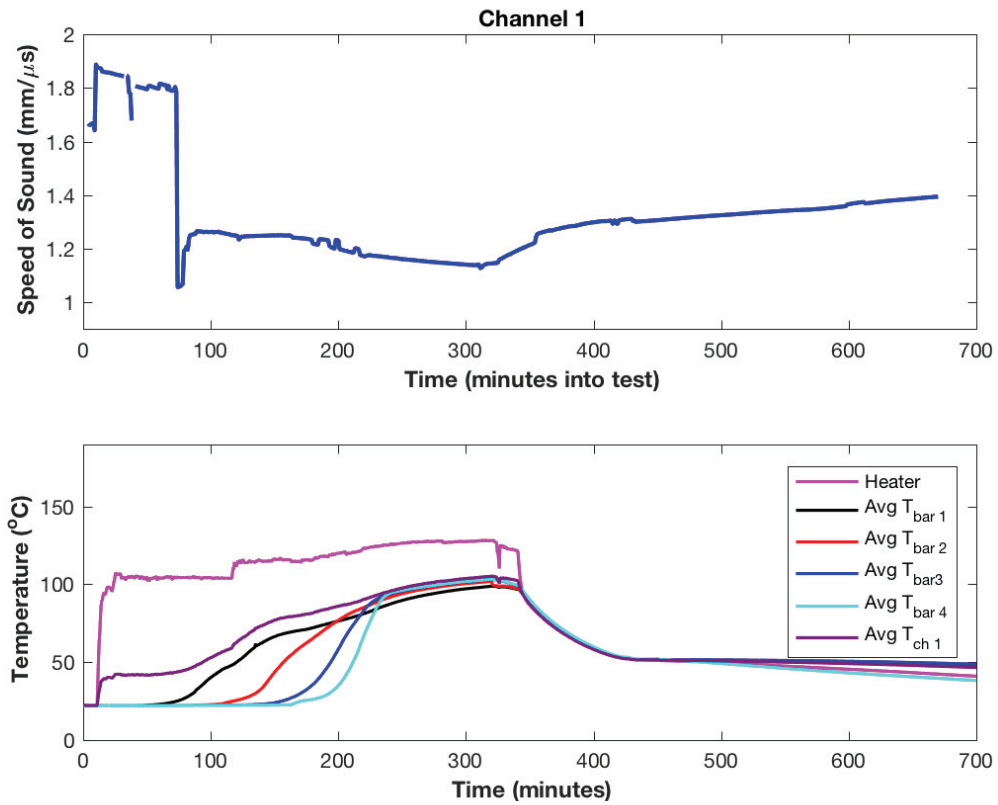


Figure B.44 The speed of sound for channel 1 (top), which is located closest to the heater, and the temperature measured via thermocouples throughout the experiment (bottom).

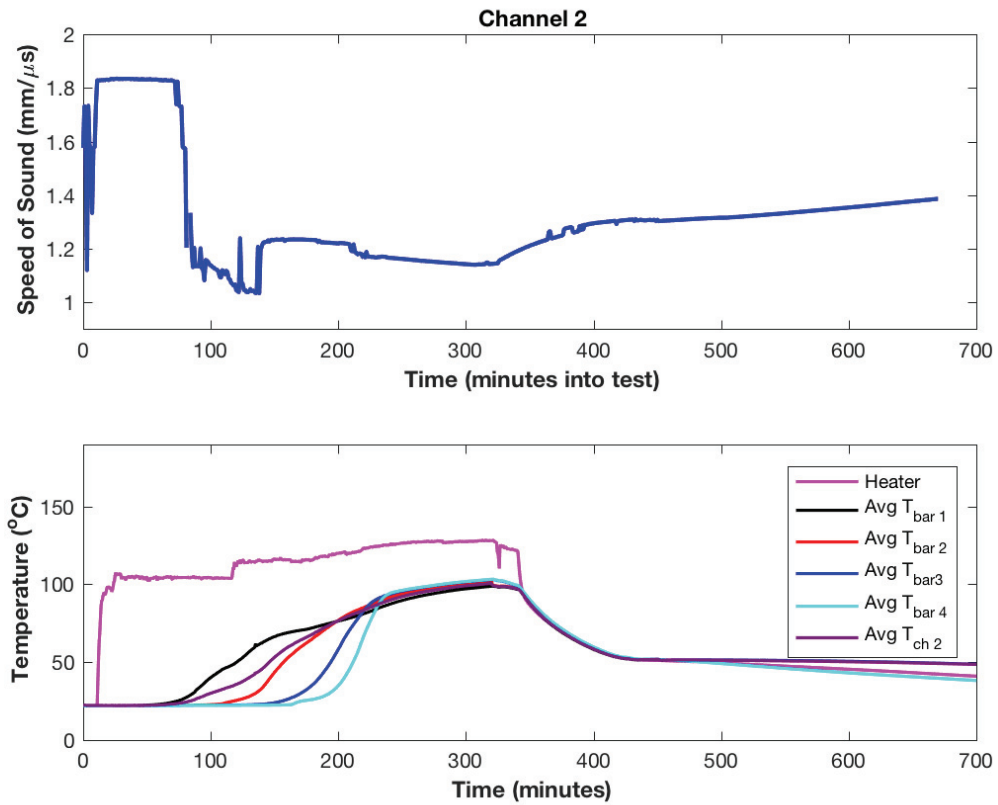


Figure B.45 The speed of sound for channel 2 (top), and the temperature measured via thermocouples throughout the experiment (bottom).

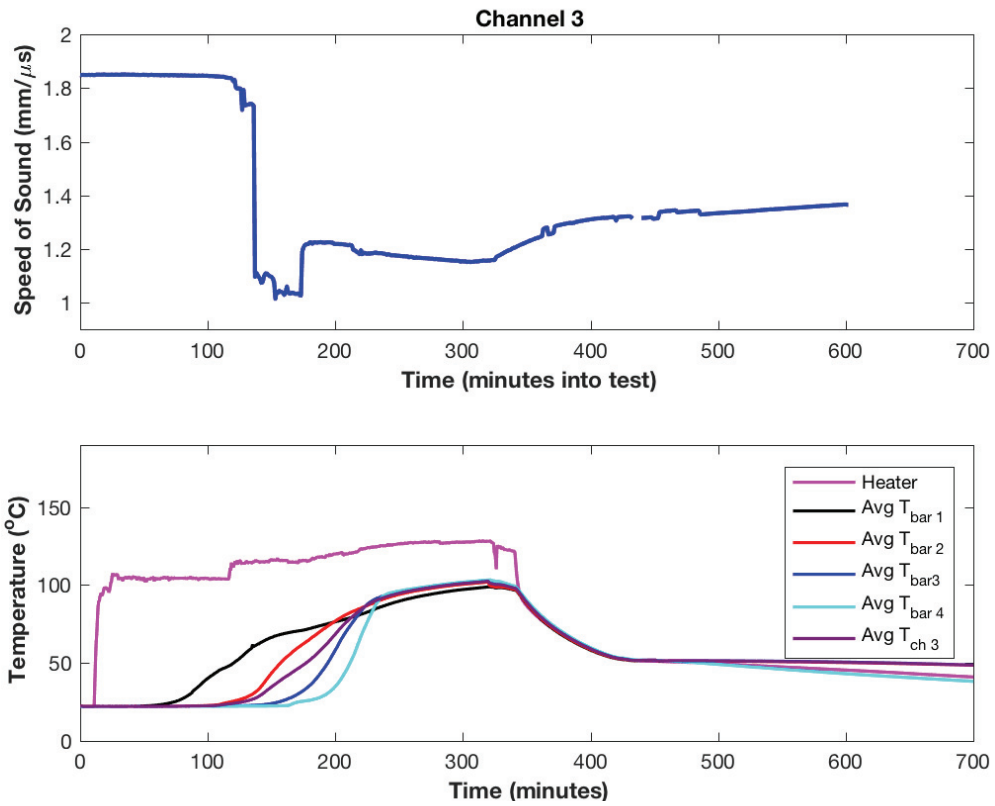


Figure B.46 The speed of sound for channel 3 (top), and the temperature measured via thermocouples throughout the experiment (bottom).

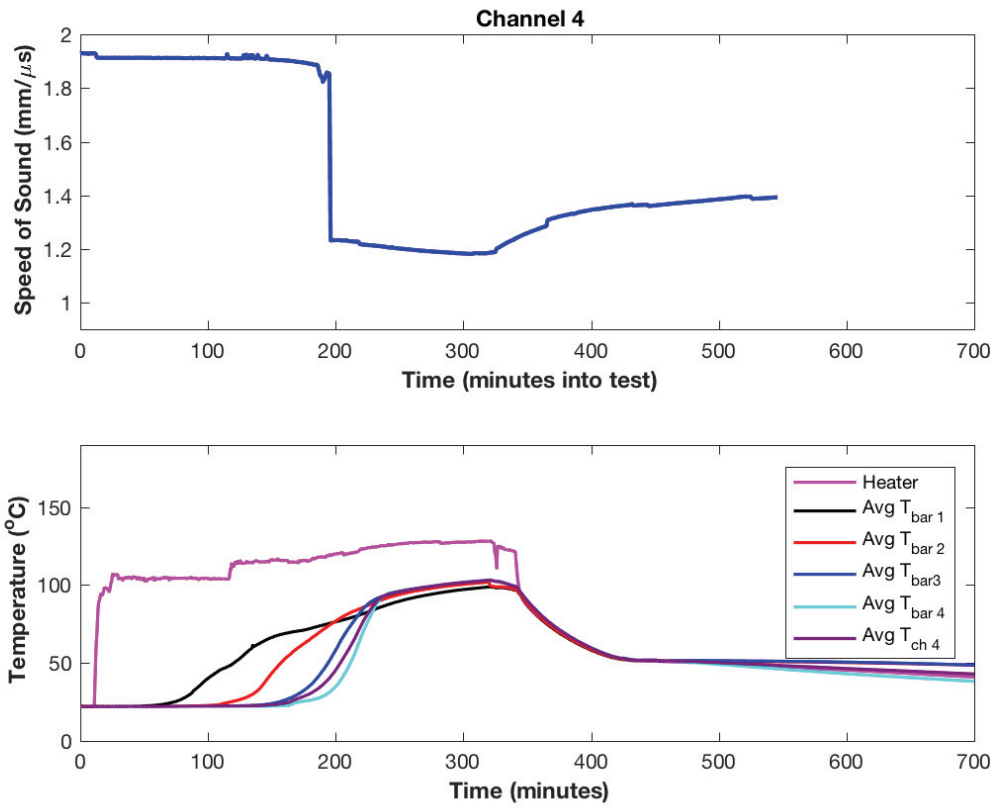


Figure B.47 The speed of sound for channel 4 (top), and the temperature measured via thermocouples throughout the experiment (bottom).

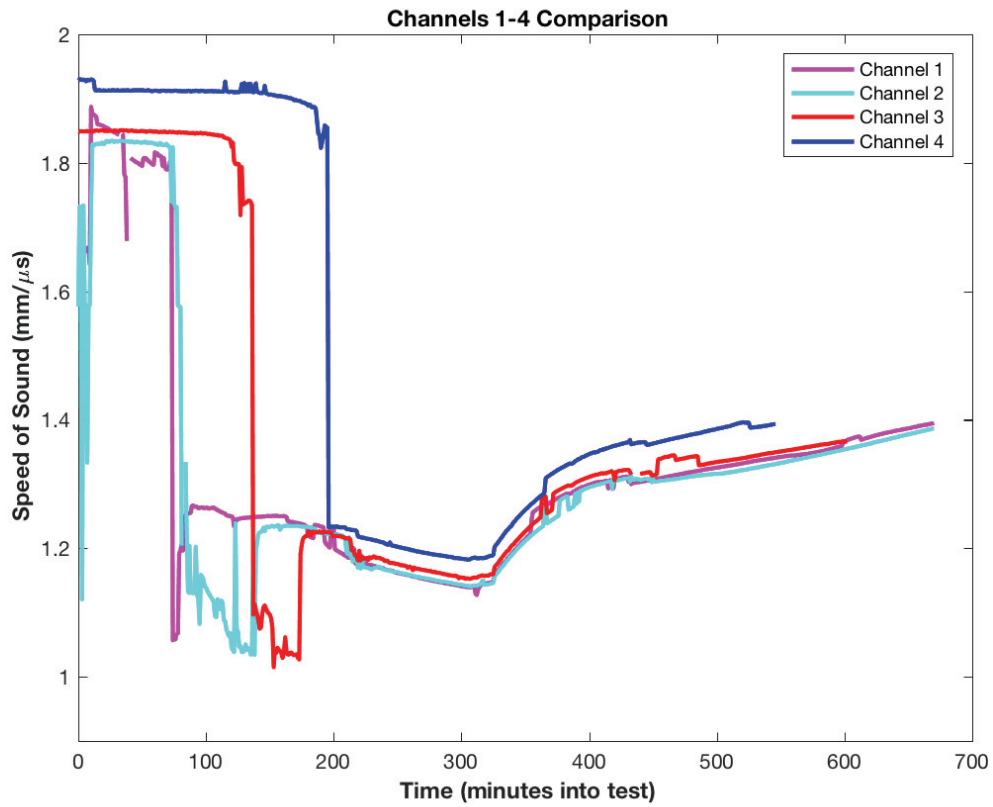


Figure B.48 Comparing the calculated speed of sound for channels 1 through 4.

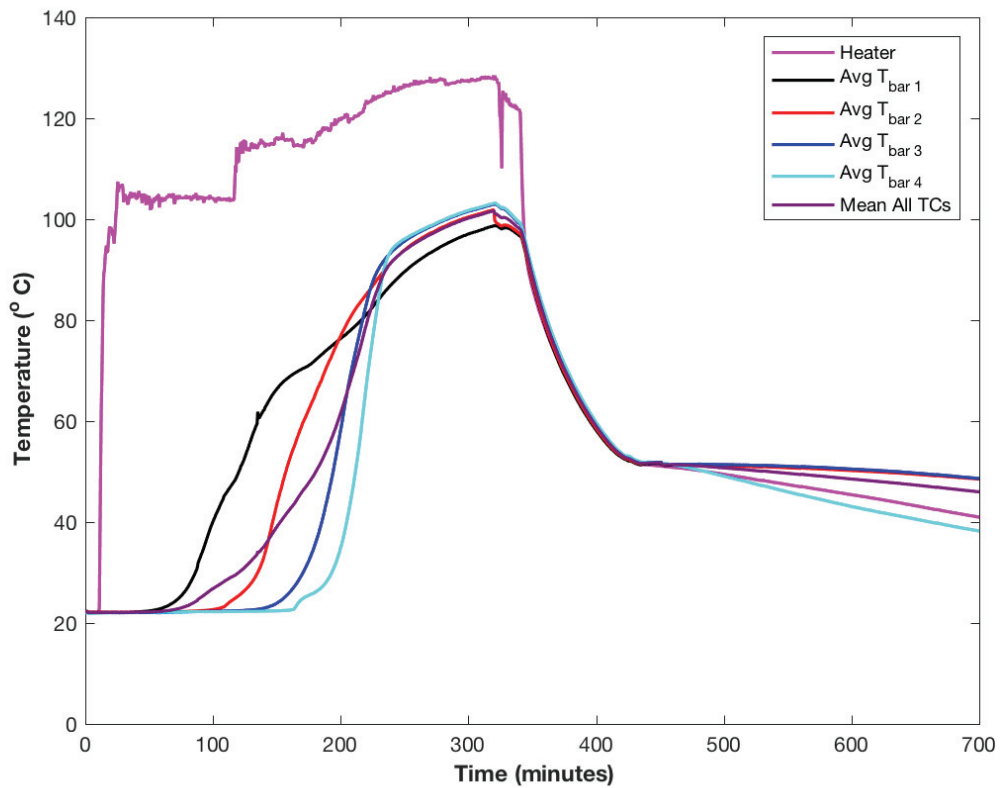


Figure B.49 The temperatures throughout the experimental setup as monitored by the thermocouples. The average temperature for each bar of thermocouples has been included in this image along with the temperature at the heater block.

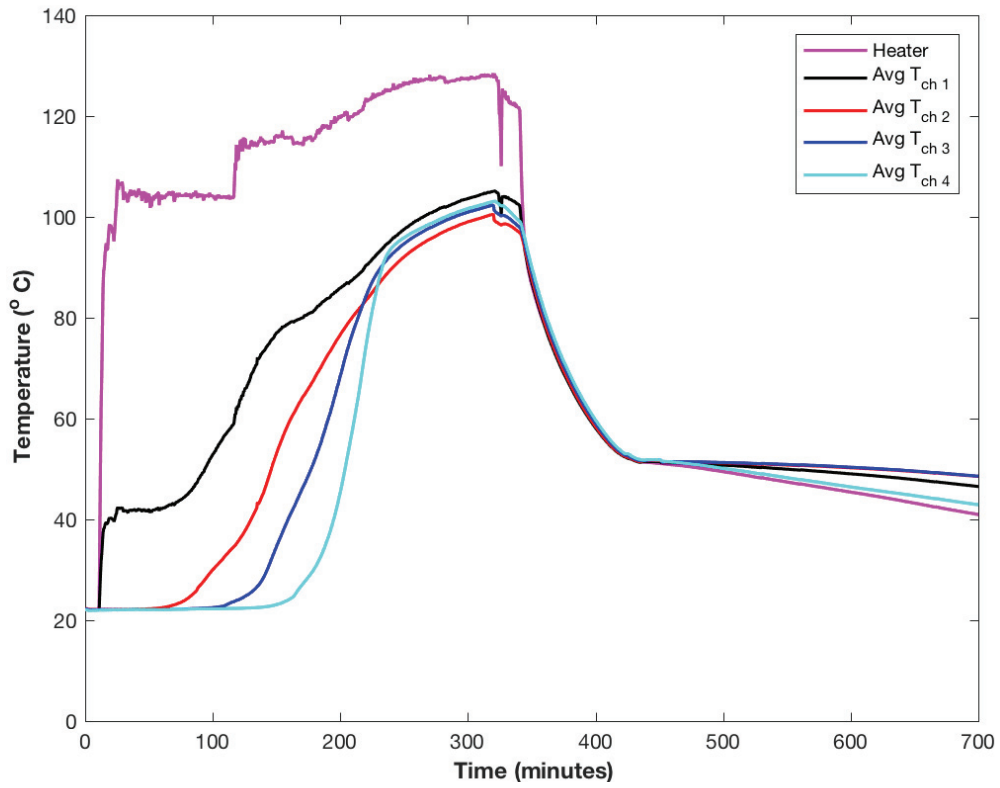


Figure B.50 The temperatures calculated along the ultrasound probe path for channels 1 through 4.

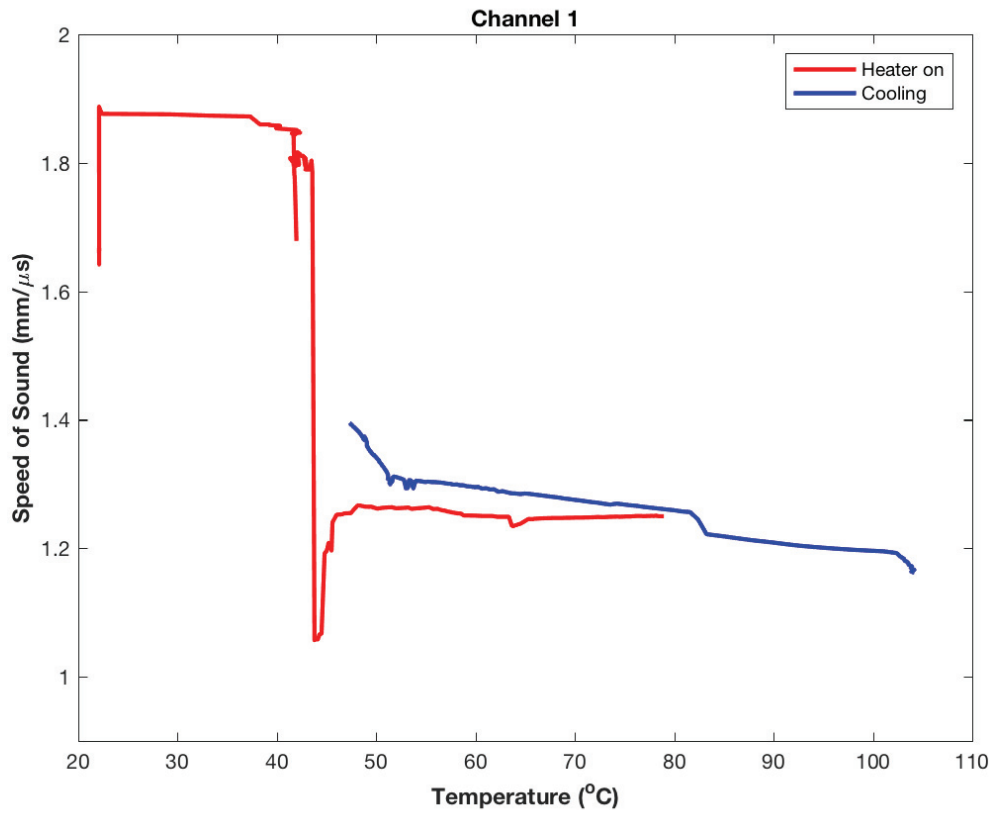


Figure B.51 The speed of sound versus temperature for channel 1, which is located closest to the heater block.

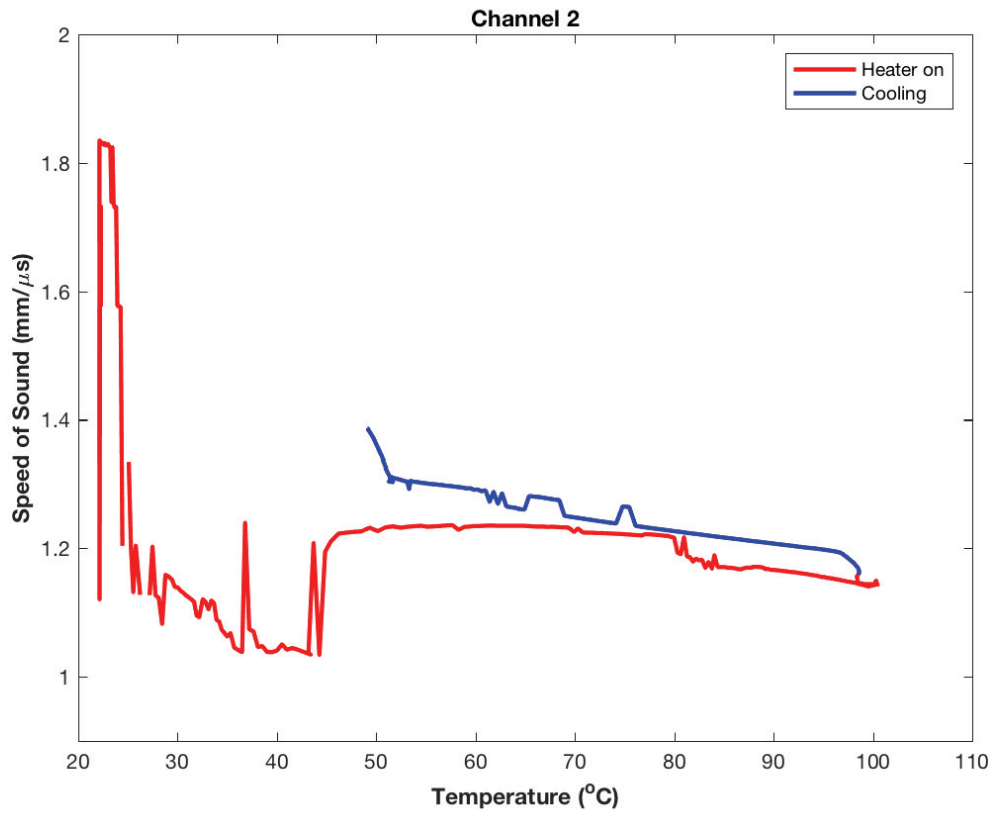


Figure B.52 The speed of sound versus temperature for channel 2.

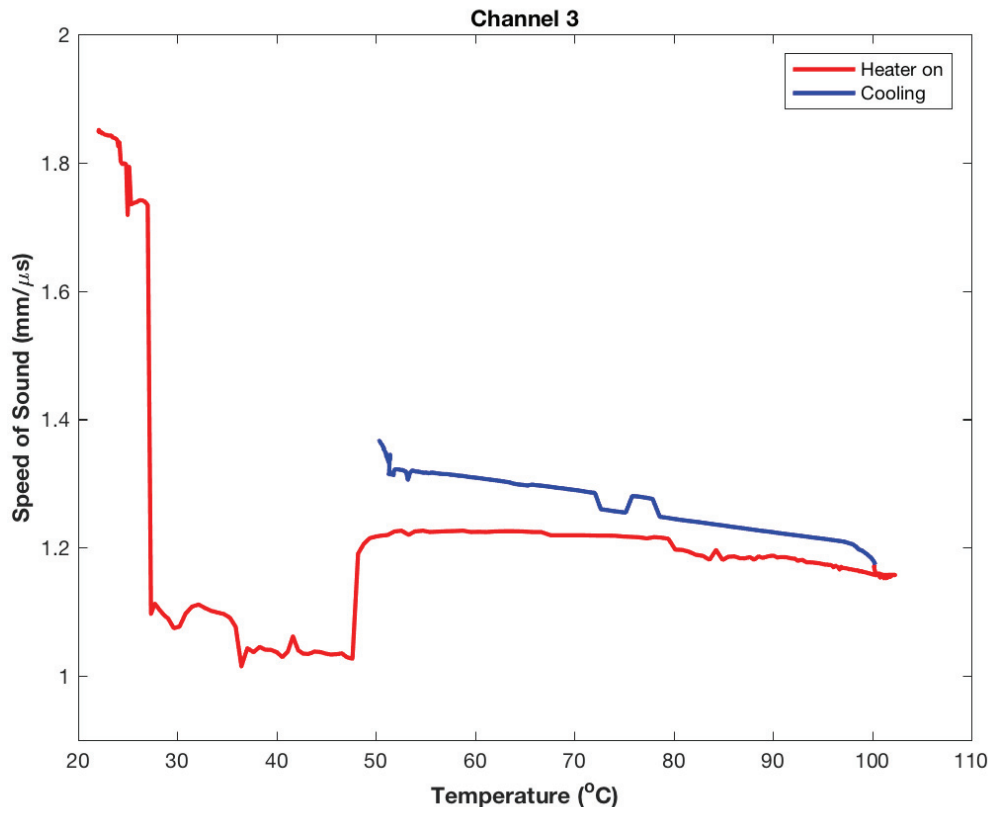


Figure B.53 The speed of sound versus temperature for channel 3.

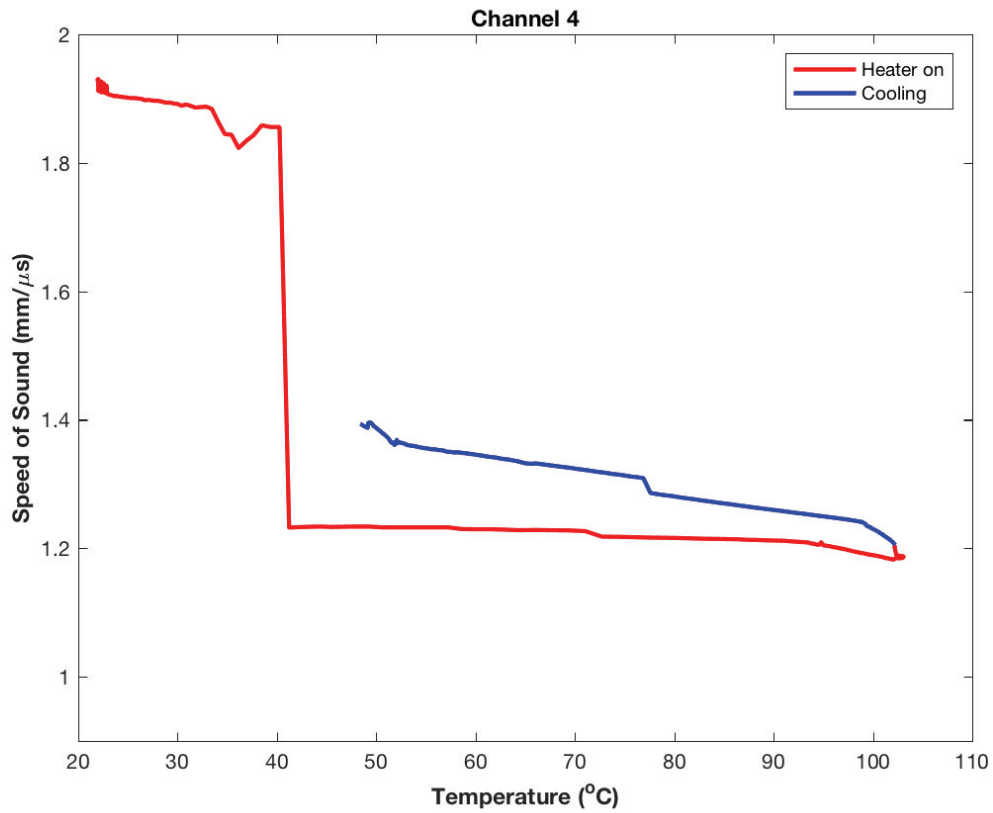


Figure B.54 The speed of sound versus temperature for channel 4.

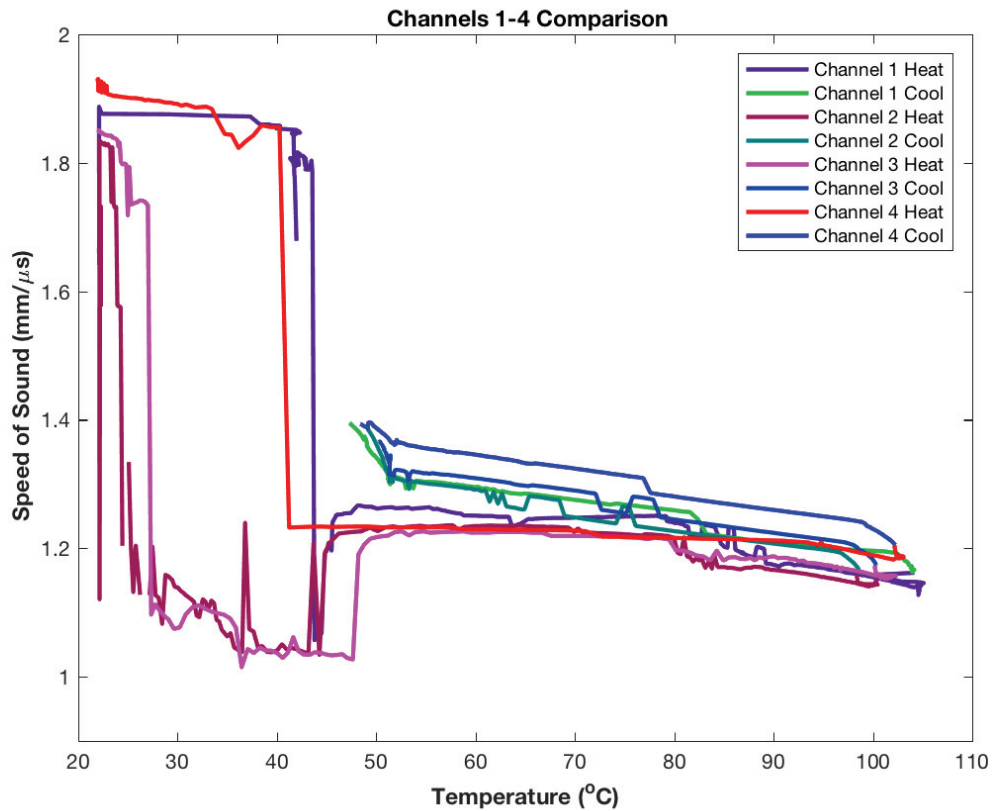


Figure B.55 Comparison of the speed of sound versus temperature plots for channels 1 through 4. The heating portion of the curves is provided in the red and purple colors whereas the cooling portion of the curves (when the heater is off) is provided in the blue and green colors.

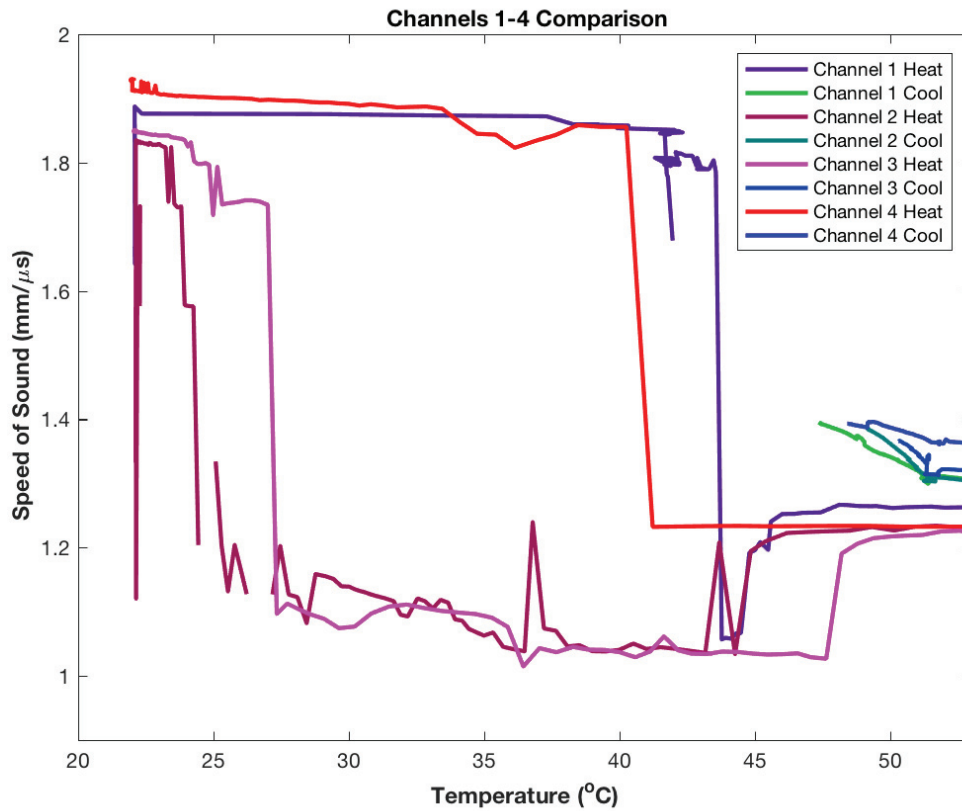


Figure B.56 Speed of sound versus temperature where the axes have been reduced such that the material's transition from solid to liquid during the melting stage is highlighted by the near step change in speed of sound.

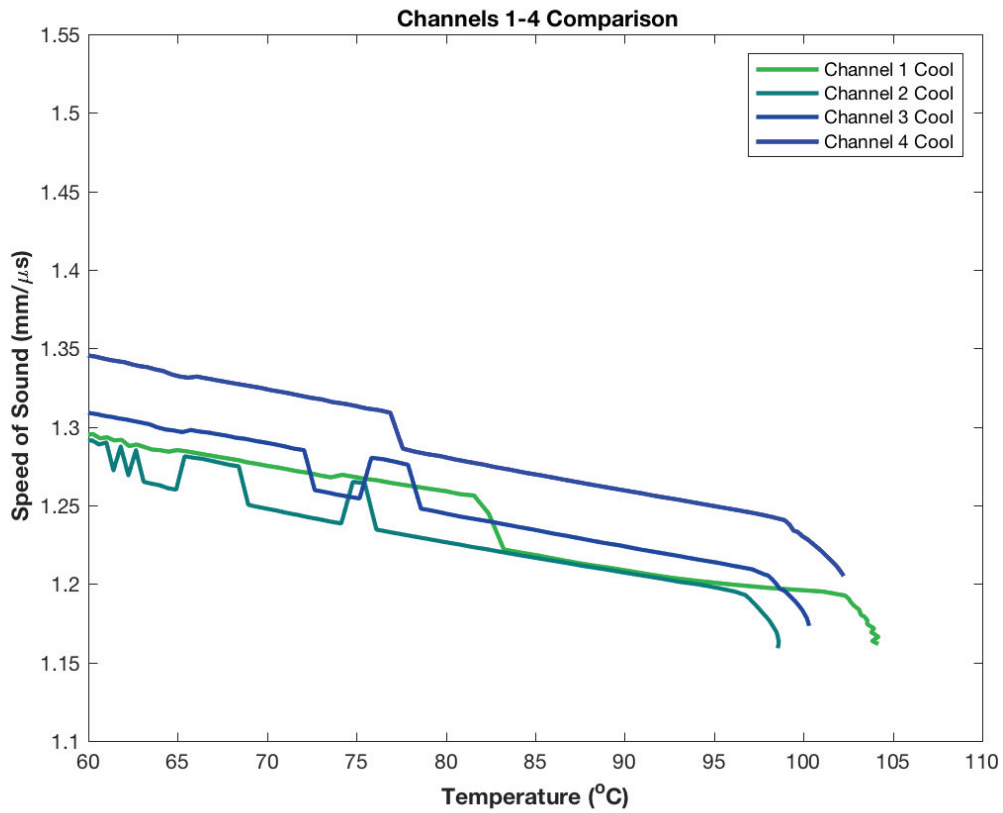
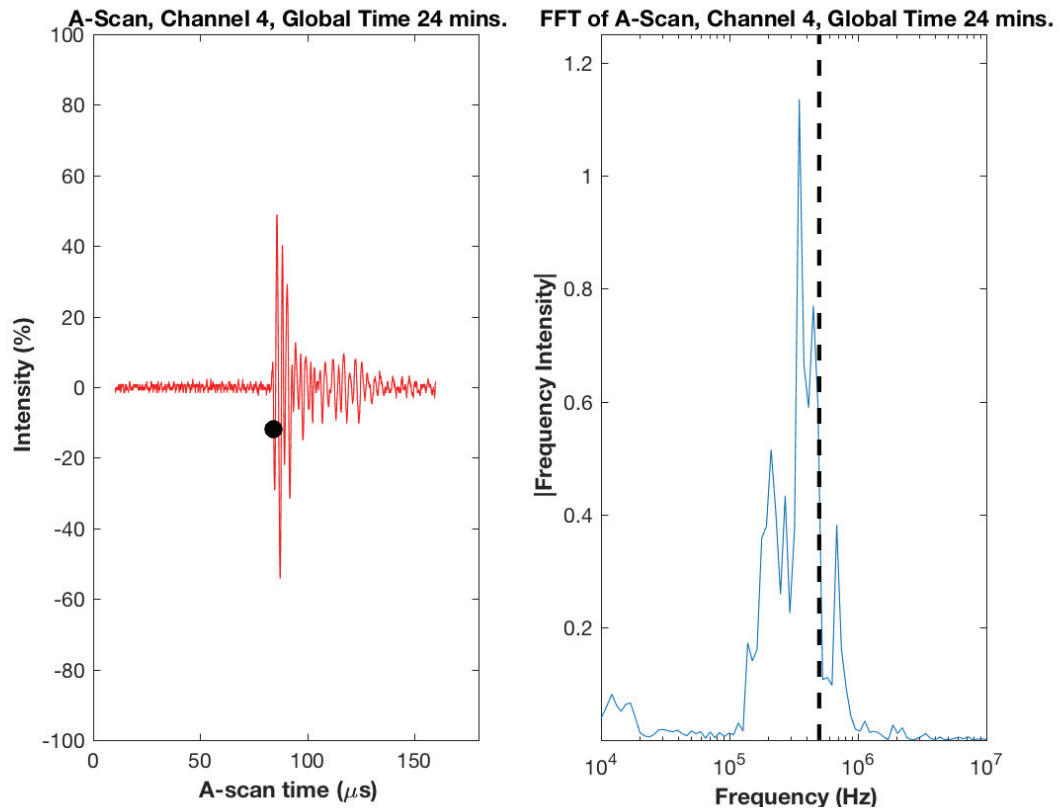


Figure B.57 Speed of sound versus temperature as the material is cooling.



B.58 A-scan (left) and Fast Fourier Transform (right) results for solid EcoSoya wax at 24 minutes into the test.

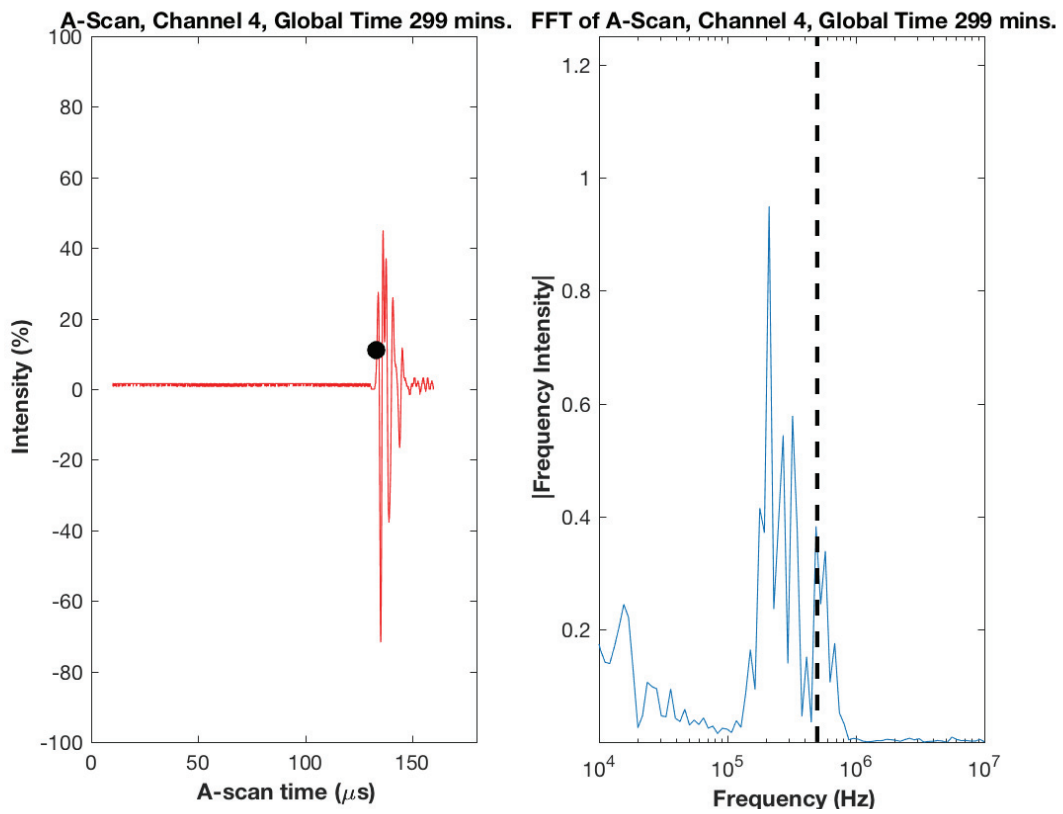


Figure B.59 A-scan (left) and Fast Fourier Transform (right) results for liquid EcoSoya wax at 299 minutes into the test.

B.4 Results from Machinist Wax in Small Acrylic Box Experiment Two

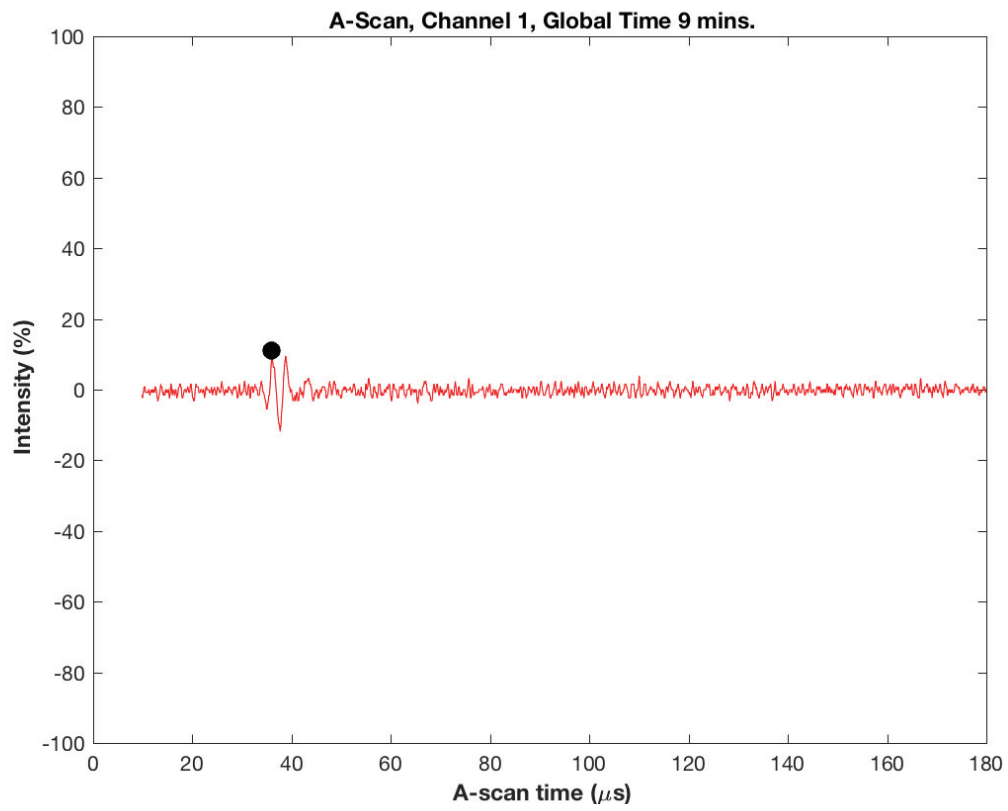


Figure B.60 A-scan associated with the solid machinist wax at 9 minutes into the test.

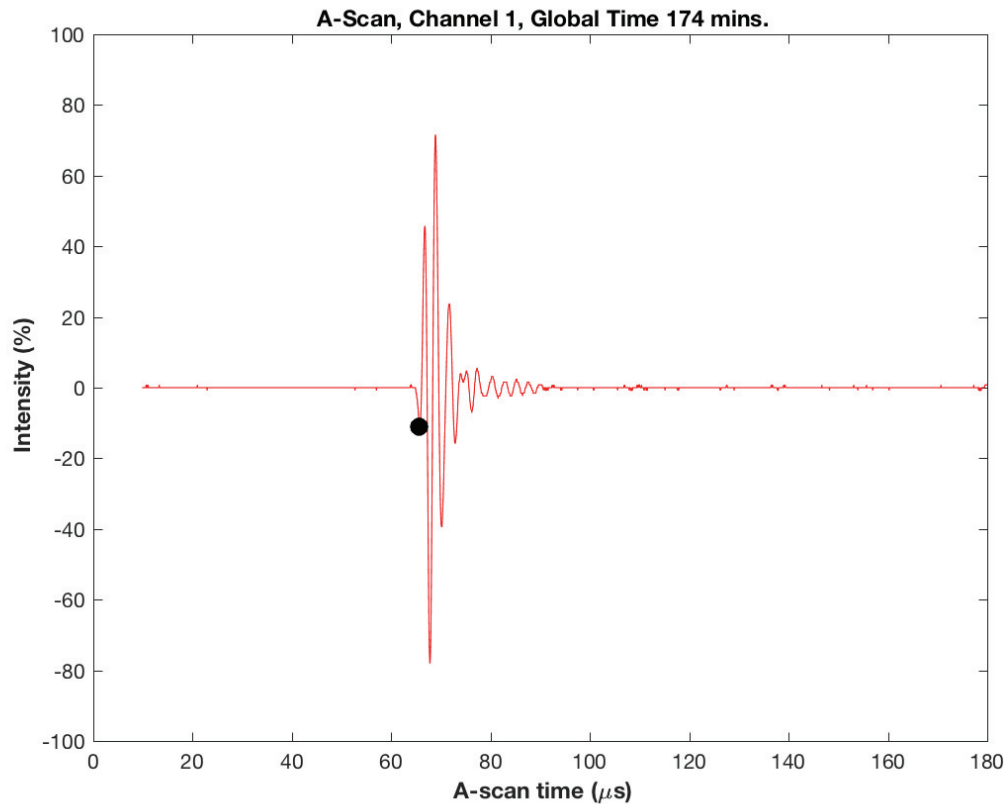


Figure B.61 A-scan associated with the liquid machinist wax at 174 minutes into the test.

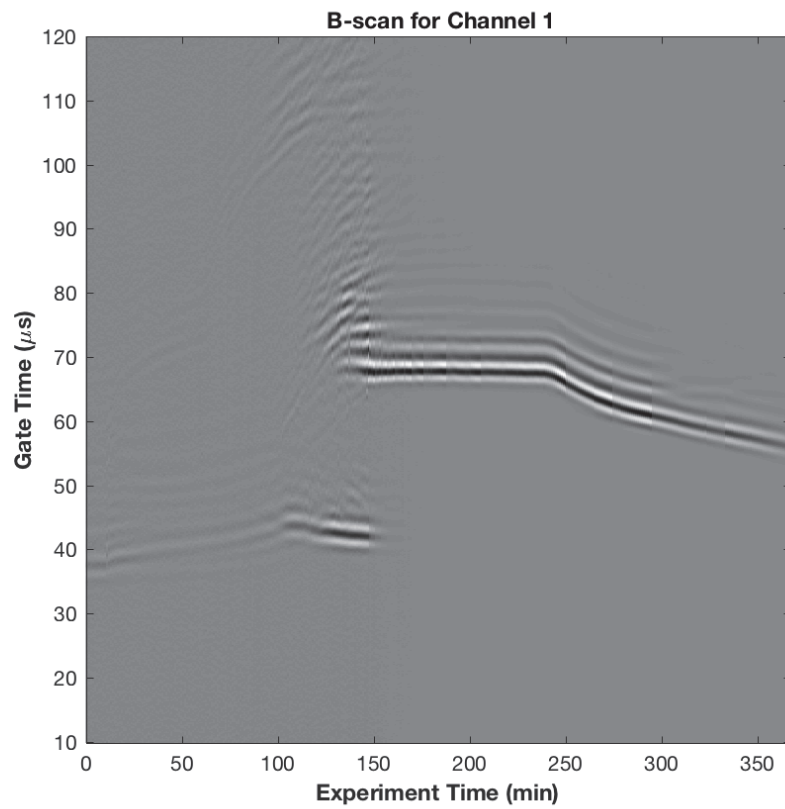


Figure B.62 B-scan for channel 1 data

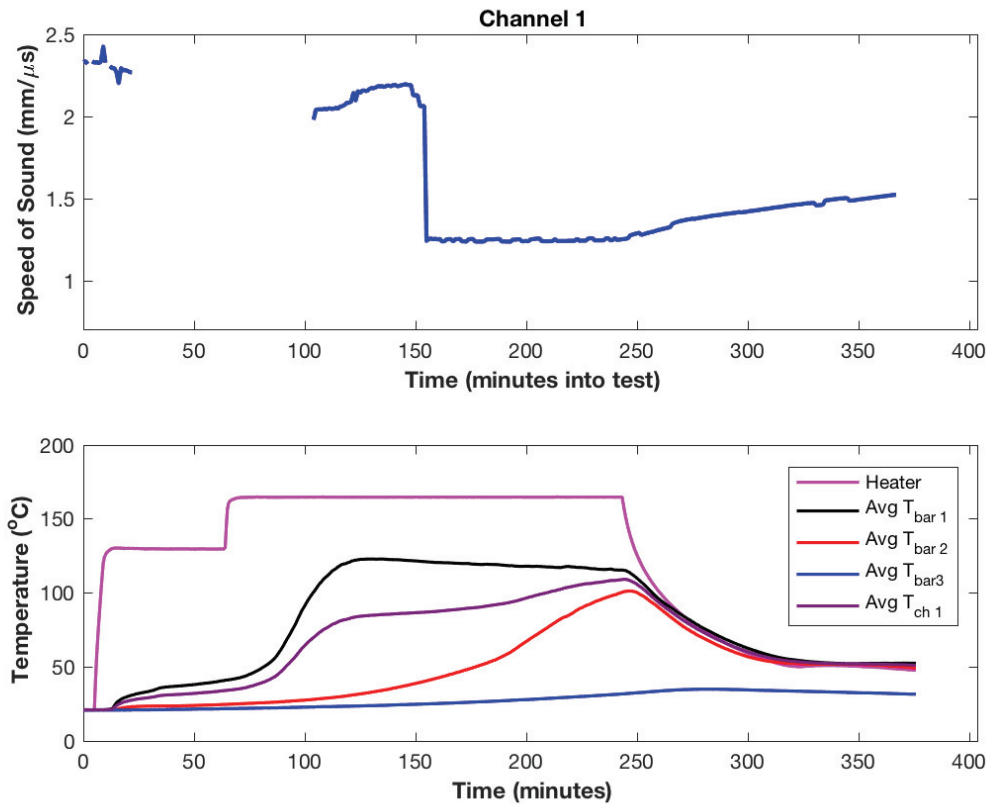


Figure B.63 Speed of sound (top) and temperature as measured by thermocouples (bottom) for data collected at channel 1, which is closest to the heater block.

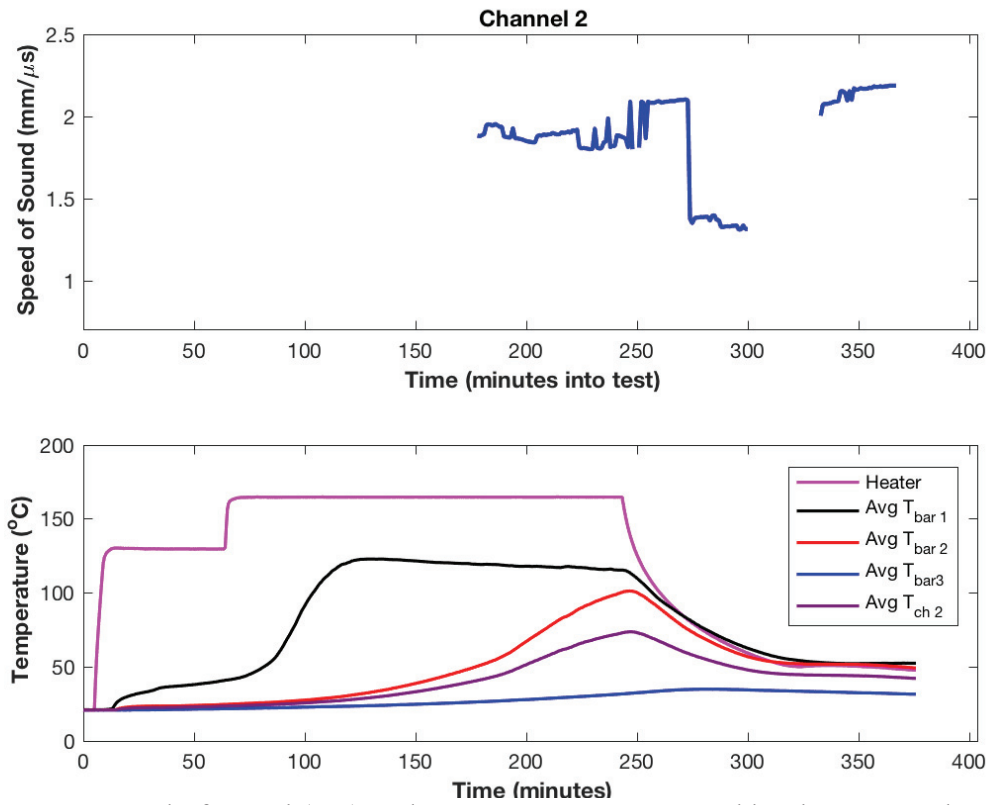


Figure B.64 Speed of sound (top) and temperature as measured by thermocouples (bottom) for data collected at channel 2, which is farthest from the heater block.

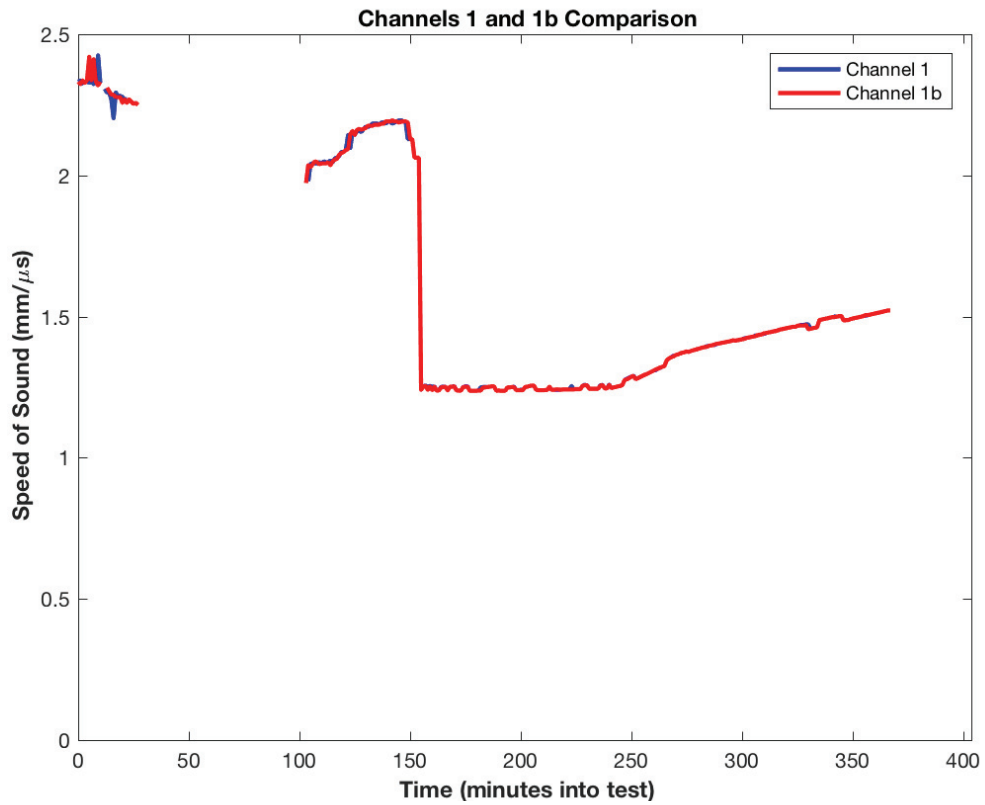


Figure B.65 Comparison of the speed of sound results for channels 1 and 1b.

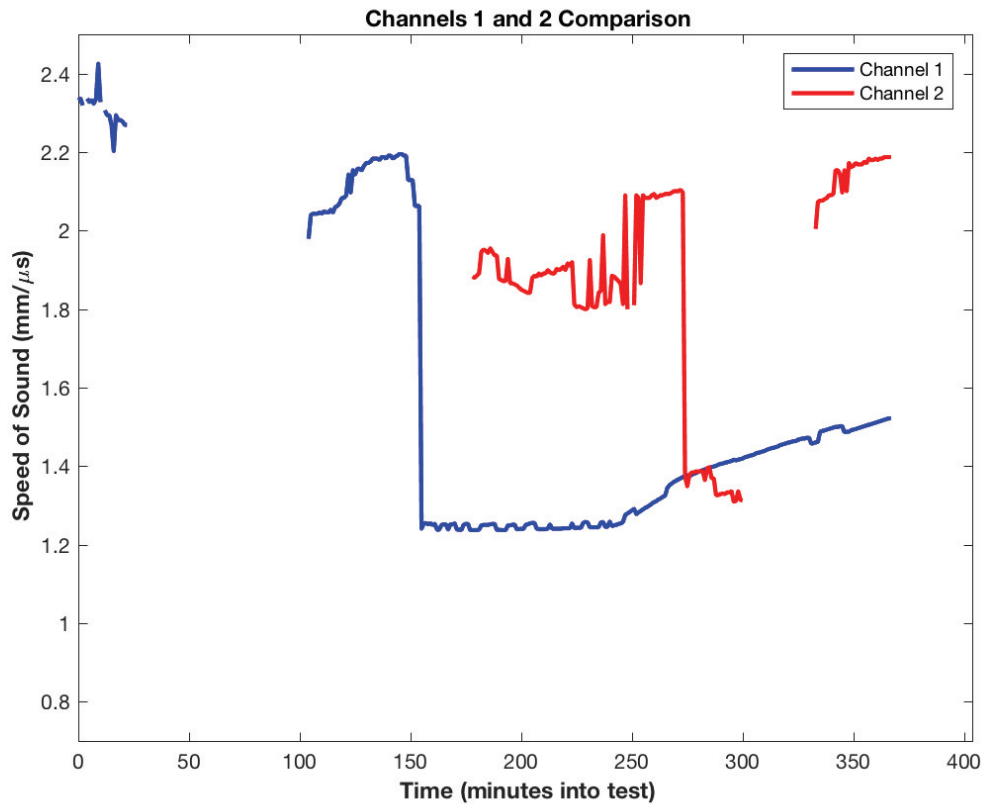


Figure B.66 Comparison of the speed of sound results for channels 1 (closest to the heater block) and 2 (farthest from the heater block).

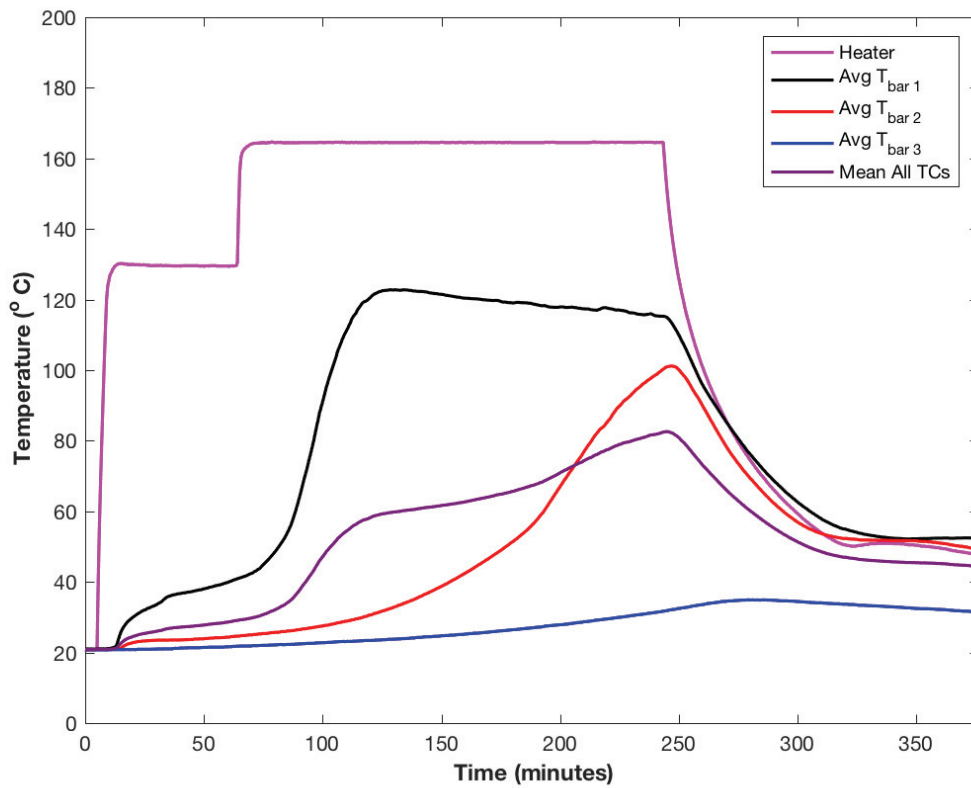


Figure B.67 Temperature values as obtained from thermocouple measurements throughout the experiment.

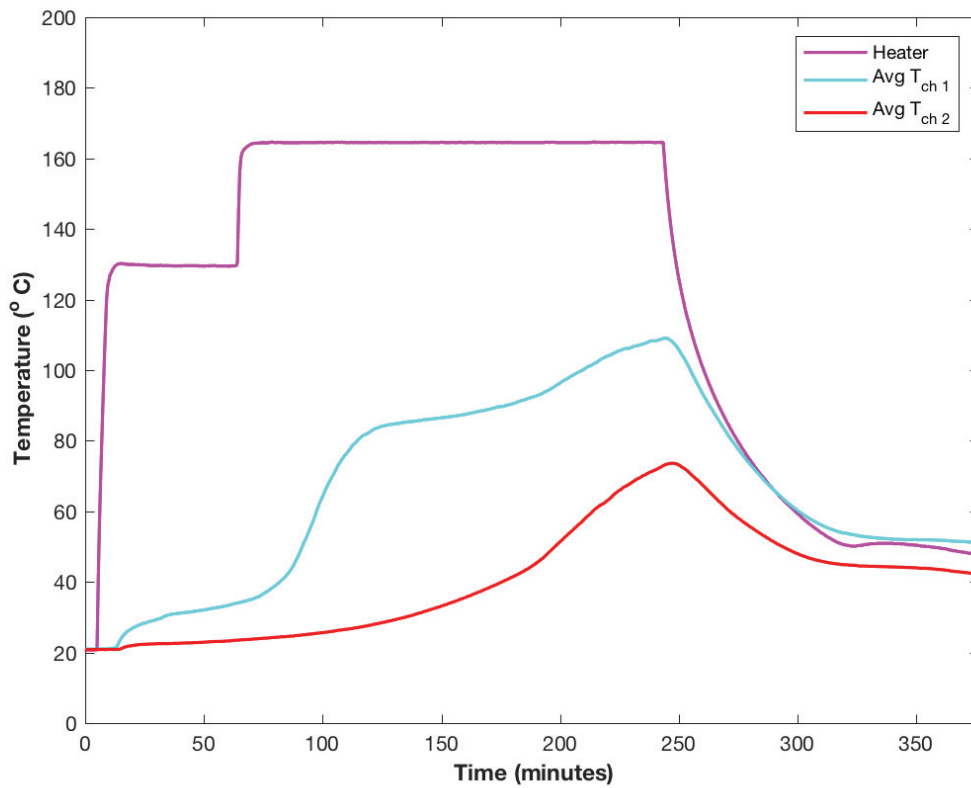


Figure B.68 The average temperature estimates obtained for the ultrasound probe path at channels 1 and 2 in the experimental setup.

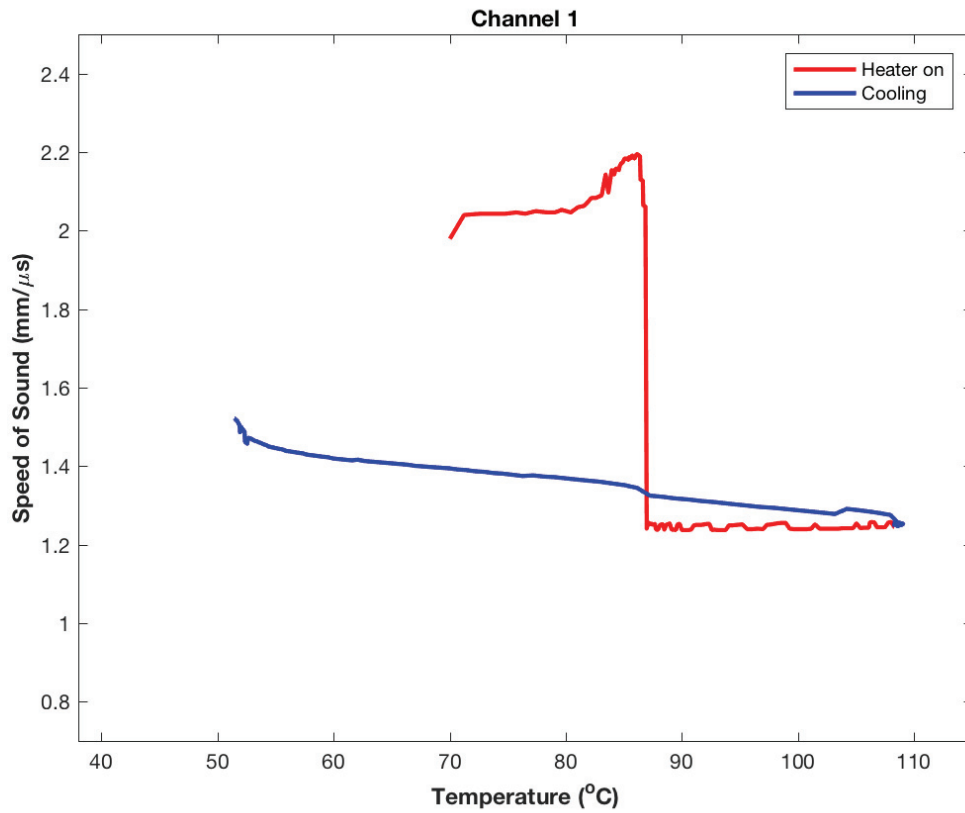


Figure B.69 Speed of sound versus temperature plot for channel 1.

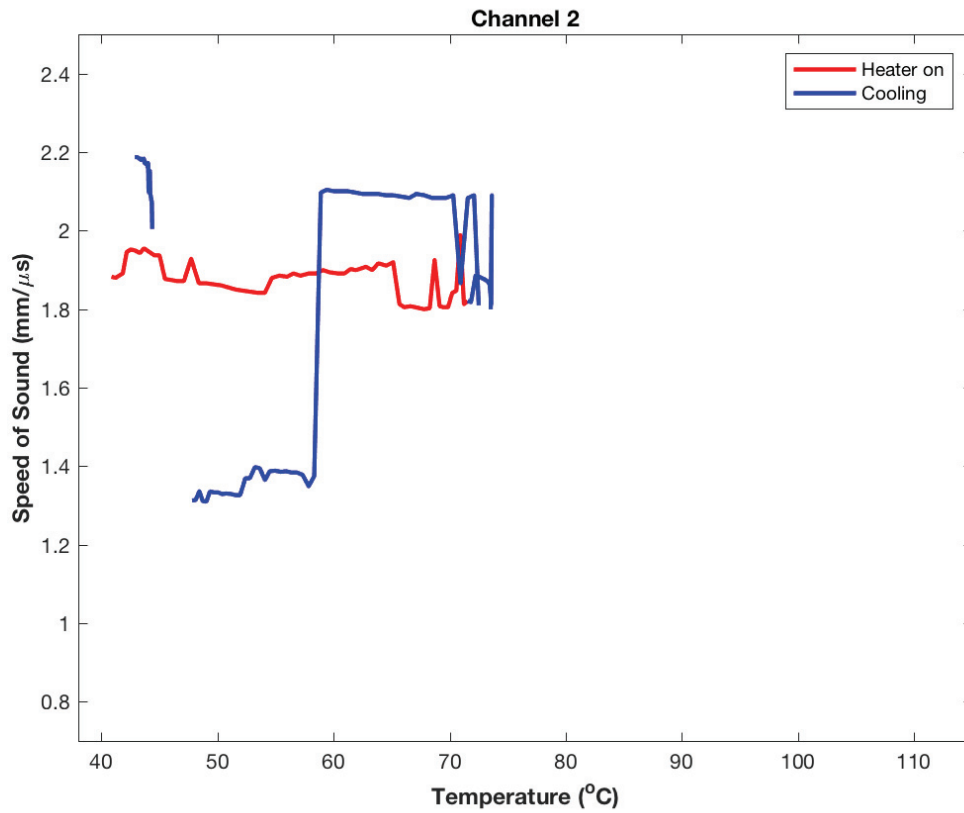


Figure B.70 Speed of sound versus temperature plot for channel 2.

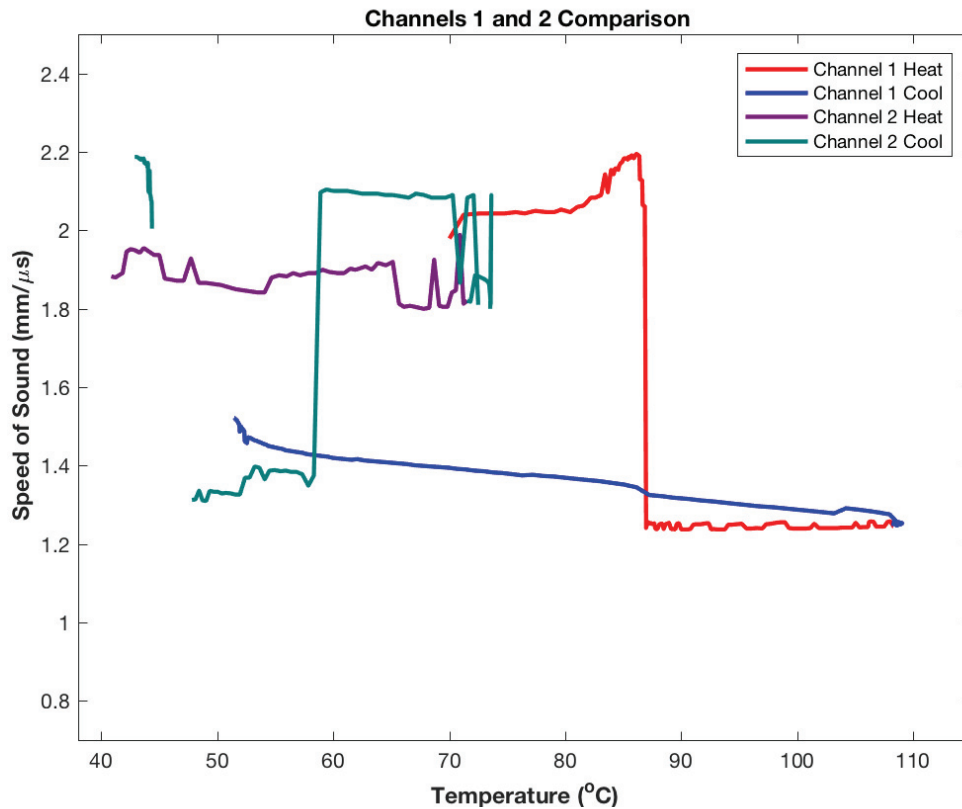


Figure B.71 Comparison of the speed of sound versus temperature plot for channel 1 and channel 2. The red and purple lines represent the heater being on during each test whereas the blue and green lines correspond to the cooling portion of each experiment.

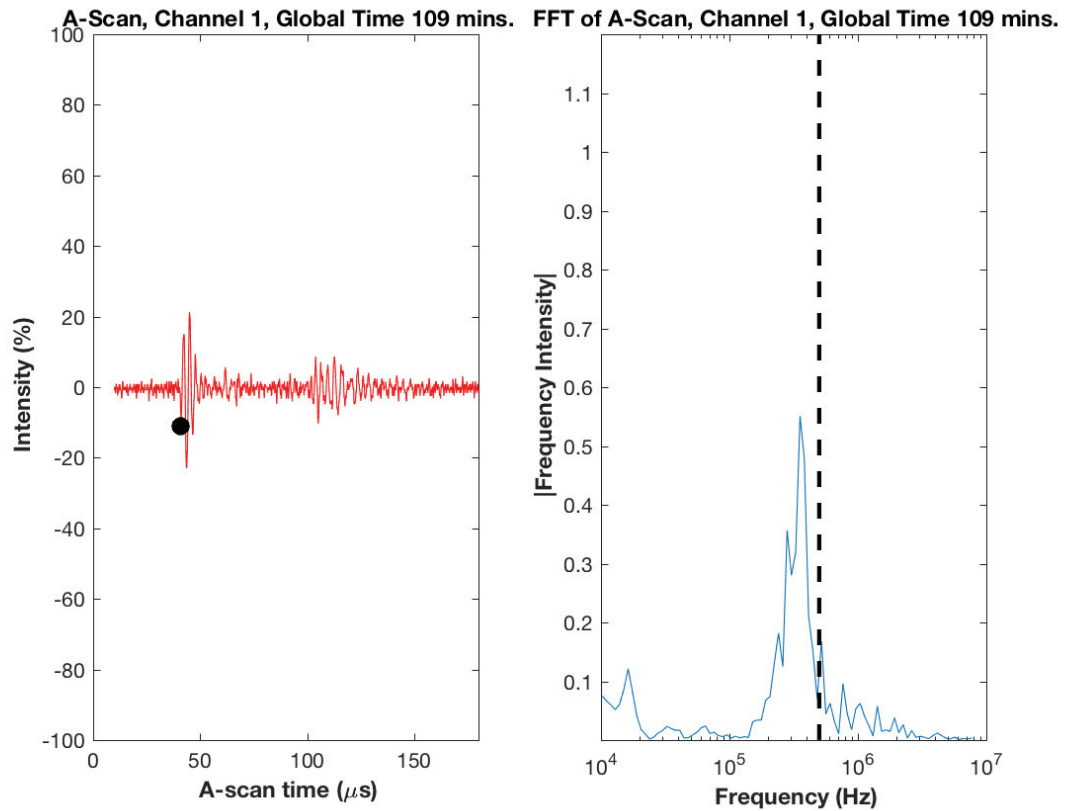


Figure B.72 A-scan (left) and Fast Fourier Transform (right) results for solid machinist wax at 109 minutes into the test.

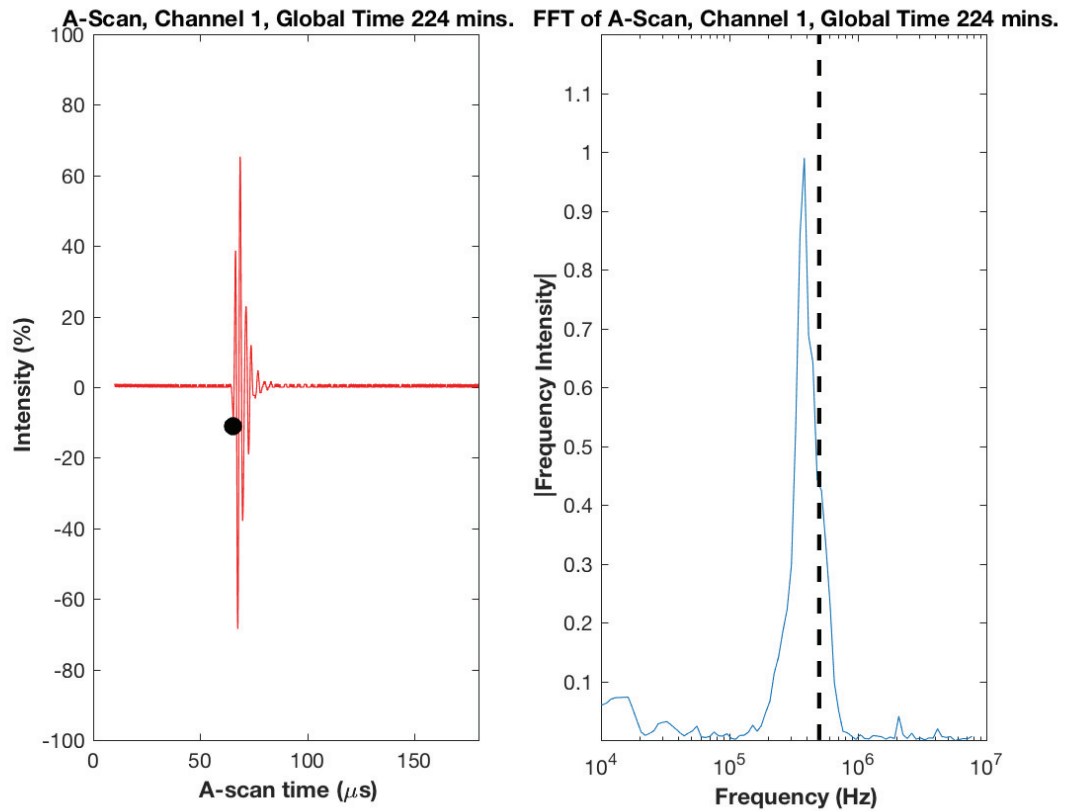


Figure B.73 A-scan (left) and Fast Fourier Transform (right) results for liquid machinist wax at 224 minutes into the test.

BIBLIOGRAPHY

- [1] B.P. Newberry. Paraxial Approximations for Ultrasonic Beam Propagation in Liquid and Solid Media with Applications to Nondestructive Evaluation, PhD Dissertation, Iowa State University, Engineering Mechanics Department, 1988.
- [2] M. Russon. United Launch Alliance Saves \$1m a Year By 3D Printing Rocket Components from Plastic. April 15, 2015. www.ibtimes.co.uk. Obtained: June 23, 2016.
- [3] M. Russon. Airbus Files Revolutionary Patent for 3D Printing an Aircraft's Exterior in Its Entirety. May 26, 2016. www.ibtimes.co.uk. Accessed June 23, 2016.
- [4] Nondestructive Bond Testing for Aircraft Composites. *Resources: Application Notes*. Olympus. Obtained from: <http://www.olympus-ims.com>. Obtained on July 19, 2016.
- [5] Photo taken by S. Stair at the Society of Plastics Engineers Automotive Composites Conference and Exhibition, Novi, MI, 2015.
- [6] B.W. Lewis. The Use of the Flexural Modulus in the Comparison of Fiber Orientation Models for Concentrated Suspensions in Short Fiber-Filled Thermoplastics. Master's thesis, Baylor University, August 2013.
- [7] Based on information received at a tour of the Waco Composites Facility on October 17, 2013.
- [8] A. Baker. Bonded Composite Repair of Metallic Aircraft Components – Overview of Australian Activities. AGARD-CP-550. 1995. pp. 1-14.
- [9] E.J. Barbero. *Introduction to Composite Materials Design*. CRC Press, 1998.
- [10] S.L. Stair. Non-Destructive Evaluation of Carbon Fiber-Reinforced Laminated Composites. Master's thesis, Baylor University, August 2014.
- [11] R.M. Jones. *Mechanics of Composite Materials: Second Edition*. Taylor and Francis, Inc., Philadelphia, PA (1999).
- [12] A. Siver. Mechanistic Effects of Porosity on Structural Composite Materials. Master's thesis, University of California, Los Angeles, August 2014
- [13] Baylor University Scientific Innovations in Complex Engineering Materials Laminate Quality Control Form, 2016.

- [14] R.W. Mailen. Investigation of Induced Thermo-Mechanical Response and Cure Kinetics During Processing of Carbon Fiber Reinforced Plastics. Master's thesis, Baylor University, December 2012.
- [15] G.V. Crowe. *An Introduction to Nondestructive Testing: Second Edition*, The American Society for Nondestructive Testing, 2009. <https://www.asnt.org/Store/ProductDetail?productKey=ba63a627-3222-4edc-bb3b-2b0c777366d3>.
- [16] M. Amirkhosravi, M. Pishvar, and M. Cengiz Altan. Improving laminate quality in wet lay-up/vacuum bag processes by magnet assisted composite manufacturing (MACM). *Composites: Part A*, March 2017.
- [17] H.F. Brinson and L.C. Brinson. *Polymer Engineering Science and Viscoelasticity: An Introduction*. Springer Publishing, 2008.
- [18] Sciolti, M.S., Frigione, M., and Aiello, M.A., Wet Lay-up Manufactured FRPs for Concrete and Masonry Repair: Influence of Water on the Properties of Composites and on Their Epoxy Components. *Jn. of Composites for Construction*, **14**(6):823-833, 2010.
- [19] M. Mariatti. and P.K. Chum. Effect of Laminate Configuration on the Properties of Glass Fiber-reinforced Plastics (GFRPs) Mixed Composites. *Jn. Of Reinforced Plastics and Composites*, **24**(16), pp. 1713-1721, 2005.
- [20] Hexion Technical Data Sheet for EPON 862, <http://www.hexion.com/Products/TechnicalDataSheet.aspx?id=3950>, Accessed July 25, 2016.
- [21] Pro-set Technical Data Sheet for 125 Resin/237 Hardener, <http://www.prosetepoxy.com/pdf/1%20laminating%20epoxy/125-237.pdf>, Accessed March 15, 2012,
- [22] ACP Composites Product Specification Sheet for 2x2 Twill Carbon Fiber Prepreg, <http://www.acpsales.com/pdfPrepreg-CF-2x2Twill.pdf>, Accessed October 2, 2013.
- [23] TCR Composites Resin Selector Guide, <http://tcrcomposites.com/portals/0/pdf/PrepregBasics/ResinSelectorGuide.pdf>, Accessed July 25, 2016.
- [24] B. Grimsley, P. Hubert, X. Song, R. Cano, A. Loos, and R. Pipes. Flow and Compaction During the Vacuum Assisted Resin Transfer Molding Process. *Proceedings of the 33rd International SAMPE Technical Conference*, Seattle, WA. November 2001. pp. 140-153
- [25] L. Khoun and P. Hubert. Cure shrinkage characterization of an epoxy resin system by two in situ measurement methods. *Polymer Composites*, pp. 1603-1610, 2010.

- [26] P. Hubert. Aspects of Flow and Compaction of Laminated Composite Shapes During Cure. Doctorate of Philosophy Thesis, The University of British Columbia, July 1996.
- [27] Md. Afendi, W.M. Banks, and D. Kirkwood. Bubble Free Resin for Infusion Process. *Composites Part A: Applied Science and Manufacturing*, **36**, pp. 739-746, 2005.
- [28] N.C. Correia, F. Robitaille, A. C. Long, C.D. Rudd, P. Simacek, and S.G. Advani. Analysis of the Vacuum Infusion Moulding Process: I. Analytical Formulation. *Composites Part A: Applied Science and Manufacturing*, **36**, pp. 1645-1656, 2005.
- [29] D. Modi, N. Correia, M. Johnson, A. Long, C. Rudd, and F. Robitaille. Active Control of the Vacuum Infusion Process. *Composites Part A: Applied Science and Manufacturing*, **38**, pp. 1271-1287, 2007.
- [30] A.T. Gunnarsson. Icelandic Boat Builders Switch to Resin Infusion. *REINFORCEDplastics*, **48**(5), pp. 34-36, May 2004.
- [31] G. Marsh. Prepregs – Raw Material for High Performance Composites. *REINFORCEDplastics*, **46**(10), pp. 24-28, October 2002.
- [32] Technology update: prepregs. *REINFORCEDplastics*, **47**(6), pp. 20-21, June 2003.
- [33] TORAY Industries, Inc.; “Carbon Fiber Prepreg, Method for Producing Same and Carbon Fiber Reinforced Composite Material” in Patent Application and Approval Process. *Politics and Government Week*, November 2013.
- [34] A.S. Generalov, A.S. Boichuck, and V.V. Murashov. Ultrasonic Strength Monitoring of Carbon-Fiber-Reinforced Plastics Based on Adhesive Prepregs. *Polymer Science, series D. Glues and Sealing Materials*, **6**(2), pp. 143-147, 2013.
- [35] ASNT. Introduction to Nondestructive Testing. <https://www.asnt.org/MinorSiteSections/AboutASNT/Intro-to-NDT>. Accessed July 13, 2016.
- [36] Z. Guo, L. Liu, B. Zhang, and S. Du, “Critical Void Content for Thermoset Composite Laminates,” *Journal of Composite Materials*, **43**(17) 2009.
- [37] S. Almeida and Z. dos Santos Nogueira Neto, “Effect of void content on the strength of composite laminates,” *Composite Structures*, **28**(2), p. 139-148, 1994.
- [38] R.D. Adams, and P. Cawley. Defect Types and Non-Destructive Testing Techniques for Composites and Bonded Joints. *Construction & Building Materials*, **3**(4), December 1989.

- [39] NDT for Composites Market to Experience Healthy Expansion. *Quality Magazine*, **52(6):S4(2)**, June 2013.
- [40] R. Bogue. New NDT Techniques for New Materials and Applications. *Assembly Automation*, **32(3)**, pp. 211-215, 2012.
- [41] J. Goglia. Composite Aircraft Damage: Assessment and Maintenance Require Specialized Training. *Aircraft Maintenance Technology Magazine*, September 2013.
- [42] GE Breaks Ground on World-Class Inspection Technologies Customer Applications Center and Training Academy at Lewistown, Pa Facility. *Defense & Aerospace Week*, pp. 48, October 2011.
- [43] B.C. Ray, S.T. Hasan, and D.W. Clegg. Evaluation of Defects in FRP Composites by NDT Techniques. *Jn. of Reinforced Plastics and Composites*, **26(12)**, pp. 1187-1192, June 2007.
- [44] A. Bendada, A. Sfarra, M. Genest, D. Paoletti, S. Rott, E. Talmy, C. Ibarra-Castanedo, and X. Maldague. How to Reveal Subsurface Defects in Kevlar Composite Materials After an Impact Loading Using Infrared and Optical NDT Techniques? *Engineering Fracture Mechanics*, **108**, pp. 195-208, August 2013.
- [45] J. Gryzagoridis, and D. Findeis. Impact Damage Detection on Composites Using Optical NDT Techniques. *Insight*, **52(5)**, pp. 248-251, May 2010.
- [46] J. Cuadra, P. Vanniamparambil, K. Hazeli, I. Bartoli, and A. Kontsos. Damage Quantification in Polymer Composites Using a Hybrid NDT Approach. *Composites Science and Technology*, **83**, pp. 11-21, April 2013.
- [47] A.M. Amaro, P.N.B. Reis, M.F.S.F. de Moura, and J.B. Santos. Damage Detection on Laminated Composite Materials Using Several NDT Techniques. *Insight: Non-Destructive Testing and Condition Monitoring*, **54(1)**, pp. 14-20, January 2012.
- [48] A.M. Amaro, J.B. Santos, and J.S. Cirne. Delamination Depth in Composites Laminates with Interface Elements and Ultrasound Analysis. *Strain: an Int. Jn. for Experimental Mechanics*, **47(2)**, pp. 138-145, April 2011.
- [49] B.S. Ben, B.A. Ben, Ch. Ratnam, and S.H. Yang. Ultrasonic Based Method for Damage Identification in Composite Materials. *Int. Jn. of Mechanics and Materials in Design*, **8(4)**, pp. 297-309, December 2012.
- [50] R. Asmatulu, and V. Movva. Evaluation of Fiber Reinforced Aircraft Composites Via Nondestructive Testing Techniques. *Proceedings of American Society for Mechanical Engineers (ASME) International Mechanical Engineering Congress and Exhibition (IMECE) 2012*, Houston, Texas, November 2012.

- [51] D.C. Giancoli. *Physics for Scientists & Engineers with Modern Physics, 4th Ed.*, Prentice Hall, NJ, (2008).
- [52] M.F. Markham. Measurement of the Elastic Constants of Fibre Composites by Ultrasonics. Division of Molecular Science, National Physical Laboratory, Teddington, Middlesex, England, *Composites*, pp. 145-179, March 1970.
- [53] S.I. Rokhlin, and W. Wang. Double Through-Transmission Bulk Wave Method for Ultrasonic Phase Velocity Measurements and Determination of Elastic Constants of Composite Materials. The Ohio State University, Columbus, OH, *American Journal of Acoustics Society*, **91**, pp. 3303-3312, June 6, 1992.
- [54] S.I. Rokhlin, and W. Wang. Ultrasonic Evaluation of In-Plane and Out-of-Plane Elastic Properties of Composite Materials. *Review of Progress in Quantitative Nondestructive Evaluation*, **8B**, pp. 1489-1496, 1989.
- [55] S. Stair, D.A. Jack, and J. Fitch. Non-Destructive Characterization of Ply Orientation and Ply Type of Carbon Fiber Reinforced Laminated Composites. *Proceedings of the Society of Plastics Engineers Automotive Composites Conference and Exhibition*, September 2014.
- [56] D.A. Jack, J. Fitch, and T. Vo. Method and system for non-destructive testing of composites. 2013. Patent Pending, PCT/US13/33187.
- [57] D.A. Jack, J.E. Fitch, T. Vo, C. Heimsoth, and S. Stair. Method and system for non-destructive testing of curved composites. 2015. Patent Pending, Application number 14/848009.
- [58] P.T. Marks, *Ultrasonic Testing Classroom Training Book*, American Society for Nondestructive Testing, Inc. Columbus, OH, 2007.
- [59] J. Rose, *Ultrasonic Waves in Solid Media*, Cambridge University Press, Cambridge, United Kingdom, 1999.
- [60] S. Stair, D. A. Jack, and J. Fitch. Ultrasonic Characterization of Fiber Reinforced Composites. *Proceedings of the Society of Plastics Engineers Automotive Composites Conference and Exhibition*, September 2013.
- [61] S. Stair, D.A. Jack, and J. Fitch. Characterization of Carbon Fiber Laminates: Determining Ply Orientation and Ply Type via Ultrasonic A-Scan and C-Scan Techniques. *SPE ANTEC 2014 – Proceedings of the Society of Plastics Engineers 72nd Annual Technical Conference and Exhibition*, Las Vegas, Nevada, April 2014.
- [62] A. Pilarski, and J.L. Rose. Ultrasonic Oblique Incidence for Improved Sensitivity in Interface Weakness Determination. *NDT International*, **21**(4), pp. 241-246, 1988.

- [63] A. S. Birks, and R.E. Green Jr. *Nondestructive Testing Handbook: Second Edition*. Volume 7: Ultrasonic Testing. American Society for Nondestructive Testing, Inc. 1991.
- [64] Ultrasonic Transducers Technical Notes, Olympus NDT. Obtained from www.olympusNDT.com
- [65] G. Workman and D. Kishoni, *Ultrasonic Testing (Nondestructive Testing Handbook Volume 7)*, American Society for Nondestructive Testing, Inc., Columbus, OH, 2007.
- [66] S. Stair, D. Moore, and D. Jack. Longitudinal and Shear Velocity Measurements in a Woven Fiber Reinforced Laminated Composite. *American Society of Non-Destructive Testing 24th Research Symposium*, Anaheim, California, March 2015.
- [67] R. B. Thompson, and T.A. Gray. A Model Relating Ultrasonic Scattering Measurements Through Liquid-Solid Interfaces to Unbounded Medium Scattering Amplitudes. Ames Laboratory, USDOE, Iowa State University, Ames, Iowa, *Jn. of the Acoustic Society of America*, **74**, pp. 1279-1290, October 1983.
- [68] S. Lonne, A. Lhemery, P. Calmon, S. Biwa, and F. Thevenot. Modeling of Ultrasonic Attenuation in Unidirectional Fiber Reinforced Composites Combining Multiple-Scattering and Viscoelastic Losses. *Review of Quantitative Nondestructive Evaluation*, **23**, pp. 875-882, 2004.
- [69] F. Simonetti, and P. Cawley. A Guided Wave Technique for the Characterization of Highly Attenuative Viscoelastic Materials. *Jn. of the Acoustical Society of America*, **114**(1), pp. 158-165, July 2003.
- [70] A.O.K. Nieminen, and J.L. Koenig. Macroscopic and Modern Microscopic NDE Methods for Adhesive-Bonded Structures. *Int. Jn. of Adhesion and Adhesives*, **11**(1):5-10, 1991.
- [71] W. Sachse and Y. Pao. On the determination of phase and group velocities of dispersive waves in solids. *J. Appl. Phys.* **49**(8), pp. 4320-4327, August 1978.
- [72] E.M. Strohm and M.C. Kolios. Sound velocity and attenuation measurements of perfluorocarbon liquids using photoacoustic methods. *IEEE International Ultrasonics Symposium Proceedings*, pp. 2368-2371, 2011.
- [73] P.L. Edwards. Ultrasonic signal distortion and its effects on velocity measurements in dispersive constant-group-velocity media. *J. Acoust. Soc. Am.* **73**(5), pp. 1608 -1615, May 1983.
- [74] W. Tsai, H. Chen, and T. Liao. An ultrasonic air temperature measurement system with self-correction function for humidity. *Measurement Science and Technology*, **16**, pp. 548-555, 2005.

- [75] K. N. Huang, C.F. Huang, Y.C. Li., and M.S. Young. High precision, fast ultrasonic thermometer based on measurement of the speed of sound in air. *Review of Scientific Instruments*, **73**, pp. 4022-4027, 2002.
- [76] T. Chen, K. T. Nguyen, S.L. Wen and C. Jen. Temperature measurement of polymer extrusion by ultrasonic techniques. *Meas. Sci. Technol.*, **10**, pp. 139-145, 1999.
- [77] K. Balasubramaniam, V.V. Shah, R. D. Costley, G. Boudreaux, and J.P. Singh. High temperature ultrasonic sensor for the simultaneous measurement of viscosity and temperature of melts. *Review of Scientific Instruments*, **70**(12), pp. 4618-4623, 1999.
- [78] I. Ihara and T. Tomomatsu. In-Situ measurement of internal temperature distribution of sintered materials using ultrasonic technique. *Materials Science and Engineering*, **18**, 2011.
- [79] I. Ihara and M. Takahashi. Ultrasound thermometry for monitoring internal temperature gradient in a heated material. *IEEE International Ultrasonics Symposium Proceedings*, pp. 1199-1202, 2009.
- [80] C. Simon, P. VanBaren, and E.S. Ebbini. Two-dimensional temperature estimation using diagnostic ultrasound. *Transactions on Ultrasonics, Ferroelectrics, and Frequency Control*, **45**(4), pp. 1088-1099, 1998.
- [81] D.G. Moore, C.C. Ober, P.J. Rodacy, and C.L. Nelson. Wave speed propagation measurements on highly attenuative heated materials. *2015 International Congress on Ultrasonics (2015 ICU Metz)*, France, 2015.
- [82] D.G. Moore, S.L. Stair, and D.A. Jack. Comparison of ultrasonic wave speed measurements on wax at elevated temperatures to numerical method predictions. *Review of Progress in Quantitative Nondestructive Evaluation*, July 2016.
- [83] C. M. Gregg. The Observation of Phase State and Temperature Using Noninvasive Ultrasonic Waves. Masters Thesis, Baylor University, May 2017.
- [84] S.J. Lau, D.G. Moore, S.L. Stair, and C.L. Nelson. Application of temporal moments and other signal processing algorithms to analysis of ultrasonic signals through melting wax. *Review of Progress in Quantitative Nondestructive Evaluation*, July 2015.
- [85] D.G. Moore, S.L. Stair, and D.A. Jack. The relationship between experimental geometry, heat rate, and ultrasound wave speed measurement while observing phase changes in highly attenuative materials. *Review of Progress in Quantitative Nondestructive Evaluation*, July 2017.

- [86] D.K. Hsu, and S.M. Nair. Evaluation of Porosity in Graphite-Epoxy Composite by Frequency Dependence of Ultrasonic Attenuation. *Review of Progress in Quantitative Nondestructive Evaluation*, **6B**, pp. 1185-1193, 1987.
- [87] I.M. Daniel, S.C. Wooh, and I. Komsky. Quantitative Porosity Characterization of Composite Materials by Means of Ultrasonic Attenuation Measurements. *Journal of Nondestructive Evaluation*, **11**(1), pp. 1-8, 1992.
- [88] W.N. Reynolds, and S.J. Wilkinson. The Analysis of Fiber-Reinforced Porous Composite Materials by the Measurement of Ultrasonic Wave Velocities. Nondestructive Centre, AERE Harwell, Didcot Oxfordshire, United Kingdom, *Ultrasonics*, IPC Press, pp. 159-163, July 1978.
- [89] P.C. Waterman, and R. Truell. Multiple Scattering of Waves. *Jn. Math. Phys.* **2**, pp. 512-537, 1961.
- [90] C.F. Ying, and R. Truell. Scattering of a Plane Longitudinal Wave by a Spherical Obstacle in an Isotropically Elastic Solid. *Jn. of Applied Physics*, **27**, pp. 1086-1097, 1956.
- [91] C.M. Sayers, and R.L. Smith. The Propagation of Ultrasound in Porous Media. Butterworth & Company, *Ultrasonics*, pp. 201-205, September 1982.
- [92] Wolfram MathWorld, Cubic Formula, (Searched Cardano's Formula), <http://mathworld.wolfram.com/CubicFormula.html>, Accessed July 14, 2016.
- [93] B.K. Sinha, E. Simsek, and Q.H. Liu. Elastic-Wave Propagation in Deviated Wells in Anisotropic Formations. *Geophysics*, **71**(6), pp. D191-D202, 2006.
- [94] A. Minachi, D.K. Hsu, and R.B. Thompson. Single-sided Determination of Elastic Constants of Thick Composites Using Acoustoultrasonic Technique. *J. Acoustical Society of America*, **96**(1), pp. 353-362, July 1994.
- [95] A.O.K. Nieminen. and J.L. Koenig. Macroscopic and Modern Microscopic NDE Methods for Adhesive-Bonded Structures. *Int. Jn. of Adhesion and Adhesives*, **11**(1), pp. 5-10, 1991.
- [96] A. Baker. Issues in the Certification of Bonded Composite Patch Repairs for Cracked Metallic Aircraft Structures. *Proceedings of the 20th Symposium of the International Committee on Aeronautical Fatigue (ICAF)*, Seattle, Washington, July 1999.
- [97] S. Stair and D.A. Jack, Comparison of experimental and modeling results for cure induced curvature of a carbon fiber laminate. *Polymer Composites*. Available online 11 December 2015. Doi: 10.1002/pc.23838.

- [98] B. Drinkwater, and P. Cawley. Measurement of the Frequency Dependence of the Ultrasonic Reflection Coefficient from Thin Interface Layers and Partially Contacting Interfaces. *Ultrasonics*, **35**, pp. 479-488, 1997.
- [99] W. Wang, B. Li, and S.I. Rokhlin. Ultrasonic Reflectivity Determination of Interfacial Properties in Adhesive Joints of Aluminum Alloys. *Review of Progress in Quantitative Nondestructive Evaluation*, **10B**, Ed. D.O. Thompson and D.E. Chimenti, Plenum Press, New York, pp. 1311-1318, 1991.
- [100] P. Cawley, and M.J. Hodson. The NDT of Adhesive Joints using Ultrasonic Spectroscopy. *Review of Progress in Quantitative Nondestructive Evaluation*, **8B**, pp. 1377-1384, 1989.
- [101] C.C.H. Guyott, and P. Cawley. Evaluation of the Cohesive Properties of Adhesive Joints Using Ultrasonic Spectroscopy. *NDT International*, **21**(4), pp. 233-240, August 1988.
- [102] B.W. Drinkwater, R.S. Dwyer-Joyce, and P. Cawley. A Study of the Interaction between Ultrasound and a Partially Contacting Solid-Solid Interface. *Proceedings: Mathematical, Physical and Engineering Sciences*, The Royal Society Publishing, **452**(1955), pp. 2613-2628, December 8, 1996. Obtained from <http://www.jstor.org/stable/52862>. Date obtained: June 15, 2015.
- [103] B.W. Drinkwater, R.S. Dwyer-Joyce, and A.M. Robinson. The Use of Ultrasound to Investigate Rough Surface Contact Phenomena. *Review of Progress in Quantitative Nondestructive Evaluation*, **18**, Ed. D.O. Thompson and D.E. Chimenti, Plenum Press, New York, pp. 1455-1462, 1999.
- [104] K. Vine, P. Cawley, and A.J. Kinloch. The Correlation of ultrasonic Measurements with Toughness Changes Durign the Environmental Degradataion of Adhesive Joints. *Review of Progress in Quantitative Nondestructive Evaluation*, **18**, Ed. D.O. Thompson and D.E. Chimenti, Plenum Press, New York, pp. 1525-1532, 1999.
- [105] K. Vine, P. Cawley, and A.J. Kinloch. Degradation Mechanisms in Adhesive Joints and the Implications for NDE. *AIP Conference Proceedings, Review of Progress in Quantitative Nondestructive Evaluation*, Edited by D.O. Thompson and D.E. Chimenti, **509**, pp. 1301-1308, 2000.
- [106] M.N. Webster, and R.S. Sayles. A Numerical Model for the Elastic Frictionless Contact of Real Rough Surfaces. *Transactions of the ASME: Jn. of Tribology*, **108**, pp.314-320, 1986.
- [107] A.M. Robinson, B.W. Drinkwater, and R.S. Dwyer-Joyce. Ultrasonic Investigation of the Stiffness of Graphite-Graphite Interfaces. *Review of Progress in Quantitative Nondestructive Evaluation*, **18B**, Ed. by D.O. Thompson and D.E. Chimenti, Kluwer Academic/Plenum Publishers, pp 1495-1500, 1999.

- [108] R.L. Vijaya Kumar, M.R. Bhat, and C.R.L. Murthy. Some Studies on Evaluation of Degradation in Composite Adhesive Joints Using Ultrasonic Techniques. *Ultrasonics*, **53**, pp. 1150-1162, March 2013.
- [109] L. Adler, S. Rokhlin, C. Mattei, G. Blaho, and Q. Xie. Angle Beam Ultrasonic Spectroscopy System for Quantitative Inspection of Adhesive Bonds. *Review of Progress in Quantitative Nondestructive Evaluation*, **18B**, Ed. by D.O. Thompson and D.E. Chimenti, Kluwer Academic/Plenum Publishers, pp. 1553-1559, 1999.
- [110] R. Maev and S. Titov, "Pulse-echo Ultrasonic NDE of Adhesive Bonds in Automotive Assembly," 9th European Conference on NDT, Berlin, 2006.
- [111] S.L. Stair, D.A. Jack, D.G. Moore, and C.L. Nelson. Investigation and Identification of the Bondline between a Carbon Fiber Reinforced Laminated Composite and a Metal Structure via Ultrasonic Techniques. *Proceedings of Society of Plastics Engineers (SPE) Automotive Composites Conference and Exhibition (ACCE)*, Novi, Michigan, September 2016.
- [112] G. Mantong, X. Changgan, D. Zeyi, and W. Tiemin. Contact Corrosion between Carbon Fiber Reinforced Composite Materials and High-Strength Metals. *ACTA Aeronautica et Astronautica Sinica (Hangkong Xuebao)*, Translation prepared by Edward A. Suter on August 9, 1995 (NAIC-ID(RS)T-0413-95), **14**(12), pp. 8662-8667, December 1993.
- [113] S.L. Stair, D.G. Moore, and C.L. Nelson. Bondline Boundary Assessment of Cohesive Bonded Solid Woven Carbon Fiber Composites using Advanced Diagnostic Methods. *19th World Conference on Non-Destructive Testing*, Munich, Germany, June 2016.
- [114] S.L. Stair, D.G. Moore, D.A. Jack, and C.L. Nelson. Ultrasonic Techniques for Inspecting the Bondline between a Composite and a Metal Structure, Journal article under review, 2016.
- [115] R. B. Pipes, J. Goodshell, A. Ritchey, J. Dustin and J. Gosse. Interlaminar stresses in composite laminates: Thermoelastic deformation. *Composites Science and Technology*, **70**:1605-1611, 2010.
- [116] Material Sound Velocities, Olympus NDT. Obtained from www.olympus-ims.com on May 17, 2017.
- [117] L. W. Schmerr Jr., *Fundamentals of Ultrasonic Nondestructive Evaluation: A Modeling Approach*, Springer US, 1998.

- [118] B. Praher, K. Straka, and G. Steinbichler, An Ultrasound-Based System for Temperature Distribution Measurements in Injection Moulding: System Design, Simulations, and Off-line Test Measurements in Water. *Meas. Sci. Tech.* **24**(8), August 2013.
- [119] A.A. El Sariti, J.A. Evans, and J.G. Truscott. The Temperature Dependence of the Speed of Sound in Bovine Bone Marrow at 750 kHz. *Ultrasound Med. Biol.*, **32**(6), June 2016.
- [120] N. Ukrainczyk, S. Kurajica, and J. Sipusiae. Thermophysical Comparison of Five Commercial Paraffin Waxes as Latent Heat Storage Materials. *Chemical and Biochemical Engineering Quarterly*, **24**(2), July 2010. Accessed April 29, 2017.
- [121] J.N. Reddy. *An Introduction to the Finite Element Method, Third Edition*. McGraw-Hill, New York, 2006.
- [122] Part 3: Reflection and Transmission of Ultrasonic Waves, Course material, Obtained from www.fast.u-psud.fr on May 19, 2017.
- [123] A.M. Dorado, and D.G. Moore. Composite Material Characterization using Acoustic Wave Speed Measurements. *ASNT Annual Conference 2015*, Salt Lake City, Utah, October 2015.